

# **Wear of Articulating Surfaces: Understanding Joint Simulation**

**STP 1472**

**Stanley Brown  
Lesley Gilbertson  
Victoria Good  
Editors**



STP 1472

*Wear of Articulating Surfaces:  
Understanding Joint Simulation*

Stanley A. Brown, Leslie N. Gilbertson  
and Victoria D. Good, editors

ASTM Stock Number: STP1472



ASTM  
100 Barr Harbor Drive  
PO Box C700  
West Conshohocken, PA 19428-2959

Printed in the U.S.A.

**ISBN: 0-8031-3415-0**  
**ISBN: 978-0-8031-3415-7**

Copyright © 2006 AMERICAN SOCIETY FOR TESTING AND MATERIALS INTERNATIONAL, West Conshohocken, PA. All rights reserved. This material may not be reproduced or copied in whole or in part, in any printed, mechanical, electronic, film, or other distribution and storage media, without the written consent of the publisher.

### **Photocopy Rights**

**Authorization to photocopy items for internal, personal, or educational classroom use, or the internal, personal, or educational classroom use of specific clients, is granted by the American Society for Testing and Materials International (ASTM) provided that the appropriate fee is paid to the Copyright Clearance Center, 222 Rosewood Drive, Danvers, MA 01923; Tel: 978-750-8400; online: <http://www.copyright.com/>.**

### **Peer Review Policy**

Each paper published in this volume was evaluated by two peer reviewers and at least one editor. The authors addressed all of the reviewers' comments to the satisfaction of both the technical editor(s) and the ASTM International Committee on Publications.

The quality of the papers in this publication reflects not only the obvious efforts of the authors and the technical editor(s), but also the work of the peer reviewers. In keeping with long-standing publication practices, ASTM International maintains the anonymity of the peer reviewers. The ASTM International Committee on Publications acknowledges with appreciation their dedication and contribution of time and effort on behalf of ASTM International.

Printed in Lancaster, PA  
January 2007

## Foreword

---

This publication *Wear of Articulating Surfaces: Understanding Joint Simulation*, contains papers presented at the symposium of the same name, held in Dallas Texas, on November 8, 2005. The symposium was sponsored by ASTM Committee F04 on Medical and Surgical Materials and Devices. Stanley A. Brown of the FDA Center for Devices and Radiological Health in Rockville Maryland, Leslie N. Gilbertson of Zimmer, Inc. in Warsaw, Indiana, and Victoria D. Good of Smith and Nephew in Memphis, Tennessee, presided as symposium chairmen and are the editors of the resulting publication. The editors would like to thank Joanne Tipper from the University of Leeds, UK for presenting an invited paper. We would also like to congratulate Dong Zhao a graduate student from the University of Florida, in Gainesville, Florida, who was the winner of the student paper contest. We would also thank the other authors who contributed to the symposium, some of whom traveled from the United States, Switzerland, Australia, Austria, and the United Kingdom. We would also like to express our thanks to the ASTM staff that helped make the symposium and publication possible: most notably Dorothy Fitzpatrick for her help with the symposium planning and Maria Langiewicz for handling the manuscript submissions and Teri Vail, Vera Langstone, and Kristen Girardi from the Journal of ASTM International at the American Institute of Physics who handled the electronic submissions and the publication preparation. We are indebted to all the reviewers who volunteered their time and expertise for their careful consideration and critique of the manuscripts. Stanley A. Brown FDA / CDRH, Rockville, Maryland, USA Leslie N. Gilbertson Zimmer Inc. Warsaw, Indiana, USA Victoria D. Good Smith and Nephew Memphis, Tennessee, USA

# Contents

---

<b>Overview</b>	vii
TOTAL KNEE	
<b>Effects of Patient and Surgical Alignment Variables on Kinematics in TKR Simulation Under Force-Control</b> —HANI HAIDER, PETER WALKER, JOHN DESJARDINS, AND GORDON BLUNN	3
<b>Wear Scar Prediction Based on Wear Simulator Input Data - A Preliminary Artificial Neural Network Approach</b> —DIEGO OROZCO, THORSTEN SCHWENKE, AND MARKUS A. WIMMER	17
<b>Slip Velocity Direction Impacts Wear in TKA</b> —THORSTEN SCHWENKE, LAURA L. BORGSTEDTE, ERICH SCHNEIDER, AND MARKUS A. WIMMER	25
<b>A Simulator study of TKR kinematics using modeled soft tissue constraint: Virtual soft tissue control for knee simulation</b> —BRUCE F. WHITE, DARRYL D'LIMA, ALBERT C. DRUEDING, JOHN COX, AND FOREST J. CARIGNAN	30
<b>Computational Wear Prediction of UHMWPE in Knee Replacements</b> —DONG ZHAO, W. GREGORY SAWYER, AND BENJAMIN J. FREGLY	45
VERTEBRAL DISC	
<b>Retrieval Analysis of Total Disc Replacements: Implications for Standardized Wear Testing</b> —STEVEN KURTZ, RYAN SISKEY, LAUREN CICCARELLI, ANDRÉ VAN OOIJ, JOHN PELOZA, AND MARTA VILLARRAGA	53
<b>Surface Texture Analysis of Artificial Discs Wear-Tested under Different Conditions and Comparison to a Retrieved Implant</b> —PHILIPPE E. PARE, FRANK W. CHAN, PATRICK BUCHHOLZ, STEVEN KURTZ, AND MCCOMBE PETER	65
LUBRICANTS AND GENERAL	
<b>Estimation of Osteolytic Potential of Non-Crosslinked and crosslinked Polyethylenes and Ceramic-on-Ceramic Total Hip Prostheses</b> —JOANNE L TIPPER, ALISON L. GALVIN, EILEEN INGHAM, AND JOHN FISHER	75
<b>The Effects of Implant Temperature on Lubricant Protein Precipitation and Polyethylene Wear in Joint Simulation Studies</b> —YEN-SHUO LIAO AND MARK HANES	91
<b>Load Profile and Fluid Composition Influence the Soak Behavior of UHMWPE Implants</b> —THORSTEN SCHWENKE, ERICH SCHNEIDER, AND MARKUS A. WIMMER	97

<b>The Effects of Load Soak Control on the Wear of UHMWPE at Various Hydration Levels in a Joint Simulation Study—YEN-SHUO LIAO AND MARK HANES</b>	102
<b>A Tracer Method to Determine Extremely Low Wear Rates of Ultra-High Molecular Weight Polyethylene—JOACHIM KUNZE AND MARKUS A. WIMMER</b>	107
TOTAL HIP	
<b>Differences of the Mechanical Setup of Hip Simulators and their Consequences on the Outcome of Hip Wear Testing —GEORG REINISCH, JOACHIM SCHOERG, KURT P. JUDMANN, WOLFGANG PLITZ, AND FRIEDRICH FRANEK</b>	115

# Overview

---

Papers were invited for the Symposium on Wear of Articulating Surfaces: Understanding Joint Simulation, sponsored by ASTM Committee F04 on Medical and Surgical Materials and Devices. The symposium was held November 8, 2005 in Dallas, Texas, in conjunction with the November 8-11, 2005 standards development meetings of Committee F04.

Simulator wear testing of orthopedic joint systems is a work-in-progress. The current hip simulator wear testing methodology has come the closest to simulating clinical results in terms of ranking of articulating systems. However, there continue to be opportunities for improvement since simulator results tend to be significantly lower than clinical wear. Knee wear simulation is not as well understood as the hip and is much more complicated to simulate than hips. Kinematics and loads can vary with implant design and produce significantly different results. Additionally, due to the complex shape of the implant, it is difficult to quantify and compare retrievals to simulator worn implants. Simulator wear of the spinal joint implant is in its infancy. There is even less knowledge about the requirements for wear simulation than either of the other two joint systems. Clearly there is a need for understanding in all these articulating joint simulations. The goals of the symposium were to increase our knowledge of wear simulation, gain knowledge about the relationship of simulated wear to clinical wear, and to ultimately create standards that are useful in evaluating the systems of the future.

The papers in this proceedings are in the same order in which they were presented at the symposium. Therefore the sequencing is based in part on the timing of a daily schedule. The first session addressed issues of modeling and motion constraints of total knee simulation. These included force control, soft tissue constraints, and slip velocity. Two papers presented new concepts of modeling with neural networks or computational prediction of wear. The second session addressed simulation of total disc prostheses. These papers represent the early stages of establishing a correlation between wear patterns seen in simulators with those seen in the limited number of retrievals. The third session contained a variety of papers on lubricants and examination of wear debris and their biological effects. Emphasis was made on the importance, yet complexity of effectively separating lubricant absorption from effects of wear and the problem of measuring low wear rates associated with radiation modified polyethylene. The final paper examined different setups for total hip simulators.

*Stanley A. Brown*  
FDA / CDRH,  
Rockville, Maryland, USA

*Leslie N. Gilbertson*  
Zimmer Inc.  
Warsaw, Indiana, USA

*Victoria D. Good*  
Smith and Nephew  
Memphis, Tennessee, USA

## **SECTION I: TOTAL KNEE**

Hani Haider, Ph.D.,<sup>1</sup> Peter Walker, Ph.D.,<sup>2</sup> John DesJardins, M.S.,<sup>3</sup> and Gordon Blunn, Ph.D.<sup>4</sup>

## Effects of Patient and Surgical Alignment Variables on Kinematics in TKR Simulation Under Force-Control

**ABSTRACT:** Simulation of total knee replacement (TKR) is typically achieved by integrating sliding/rolling motions and loads between the implant's articulating surfaces during an activity cycle such as walking. Clinically, however, important variations in implant alignment and duty occur due to variability in patient anatomy/arthritis deformity, compounded by choices or errors in surgical installation. This study investigated the effects of the activity cycle severity, frontal plane alignment, relative femoral/tibial component rotational position, and the tightness of the posterior cruciate ligament (PCL). Seven different (four fixed-bearing and three mobile-bearing) cruciate-retaining TKRs with different inherent constraints were tested on a force-control knee simulator. As well as the ISO standard wave forms for walking, an Enhanced Duty Cycle was used. The resulting anterior-posterior displacements and axial rotations were increased with the Enhanced Duty Cycle. Changing the line of action of the compressive force in the frontal plane (varus-valgus over/under-correction) did not appreciably change the kinematics. Rotating the tibial component shifted the rotational curves in the same direction as the misalignment. The PCL tightness produced the most noticeable effect on kinematics; a tight PCL reduced both displacements and rotations, and a loose PCL did the opposite.

**KEYWORDS:** knee simulator, knee kinematics, mobile bearing knee, knee surgical technique, TKR wear

### Introduction

Two important design goals of total knee replacement are often stated. They are to restore the normal function of the knee and to minimize the deformation and wear of the bearing surfaces. Both function and durability are influenced by the femoral-tibial kinematics. In order to study these factors, knee-simulating machines can play an important role. When testing different total knee replacements (TKRs) in a knee simulator, the kinematic outputs of different TKR designs should be related to their inherent constraints. This is important for predicting the relative amounts of wear, which will be related to the sliding distance and the loads acting between the metal and plastic surfaces incremented during each activity cycle. Previous studies on knee test rigs have shown the importance of input force variables, including simulated muscle actions, on the output displacements and rotations [1–8]. In dynamic studies using the Instron-Stanmore Knee Simulator, the kinematics of different TKR designs subjected to the same input forces, including anterior-posterior (A-P) shear and internal-external torque, were shown to be highly variable [7,9,10]. Such differences in kinematics have also been measured in vivo using fluoroscopic and RSA imaging techniques [11–17]. These studies have also shown considerable variations in the kinematics between different patients, even with the same design of TKR implanted.

A key question is to what extent the patient and surgical factors affect the kinematics of total knee replacements. This will indicate the relative importance of these factors, and also determine if some designs are more sensitive to variations than others. It is interesting to compare the behavior of fixed-bearing and mobile-bearing knees, which have totally different constraint mechanics. This study will address the effect of the input activity cycle (standard walking cycle and enhanced duty cycle), the frontal

---

Manuscript received January 12, 2006; accepted for publication August 31, 2006; published online November 2006. Presented at ASTM Symposium on Wear of Articulating Surfaces on 8 November 2005 in Dallas, TX; S. A. Brown, L. N. Gilbertson, and V. D. Good, Guest Editors.

<sup>1</sup> Associate Professor, Department of Orthopaedic Surgery and Rehabilitation, University of Nebraska Medical Center, Omaha, NE 68198-5360, e-mail: hhaider@unmc.edu

<sup>2</sup> Research Professor, New York University Medical Center and Hospital for Joint Diseases, New York, NY 10010.

<sup>3</sup> Research Associate, Department of Bioengineering, Clemson University, Clemson, South Carolina 29634-0905.

<sup>4</sup> Professor, Centre for Biomedical Engineering, Royal Free and University College Medical School, Stanmore, UK.

## 4 WEAR OF ARTICULATING SURFACES

TABLE 1—Details of the seven TKR designs tested.

				
<b>Name &amp; manufacturer</b>	J&J DePuy PFC $\Sigma$	Stratec CC	Smith & Nephew Genesis II	Zimmer NexGen CR
<b>Type &amp; Description</b>	Fixed Bearing. Moderate Constraint	Fixed Bearing. Low Constraint	Fixed Bearing. External pre-rotation inherent in the femoral design	Fixed Bearing
<b>Tibial Alignment</b>	Horizontal	5° posterior slope	3° posterior slope	5° posterior slope

			
<b>Name &amp; manufacturer</b>	J&J DePuy LCS	Zimmer MBK	Sulzer SAL MBK
<b>Type &amp; Description</b>	Rotating Platform. Unrestricted rotation	Mobile Bearing. Freedom of motion: $\pm 20^\circ$ rotation. 4-5 mm AP travel	Mobile Bearing. Unrestricted rotation. Limited AP
<b>Tibial Alignment</b>	10° posterior slope	5° posterior slope	3° posterior slope

*Knee Simulator*

plane alignment (varus and valgus), the relative rotational position between the femoral and tibial components (internal-external), and the tightness of the posterior cruciate ligament (PCL; tight and loose).

### Materials and Methods

#### *TKR's Tested*

One sample of each of seven different TKR designs was tested. Four were fixed-bearing designs, and three were mobile bearings, as described in Table 1. All of the fixed-bearing TKRs were designed for PCL retention although partial release or “recession” is sometimes carried out in order to obtain acceptable motion at surgery and to avoid excessive tightness in high flexion. Posterior cruciate substituting (PS) designs were not included because an important part of our protocol was to assess the effect of PCL tightness. In any case, the cam in most PS designs is not operative in the flexion range of the stance phase of walking used in our tests.

#### *Knee Simulator*

The Instron-Stanmore 4-Station Knee Simulator (Instron Corp., Canton, Massachusetts, USA) was used [7,9,18–20]. The femoral components were mounted in the fixtures such that the axis of flexion-extension imposed by the machine passed through the average radius of curvature of the distal-posterior arc of the femoral condyles, in order to minimize camming (Fig. 1). “Camming” is a term coined by the authors to represent the vertical fluctuation in the distal contact points of the femoral condyles during flexion. Therefore, any variation in the femoral sagittal distal and posterior radii would cause the force-engaged tibial component to fluctuate vertically during flexion (following the femoral distal contact points as if they were a cam shaft). Therefore, camming is inherent in all current knee wear simulators which all do have a proximally-distally fixed flexion axis. In our tests, this effect was minimized by fine adjustment/alignment of the femoral component in the anterior posterior (A-P), proximal-distal, and varus-valgus directions. The camming was measured and found to be less than 0.85 mm for the range of TKRs tested.

The tibial components were mounted either horizontally or with a posterior slope according to the surgical technique. Prealignment of the components was carried out at zero degrees flexion with a small axial force in the range 10–100 N, so that the femoral condyles were seated in the bottom of the tibial dishes.

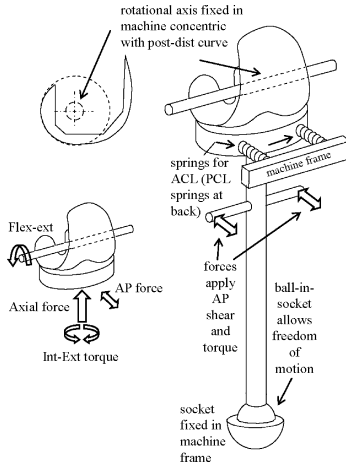


FIG. 1—Mechanical layout of the knee simulator.

The holder for the tibial component was free to move in A-P and medial-lateral translations and internal-external and varus-valgus rotations. However, to simulate the restraint of ligaments and capsular structures, linear springs were mounted between the holder and the frame of the machine (Figs. 2). These springs were set as recommended in the studies of [21–23], which provided the closest approximation with this mechanism to the physiological role of ligamentous restraint from published cadaveric studies [24].

Anterior tibial translation (ACL resected) was restrained by a pair of springs with 7.24 N/mm stiffness each, initially set with a 2.5-mm gap to remove stiffness around the neutral position. Posterior tibial

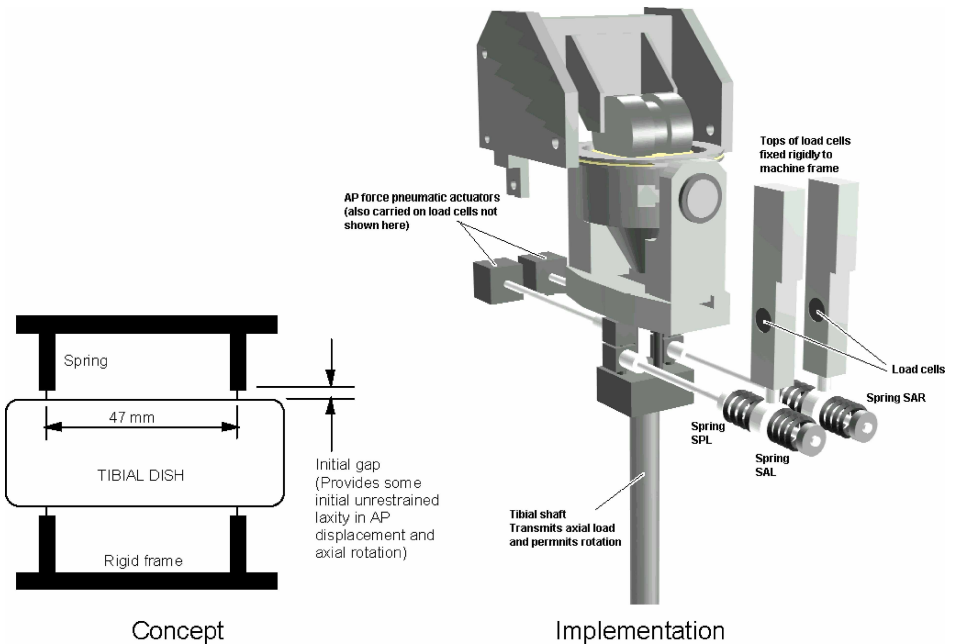


FIG. 2—Soft tissue restraint simulation system on the knee simulator.

6 WEAR OF ARTICULATING SURFACES

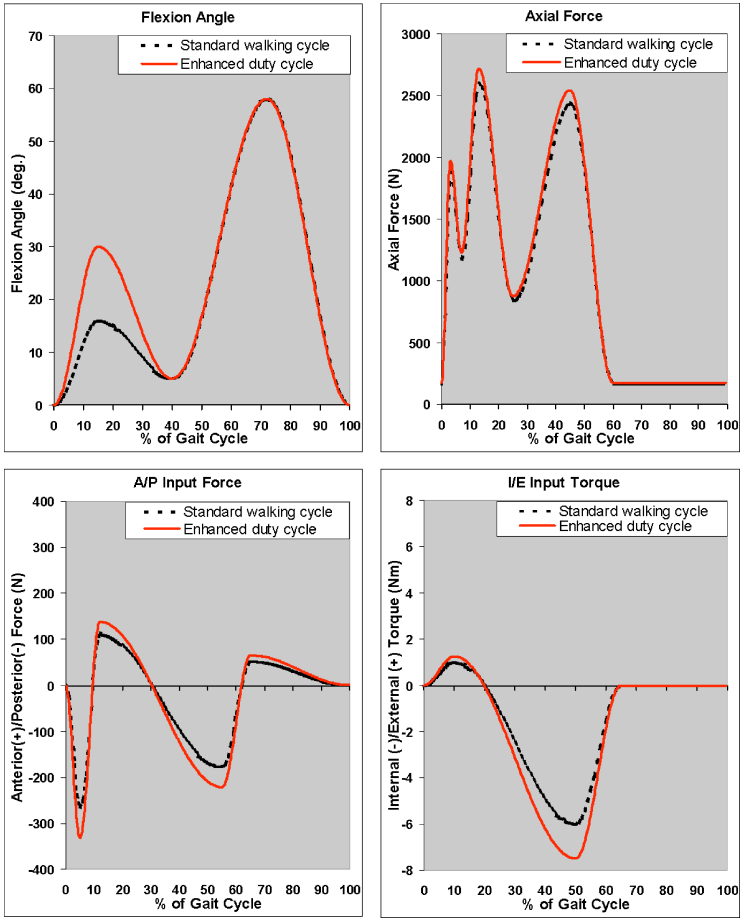


FIG. 3—The ISO Walking Cycle and the Enhanced Duty Cycle. The axial force was applied at 5 mm towards the medial side. Negative A-P force would tense the PCL. Negative internal-external torque tended to rotate the tibia inwards.

translation (PCL retained) was restrained by a pair of springs with 33.8 N/mm stiffness each, again with a 2.5–mm gap. Because of the spacing apart of the pairs of springs by 47 mm, internal-external restraint was also provided to the tibial component.

*Input Flexion and Load Cycles*

The reference inputs were those specified in the ISO standard [25] representing a walking cycle (Fig. 3). During stance the maximum flexion angle was 15°, reaching 58° during swing. There were three force peaks, the two major ones of around 2600 N occurring near heel-strike and toe-off. Viewed in the frontal plane, the line of action of the axial force was 5 mm medial to the center, to represent the medial bias believed to occur in vivo [26,27]. The A-P shear force was on the tibial component, in the direction to tense first the PCL, then the ACL, and finally the PCL, during the stance phase. The torque about the tibial axis was predominantly inwards on the tibia [25–28].

Early experience with the simulator showed that with the above Standard ISO Walking Cycle, the wear rates of total knees were generally small [19]. In that study, it was suggested that inputting higher flexion

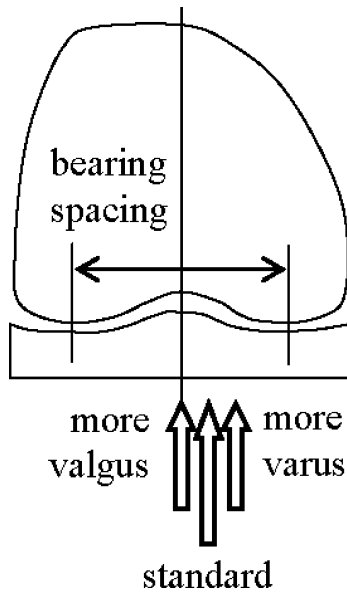


FIG. 4—Frontal plane alignment.

angles and forces, the wear rate could be increased. In the present study, we formulated an Enhanced Duty Cycle primarily to simulate more energetic activities. Compared with the ISO cycle, the peak flexion in the stance phase was doubled to  $30^\circ$ , the axial compressive force was increased by 5 %, and the A-P force and axial torque by 25 %. These new values were intended to represent in a general way faster walking and activities involving slopes or steps. These activities involve higher flexion angles and loads than level walking.

#### *Test Protocol*

The tibial holders were supplied with calf serum (diluted with deionized water to contain approx. 20 g/l protein concentration) at  $37^\circ\text{C}$ . After alignment and tuning of each station, the standard ISO test was run for approximately 1000 cycles to allow the deformation of the plastic and the motion pattern to stabilize. Data points of the input forces, torques, and flexion angles, and the resulting A-P displacements and internal-external rotations of each tibial holder relative to its femoral component, were then collected at 50 Hz. After the 1000 cycles (about 15 min), the interpolated values of 100 evenly spaced time increments during each gait-cycle were averaged for 28–29 successive cycles. This minimized the effect of mechanical and electronic noise in the simulator signals. The tuning and test were then repeated for the Enhanced Duty Cycle. The following tests were carried out for both the Standard and the Enhanced Duty Cycles.

#### *Effect of Frontal Plane Alignment*

In the standard case, the line of action of the axial force passed 5 mm medial of the centerline (see Fig. 4). For a “varus” test, the axial force was offset a total of 10 mm medially from the centerline. For a “valgus” test, the axial force passed through the center of the knee. We estimate those to approximate to  $7^\circ$  varus and valgus TKR misalignments on a patient with average anatomy. They are therefore not unrealistic for significant, but not extreme, clinical TKR misalignments.

#### *Effect of Rotational Position of the Tibia*

Relative to the axis of rotation of the femoral component, the tibial component was mounted at  $10^\circ$  internal rotation, and then  $10^\circ$  external rotation (see Fig. 5). At each of these, the spring-gaps were

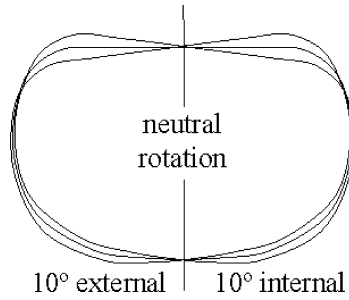


FIG. 5—Rotational position of tibia.

balanced (centered) around the now rotationally offset tibial holder position. On loading, the tibial bearing inserts (and/or baseplates) tended to rotate towards the zero (neutral position in Fig. 5) due to the tibial dishing, thus being subject to spring (soft tissue) forces.

*Effect of PCL Tension*

To simulate a tight PCL, the initial 2.5-mm gaps between the PCL springs and the tibial holder illustrated schematically in Fig. 6(a) were eliminated as shown in Fig. 6(b). For a loose PCL, the springs with reduced stiffness as for the absent ACL were used on the PCL side, too (Fig. 6(c)).

**Results**

*Standard ISO Walking Cycle versus Enhanced Duty Cycle*

A comparison is shown between all of the seven TKRs for the Standard ISO Walking Cycle and the Enhanced Duty Cycle (Fig. 7). The limits and ranges of the displacements and rotations in the stance phase are shown in Table 2. For the ISO Cycle, the tibia moved posteriorly in early and late stance, in parallel with the direction of the applied A-P force, but the displacements were greater at the end of stance due to the reducing axial compressive force. These magnitudes were similar for all designs except the Zimmer MBK, which had a smaller value of less than 3 mm. The highest value was found for the LCS, almost double that of the MBK. In axial rotation, all tibias rotated internally, but for the mobile-bearing designs, the initiation of the rotation lagged behind the applied torque. The NexGen CR rotated the most in the stance phase (13.3°) while the Zimmer MBK rotated the least (1.8°). Of the fixed-bearing designs, the least rotation was seen in the PFC sigma (3.1°).

The effect of the Enhanced Duty Cycle was to increase the displacements and rotations as expected. For the NexGen CR and the Sulzer SAL, the displacements nearly doubled. For the other designs, the increases were much smaller. The axial rotation for all the fixed-bearing designs increased only slightly. However, for two of the mobile bearings, the Zimmer MBK and the Sulzer SAL, the rotations increased dramatically.

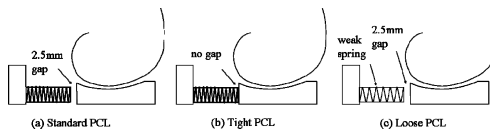


FIG. 6—Simulation of tightness or looseness of the PCL. (a) Standard PCL. (b) Tight PCL. (c) Loose PCL.

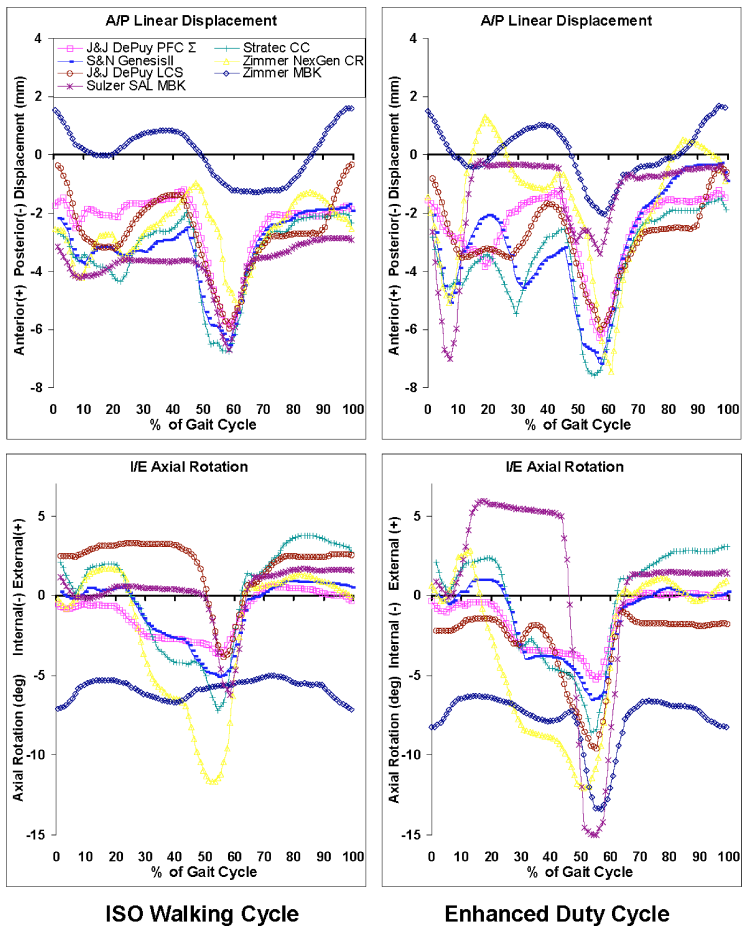


FIG. 7—The displacement and rotation kinematics measured for all implants, comparing the Standard ISO Walking Cycle (left) with the Enhanced Duty Cycle (right). (The curve symbols and legends are identical for all graphs.)

#### *Effect of Frontal Plane Alignment (varus versus valgus loading)*

Differences in kinematics were most strikingly seen by comparing varus and valgus conditions during the Enhanced Duty Cycle, as shown in Fig. 8. For all of the TKRs, valgus loading had minimal effect on the curves for both A-P displacement and axial rotation.

In varus loading, the curves for all of the fixed-bearing designs were very similar to neutral loading. However the LCS mobile-bearing knee showed large increases in both A-P displacement and rotation, while the Zimmer MBK showed a large increase in axial rotation.

#### *Effect of Rotational Position of the Tibia*

Figure 9 shows the kinematics between the internal and external prerotations for the Enhanced Duty Cycle, where the differences were most clearly seen. There was little change in the A-P displacements, except that the NexGen CR showed less displacement for an externally rotated tibia. The rotational curves were all shifted in the direction of the tibial prerotation. This was because the rotations were measured relative to a neutrally positioned tibial tray.

TABLE 2—Comparison between the Standard ISO Walking Cycle and the Enhanced Duty Cycle showing maximum, minimum, and ranges of the A-P displacements and internal-external rotations in the stance phase (0 %–60 % of cycle). The first four implants were fixed bearing; the last three implants were mobile bearing.

A-P Displacement (mm)	Standard ISO Walking Cycle			Enhanced Duty Cycle		
	Min	Max	Range	Min	Max	Range
J&J-DePuy PFC $\Sigma$	-5.9	-1.2	4.7	-6.3	-1.3	5.0
Stratec CC	-6.8	-2.0	4.8	-7.6	-2.4	5.2
S&N GenesisII	-6.5	-2.1	4.4	-7.2	-1.5	5.7
Zimmer NexGen CR	-4.7	-1.0	3.7	-6.9	1.3	8.2
J&J-DePuy LCS	-6.0	-0.3	5.7	-6.0	-0.7	5.3
Zimmer MBK	-1.2	1.5	2.7	-2.1	1.5	3.6
Sulzer SAL MBK	-6.7	-3.0	3.7	-7.0	-0.2	6.8
IE Rotation ( $^{\circ}$ )	Min	Max	Range	Min	Max	Range
J&J-DePuy PFC $\Sigma$	-3.6	-0.5	3.1	-5.2	-0.3	4.9
Stratec CC	-7.2	2.5	9.7	-8.6	2.6	11.2
S&N GenesisII	-5.1	0.6	5.7	-6.5	1.0	7.5
Zimmer NexGen CR	-11.6	1.7	13.3	-12.0	2.8	14.8
J&J-DePuy LCS	-3.9	3.3	7.2	-9.6	-1.4	8.2
Zimmer MBK	-7.1	-5.3	1.8	-13.4	-6.3	7.1
Sulzer SAL MBK	-6.2	1.4	7.6	-15.0	6.0	21.0

Most of the *ranges* of displacement and rotation were similar to the neutral condition. However, there were a few exceptions. For an externally rotated tibia, the NexGen CR increased in axial rotation, while the LCS dramatically increased in axial rotation. For both an internally and externally rotated tibia, the PFC increased its axial rotation.

*Effect of PCL Tension*

The status of the PCL had a major effect on the A-P displacement curves (Fig. 10). The effect of a loose PCL was a large increase in the displacements; the effect being particularly pronounced in late stance, where the axial compressive load was reducing. For a tight PCL, while there was a general reduction in AP displacements, the effect was not so dramatic. For a loose PCL, the axial rotations were generally increased, with the largest increases for the LCS and the Zimmer MBK. For a tight PCL, the axial rotations were generally decreased.

**Discussion**

Use of the force-input knee-simulating machine to compare different designs of TKR has been described previously [7,9,19]. The force inputs for the walking cycle, namely the axial compressive force, the A-P force, and the internal-external torque, were determined from data obtained by Morrison [26] and by Mikosz [28] and is described in the ISO standard [25]. This data relied on a geometrical model of the knee, together with EMG data of muscle activity, ground-to-foot force data, and kinematic data. Recently, force data were obtained directly by telemetry on a subject with a distal femoral replacement [27], and one with a telemetric tibial baseplate [29]. Both these studies were consistent with the general shape and approximate magnitudes of the compressive axial force waveforms used in this study. In-vivo kinematic data using fluoroscopy have shown values which reflect the inherent constraint of the particular TKR design being tested providing further justification for using the force input approach in a simulator test. During the stance phase, the displacements and rotations were related to the A-P force and the torque, together with the axial compressive force. Such relationships have been noted before in laboratory testing of different designs [4].

Surface wear is likely to be related to the product of load and sliding distance, integrated throughout the cycle. However, the relation will need to account for the sliding on the lateral and medial condyles separately, which will require the data of displacements and rotations in combination. Contact pressures at the different increments will also affect the instantaneous wear factor. Nevertheless, the variations in the kinematics are likely to imply differences in wear rate between the designs. Kinematic variations also have implications for the ease of performing certain functions.

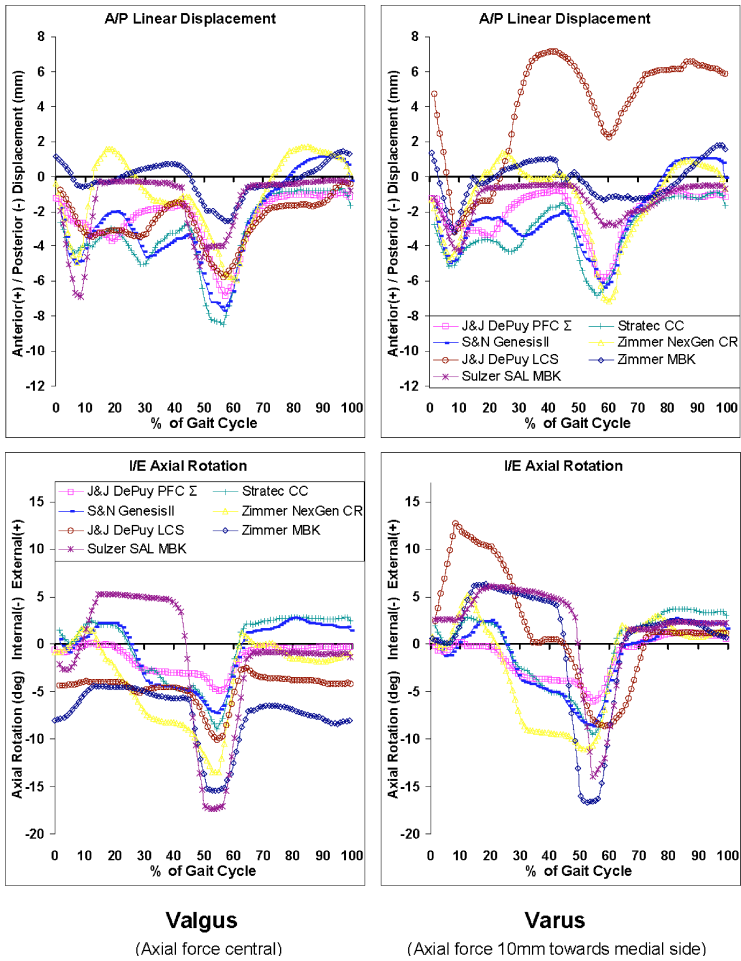


FIG. 8—The measured displacement and rotation kinematics as a function of varus-valgus loading under the Enhanced Duty Cycle.

Surprisingly the rotations in the mobile bearing designs were in the same range or even smaller when compared with the fixed bearing designs, even though the rotation in the mobile bearing was nominally unconstrained. This finding may be explained by a higher frictional torque between the plastic bearing and the tibial plate, due to a combination of a very large surface area and a higher friction coefficient for lower contact pressures [30]. The finding is also consistent with fluoroscopy results [12,15,31] or RSA results [32], where the rotations and displacements of fixed-bearing and mobile-bearing knees were generally similar.

Using the standard ISO test, early wear testing on the simulator produced low wear rates on typical TKRs in tests even in excess of  $10 \times 10^6$  cycles. As the wear progressed, the displacements reduced, probably due to the increase in conformity caused by the wear [19]. While the low wear rate may be representative of the in vivo data for well-aligned knees, it would be an advantage to devise a test which increased wear rate in order to reduce testing times during the design and evaluation process. The Enhanced Duty Cycle was formulated for this purpose.

The main difference in the Enhanced Duty Cycle was the doubling of the peak flexion angle in mid-stance, while the forces were increased by only 25 % or less, with care taken not to introduce heating

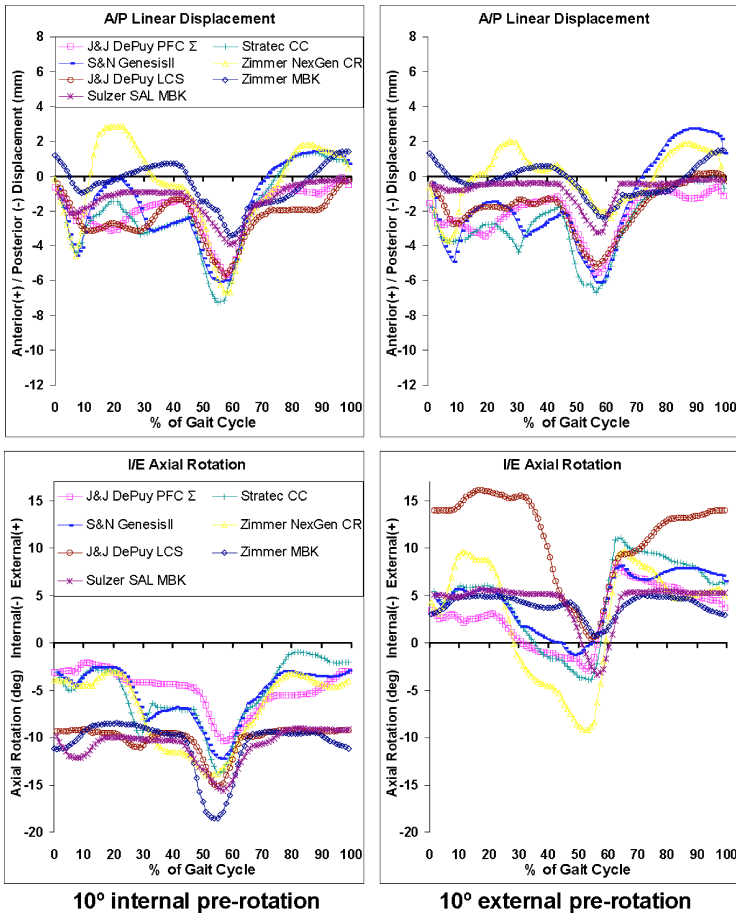


FIG. 9—Tibial baseplates pre-rotated during alignment—Enhanced Duty Cycle.

effects that might be detrimental. The A-P displacements and internal-external rotations were found to be generally increased for all designs. Hence, for our purposes of highlighting the effects of the different surgical misalignments, the kinematic data from the Enhanced Duty Cycle was chosen. It should be noted, however, that there was a proportionately greater effect on two of the mobile-bearing knees; notably, a large increase in rotation. This is likely to be due to these designs overcoming the frictional torque, after which there was little constraint other than the springs (soft tissues) themselves. On the other hand, in fixed-bearing designs, the curvature of the tibial surfaces provided constraint that increased with displacement.

Changing the line of action of the axial compressive force, equivalent to altering the varus alignment in the frontal plane, made little difference to the A-P or rotational curves. It is noted that in our tests the line of action still passed between the lateral and medial condylar contact points, and hence there was no tendency for lift-off. Changing the line of action would increase the axial force on one condyle and reduce it on the other. This would result in reduced laxity on one side and increased laxity on the other, with the net effect that the overall A-P displacement and internal-external rotation would be similar.

Changing the neutral position for internal-external rotation would have a more complex effect. When the femoral condyles were riding up the curvature of the plastic, this would increase the stiffness to displacement in one direction but reduce the stiffness in the other direction. The only overall effect of

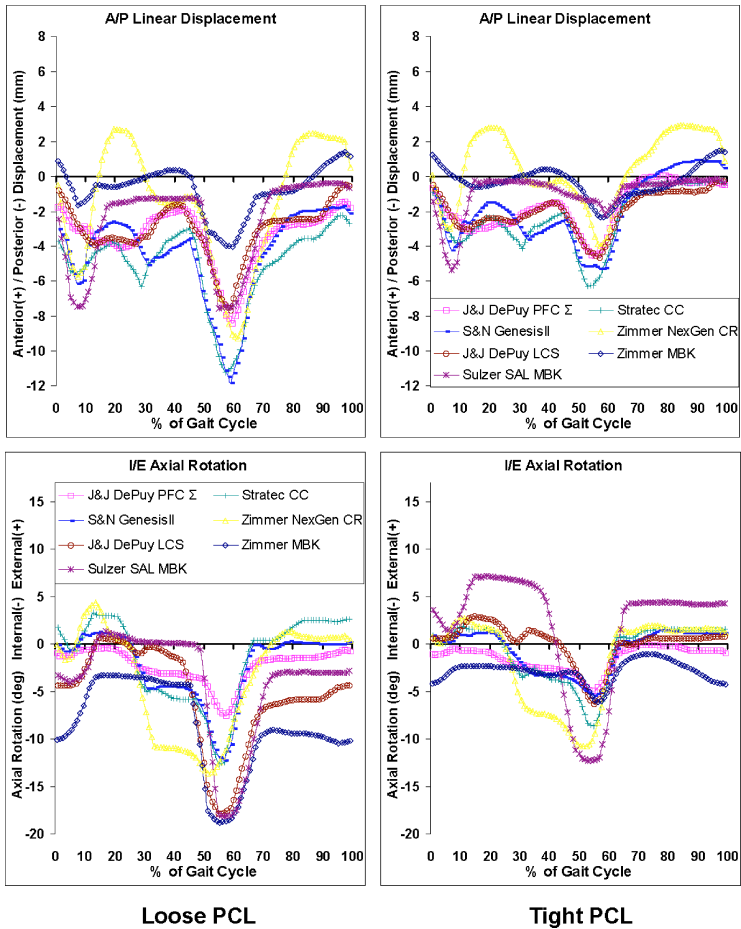


FIG. 10—Kinematics with loose posterior cruciate ligament (left) and tight posterior cruciate ligament (right) under the Enhanced Duty Cycle.

rotational misalignment was in fact a shifting of the internal-external rotational range in the direction of the misalignment. Apart from a few instances of large increases or decreases in the displacements and rotations with individual designs, there were no apparent general kinematic effects of changing the rotational position of the tibia. However, in vivo, there might well be important effects on the patella tracking due to the consistent rotational shift.

The greatest effect on the displacements and rotations was found by altering the stiffness of the posterior cruciate ligament. The increased stiffness was achieved by removing the gap in the springs, representing a ligament that would be taut throughout the entire flexion range. The reduced stiffness was equivalent to a nonfunctional ligament, as would occur if the TKR components were inserted “loosely” or where the PCL was recessed or released. In the stance phase of walking, with maximum flexion of 30°–40° in late stance, both of these situations appear to be realistic. Our results support the observations made by surgeons at the time of surgery, that there can be considerable differences in the A-P laxity depending upon the status of the PCL. A further factor would be the posterior slope of the tibial component [33], although the effect of this may be more evident at higher angles of flexion.

It appears that if consistent kinematics are required in a TKR that preserves the PCL, the tension in the PCL must be controlled in a more reproducible way than present surgical techniques allow [34]. This topic

is frequently discussed in relation to both controlling kinematics and facilitating a high range of flexion. One surgical approach that is sometimes advocated is to err on the side of the loose PCL. In this case, the stability in function would be derived primarily from the partial conformity of the femoral-tibial bearing surfaces, while the PCL would then act as a check against the larger displacements that might occur, particularly in higher flexion. On the other hand, a PCL that is too tight in flexion might limit the range of flexion which can be obtained.

In previous work [9], we have demonstrated our ability to control the input variables of this simulator system to within the following RMS deviations: flexion 1 %, axial force 2.8 %, A-P force 6.4 %, axial torque 3.9 %. For the present study, these deviations were further reduced using iterative tuning as previously described in [35,36]. Repeatability between different cycles was also addressed in previous studies [37]. Standard deviations were calculated at 100 different time intervals in the walking cycle for ten successive cycles, analogous to the current study. These average standard deviations for eight different TKR designs ranged from 0.05 mm to 0.27 mm (max 0.9 mm) for A-P displacement and from 0.18° to 0.56° (max 1.5°) for internal-external rotation. In the current study, 28–29 successive cycles were averaged in all the data logs, yielding even more stable averages.

One of the advantages of an in vitro simulator test is greater control and measurement of the input variables than would be possible in an in vivo study, which would require the impossible task of identical implantations in patients with identical anatomy and identical gaits. While it would have been desirable to test more than one sample of each TKR design, such a study would be prohibitively time consuming. One sample of each of the seven TKR designs was tested, at seven different alignment situations and two gait patterns, which required 98 tests (including separate tunings of each station) and over two years to complete. We are confident that our tuning process allowed a high degree of consistency and repeatability in the kinematics of each TKR design in a given alignment, thus ensuring that the data were reproducible and representative of that design and that any remaining deviations were much smaller than differences due to the gait and alignment variables being studied.

This study demonstrated the effect of the different patient and surgical variables on the kinematics of different total knees, by isolating these effects in vitro without any of the variable surgical and patient factors of in vivo clinical studies. This data has implications to the surgical techniques used. In addition, the data provides new possibilities for testing total knees, such as adding new tests to the present ISO standard, or even modifying the standard itself.

### *Acknowledgments*

This work was supported by a consortium of the Medical Devices Agency, Department of Health, UK, and the following orthopaedic companies: Stryker-Howmedica-Osteonics, DePuy, Zimmer, Smith & Nephew, Biomet, and Waldemar Link. The technical support of Mark Harrison, Bob Skinner, and Keith Rayner, is appreciated as this work was partly carried out at the Center for Biomedical Engineering, University College London, UK, and partly at the Orthopaedic Surgery Research Laboratories of the University of Nebraska Medical Center, USA.

### **References**

- [1] Arima, J., Whiteside, L. A., Martin, J. W., Miura, H., White, S. E., and McCarthy, D. S., "Effect of Partial Release of the Posterior Cruciate Ligament in Total Knee Arthroplasty," *Clin. Orthop. Relat. Res.*, Vol. 353, 1998, pp. 194–202.
- [2] Bach, J. M., and Hull, M. L., "A New Load Application System for in Vitro Study of Ligamentous Injuries to the Human Knee Joint," *J. Biomech. Eng.*, Vol. 117, 1995, pp. 373–381.
- [3] Churchill, D. L., Incavo, S. J., Johnson, C. C., and Beynon, B. D., "The Effect of Posterior Stabilizing Post Position on Femoral Rollback and Patello-Femoral Contact Load in Total Knee Arthroplasty," *Trans. Annu. Meet. - Orthop. Res. Soc.*, 1996.
- [4] Luger, E., Sathasivam, S., and Walker, P. S., "Inherent Differences in the Laxity and Stability Between the Intact Knee and Total Knee Replacements," *The Knee*, Vol. 4, 1997, pp. 7–14.
- [5] MacWilliams, B. A., Wilson, D. R., DesJardins, J. D., Romero, J., and Chao, E. Y. S., "Hamstrings Cocontraction Reduces Internal Rotation, Anterior Translation, and Anterior Cruciate Ligament Load

- in Weight-Bearing Flexion," *J. Orthop. Res.*, Vol. 17, 1999, pp. 817–822.
- [6] Mahoney, O. M., Nobel, P. C., Rhoads, D. D., Alexander, J. W., and Tullos, H. S., "Posterior Cruciate Function Following Total Knee Arthroplasty," *J. Arthroplasty*, Vol. 9, 1994, pp. 569–578.
- [7] Walker, P. S., Blunn, G. W., Broome, D. R., Perry, J., Watkins, A., Sathasivam, S., Dewar, M. E., and Paul, J. P., "A Knee Simulating Machine for the Performance Evaluation of Total Knee Replacements," *J. Biomech.*, Vol. 30, No. 1, 1997, pp. 83–89.
- [8] Haider, H., and Walker, P. S., "Measurements of Constraint of Total Knee Replacement," *J. Biomech.*, Vol. 38, No. 2, 2005, pp. 341–348.
- [9] DesJardins, J. D., Walker, P. S., Haider, H., Perry, J., "The Use of a Force-Controlled Dynamic Knee Simulator to Quantify the Mechanical Performance of Total Knee Replacement Designs," *Bull. Jpn. Inst. Met.*, Vol. 33, 2000, pp. 1231–1242.
- [10] Haider, H., Walker, P. S., and Blunn, G. W., "Are the Kinematics of Different TKR Designs Targeted for the Same Patient The Same?," *Trans. Annu. Meet. - Orthop. Res. Soc.*, 2002.
- [11] Banks, S. A., Markovich, G. D., and Hodge, W. A., "In Vivo Kinematics of Cruciate-Retaining and Substituting Knee Arthroplasties," *J. Arthroplasty*, Vol. 12, 1997, pp. 297–304.
- [12] Dennis, D. A., Komistek, R. D., Hoff, W. A., and Gabriel, S. M., "In Vivo Knee Kinematics Derived Using an Inverse Perspective Technique," *Clinical Orthopedics*, Vol. 331, 1996, pp. 107–117.
- [13] Schmidt, R., Komistek, R. D., Blaha, J. D., Penenberg, B. L., and Maloney, W. J., "Fluoroscopic Analyses of Cruciate-Retaining and Medial Pivot Knee Implants," *Clin. Orthop. Relat. Res.*, Vol. 410, 2003, pp. 139–147.
- [14] Hoff, W. A., Komistek, R. D., Dennis, D. A., Gabriel, S. M., and Walker, S. A., "Three-Dimensional Determination of Femoral-Tibial Contact Position Under in Vivo Conditions Using Fluoroscopy," *Clinical Biomechanics*, Vol. 13, 1998, pp. 455–472.
- [15] Stiehl, J. B., Dennis, D. A., Komistek, R. D., and Crane, H. S., "In Vivo Determination of Condylar Lift-off and Screw-Home in a Mobile-Bearing Total Knee Arthroplasty," *J. Arthroplasty*, Vol. 14, 1999, pp. 293–299.
- [16] Stiehl, J. B., Komistek, R. D., Cloutier, J.-M., and Dennis, D. A., "The Cruciate Ligaments in Total Knee Arthroplasty," *J. Arthroplasty*, Vol. 15, 2000, pp. 545–550.
- [17] Uvehammer, J., Karrholm, J., and Brandsson, S., "In Vivo Kinematics of Total Knee Arthroplasty," *J. Bone Jt. Surg.*, Vol. 82-B, 2000, pp. 499–505.
- [18] Haider, H., Walker, P. S., Blunn, G. W., Perry, J., and DesJardins, J. D., "A Four Channel Force Control Knee Simulator: From Concept to Production," *Proceedings of the 11th Annual Symposium, International Society for Technology in Arthroplasty (ISTA)*, France, 1998.
- [19] Walker, P. S., Blunn, G. W., Perry, J. P., Bell, C. J., Sathasivam, S., Andriacchi, T. P., Paul, J. P., Haider, H., and Campbell, P., "Methodology for Long-Term Wear Testing of Total Knee Replacement," *Clin. Orthop. Relat. Res.*, Vol. 372, 2000, pp. 290–301.
- [20] Haider, H., Walker, P. S., Blunn, G. W., and Bell, C. J., "The Sensitivity of Total Knee Kinematics to Misaligned Installation," *Trans. Annu. Meet. - Orthop. Res. Soc.*, 2001.
- [21] Haider, H., and Walker, P. S., "Analysis and Recommendations for the Optimum Spring Configurations for Soft Tissue Restraint in Force-Control Knee Simulator Testing," *Trans. Annu. Meet. - Orthop. Res. Soc.*, 2002.
- [22] Walker, P. S., and Haider, H., "Characterizing the Motion of Total Knee Replacements in Laboratory Tests," *Clin. Orthop. Relat. Res.*, Vol. 410, 2003, pp. 54–68.
- [23] Haider, H., Sekundiak, T. D., and Garvin, K. L., "Simulation of the Spring-Based Soft Tissue Restraint in Testing Knee Wear Under Force Control," *First International Conference on Mechanics of Biomaterials & Tissues*, Hawaii, 2005.
- [24] Fukubayashi, T., Torzilli, P. A., Sherman, M. F., and Warren, R. F. "An in-Vitro Biomechanical Evaluation of Anterior-Posterior Motion of the Knee. Tibial displacement, rotation, and torque," *J. Bone Jt. Surg.*, Vol. 64, 1982, 258–264.
- [25] International Standards Organization. ISO/CD/14243-1, Implants for Surgery—Wear of Total Knee Joint Prostheses—Part 1. Loading and Displacement Parameters of Wear Testing Machines With Load Control and Corresponding Environmental Conditions for Tests, 1999.
- [26] Morrison, J. B., "The Mechanics of the Knee Joint in Relation to Normal Walking," *J. Biomech.*, Vol. 3, 1970, pp. 51–61.

- [27] Taylor, S., Walker, P. S., Perry, J., Cannon, S. R., and Woledge, R., "The Forces in the Distal Femur and the Knee During Walking and Other Activities Measured by Telemetry," *J. Arthroplasty*, Vol. 13, 1998, pp. 428–437.
- [28] Mikosz, R. P., Andriacchi, T. P., and Andersson, G. B. J., "Model Analysis of Factors Influencing the Prediction of Muscle Forces at the Knee," *J. Orthop. Res.*, Vol. 6, 1988, pp. 205–214.
- [29] D'Lima, D. D., Patil, S., Steklov, N., Slamin, J. E., and Colwell, C. W., "In Vivo Knee Forces After Total Knee Arthroplasty," *Clin. Orthop. Relat. Res.*, Vol. 440, 2005, pp. 45–49.
- [30] Wang, A., and Klein, R., "Effect of Contact Stress on Friction and Wear of Ultra-High Molecular Weight Polyethylene in Total Hip Replacement," *Proc. Inst. Mech. Eng., Part H: J. Eng. Med.*, Vol. 215, 2001, pp. 133–139.
- [31] Stiehl, J. B., Komistek, R. D., Dennis, D. A., and Paxson, R. D., "Fluoroscopic Analysis of Kinematics After Posterior-Cruciate-Retaining Knee Arthroplasty," *J. Bone Jt. Surg.*, Vol. 77B, 1995, pp. 884–889.
- [32] Nilsson, K. G., Dalen, T., Brostrom, L. A., and Karrholm, J., "In Vivo Kinematics in Knee Replacements With Fixed or Mobile Polyethylene Bearings," *Proc Orthop Res Soc*, 1997.
- [33] Garg, A., and Walker, P. S., "Range of Motion in Total Knee Arthroplasty," *Clin. Orthop. Relat. Res.*, Vol. 262, 1991, pp. 227–235.
- [34] Sambatakakis, A., Attfield, S. F., and Newton, G., "Quantification of Soft-Tissue Imbalance in Condylar Knee Arthroplasty," *J. Biomed. Eng.*, Vol. 15, 1993, pp. 339–343.
- [35] Haider, H., Walker, P. S., Bell, C. J., and Blunn, G. W., "On the 'Real' Input of Prescribed Force-Control Conditions in TKR Simulation and Wear Testing," *Transactions of the Sixth World Biomaterials Congress*, Hawaii, 2000.
- [36] Haider, H., Alberts, L. R., Laurent, M. P., Johnson, T. S., Yao, J., Gilbertson, L. N., Walker, P. S., Neff, J. R., and Garvin, K. L., "Comparison Between Force-Controlled and Displacement-Controlled in-Vitro Wear Testing on a Widely Used TKR Implant," *Trans. Annu. Meet. - Orthop. Res. Soc.*, 2002.
- [37] Benson, L. C., DesJardins, J. D., and LaBerge, M., "Effects of in Vitro Wear of Mechanical and Molded UHMWPE Tibial Inserts on TKR Kinematics," *J. Biomed. Mater. Res.*, Vol. 58, 2001, pp. 496–504.

Diego Orozco,<sup>1</sup> Thorsten Schwenke,<sup>1</sup> and Markus A. Wimmer<sup>1</sup>

## Wear Scar Prediction Based on Wear Simulator Input Data— A Preliminary Artificial Neural Network Approach

**ABSTRACT:** A significant difference in wear scar formation between tested and retrieved knee implants of the same type has been reported. In this study, an Artificial Neural Network (ANN) model has been designed with the aim to gain knowledge of relationships between simulator input parameters and generated wear scars. One hundred twenty-four short-term tests were conducted with four implants of a single design using a four-station knee simulator in load control mode. Data points of the wear scar boundaries were transferred into bitmap images for computer analysis. Eighty percent of these discretized wear scars formed the output training set for a back-propagation neural network. The input training set was selected from the related simulator input motion and load parameters. The remainder of the testing matrix was used for network cross-validation and testing. Training resulted in 82.9% accuracy of the input-to-output relationship and 69.3% predictive capability. The predictive capabilities of the network may be further enhanced by utilizing a modification of the learning algorithm.

**KEYWORDS:** wear, total knee prosthesis, wear simulation, polyethylene, UHMWPE, simulator tuning, backpropagation network

### Nomenclature

Symbol = Definition

- $\mathbf{a}^0$  = output of input layer, i.e., the input vector
- $\mathbf{a}^m$  = output of layer  $m$  (vector)
- $\mathbf{b}$  = bias (vector)
- $\mathbf{e}$  = mean square error at  $i^{\text{th}}$  epoch (vector)
- $\mathbf{f}$  = transfer function of layer (vector)
- $k$  = new weight index
- $m$  = layer index
- $M$  = total layer count
- $\mathbf{n}^m$  = layer  $m$  output before transfer function (vector)
- $\mathbf{p}$  = output of input layer (vector)
- $\mathbf{r}$  = input vector
- $\mathbf{t}$  = target or desired vector
- $\mathbf{W}$  = weight matrix
- $A$  = learning rate

NOTE: Scalars are displayed in lower case letters being nonbold; vectors are represented using bold lower case letters; and matrices are represented with capital letters in boldface type.

### Introduction

Total knee replacements (TKRs) play an important role in improving the health and functional mobility of individuals with end-stage knee osteoarthritis. However, loosening of the implant due to wear of the

---

Manuscript received November 14, 2005; accepted for publication June 12, 2006; published online July 2006. Presented at ASTM Symposium on Wear of Articulating Surfaces on 8 November 2005 in Dallas, TX; S. A. Brown, L. N. Gilbertson, and V. D. Good, Guest Editors.

<sup>1</sup> Graduate Student, Laboratory Manager, and Assistant Professor and Director, respectively, Section of Tribology, Rush University Medical Center, IL 60612.

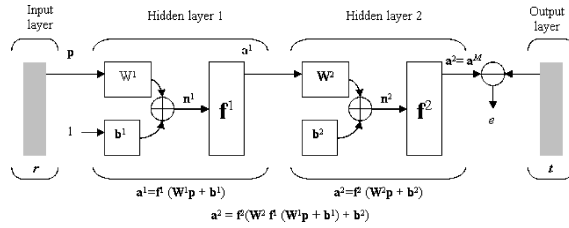


FIG. 1—Simplified structure of the multilayer network for this study. Matrix and vector notations are used. Refer to the nomenclature for detailed information.

components is a major problem and most likely leads to revision surgery. In order to predict the longevity of new prosthetic materials, knee wear simulation is common practice and required by many regulatory bodies [1,2]. The testing procedure itself relies on the application of a normal walking cycle with five million repetitions. Time constraints—a test lasts typically up to ten weeks—prohibit the analysis of other activities or gait patterns, or both, even though their relative importance for the overall wear outcome is mostly unknown. Hence, recent research demonstrated that the wear scars generated from knee simulators show considerable discrepancy with regard to the damage area when compared to retrieved implants of the same type [3–5].

In this study, an Artificial Neural Network (ANN) approach was conducted to model the relationship between simulator input parameters and the generated wear scars.

**Background**

*Artificial Neural Networks*

The artificial neuron is an abstraction of the biological neuron (nerve cells that build the nervous system). It finds its application in programs or in circuitry. Although a network composed of artificial neurons does not have the same power as the human brain, it actually can be trained to solve a vast variety of problems [6]. ANNs are well known for their ability to generalize any type of problem in a significantly reduced effort compared with conventional nonlinear optimization algorithms. Similar to the human brain, an ANN is able to learn from experience by adjusting itself through multiple confrontations with the same data. The learning process can be performed in a supervised or unsupervised manner. Thus, a network composed of artificial neurons does not only follow the structural composition of the brain, it also resembles its learning rules.

*The Backpropagation Network*

From several reported ANN structures, a backpropagation neural network (BPN) approach has been chosen because of its capability to generalize multidimensional or nonlinear problems, or both. The backpropagation network is based on an optimization algorithm published by Widrow and Hoff [7,8]. However, this single-layer network was only capable to solve linearly separable classification problems. Therefore, Rumelhart published the multilayer BP algorithm in 1980. His code was suitable to deal with complex, nonlinear classification tasks. As of today, the multilayer BPN is the most widely used neural network. While the number of layers can theoretically be expanded as needed, a restriction to two hidden layers has been recommended for practical applications [9].

Speaking in general terms, a BPN consists of several layers with neurons. The neurons of each layer communicate and exchange information with the neurons of the neighboring layers. The final structure consists of an “input layer,” an “output layer,” and so-called “hidden layers” in between (see Fig. 1 for illustration). The connections between the neurons of each layer can be trained (i.e., adjusted) to create an input-to-output relationship. The input and output are presented in the form of vectors to the network and

compared steadily during training. For each network interaction an error value is computed and “back-propagated” through the different layers of the network. This allows adjustment of the neuron connections (through so-called “weights,  $\mathbf{W}$ ” and “biases,  $\mathbf{b}$ ”) to minimize the error.

Figure 1 depicts the mathematical scheme of the utilized multilayer neural network of this study. While the number of neurons is flexible for the hidden layers, it is set for the input and output layers and represents the dimensionality of the input and output data, respectively. Each network training cycle consists of three main steps. In the first step the input data are propagated through the network. Starting from the input layer, through the hidden layers to the output layer, this training step is called forward propagation ( $\mathbf{a}^2$ ) and mathematically formulated in Eq 1, where  $\mathbf{a}^m$  describes the various layers  $m$  in the network.

$$\begin{aligned} \mathbf{a}^0 &= \mathbf{p} \\ \mathbf{a}^{m+1} &= \mathbf{f}^{m+1}(\mathbf{W}^{m+1}\mathbf{a}^m + \mathbf{b}^{m+1}) \quad \text{for } m = 0, 1, \dots, M-1 \\ \mathbf{a} &= \mathbf{a}^M \end{aligned} \quad (1)$$

After the forward propagation has finished, an error (“ $e$ ”) is computed depicting the difference of the corresponding target output  $t$  and the actual network output  $\mathbf{a}$ :

$$f(\mathbf{x}) = E[e^2] = E[(t - a)^2] \quad (2)$$

In order to provide learning to the hidden layers, the error needs to be “back-propagated;” this comprises the next step of the training process. The learning success is then plotted in terms of the sensitivity ( $s^m$ ) to changes in the  $i^{\text{th}}$  element of the network layer  $m$ . Equation 3 describes the recurrent relationship in which the sensitivity at layer  $m$  is computed from the sensitivity at layer  $m+1$ .

$$s^m = -2\dot{\mathbf{f}}^m(\mathbf{n}^m)(\mathbf{t} - \mathbf{a}), \quad \text{from } m = M-1, \dots, 2, 1 \quad (3)$$

After computation of the sensitivities for all the hidden layers, the weights and biases are updated using Eqs 4 and 5, respectively. This comprises the final step of the training cycle.

$$\mathbf{W}^m(k+1) = \mathbf{W}^m(k) - \alpha s^m(\mathbf{a}^{m-1})^t \quad (4)$$

$$\mathbf{b}^m(k+1) = \mathbf{b}^m(k) - \alpha s^m \quad (5)$$

Multiple training cycles (so-called “epochs”) are necessary to reach a satisfying error between input and output of the network. In order to test the capability of the network to generalize the specific problem (rather than memorize the input-output relationships), previously not presented input vectors are propagated through the BPN and compared with (known) output. During this “cross-validation” phase all weights and biases of the network are frozen, i.e., the network is no longer allowed to learn. The determined error is then simply used to formulate the general predictability of the network to solve a specific problem. After closing this phase successfully, the BPN may be utilized for testing tasks.

## Materials and Methods

In order to generate the input and output for network training, cross-validation, and testing, four implants of a single design (MG II, Zimmer, Inc.) were utilized. With those implants, 31 short-term tests were conducted using a servo-hydraulic, four-station knee simulator in load control mode (Endolab, Inc., Germany). The test matrix has been put together based on dynamic and static force waveforms as depicted in Table 1. Thereby, each of the four wear testing stations was handled as an individual dataset creating 124 related input and output datasets.

### Network Input

In order to create independent datasets and to allow an optimal representation of the input-to-output relationship, the input for the BPN was selected from *measured* simulator input variables. One hundred nineteen data points from data for compressive axial force, flexion/extension angle, anterior/posterior force, and internal/external moment were read out and arranged into a single 476 dimensional vector (Fig. 2).

20 WEAR OF ARTICULATING SURFACES

TABLE 1—A total of 31 test scenarios with four samples each were conducted as listed below. ISO refers to the respective profiles as outlined and plotted in ISO 14243-1 [1]. Magnitudes may have been modified as indicated (e.g., 2\*ISO=two-fold increase over standard). Sinus=sinusoid.

Test No.	Axial Force (N)	Flexion (deg.)	Ant/Post Force (N)	Int/Ext Moment (Nm)
1	const. 1000 N and ISO	0	0	0
2	ISO	ISO	ISO	ISO
3	const. 2000 N	Sinus (0–30 deg)	0	0
4	const. 1000 N	Sinus (0–50 deg)	0	0
5	const. 1000 N	Sinus (0–70 deg)	0	0
6	const. 1000 N	Sinus (0–30 deg)	0	0
7	const. 500 N	0	Sinus (–50–+50 N)	0
8	const. 500 N	0	Sinus (–50–+50 N)	0
9	const. 500 N	0	Sinus (–100–+100 N)	0
10	const. 500 N	0	Sinus (–150–+150 N)	0
11	const. 500 N	0	0	Sinus (–2–+2 Nm)
12	const. 500 N	0	0	Sinus (–4–+4 Nm)
13	const. 500 N	0	0	Sinus (–6–+6 Nm)
14	ISO	ISO	2*ISO	ISO
15	ISO	ISO	0.5*ISO	ISO
16	const. 1500 N	0	Sinus (–50–+50 N)	0
17	const. 1500 N	0	Sinus (–150–+150 N)	0
18	const. 1500 N	0	0	Sinus (–6–+6 Nm)
19	const. 1000 N	0	0	Sinus (–6–+6 Nm)
20	const. 1000 N	0	Sinus (–150–+150 N)	0
21	const. 1000 N	0	Sinus (–300–+300 N)	0
22	const. 1000 N	0	Sinus (–50–+50 N)	0
23	const. 1000 N	1	Sinus (–100–+100 N)	0
24	const. 1000 N	2	0	Sinus (–2–+2 Nm)
25	const. 1000 N	3	0	Sinus (–4–+4 Nm)
26	const. 1000 N	Sinus (0–30 deg)	Sinus (–50–+50 N)	0
27	const. 1000 N	Sinus (0–50 deg)	Sinus (–150–+150 N)	0
28	const. 1000 N	0	Sinus (–50–+50 N)	Sinus (–4–+4 Nm)
29	const. 1000 N	0	Sinus (–150–+150 N)	Sinus (–6–+6 Nm)
30	const. 1000 N	Sinus (0–30 deg)	0	Sinus (–4–+4 Nm)
31	const. 1000 N	Sinus (0–70 deg)	0	Sinus (–6–+6 Nm)

Generation of Network Output

For wear testing the tibial liners were “coated” with an ultra-thin layer of carbon powder, which has shown not to influence the friction and wear properties of polyethylene in a pin-on-disk study (unpublished data). The “coating” typically vanishes after ten cycles and allows to identify the demarcation line of the newly formed “wear scar” clearly from the untouched, surrounding polyethylene area already after 5000 cycles of testing. Each test was run on load-controlled mode at 1 Hz. Bovine serum diluted to 30 g/L containing Tris and EDTA as additives was used as a lubricant. The media was kept at 37°C all the time. A

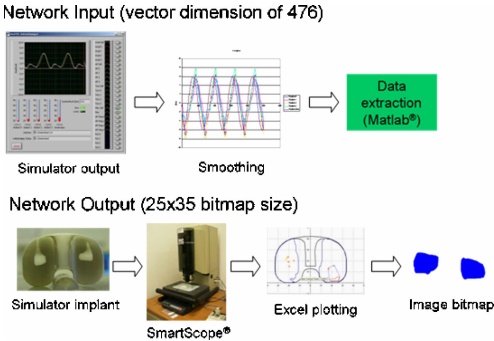


FIG. 2—Flow chart for the generation of the BP network input (top) and output (bottom) datasets.

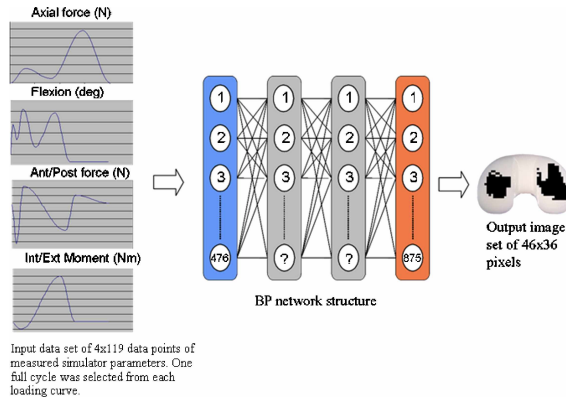


FIG. 3—General BPN structure of this study.

comparison between area and shape of wear scars generated after a full ISO test in force control and those generated in this study following the ISO protocol up to 5000 cycles yielded very similar results (data not shown).

After each test, the components were rinsed in water and after drying the generated wear scars on the tibial plateaus were manually digitized by means of a video-based measuring system (SmartScope<sup>®</sup>). Data points of the wear scar contour (medial and lateral) were then transferred into 46 by 36 pixel bitmap images for computer analysis (Fig. 2). One hundred of these images formed the output training set for a BPN. The remaining samples were used for both cross-validation (22) and preliminary testing 2.

#### Network Structure

A network structure with two hidden layers has been built to pay attention to the high-dimensionality and nonlinearity of the problem. There is no predetermined way to find the most efficient network structure with the least error. Therefore, in order to find the optimal number of neurons for the first and second hidden layer, a sensitivity analysis was conducted varying the number of epochs as well as the numbers of neurons per hidden layer. The number of neurons for the input and output layers were selected from the dimensionality of the input and output datasets. The transfer functions (“ $f$ ”) were sigmoid for all the layers except for the output layer. In this case it was linear since a 1 or a 0 was the desired output (1=white pixel and 0=black pixel of the bitmap image). Figure 3 displays the overall BPN structure.

#### Network Training

One hundred out of 124 datasets were used for training. As mentioned above, it was the only stage where learning was allowed. Backpropagation with “momentum” was the learning method of choice to train the network. The applied “momentum” prevented metastable solutions and was applied after the learning rate dropped below a certain limit. The training process stopped when at least 20 % error (desired error) was reached or when the number of specified epochs was covered.

The procedure was as follows:

- An input vector (simulator input loading parameters) was presented to the input layer.
- The input vector was propagated (forward direction) through the hidden layers to the output layer, generating an output vector.
- An error was computed when the output vector was compared to the desired output vector.
- The error was backpropagated from the output layer to the hidden layers. The network connections were then adjusted in that the error was minimized.
- Additional momentum was applied through changing the weights of the neuron connections into the opposite direction of learning.

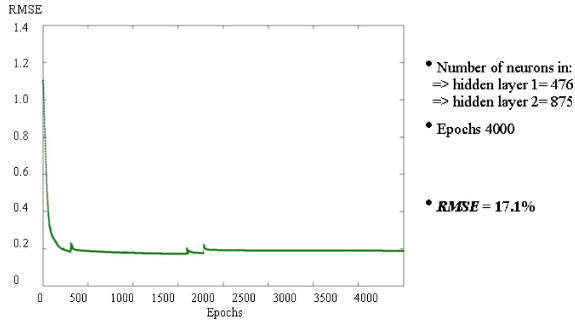


FIG. 4—Sensitivity analysis. The training results of the best network configuration are shown in the above figure. RMSE=root mean square error.

Network Cross-validation and Testing

Twenty-two datasets were used for cross-validation in order to test the network capabilities to generalize a solution. Each dataset was back-propagated through the network after a complete epoch was reached. This allowed the computation of an error; however, the error was not used for the learning algorithm but read out for comparison only. The error should be in the range of what has been achieved during the learning process to demonstrate the “generalizability” of a solution. After successful completion, two samples, so far unknown to the ANN, were presented to the network for analysis. This preliminary testing has been conducted to visualize the predicting capabilities of the network (which is numerically manifested by the cross-validation root mean square error). For testing, the network was set into the production mode, meaning it generated an output based on an input vector. The two loading scenarios (the testing set) was put through the already-trained network, producing lateral and medial wear scars, one for each input scenario. The generated pictorials were then graphically compared with the real wear scars.

Results

Three different network configurations were tried in order to identify the most feasible network for this study. The result of the network with the lowest training error is provided in Fig. 4.

The network with the lowest error (i.e., 17.1 %) was selected. Hence, after training based on input simulator parameters alone, each wear scar configuration within the training could be rebuilt with an 82.9 % accuracy. The capability of the network to generalize the problem (cross-validation error) was performed at an accuracy of 69.3 %.

In order to visualize these predictive capabilities, the network was then utilized to predict the wear scars of two unknown loading scenarios. The achieved output was evaluated qualitatively and compared with the pictorials of the actual wear scars generated during simulator testing. Figure 5 displays these two examples. For easier comparison the actual wear scars are shown with the same degree of pixelation as the ANN.

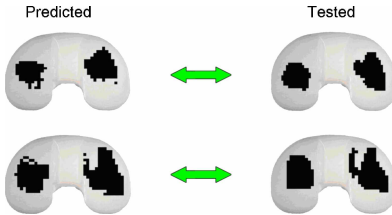


FIG. 5—Predicted wear scars using ANN (left column) contrasted against wear scars generated on the simulator (right column). To simplify comparison the actually worn components are shown with the same pixel resolution as utilized by ANN.

predicted scars of wear scars predicted by the network versus actually tested ones. As expected from the cross-validation error, there was sufficient accuracy to recognize the relationship between predicted and actually generated wear scars, leaving room for improvements.

## Discussion

An artificial neural network has been trained to predict the wear scar formation based on wear simulator input data. To the best of our knowledge this is the first attempt to use an ANN for such a task and, thus, this report has preliminary character. To solve image related problems with the help of ANNs is not new [10–13]. In particular, in the medical field many image pattern recognition algorithms have been built on neural networks. Most of these programs rely on back-propagation similar to this study. Also in the field of tribology the application of ANN is not uncommon. Here, neural networks have been consulted to optimize the wear properties of cutting tools [14–16].

The back-propagation neural network of this study could be sufficiently trained to predict the wear scar formation at the tibial plateau for a single implant type and size. Based on the cross-validation error and subjective observation the predicted wear scars were reflective of those generated by the wear simulator, similar not only in shape, but also in the area and the location on the tibial plateaus. The obtained predictive error of roughly 30 % is comparable to other image related studies [10–13] and together with a <20 % training error acceptable for such preliminary study.

Obviously, this study can only be regarded as a first attempt to extrapolate wear from one kinetic wear input scenario to another. It is well recognized that two-dimensional wear scars do not determine wear volume since the third dimension “wear depth” is missing. However, retrieval analysis has demonstrated that wear scars *in vivo* are particularly variable in antero-posterior location and spread. The latter has been related to variations in the kinetic profile of patients [17]. Most likely, the predictive capabilities of the BP network could be further enhanced utilizing a modification of the BP learning algorithm, such that the backpropagation with adaptive learning rate. It is important to mention that no such study has been conducted before and that further work is needed to refine it. It is the hope of the authors that in the future it will be possible to computationally investigate many different simulator input scenarios that are based on various activities of the patient. This way it may be possible that an actual wear test of level walking is sufficient to make projections in wear behavior with regard to other loading conditions (e.g., bicycling [18]). It also may be speculated that the input-to-output direction of the network is turned around utilizing retrieved implants to predict simulator input parameters for their generation.

## Conclusion

In this preliminary study a back-propagation artificial neural network has been sufficiently trained to predict TKR wear scars, purely based on simulator input. In the future such a network may be helpful in backing long-term wear tests on a simulator. ANN would allow the evaluation of several input scenarios in a relatively short period of time and determine the most critical one, which then could be (mechanically) tested.

## References

- [1] ISO 14243-1, “Implants for Surgery—Part 1: Loading and Displacement Parameters for Wear-testing Machines with Load Control and Corresponding Environmental Conditions for Test,” Geneva: International Organization for Standardization, 2002.
- [2] ISO 14243-3, “Implants for Surgery—Part 1: Loading and Displacement Parameters for Wear-testing Machines with Displacement Control,” Geneva: International Organization for Standardization, 2002.
- [3] Harman, M. K., Banks, S., Benson, L., LaBerge, M., and Hodge, W., “Damage Patterns on Polyethylene Inserts After Retrieval and After Wear Simulation,” *Trans. Annu. Meet. - Orthop. Res. Soc.*, Vol. 26, 2001, p. 1003.
- [4] Schwenke, T., Wimmer, M. A., Schneider, E., Rosenberg, A. G., and Jacobs, J. J., “Kinetics and

- Wear of Retrieved and Simulator Tested Implants in TKA,” Transactions of the 51st Annual Orthopaedic Research Society, Vol. 30, 2005, p. 835.
- [5] Orozco, D. A., Schwenke, T., and Wimmer, M. A., “Wear Scar Similarities of Retrieved and Tested Tibial Components—An Artificial Neural Network Approach,” Transactions of the 30th Annual Meeting of the Society for Biomaterials, 2005.
- [6] Graupe, D., “*Principles of Artificial Neural Networks*,” World Scientific Publishing Co. Pte. Ltd., 1997, 238pp.
- [7] Rumelhart, D. E. and McClelland, J. L., “Parallel Distributed Processing: Exploration in the Microstructure in Cognition,” D. E. Rumelhart, G. E. Hilton, and R. J. Williams, Eds., “*Learning Internal Representations by Error Propagation*,” Cambridge, MA: MIT Press, 1986, pp. 318–362.
- [8] Widrow, B. and Hoff, M., “Adaptative Switching Circuits,” IRE WESCON Convention Record, IRE Part 4, 1960, pp. 96–104.
- [9] Hagan, M. T., “*Neural Network Design*,” Boston, MA: Thomson Learning, 1996.
- [10] Hunter, A., Kennedy, L., Henry, J., and Ferguson, I., “Application of Neural Networks and Sensitivity Analysis to Improved Prediction of Trauma Survival,” *Comput. Methods Programs Biomed.*, Vol. 62, No. 1, 2000, pp. 11–19.
- [11] Lo, S.-C. B., Chan, H.-P., Lin, J.-S., Li, H., Freedman, M. T., and Mun, S. K., “Artificial Convolution Neural Network for Medical Image Pattern Recognition,” *Neural Networks*, Vol. 8, Nos. 7 and 8, 1995, pp. 1201–1214.
- [12] Gader, P. D., Miramonti, J. R., Won, Y., and Coffield, P., “Segmentation Free Shared Weight Networks for Automatic Vehicle Detection,” *Neural Networks*, Vol. 8, No. 9, 1995, pp. 1457–1473.
- [13] Silverman, R. H. and Noetzel, A. S., Image Processing and Pattern Recognition in Ultrasonograms by Backpropagation,” *Neural Networks*, Vol. 3, No. 5, 1990, pp. 593–603.
- [14] Frangu, L. and Ripa, M., “Artificial Neural Networks Applications in Tribology—A Survey,” NIMIA-SC2001 0 2001 NATO Advance Study Institute of Neural Networks for Instrumentations, Measurements and Related Industrial Applications: Study Cases, Crema, Italy, 9–20 October 2001.
- [15] Kuo, R. J. and Cohen, P. H., “Multi-sensor Integration for On-line Tool Wear Estimation Through Radial Basis Function Networks and Fuzzy Neural Network,” *Neural Networks*, Vol. 12, No. 2, 1999, pp. 355–370.
- [16] Murthy, A. S., Chattopadhyay, A. B., and Das, S., Force Parameters for On-line Tool Wear Estimation: A Neural Network Approach,” *Neural Networks*, Vol. 9, No. 9, 1996, pp. 1639–1645.
- [17] Benson, L. C., DesJardins, J. D., Harman, M. K., and LaBerge, M. “Effect of Stair Descent Loading on Ultra-high Molecular Weight Polyethylene Wear in a Force-Controlled Knee Simulator,” *Proceedings of the Institute of Mechanical Engineering [H]*, Vol. 216, No. 6, 2002, pp. 409–418.
- [18] Martin, A., Caglar, O., Muller, M., Andriacchi, T. P., Sheikop, M. B., and Wimmer, M. A., “Knee Biomechanics During Cycling in Patients With Total Knee Arthroplasty,” 52nd Annual Meeting of the Orthopaedic Research Society, Vol. 31, 2006, p. 427.

Thorsten Schwenke, M.Sc.,<sup>1</sup> Laura L. Borgstede, M.Sc.,<sup>1,2</sup> Erich Schneider, Ph.D.,<sup>3</sup> and Markus A. Wimmer, Ph.D.<sup>1</sup>

## Slip Velocity Direction Impacts Wear in Total Knee Arthroplasty

**ABSTRACT:** Total knee arthroplasties are subjected to high slip velocities and constantly changing velocity vector directions, as they mimic the anatomical conditions of the natural joint. Together with fluid film thickness and applied load, the velocity difference between the two bodies defines the amount of energy that is induced into the contact. Particularly for polyethylene (PE), it is known that the angle describing the difference in motion direction is an important variable for material loss. In this study, a wheel-on-flat simulator scenario was used to apply a slip velocity vector with a constant magnitude and changing direction over the length of a polyethylene sample. The difference in vector orientation ranged from zero to 20.4°, while a constant axial load of 1600 N was applied, and the contact area was submerged in physiological testing fluid. After 500k cycles, the surface of the PE specimen was visually examined and scanned with a video-based measurement system to analyze the wear profile. Polishing was the predominant wear pattern, and minor striations were found in the end zone of the wear area. The wear depth increased with higher velocity angles—this relationship appeared to be linear. This study supports earlier publications that reported a correlation between cross-shear motion and wear. The presented experimental results will help in attempts to numerically simulate wear generation.

**KEYWORDS:** wear, UHMWPE, total knee arthroplasty, slip velocity, cross-shear motion

### Introduction

Contemporary designs of total knee arthroplasty (TKA) mimic the anatomical conditions of the natural joint and, thus undergo complex kinematics and kinetics during motion. Typically, during gait, the femur rolls, slides, and rotates over the tibial plateau [1]. Since the articulation must transmit high forces while allowing for the mobility for normal function, wear is a major reason for implant failure. The particles can induce, depending on their size and shape, biochemical reactions in the implant-bone interface that lead to osteolysis and subsequent loosening of the device. Reduction of wear is therefore a major concern in implant development.

The combination of contact force, sliding velocity, distance, and directional changes, impacts the wear outcome [2]. These parameters define the amount of energy that is induced into the contact region, as well as the fluid film characteristics. This, in turn, influences the friction of the system causing wear of polyethylene. An earlier study has shown that the slack, the sliding velocity based on the total velocity of both acting bodies, can be directly linked to those parameters [3–5]. The sliding or slip velocity in artificial joints is defined as the difference in speed between the two contacting bodies. Multi directional loading proves especially harmful to ultra-high molecular weight polyethylene (PE) implants [6–8]. Since the molecular chains of the crystalline phase align along the main axis of motion, shear forces as a result of cross-shearing leads to rupture of the bonds between chains and subsequent particle loss [9,10].

A directional wear intensity factor has been introduced to estimate the magnitude of wear, taking above parameters into account [7,8]. The correlation of wear with directional changes has been described qualitatively in numerous studies [11], but remains to be quantified. The purpose of this study was to parametrically analyze the correlation of wear and angular change of the slip velocity vector. It is hypoth-

---

Manuscript received January 13, 2006; accepted for publication April 19, 2006; published online June 2006. Presented at ASTM Symposium on Wear of Articulating Surfaces on 8 November 2005 in Dallas, TX; S. A. Brown, L. N. Gilbertson, and V. D. Good, Guest Editors.

<sup>1</sup> Tribology, Department of Orthopedic Surgery, Rush University Medical Center, Chicago, IL, USA.

<sup>2</sup> Zimmer, Inc., Warsaw, IN, USA.

<sup>3</sup> AO Research Institute, Davos, Switzerland.

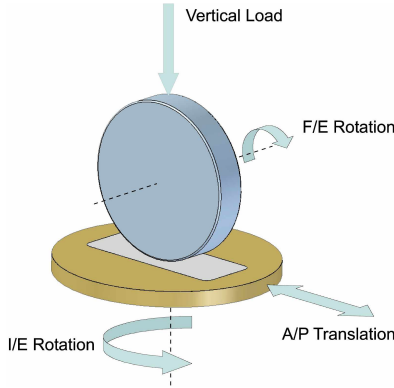


FIG. 1—Wheel-on-flat simulator concept. The wheel applies flexion-extension rotation, while the PE specimen translates in anterior-posterior direction as well as rotates internal-externally. A constant vertical axial force is applied.

esized that the wear volume increases with rising angular velocity vector changes.

**Materials and Methods**

This study was conducted on a wheel-on-flat simulator set-up as described previously [5,6] (Fig. 1). A highly polished cobalt-chromium wheel (CoCr, 100 mm diameter, 20 mm thick) acted against a flat, rectangular specimen machined from ultra-high molecular weight polyethylene (PE, 100 by 40 by 8 mm<sup>3</sup>). The flat sample was slab molded and machined from GUR 1050 resin, and subsequently gamma-sterilized in air. Motions of the simulator were driven by servo-controlled hydraulic actuators, allowing for custom input profiles.

One test cycle included two wear paths: While the PE specimen translated for about 50 mm, the wheel and internal-external PE specimen rotations led to a constant magnitude velocity vector that rotated from 0° to +10.2° (Fig. 2). A constant vertical force of 1600 N was applied during this part of the test cycle. Wheel and PE sample then returned to their starting positions (without contact at zero vertical load), to repeat the wear path with the velocity vector rotating in opposite direction from 0° to -10.2°, once again under constant vertical load. This led to an overall angular spread of 0° to 20.4°, distributed over the wear path length on the PE plateau.

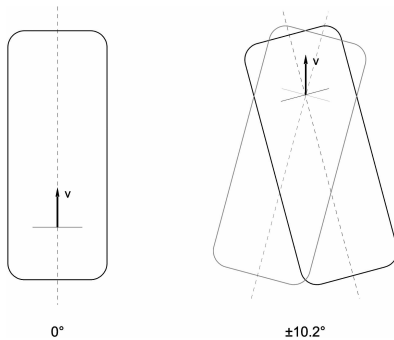


FIG. 2—Slip velocity vector *v* at start (left) and end (right) of the contact area. The PE specimen rotates in the opposite direction every second run, allowing for a total angular difference of 20.4°.

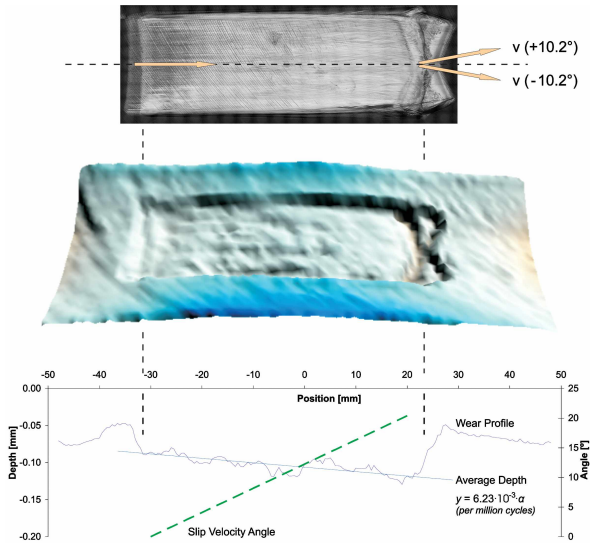


FIG. 3—Macroscopic picture of the wear profile (top). The arrows indicate slip velocity directions. Visualization of the results of the profilometric scan (middle). The graph shows wear depth in the cross-sectional view over contact position, with the dotted line giving the velocity angle (bottom).

The magnitude of the slip velocity vector was chosen constant at 50 mm/s, independent of its angular position, while the PE sample rotated with constant angular velocity of  $4.6^\circ/\text{s}$ . These magnitudes were estimated based on kinetic calculations from gait analysis [5]. In the gait laboratory, the walking kinetics of a set of patients with total knee replacements have been examined [12]. The calculated motions were combined with geometrical data of the patient's specific implant (MG II, Zimmer, Inc., USA). From the resulting slip velocity vector profiles, the representative ranges listed above were chosen for this wear study.

The contact area was submerged in physiological fluid during testing—a mix of bovine calf serum and de-ionized water, with a final protein content of 30 g/l. Ethylenediaminetetraacetic Acid (EDTA) and Tris(hydroxymethyl) methylamine (Tris) were added to the fluid to avoid calcium precipitation, to stabilize the pH-value throughout the testing period of 500k cycles, and to retard bacterial growth. The chamber was fully enclosed to prevent contamination or fluid dissipation and kept at room temperature ( $22 \pm 2^\circ\text{C}$ ).

The test ran for one million cycles, 500k cycles in each rotational direction. The wheel and PE sample were cleaned and dried upon test completion. They were visually examined and microscopically inspected at  $5\times$  magnification (Nikon, Inc., USA) for adhering particles and wear appearance. The surface profile on the PE specimen was tracked using a video-based measuring system (SmartScope®, Optical Gaging Products, Inc., USA) with a  $(0.5 \text{ mm})^2$  grid.

## Results

The predominant wear pattern on the tested PE specimen was polishing. Normal visual and microscopic examinations indicated an increase in wear with increasing vector angles. The initial machining marks were still visible in the low-wear area at the starting zone with low-velocity angles. They were entirely worn away at the end of the wear track. This finding was confirmed by the video-based wear depth measurements. The wear profile deepened as the vector angle increased (Fig. 3). The end zone of the test area showed the highest degree of polishing. Striations formed in this zone as an additional wear pattern.

The examination of the CoCr wheel revealed no visible wear in terms of scratches or other patterns. No adhering particles from the counter body or the surrounding medium were found.

## Discussion

The results support the hypothesis that wear is dependent on vector direction changes of the slip velocities in TKA. This study suggests that a strong correlation exists between the two parameters, albeit in this study the observation is limited to one sample and short testing. Earlier investigations looked at the shape of the slide track with different aspect ratios of cross-shear motion, rather than at vector direction changes. It was shown that increasing cross-shear leads to elevated wear generation [13,14]. Using the wheel-on-flat testing setup, it was possible to investigate changes in the direction of the slip velocity vector while keeping the motion path constant. The observed linear relationship between wear and opening angle of the slip velocity vector suggests that the direction of the slip velocity vector is one key parameter in explaining wear behavior of polyethylene materials. While similar conclusions have been drawn previously, this study investigated angles which are particularly important for TKA. In addition, none of the above cited studies took a continuous approach.

The predominant wear pattern observed was polishing. Interestingly, a striated pattern, as reported from many retrieval studies, formed at the end of the wear path. While this pattern is a consistent finding on components that have been nine months in vivo or more [15], it has been rarely reported in laboratory studies. The detailed kinetic conditions in those areas have to be further examined since they may provide a link to understand the mechanism behind its formation.

Fluid film influences have to be taken into account to explain the findings of this study. Lubrication type and film thickness impact energy dissipation and frictional conditions, thus highly influencing wear generation. It would need further examination whether the findings persisted when the direction of angle is reversed (i.e., maximum angle at cycle start).

In general, the parametric approach of the present study proves useful to obtain quantitative information for mathematical modeling of wear. Different slip velocity levels and angular velocities can be incorporated into numerical models. Such models may be helpful in the attempt to predicting wear generation of artificial implants.

## Conclusion

This study emphasized the importance of direction of the slip velocity vector in wear generation: the larger the angle between two crossing slip velocity vectors, the higher the wear. The wear increase appears to be linearly related to the crossing angle. This study confirms earlier reports and provides the basis for numerical wear simulation in artificial knee joints.

## Acknowledgments

This study was made possible through a research grant by Zimmer, Inc. (Warsaw, IN) and an in-kind donation of the AO Research Institute (Davos, Switzerland).

## References

- [1] Kapandji, I. A., "The Knee," in: *The Physiology of Joints*, Church Livingstone, London, NY, 1970, pp. 72–106.
- [2] Miura, H., Higaki, H., Nakanishi, Y., Mawatari, T., Moro-Oka, T., Murakami, T., and Iwamoto, Y., "Prediction of Total Knee Arthroplasty Polyethylene Wear Using the Wear Index," *J. Arthroplasty*, Vol. 17, No. 6, 2002, pp. 760–766.
- [3] Wimmer, M. A., "Damage Due to Tractive Rolling on the Tibial Plateau," in: *Wear of the Polyethylene Component Created by Rolling Motion of the Artificial Knee Joint*, Ph.D. thesis, Shaker Verlag, Aachen, Germany, 1999, pp. 117–135.
- [4] Schwenke, T., Borgstede, L. L., Schneider, E., Andriacchi, T. P., and Wimmer, M. A., "The Influence of Slip Velocity on Wear of Total Knee Arthroplasty," *Wear*, Vol. 259, 2005, pp. 926–932.
- [5] Borgstede, L. L., "The Influence of Sliding Velocity on the Wear of Polyethylene in Total Knee Arthroplasty," Masters thesis, University of Illinois at Chicago, Chicago, 2004.
- [6] Laurent, M. P., Johnson, T. S., Yao, J. Q., Blanchard, C. R., and Crowninshield, R. D., "In vitro

- Lateral Versus Medial Wear of a Knee Prosthesis," *Wear*, Vol. 255, 2003, pp. 1101–1106.
- [7] Johnson, T. S., Laurent, M. P., Yao, J. Q., and Gilbertson, L. N., "The Effect of Displacement Control Input Parameters on Tibiofemoral Prosthetic Knee Wear," *Wear*, Vol. 250, 2001, pp. 222–226.
- [8] Czichos, H., Habig, K. H., *Tribologie Handbuch—Reibung und Verschleiss*, Vieweg Verlag, Braunschweig, Germany, 1992.
- [9] Wang, A., Stark, C., and Dumbleton, J. H., "Mechanistic and Morphological Origins of Ultra-High Molecular Weight Polyethylene Wear Debris in Total Joint Replacement Prostheses," *Proc. Inst. Mech. Eng., Part H: J. Eng. Med.*, Vol. 210, No. 3, 1996, pp. 137–140.
- [10] Marrs, H., Barton, D. C., Doyle, C., Jones, R. A., Lewis, E. L. V., Ward, I. M., and Fisher, J., "The Effect of Molecular Orientation and Acetylene-Enhanced Crosslinking on the Wear of UHMWPE in total Artificial Joints," *J. Mater. Sci.: Mater. Med.*, Vol. 12, 2001, pp. 621–628.
- [11] Saikko, V. and Calonius, O., "Slide Track Analysis of the Relative Motion Between Femoral Head and Acetabular Cup in Walking and in Hip Simulators," *J. Biomech.*, Vol. 35, No. 4, 2002, pp. 455–464.
- [12] Andriacchi, T. P., Alexander, E. J., Toney, M. K., Dyrby, C., and Sum, J., "A Point Cluster Method for in vivo Motion Analysis: Applied to a Study of Knee Kinematics," *J. Biomech. Eng.*, Vol. 120, No. 6, 1998, pp. 743–749.
- [13] Bragdon, C. R., O'Connor, D. O., Lowenstein, J. D., Jasty, M., and Syniuta, W. D., "The Importance of Multidirectional Motion on the Wear of Polyethylene," *Proc. Inst. Mech. Eng., Part H: J. Eng. Med.*, Vol. 210, 1996, pp. 157–165.
- [14] Saikko, V., Calonius, O., and Keranen, J., "Effect of Slide Track Shape on the Wear of Ultra-high Molecular Weight Polyethylene in a Pin-on-Disk Wear Simulation of Total Hip Prosthesis," *J. Biomed. Mater. Res.*, Vol. 69B, No. 2, 2004, pp. 141–148.
- [15] Wimmer, M. A., Andriacchi, T. P., Natarajan, R. N., Loos, J., Karlhuber, M., Petermann, J., Schneider, E., and Rosenberg, A. G., "A Striated Pattern of Wear in Ultrahigh-Molecular-Weight Polyethylene Components of Miller-Galante Total Knee Arthroplasty," *J. Arthroplasty*, Vol. 13, No. 1 1998, pp. 8–16.

Bruce F. White,<sup>1</sup> Darryl D'Lima, M.D.,<sup>1</sup> Albert C. Drueding,<sup>3</sup> John Cox,<sup>4</sup> and Forest J. Carignan<sup>5</sup>

# A Simulator Study of TKR Kinematics Using Modeled Soft-Tissue Constraint: Virtual Soft-Tissue Control for Knee Simulation

**ABSTRACT:** The clinical relevance of knee simulation relies on the accurate reproduction of in vivo TKR kinematics. Current generation force-control knee simulators use mechanical springs to simulate the knee's soft-tissue constraint. Because the constraint provided by the soft tissue is complex in nature, with nonlinear force displacement characteristics and axis coupled behavior, it is difficult or impossible to model this behavior with mechanical springs. This paper describes a virtual soft-tissue control methodology, which provides enhanced modeling of the knee's soft tissue. TKR kinematics were evaluated for a posteriorly stabilized prosthetic device using a range of plausible soft-tissue models derived from the literature. The device was exercised with the standard ISO force-control waveforms while varying the constraint model to compare several different soft-tissue models. Kinematic and kinetic data were taken and tracking performance analyzed for several different constraint models.

**KEYWORDS:** TKR kinematics, knee simulator, knee simulation, soft-tissue constraint, knee wear, knee testing, TKA, knee implant testing

## Nomenclature

	$x$	$y$	$z$
Linear displacement of tibia: ML, AP, Axial	$d_x^t$	$d_y^t$	$d_z^t$
Displacement of the COP measured contact point: ML, AP	$d_x^c$	$d_y^c$	...
Distance from contact point to load cell origin	...	...	$d_z$
Reference force waveforms: AP, Axial	...	$f_y^r$	$f_z^r$
Tibial reaction force: ML, AP, and Axial: load cell $f_x, f_y, f_z$	$f_x^c$	$f_y^c$	$f_z^c$
Soft-tissue constraint force: AP	...	$f_y^s$	...
Sum of soft-tissue constraint contact force sum: AP	...	$f_y^{s+c}$	...
Reference waveform input: IE	...	...	$m_z^r$
Tibial reaction moments: load cell outputs $m_x, m_y, m_z$	$m_x^c$	$m_y^c$	$m_z^c$
Soft-tissue constraint moment: IE	...	...	$m_z^s$
Sum of soft-tissue constraint reaction moment sum: IE	...	...	$m_z^{s+c}$
Reference angular waveform: Flexion, IE	$\theta_x$	...	$\theta_z$
Measured angular displacement: Flexion, IE	$\theta_x$	...	$\theta_z$

Manuscript received November 8, 2005; accepted for publication May 22, 2006; published online August 2006. Presented at ASTM Symposium on Wear of Articulating Surfaces on 8 November 2005 in Dallas, TX; S. A. Brown, L. N. Gilbertson, and V. D. Good, Guest Editors.

<sup>1</sup> Engineering Manager, Advanced Mechanical Technology, Inc. 176 Waltham St. Watertown, MA.

<sup>2</sup> Director, Joint Mechanics Laboratory, Division of Orthopaedics, Scripps Clinic, La Jolla, CA.

<sup>3</sup> Software Engineer, Advanced Mechanical Technology, Inc. 176 Waltham St. Watertown, MA.

<sup>4</sup> Senior Engineer, Advanced Mechanical Technology, Inc. 176 Waltham St. Watertown, MA.

<sup>5</sup> VP Engineering, Advanced Mechanical Technology, Inc. 176 Waltham St. Watertown, MA.

Force channel tracking error	...	$\epsilon_y^f$	$\epsilon_z^f$
Moment channel tracking error	...	...	$\epsilon_z^m$
Angular displacement tracking error	$\epsilon_x^\theta$	...	$\epsilon_z^\theta$
Soft-tissue resultant force, where xxl is the ligament specification	$f_r^{xxl}$	...	...
Soft-tissue component force, where xxl is the ligament	$f_x^{xxl}$	$f_y^{xxl}$	$f_z^{xxl}$
Muscle resultant force, where xxm is the muscle specification	$f_r^{xxm}$	...	...
Muscle component force, where xxm is the muscle specification	$f_x^{xxm}$	$f_y^{xxm}$	$f_z^{xxm}$
Articular contact force resultant	$f_r^{acs}$	...	...

## Introduction

This paper introduces a novel knee-simulation control system that facilitates force-control by providing modeled soft-tissue constraint. This virtual soft-tissue (VST) controller simulates the mechanical constraint of the ligament structure of the knee using a real time algorithm running on a DSP (digital signal processor). The control technology also includes an iterative learning control (ILC) algorithm that dramatically reduces simulator machine setup time and provides exacting waveform tracking performance.

Force-control for knee simulation is appealing because active forces of dynamic, gravitational, and physiologic origin govern the motions of the natural knee [1,2]. These forces, acting on the tibial shaft, must be constrained by the passive structure of the joint. Load bearing of both implanted and natural knees is partitioned into the structures of articular-contact and structures of the soft tissue, that is, the ligamentous, capsular, and meniscal structures [3,4]. These structures, through their passive elastic nature, provide the constraining forces necessary to balance the active force (imposed by the musculature, gravitation, and inertial dynamics) during physiologic motion [5–7]. As the soft tissue is absent in simulator testing, the elastic constraint that it naturally affords must be replicated by alternative means. In the past, mechanical spring arrangements have been used to approximate the soft-tissue constraint in AP translation and IE rotation (anterior posterior translation and internal external rotation) [8]. Although these mechanical constraint methodologies have led to creditable simulator studies, the ability of such systems to model the asymmetric, nonlinear, coupled behavior of the natural soft tissues is limited. These reasons motivate the development of the virtual soft-tissue control system reported herein.

The elastic constraint forces provided by the soft-tissue are configuration dependent (where configuration means the relative position and orientation of the femoral and tibial components). It is theoretically possible, given the force-displacement and torque-rotation relationships for the knee's relevant degrees of freedom, to determine the elastic constraint forces and torques for any configuration of the prosthetic device. The VST control system embodies the relationship between configuration and constraint force in a real-time algorithm integrated with a traditional impedance control-loop design. The VST control system currently employs a single-input single-output cubic-spline algorithm for each controlled degree of freedom. The cubic-spline is programmable and permits establishing input-output relationships, such as linear, nonlinear, and asymmetric relationships, which represent the desired characteristics of soft-tissue constraint. The published literature and ISO and ASTM standards provide data necessary to establish the required force-displacement and torque-rotation relationships. As the soft-tissue constraint relationships are software programmable, field adjustments are simpler than adjustment of mechanical spring systems and permit the employment of realistic constraint relationships.

## Methods

### *Virtual Soft-Tissue (VST) Control System*

*Software and Electronics*—Figure 1 shows a schematic of one channel of the virtual-soft-tissue control system. The real time control and data acquisition subsystems are implemented in DSP firmware and electronic hardware. The iterative learning control subsystem is implemented in software running on a PC

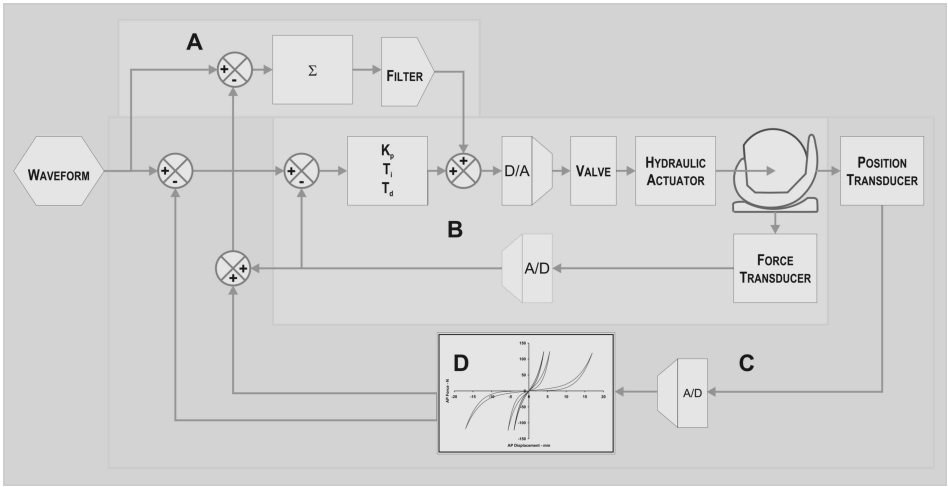


FIG. 1—Virtual soft-tissue (VST) schematic with iterative learning control (ILC) algorithm.

and provides periodic corrective signals via an Ethernet interface to the real-time control subsystem.

The reference waveform may be derived from the ISO force-control waveform ensemble for walking gait or, alternatively, from clinical or biomechanical data representative of the desired physiological function. This reference waveform input consists of one cycle of kinetic data representing the active forces (i.e., those of musculature, gravitation, and dynamics) acting across the prosthetic device.

The block labeled (D) in the figure represents the virtual soft-tissue algorithm, which determines the force response based on the current configuration of the prosthetic components. A cubic-spline implementation of the virtual soft tissue provides the flexibility to represent a wide range of soft-tissue characteristics. Soft-tissue models such as the linear model currently established by the ISO standard [9] or more complex models such as those proposed for future ISO and ASTM standards may be programmed by proper choice of spline coefficients.

The block labeled B depicts a standard form PID (proportional, integral, derivative) control loop. This loop is configured as a force-control loop for AP motion or torque control for IE rotation, which means that the loop input corresponds to a setpoint force (or torque) and the system responds by driving the controlled actuator to achieve that setpoint force. The achieved force level is measured via the multiaxis force transducer, digitized, and returned to the input summing junction of the control loop. The PID algorithm calculates proportional, integral, and derivative error signals and attempts to correct the system's response accordingly.

Section A of the schematic shows the iterative learning control portion of the algorithm, which circumscribes the PID and VST portions of the control loop. The ILC algorithm acts on the sum of the measured prosthetic constraint and the algorithmically determined soft-tissue constraint force. The iterative learning control algorithm improves the quality of control by using the error of previous iterations to develop the control signal for the current iteration [10,11]. This process is accomplished off-line on a cycle-by-cycle basis. The data from the previous iteration is stored in computer memory and when the cycle is completed an updated control signal is calculated. This updated control signal is supplied to the feed-forward summing junction of the real time controller in a synchronized manner.

*Soft-Tissue Constraint Rationale*—Force-control relies on the principle of equipollence to reduce the complex system of forces acting across the knee to a system of orthogonal forces and torques consistent with the simulator's actuators. The internal forces acting across the knee (see Fig. 2) may be aggregated into three groups: 1, the active forces of the musculature, dynamics and gravity, 2, the soft-tissue forces of the ligamentous and capsular structures, and 3, the contact forces acting on the articular surface. Under conventional force-control simulation, the machine's actuators generate the active forces, a passive mechanical constraint system simulates the soft-tissue forces, and the contact forces result directly from

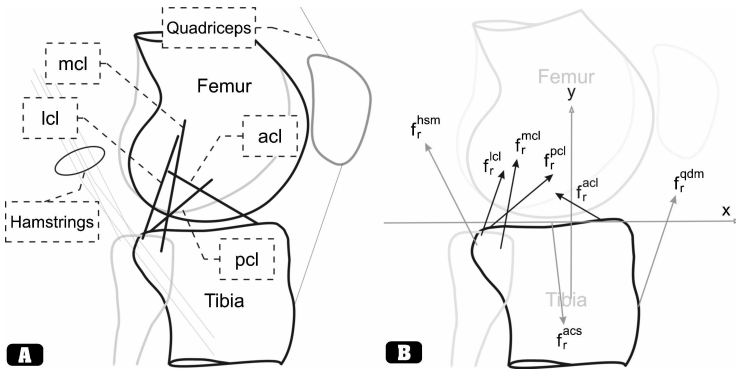


FIG. 2—The passive and active soft-tissue structures of the knee shown in (A). Ligaments shown are MCL—medial collateral, LCL—lateral collateral, ACL—anterior cruciate, and PCL—posterior cruciate. Muscle groups represented are hamstrings and quadriceps. Vector representation of the soft-tissue and articular contact forces acting across the knee are shown in (B).

tibial-femoral contact [1].

The VST system incorporates similar partitioning of the forces while providing a programmable model to represent the passive soft-tissue constraint forces [12]. The constraint model is flexible and may be programmed to provide nonlinear, asymmetric behavior such as exhibited by the structure of the natural knee. The AP (anterior posterior) components of the passive forces shown in Fig. 2 are summed to form a single soft-tissue constraint force:

$$f_y^s = f_y^{mcl} + f_y^{lcl} + f_y^{acl} + f_y^{pcl} + f_y^{pcs} \quad (1)$$

where  $f_y^{pcs}$  is the contribution of the posterior capsule structure (omitted in the figure). Likewise, the active forces of the musculature are summed to form the AP driving force:

$$f_y^f = f_y^{hsm} + f_y^{qdm} \quad (2)$$

An analogous approach was taken for IE rotation with the musculature providing the active torque and soft tissue providing the passive torque.

Figure 3 depicts the reduced force system acting on the prosthetic mounted in the simulator. The vector  $f_y^s$  represents the sum of the soft-tissue constraint from Eq. 1. The vector labeled  $f_y^f$  represents the active forces of musculature on the AP axis, while the components  $f_y^c$  and  $f_z^c$  represent the load cell measured contact force on the AP and axial axes, respectively.

*Soft-Tissue Characteristics*—The passive load displacement characteristics of the knee have been the subject of considerable research [4,13–19].

Figure 4(A) shows typical AP load-displacement curves obtained under several constraint and ligament conditions adopted from the work of Fukubayashi et al. Fukubayashi exercised intact post-mortem human knee specimens in a load frame while measuring the AP load and corresponding displacement. The three data series shown in Figure 4(A) represent the conditions: intact ligaments with tibial rotation held at a fixed (neutral) angle, intact ligaments with the tibia unconstrained in rotation and sectioned ACL and PCL. Figure 4(B) depicts typical VST soft-tissue models representing several ligament conditions: sectioned ACL intact PCL, intact ACL and PCL, and the linear spring specified ISO [9].

### Test System Hardware

*Simulator Degrees of Freedom and Coordinate System*—Figure 5 depicts the Force 5 simulator's motion axes and measurement coordinate system. The motion axes adopt a convention similar to the joint coordinate system (JCS) described by Grood [20]. The JCS considers two limb-segment embedded Cartesian coordinate systems, one femoral and the other tibial fixed. Both coordinate systems have one axis

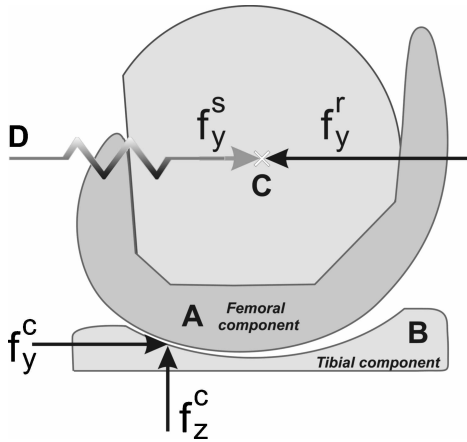


FIG. 3—Reduced system of forces acting on implant device in simulator machine. Soft-tissue constraint forces represented as displacement dependent spring force  $f_y^s$ , actuator drive force  $f_y^r$ , measured contact forces  $f_y^c$  and  $f_z^c$ .

aligned with the long axis of the bone, a second axis oriented medial-laterally, and a third oriented anterior-posteriorly. When the joint is in the reference position the coordinate systems share a common origin that serves as a reference point for translation. In addition to the two limb-segment fixed coordinate systems, a floating axis is defined mutually perpendicular to the femoral medial-lateral (ML) axis and the tibial shaft long axis.

The simulator axes are similar to the JCS. The compression-distraction (axial load) is collinear with the tibial shaft (in Fig. 5 it is shown offset from its true line of action, which lies on the  $f_z$  load cell axis). AP translation is mutually perpendicular to the flexion axis and the axial load axis and corresponds to the JCS floating axis. IE rotation occurs about the axial load axis, which is again consistent with the JCS. However, abduction-adduction and medial-lateral translation are inconsistent with the JCS. These motions are relative to the tibial fixed coordinate system rather than relative to the floating axis of the JCS.

Figure 5 shows the multiaxial load cell located beneath the tibial fixture in such a manner that it is subjected to all tibial-femoral contact loads. The load cell resolves the contact force into orthogonal components  $f_x$ ,  $f_y$ , and  $f_z$ , and moment into components  $m_x$ ,  $m_y$ , and  $m_z$ . Outputs of the load cell were supplied to the measurement and control system and appropriate channels were used for feedback to

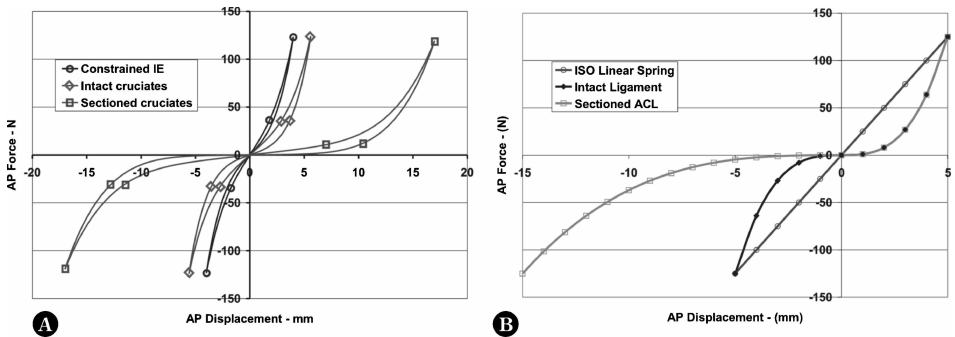


FIG. 4—Plot A left shows force-displacement curves for: intact ligaments – tibia rotationally constrained, intact ligaments – tibia free to rotate, and sectioned ACL and PCL (all curves attributed to Fukubayashi et al.) [16]. Plot B right shows VST modeled force-displacement curves representing sectioned ACL, intact ligaments, and ISO linear spring model.

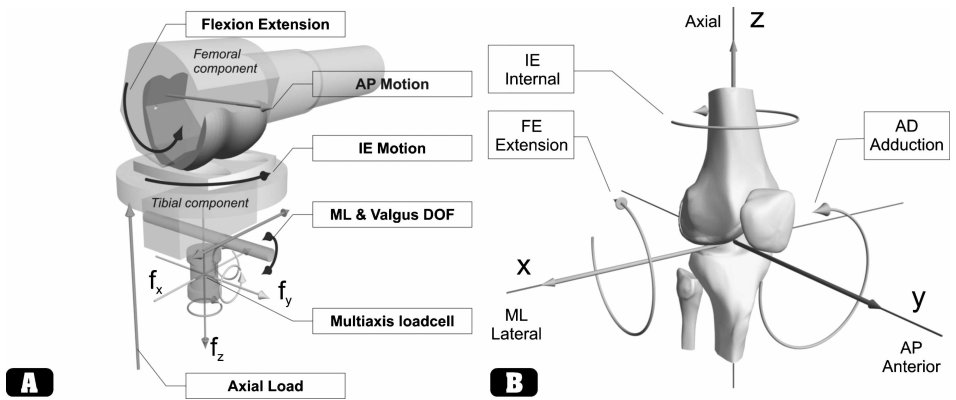


FIG. 5—Left (A) depicts the simulator machine's degrees of freedom and multi-axis load cell, which measures three orthogonal forces and three orthogonal moments. Note that the axial load is shown displaced from its true line of action, which is aligned with the  $f_z$  axis. Right (B) depicts the machine coordinate system following the JCS of Grood and Suntay.

control the machine's actuators. In particular,  $f_y$ ,  $f_z$ , and  $m_z$  were used to provide force and moment feedback for the AP, axial and IE channels of the virtual soft-tissue control system. Displacements in all degrees of freedom were monitored with linear or angular potentiometers. These outputs were routed to the signal conditioning subsystem and, subsequently, through software to the inputs of the appropriate channels of the virtual soft-tissue constraint algorithm.

**Data Acquisition**—All channels were filtered using fourth-order Butterworth analog anti-aliasing filters at 600 Hz. Data was then digitized at 16-bit resolution, 1000 sps (samples per second) per channel. A digital finite impulse response (FIR) filter (fourth-order Butterworth) permitted selection of cutoff frequencies between 30 Hz and 1 kHz. Filter settings in this work were 100 Hz for  $f_z$ , 70 Hz for  $f_y$  and  $m_z$ , and 150 Hz for all other channels. These settings were chosen empirically to provide the best operation of the control loop.

**Prosthetic Device**—A medium conformity posteriorly stabilized (PS) condylar prosthetic device was evaluated under several different constraint conditions. The tibial-femoral contact surface was lubricated periodically with mineral oil during the course of the testing.

### Test Conditions

**Reference Waveforms**—This work utilized the ISO force-control waveform [9] ensemble to provide the driving waveforms for walking gait simulation. The waveform ensemble is comprised of four waveforms, axial, flexion, IE, and AP, based on the work of Morrison and others [6,21]. As per the ISO specification, Axial load was controlled under force-control, flexion-extension under displacement control, and IE rotation and AP translation under torque and force-control respectively (constrained by virtual soft-tissue constraint). A 10-Hz low-pass filter was applied offline to all channels to remove irregularities and smooth waveform transitions. Figure 6 depicts the reference waveforms output by the VST controller's arbitrary waveform generator.

**Soft-Tissue Model**—Testing was conducted using four different soft-tissue models providing AP and IE constraint characteristics shown in Figs. 7(A) and 7(B), respectively.

The legends in these figures identify Tests A through D corresponding to the four constraint conditions. Test A represents nonlinear constraint similar to the proposed ASTM standard for cruciate substituting prosthetics. The proposed constraint is comprised of three piecewise linear segments where a laxity region is defined extending  $\pm 2.5$  mm about the neutral position and anterior and posterior segments are defined

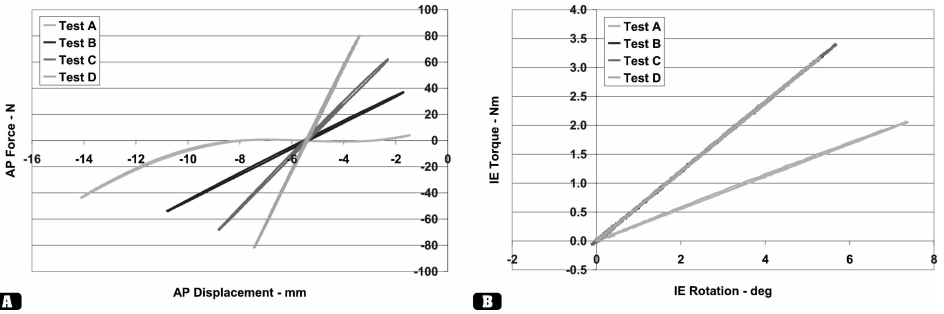


FIG. 6—Realized force deflection characteristics for the four soft-tissue models. A and B show AP and IE constraint models for four different test configurations (in B, three constraint models are superimposed).

with stiffness of 9.3 N/mm. The IE constraint for this proposed standard is linear with a torsional spring constant of 0.28 Nm/deg. Tests B, C, and D utilize 10, 20, and 40-N/mm linear AP models with stiffness bracketing as specified in the current ISO 14243-1 standard [9]. The three linear AP models all use a linear 0.6 Nm/deg torsional spring stiffness for IE constraint. The kinematics and kinetics for these four different constraint conditions are presented in the results section corresponding to Tests A, B, C, and D.

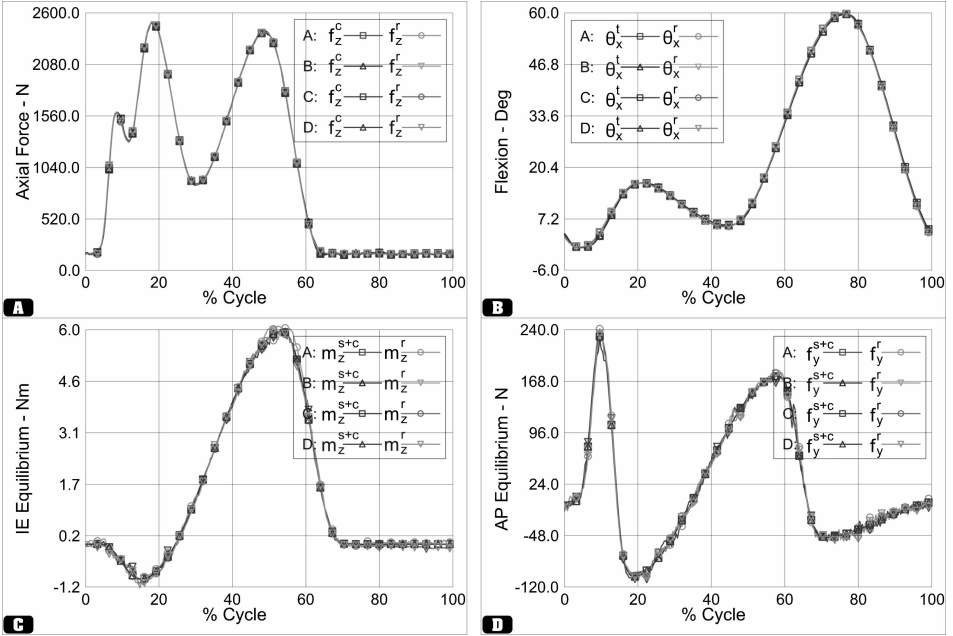


FIG. 7—Tracking error for the four controlled axes of motion: (A) axial load, (B) flexion-extension, (C) IE rotation, and (D) AP translation. AP is inverted to accommodate the machine’s electro-mechanical coordinate system.

TABLE 1—RMS, peak-to-peak, and average tracking error reported as a percentage of the full-scale reference waveform amplitude.

	RMS				Peak-to-peak				Average			
	Axial $\epsilon_z^f$	Flex $\epsilon_x^0$	IE $\epsilon_z^m$	AP $\epsilon_y^f$	Axial $\epsilon_z^f$	Flex $\epsilon_x^0$	IE $\epsilon_z^m$	AP $\epsilon_y^f$	Axial $\epsilon_z^f$	Flex $\epsilon_x^0$	IE $\epsilon_z^m$	AP $\epsilon_y^f$
Test A Mean	0.6	0.9	1.4	2.0	-1.1	0.1	-2.1	-0.8	0.0	0.0	0.1	0.0
SD	0.3	0.9	0.7	0.6	1.2	0.2	2.6	2.1	0.0	0.0	0.5	0.2
Test B Mean	0.5	0.9	2.2	1.7	-0.8	0.1	-4.2	-0.9	0.0	0.0	0.0	0.0
SD	0.2	0.9	1.9	0.4	0.9	0.3	7.2	2.3	0.0	0.0	1.2	0.2
Test C Mean	0.4	0.6	2.1	1.7	-0.5	0.0	-5.3	-0.4	0.0	0.0	0.1	0.0
SD	0.1	0.5	2.2	0.1	0.4	0.2	9.0	2.3	0.0	0.0	1.3	0.1
Test D Mean	0.4	0.5	2.4	1.5	-0.4	0.0	-3.6	-1.2	0.0	0.0	0.1	0.0
SD	0.1	0.3	2.0	0.1	0.2	0.2	6.6	2.3	0.0	0.0	1.2	0.1
<b>Average</b>	<b>0.5</b>	<b>0.7</b>	<b>2.0</b>	<b>1.7</b>	<b>-0.7</b>	<b>0.1</b>	<b>-3.8</b>	<b>-0.8</b>	<b>0.0</b>	<b>0.0</b>	<b>0.1</b>	<b>0.0</b>
<b>Mean SD</b>	<b>0.2</b>	<b>0.7</b>	<b>1.7</b>	<b>0.3</b>	<b>0.7</b>	<b>0.2</b>	<b>6.4</b>	<b>2.3</b>	<b>0.0</b>	<b>0.0</b>	<b>1.0</b>	<b>0.1</b>

## Results

### Tracking Performance

Figures 6(A)–6(D) show the tracking errors for all controlled channels. Figures 6(A) and 6(B) depict the reference waveforms and feedback signals for axial load and flexion. Figures 7(C) and 6(D) depict the waveforms and constraint-sums for IE and AP. The close correlation between feedback and waveform signals indicates exact tracking performance. Note that the plots of the four tests representing the different constraint conditions are virtually superimposed.

Absolute error for each of the controlled channels was calculated:

$$\epsilon_z^f = f_z^r - f_z^c \quad (3)$$

$$\epsilon_x^0 = \theta_x^r - \theta_x^t \quad (4)$$

$$\epsilon_z^m = m_z^r - (m_z^s + m_z^c) \quad (5)$$

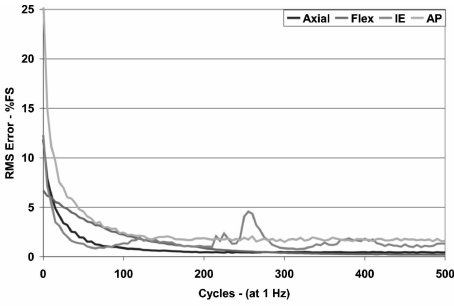
$$\epsilon_y^f = f_y^r - (f_y^s + f_y^c) \quad (6)$$

where  $\epsilon_z^f$ ,  $\epsilon_x^0$ ,  $\epsilon_z^m$ , and  $\epsilon_y^f$  correspond to the error for axial load, flexion-extension, IE rotation, and AP translation, respectively. Data was recorded for a full cycle at 5-s intervals, synchronized with the waveform onset, over the course of 500 cycles of motion. Eighty-five non-consecutive samples of data, each consisting of 1000 data points, were evaluated to determine RMS, peak-to-peak, and average error. The means and standard deviations were calculated and the results tabulated in Table 1.

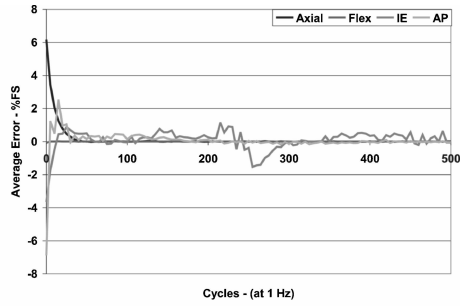
An average RMS error of less than 2 % in all cases shows extremely good tracking performance for all channels of motion. The low standard deviations indicate repeatable, stable operation over the 500-cycle measurement period.

Figures 8(A) and 8(B) show the RMS and average error over time following initial startup of the system. These figures represent the so-called “learning curve” of the ILC algorithm. Initially the system is stably but inaccurately controlled with the PID control. The tracking error is reduced over successive cycles of motion by the iterative application of the learning control algorithm. Typically, ILC results in an exponentially decreasing error, which approaches a system dependent asymptotic limit. This behavior was observed with the VST implementation, as shown by Figs. 8(A) and 8(B). Within 30 cycles of motion, the error on all channels was reduced to less than 5 % FS (percent full-scale reference waveform).

After 200 cycles, the error diminished to less than 1.7 % FS on all channels. A 4 % spike in IE-RMS error was observed at 250 cycles. Although this anomaly could arise from instability of the ILC control algorithm, it is likely the result of a transient frictional perturbation of the IE actuator. Of greater interest is that the ILC algorithm responded quickly and reduced the error to the previously achieved level. Overall, the ILC algorithm produces stable well-behaved motion over a wide variety of operating conditions with little or no operator tuning.



**A**



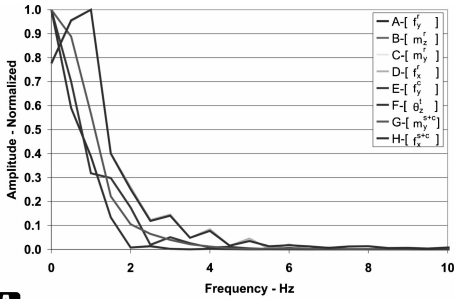
**B**

FIG. 8—Error versus time as controlled by the iterative learning control (ILC) algorithm.

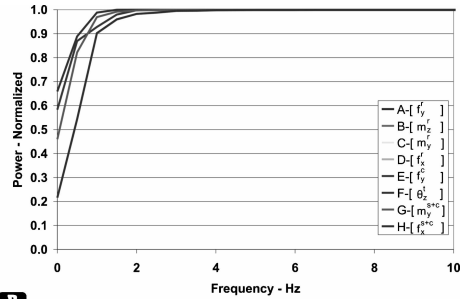
**Spectral Analysis**

Spectral analysis was performed using discrete Fourier transform (DFT) analysis. Figures 9(A) and 9(B) show the amplitude and cumulative power spectrum distribution of the reference waveforms and measured feedback signals. These signals are virtually superimposed, indicating high spectral correlation of reference inputs and kinetic outputs. Figures 9(C) and 9(D) show the results of similar analysis for the kinematic signals (i.e., translations and rotations). Table 2 shows the cumulative power at selected frequencies, 2, 4, and 8 Hz.

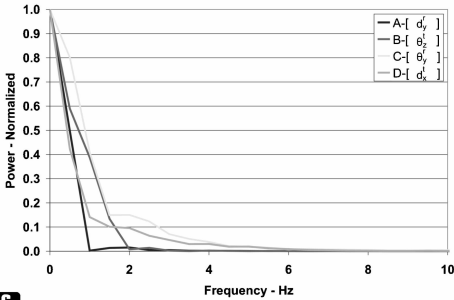
The AP constraint-sum exhibits slightly elevated spectral content, with 0.1 % of the power spectrum exceeding 8 Hz compared to the AP reference waveform where 0.0 % of the power exceeds 8 Hz. Comparison of the kinematic signals (displacement channels) spectral content to the kinetic signals (feed-



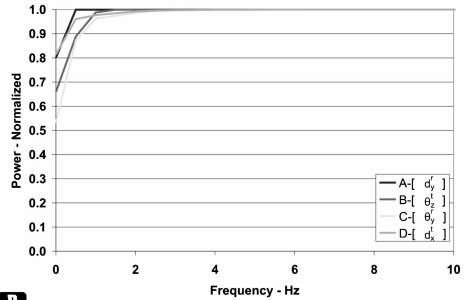
**A**



**B**



**C**



**D**

FIG. 9—Plots (A) and (B) show normalized amplitude and cumulative power spectrum of the driving waveforms and associated feedback signals. Plots (C) and (D) shows the results of similar analyses for the translational and rotational motions.

TABLE 2—Cumulative power at 2,4, and 8 Hz for waveforms, feedback, and displacements, in percent.

Hz	Reference Waveform				Feedback or Constraint-sum				Angular or Linear Displacement			
	Axial	Flex	IE	AP	Axial	Flex	IE	AP	Axial	Flex	IE	AP
2.0	99.8	100.0	99.7	98.3	99.8	100.0	99.7	98.3	100.0	100.0	98.6	99.3
4.0	100.0	100.0	100.0	99.9	100.0	100.0	100.0	99.8	100.0	100.0	99.9	99.9
8.0	100.0	100.0	100.0	100.0	100.0	100.0	100.0	99.9	100.0	100.0	100.0	100.0

back and constraint-sum signals) spectral content indicates upper-frequency bounding of all channels at the 100.0 % level at 8.0 Hz. It may be inferred from the lower frequency content of the kinematic signals that the energy of the kinetic signals at elevated frequencies is insufficient to overcome the frictional dead-band of the prosthetic tibial-femoral interface. The frequency content of all channels, except the AP constraint-sum, is contained below 8 Hz at the 100.0 % level.

### Kinematic and Kinetic Results

Figure 10 depicts the IE and AP kinetics and kinematics. Plots (A) through (D) show IE rotational results and (E) through (H) show AP translational results. Each plot is comprised of four sets of time series data representing the results of tests A through D as indicated by the legend.

Tests A through D correspond to the parameterized constraint conditions described previously. In these plots, positive AP force corresponds to an anteriorly oriented inter-component force acting on the tibia, whereas, positive AP displacement corresponds to a posterior displacement of the tibia relative to femur. Positive IE torque corresponds to an inter-component torque resisting internal rotation of the tibia relative to the femur, and positive IE rotation represents internal rotation of the tibia relative to the femur.

Predictably, the IE results (plots A through C) demonstrate that the AP constraint has little influence on torsional kinetics and kinematics while IE constraint dominates. The three test results representing the same IE soft-tissue constraint condition (0.6 Nm/deg, Tests B, C, and D) exhibited consistent behavior in tibial rotation. The peak-to-peak contact torque, soft-tissue torque, and tibial rotation show, respectively, 4 %, 8 %, and 8 % variation from maximum to minimum across the three identical IE constraint cases. Comparison of the results for the two different constraint conditions, 0.28 and 0.60 Nm/deg, corresponding to Test A and the averages of Tests B, C, and D, show a 17 % decrease in contact constraint, 40 % increase in soft-tissue constraint, and concomitant 25 % decrease in IE rotation. In Test A, the soft-tissue contributes 36 % of the torsional constraint torque, whereas it contributes 72 % in the high-constraint cases (Tests B–D).

The AP contact and soft-tissue constraint forces (plots 10E and 10F, respectively) exhibit trends consistent with the progressively increasing soft-tissue constraint conditions of Tests A through D. Plot 10E shows a progressive decrease in the AP contact constraint force with peak-to-peak values of 358, 328, 315, and 282 N for Tests A through D, respectively (in order of increasing AP stiffness). With similar consistency, the soft-tissue constraint force progressively increases with peak-to-peak values of 48, 90, 130, and 161 N. Thus, the contact constraint force decreases by 23 %, while the soft-tissue constraint force increases 240 % over the range of constraint conditions. The kinematic results shown in plot 10G show a decreasing AP displacement with peak-to-peak values of 22, 16, 14, and 13 mm over the course of the four tests. The total reduction in AP translation from the most compliant to the least compliant case was 42 %.

The center of pressure (COP) measurements shown in Figs. 10(H) and 10(D) provide estimates of the AP and ML contact positions. The COP measurement is based on the zero-moment notion, which determines the point of intersection of the line of action of the applied force and the plane of interest (the transverse plane in this case) by use of the measured force and moment components acting on the system. Using the outputs of the six-degree-of-freedom load cell the COP on the  $y$  and  $x$  axes are calculated as follows:

$$d_y^c = [m_x^c + (f_y^c \cdot d_z)]/f_z^c \quad (7)$$

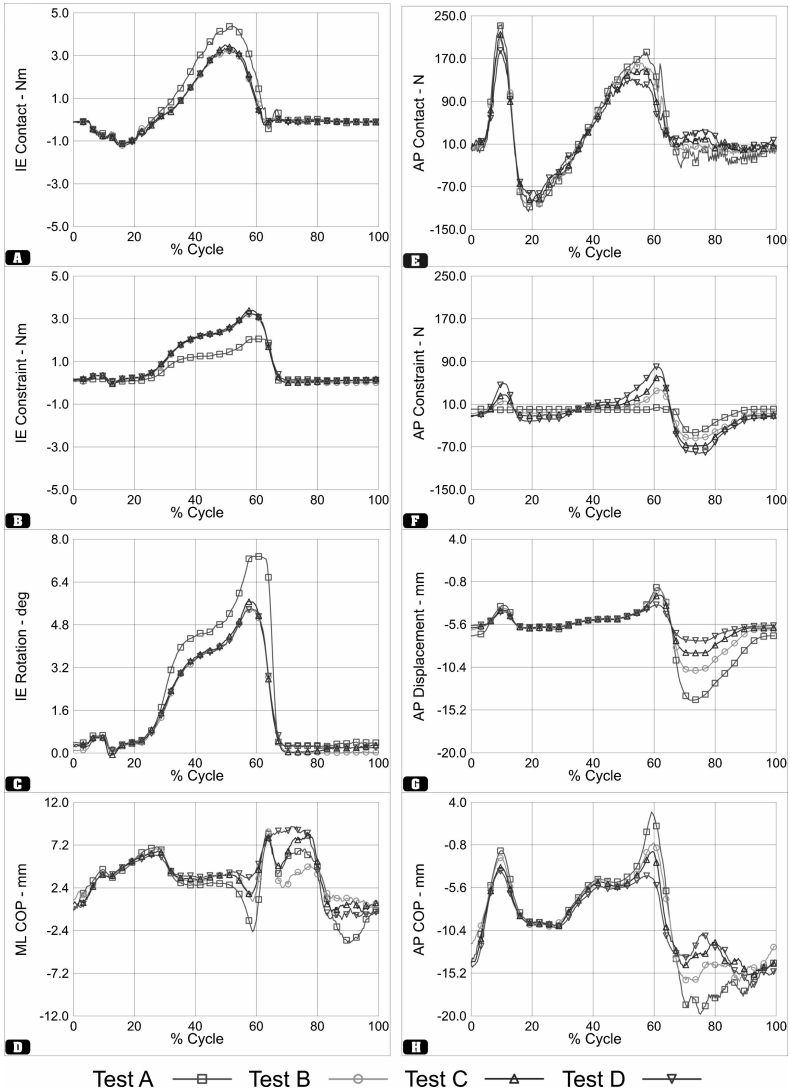


FIG. 10—Plots (A),(B),(C), and (D) correspond to IE contact torque, soft-tissue torque, IE rotation, and the ML center of pressure. Plots (E),(F),(G), and (H) correspond to AP contact constraint force, soft-tissue force, AP displacement and the AP center of pressure. Test A represents nonlinear constraint and Tests B, C, and D represent linear, 10, 20, and 40-N/mm constraint. Positive AP force corresponds to anteriorly oriented inter-component force acting on the tibia. Positive AP displacement corresponds to posterior displacement of the tibia relative to femur. Positive IE torque corresponds to an inter-component torque resisting internal rotation of the tibia relative to the femur. Positive IE rotation is internal.

$$\vec{d}_x^c = [m_y^c - (f_x^c \cdot d_z)]/f_z^c \quad (8)$$

where  $d_y^c$  and  $d_x^c$  are AP and ML COPs,  $m_x^c$  and  $m_y^c$  are the measured  $x$  and  $y$  axis moments,  $f_y^c$  and  $f_x^c$  are the measured shear forces,  $f_z^c$  is the measured axial force, and  $d_z$  is the distance from the contact point to the electromechanical origin of the transducer.

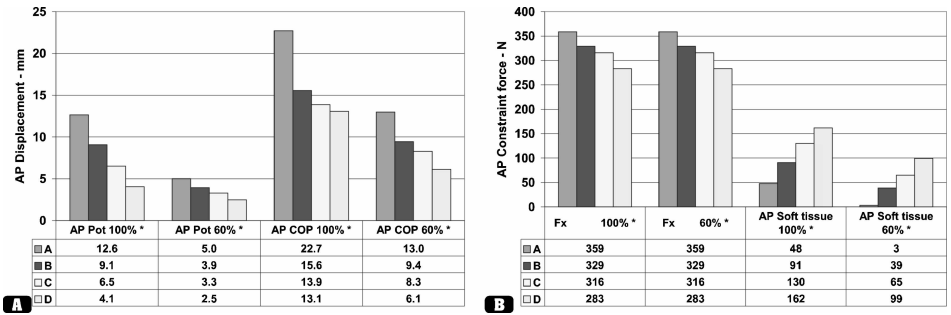


FIG. 11—Comparison of kinematic (A) and kinetic (B) results across the series of tests with progressive change of soft-tissue constraint stiffness parameter.

The total knee replacement (TKR) device will have two contact points (barring condylar liftoff) corresponding to the medial and lateral aspects of contact. The measured COP corresponds to a single point lying on the line joining these two contact points, proportionally weighted toward the contact point bearing the greatest load. In this manner, the COP measure provides a good single measurement or estimate of the contact position providing qualitative and quantitative information about the load distribution and movement on the surface of the prosthesis.

Calibration of the COP measurement was performed under dynamic conditions similar to those encountered in prosthetic testing. A plain polished stainless steel cylindrical femoral component was exercised using the ISO waveform on a flat ultra high molecular weight (UHMW) mock tibial component. With this mechanical arrangement the flexion axis position was expected to coincide with the measured COP. Over the full range of motion the deviation between the two measurements was less than 3 %.

The COP measurement is of considerable interest from a prosthetic wear perspective as it quantifies the excursion of the load-bearing contact-patch rather than the excursion of the flexion axis. This renders the measurement insensitive to mounting conditions and component geometry while providing highly relevant wear information. Geometrical considerations reveal that the excursion of the contact point will exceed the motion of the flexion axis for conforming components. In this test the average excursion, based on the COP measurement for the four soft-tissue conditions, exceeds the conventional AP displacement measurement by 150 % during the stance phase of the loading cycle.

Figure 11 presents the kinematic and kinetic peak-to-peak results for 60 % (stance phase) and for 100 % (stance and swing phases) of the gait cycle. The trends are again consistent with the increasing progression of the soft-tissue stiffness from Tests A to D.

**Discussion**

*Overall Tracking Performance*

Low RMS errors of 0.5, 0.7, 2.0, and 1.7 % FS are reported for axial, flexion, IE, and AP degrees of freedom, respectively. Similarly, peak-to-peak and average error are extremely low. When constraint-sum signals and reference waveforms are compared in plotted results, no distinguishable differences between the two are evident. DFT analysis and power spectrum analysis revealed that the frequency content of the driving waveforms and resulting constraint-sum signals or feedback signals are virtually identical.

The measured variables of contact constraint force, soft-tissue constraint force, and translational motion demonstrate consistent behavior across tests as soft-tissue constraint is parametrically varied. Increased stiffness was accompanied by increased soft-tissue constraint, decreased contact constraint, and a concomitant decrease in motion. These trends are summarized graphically in Fig. 11. The IE results from the two torsional constraint models also show consistent results. Increased torsional soft-tissue constraint is accompanied by decreased torsional contact constraint and decreased IE rotation. The IE results demonstrate low sensitivity to the AP constraint conditions.

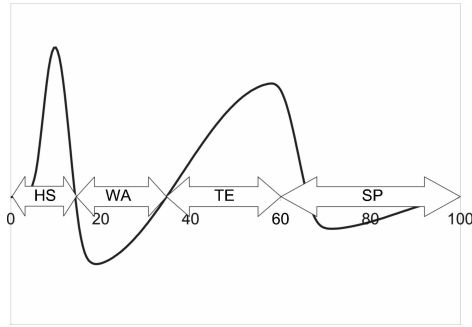


FIG. 12—Gait phases.

### Comparison with Simulator Studies

A kinematic study conducted by DesJardins on a Stanmore simulator machine provides useful published results for comparison of the VST results reported in this study [21]. DesJardins evaluated several prosthetics, none identical to the subject device; however, the range of devices provides a basis for comparison. Similarity of maxima and minima features and the phase relationships of kinematic and kinetic results demonstrate a qualitative correlation between studies. Temporal characteristics of both IE and AP kinematics and kinetics show similar primary features and concurrence of orientation of motions and loads.

One posteriorly stabilized fixed bearing implant device was described in the DesJardins study. This device serves best for comparison with the posteriorly stabilized device of this study. The two devices will be called the NGL device and the VST device, corresponding to the DesJardins and virtual soft-tissue studies, respectively. Only kinematics for similar constraint conditions are compared.

In IE rotation the NGL device reached a peak rotation of  $11.1^\circ$  at 60 % of the loading cycle, whereas the VST device reached a somewhat lower peak of  $7.3^\circ$  at the same point in the loading cycle. The torsional contact constraint of the NGL and VST devices reached maximum external torques of 4.7 and 5.6 Nm at  $50^\circ$ , respectively. Likewise, the torsional soft-tissue constraint reached maximum external torques of 2.7 Nm and 2.05 Nm at  $60^\circ$ . Overall, the NGL and VST devices exhibit very similar temporal characteristics in the three measured parameters, contact constraint, soft-tissue constraint, and internal rotation. The VST device shows a 34 % reduction in IE rotation and a 21 % reduction in soft-tissue constraint torque compared to the NGL device. As both tests use linear torsional spring approximations, the realized torsional stiffness were estimated as the ratio of the maximum rotational displacement to the maximum soft-tissue constraint torque. This ratio is 0.24 N/mm for the NGL (Stanmore test) and 0.28 N/mm for the VST (virtual soft-tissue test). The Stanmore soft-tissue constraint stiffness is approximately 14 % lower than the target torsional stiffness of 0.28 Nm/deg. If the Stanmore constraint had been adjusted to 0.28 N/mm, then the achieved rotation would have been reduced to  $9.6^\circ$ . At this level, the reduction in rotation of the VST device would have been 23 %, quite consistent with the measured 21 % difference in torsional constraint. When the Stanmore machine results are adjusted to accommodate the small discrepancy in the realized torsional spring stiffness, the NGL and VST IE kinematics and kinetics agree well. The VST device appears to provide marginally higher torsional constraint than the NGL device.

The AP translation results are discussed on a gait cycle feature basis as shown in Fig. 12, where HS, WA, TE, and SP correspond to the heel strike, weight acceptance, terminal extension and swing phase, respectively, of the gait loading cycle. Additionally, aggregate motions for the stance phase (0 to 60 %) and the swing phase (60 to 100 %) of the loading cycle are considered for the NGL and VST comparison. First, it should be noted that the driving AP waveforms in both studies are somewhat truncated at all maxima and minima when compared to the ISO 14243-1 standard. In the current (VST) study the application of the 10-Hz pre-filter causes a slight reduction of the high frequency content and a smoothing of maxima and minima of the waveform. In the Stanmore (NGL) case, the waveform was manually modified to achieve the desired output tracking performance. Note that Fig. 12 is inverted from the ISO specification to accommodate the VST study's electromechanical coordinate system (positive indicates a posterior external load applied to the tibial shaft).

Taking the gait phases in temporal order, the Stanmore NGL study shows 25 %, 32 %, and 27 % truncations in amplitude (compared to the ISO standard) for HS, WA, and TE maxima and minima features, respectively. The VST study shows 12 %, -5 %, and -3 % deviation (negative indicates overshoot) for the same features. Two points were examined in the swing phase: one at 65 % and one at 80 % of the load cycle. The NGL study shows 256 % and 131 % deviation at those points and the VST study shows 6 % and 19 % deviation at the same points. The average of the NGL study shows a 28 % reduction in the applied force during the stance phase, whereas the VST study shows a 7 % deviation from the ISO standard. The soft-tissue stiffness calculated from the range of motion and range of soft-tissue constraint for the NGL study was 17.1 N/mm, whereas linear regression applied to the VSD data shows the soft-tissue constraint stiffness of 19.98 N/mm. In both cases the target stiffness was 20 N/mm. In terms of kinematics, the Stanmore NGL study's 14 % reduction in soft-tissue constraint and concomitant 28 % reduction in applied force will partially compensate for one another. The range of motion during the stance phase of the NGL study was 3.8 mm. The VST study similarly resulted in a 3.8 mm range. Both NGL and VST results show similar temporal characteristics with an initial maxima slightly lagging the HS load maxima and a second maxima coincident with TO (toe off). The VST study shows slightly exaggerated motion at HS (2 mm), compared to the NGL study (1.4 mm), and slightly reduced motion at TO, NGL (4.2 mm), and VST (3.8 mm).

During stance phase, the results of the NGL and VST studies show high temporal correlation, similarity of maxima and minima features, and consistent empirical kinematic and kinetic results. Reduced spring stiffness in the Stanmore study is partially offset by reduced peak loading at all maxima and minima. After giving consideration to the variance in applied loads and constraint stiffness, the small differences in observed kinematic and kinetic patterns are likely attributable to differences in prosthetic design.

In the swing phase, the NGL study differs substantially from the VST study. Swing phase loading appears to have been neglected in the NGL study, perhaps because swing phase is considered to be of less relevance in wear studies. Nevertheless, nonzero swing phase loading is specified in the ISO standard and results in substantial AP motion. In the VST study, ISO specified loading was replicated accurately and resulted in a rapid 6.6-mm anterior translation of the tibial component immediately following TO. This motion in the swing phase represents the highest velocity and the greatest excursion encountered at any point in the kinematic trace. Simple contact measurements revealed that with PS stabilized devices, impingement of the femoral cam on the tibial spine occurs in this region of the loading cycle. As cam impingement represents a possible failure mode, the swing phase is of interest in the testing process. Further study should be considered focusing on specification of the kinetics in the swing phase with regard to physiologic appropriateness.

## Conclusions

The VST control system, coupled with the ILC algorithm, provides an easily adjustable control system capable of simulating a wide variety of soft-tissue behavior. In this study, the concept is applied to both AP force control and IE torque control. The VST control system provides modeled soft-tissue behavior consistent with theoretical expectations across a range of constraint conditions. Changes in constraint conditions for both IE and AP lead to appropriate changes in kinematic performance. Stable, accurate control performance was demonstrated for several modeled soft tissue characteristics. The ILC algorithm performs a crucial function in improving tracking performance and reducing setup and tuning time.

Comparisons with a mechanically constrained system reported in the literature show a high temporal correlation of both IE and AP results with similar phasing and magnitudes of kinetic and kinematic features. Slight variations, as might be expected due to the dissimilarity in tested prosthetics, were observed.

Future work should include extension of the control concept to include coupling of soft-tissue constraint characteristics with flexion and tibial rotation parameters. Additional validation conducted with wear studies, examining wear and particle morphology, wear extent, and wear rate are appropriate. Yet, as it is currently implemented, the VST control methodology represents a major advance in simulation technology and paves the way for parametric evaluation of prosthetic kinematic and durability performance.

## References

- [1] Walker, P. S. et al., "A Knee Simulating Machine for Performance Evaluation of Total Knee Replacements," *J. Biomech.*, Vol. 30, No. 1, 1997, pp. 83–89.
- [2] Walker, P. S., Blunn, G. W., and Lilley, P. A., "Wear Testing of Materials and Surfaces for Total Knee Replacement," *J. Biomech.*, Vol. 9 No. 6, 1976, pp. 397–405.
- [3] Markolf, K. L., Mensch, J. S., and Amstutz, H. C., "Stiffness and Laxity of the Knee—The Contributions of the Supporting Structures. A Quantitative in vitro Study," *J. Bone Jt. Surg., Am. Vol.*, Vol. 58, No. 5, 1976, pp. 583–594.
- [4] Ma, C. B. et al., "Significance of Changes in the Reference Position for Measurements of Tibial Translation and Diagnosis of Cruciate Ligament Deficiency," *J. Orthop. Res.*, Vol. 18, No. 2, 2000, pp. 176–182.
- [5] Morrison, J. B., "The Mechanics of the Knee Joint in Relation to Normal Walking," *J. Biomech.*, Vol. 3, No. 1, 1970, pp. 51–61.
- [6] Shelburne, K. B., Pandy, M. G., and Torry, M. R., "Comparison of Shear Forces and Ligament Loading in the Healthy and ACL-Deficient Knee During Gait," *J. Biomech.*, Vol. 37, No. 3, 2004, pp. 313–319.
- [7] Walker, P. S. et al., "Methodology for Long-Term Wear Testing of Total Knee Replacements," *Clin. Orthop.*, Vol. 372, 2000, pp. 290–301.
- [8] ISO, "Implants for Surgery - Wear of Total Knee-Joint Prostheses - Part 1: Loading and Displacement Parameters for Wear-Testing Machines with Load Control and Corresponding Environmental Conditions for test," in *ISO 14243-1:2002(E)*, 2002.
- [9] YangQuan, C. et al., "Iterative Learning Control with Iteration-Domain Adaptive Feedforward Compensation. A Separative High-order Framework for Monotonic Convergent Iterative Learning Controller Design," *IEEE Conf. on Decision and Control*, 2003, Maui, Hawaii.
- [10] Moore, K. L., "Multi-loop Control Approach to Designing Iterative Learning Controllers," 1998.
- [11] O'Connor, J. J. et al., "The Geometry of the Knee in the Sagittal Plane," *Proc. Inst. Mech. Eng., Part H: J. Eng. Med.*, Vol. 203, No. 4, 1989, pp. 223–233.
- [12] Butler, D. L., "Anterior Cruciate Ligament: Its Normal Response and Replacement," *J. Orthop. Res.*, Vol. 7, No. 6, 1989, pp. 910–921.
- [13] Butler, D. L., Noyes, F. R., and Grood, E. S., "Ligamentous Restraints to Anterior-Posterior Drawer in the Human Knee. A Biomechanical Study," *J. Bone Jt. Surg., Am. Vol.*, Vol. 62, No. 2, 1980, pp. 259–270.
- [14] Eagar, P., Hull, M. L., and Howell, S. M., "A Method for Quantifying the Anterior Load-Displacement Behavior of the Human Knee in Both the Low and High Stiffness Regions," *J. Biomech.*, Vol. 34, No. 12, 2001, pp. 1655–1660.
- [15] Fukubayashi, T. et al., "An in vitro Biomechanical Evaluation of Anterior-Posterior Motion of the Knee. Tibial Displacement, Rotation, and Torque," *J. Bone Jt. Surg., Am. Vol.*, Vol. 64, No. 2, 1982, pp. 258–264.
- [16] Huss, R. A., Holstein, H., and O'Connor, J. J., "The Effect of Cartilage Deformation on the Laxity of the Knee Joint," *Proc. Inst. Mech. Eng., Part H: J. Eng. Med.*, Vol. 213, No. 1, 1999, pp. 19–32.
- [17] Markolf, K. L., Kochan, A., and Amstutz, H. C., "Measurement of Knee Stiffness and Laxity in Patients with Documented Absence of the Anterior Cruciate Ligament," *J. Bone Jt. Surg., Am. Vol.*, Vol. 66, No. 2, 1984, pp. 242–252.
- [18] Shoemaker, S. C., and Markolf, K. L., "Effects of Joint Load on the Stiffness and Laxity of Ligament-Deficient Knees. An in vitro Study of the Anterior Cruciate and Medial Collateral Ligaments," *J. Bone Jt. Surg., Am. Vol.*, Vol. 67, No. 1, 1985, pp. 136–146.
- [19] Grood, E. S., and Suntay, W. J., "A Joint Coordinate System for the Clinical Description of Three-Dimensional Motions: Application to the Knee," *J. Biomech. Eng.*, Vol. 105, No. 5, 1983, pp. 136–144.
- [20] Morrison, J. B., "Function of the Knee Joint in Various Activities," *Biomed. Eng.*, Vol. 4, No. 12, 1969, pp. 573–580.
- [21] DesJardins, J. D. et al., "The Use of a Force-Controlled Dynamic Knee Simulator to Quantify the Mechanical Performance of Total Knee Replacement Designs During Functional Activity," *J. Biomech.*, Vol. 33, No. 10, 2000, pp. 1231–1242.

Dong Zhao,<sup>1</sup> W. Gregory Sawyer,<sup>1</sup> and Benjamin J. Fregly<sup>1</sup>

## Computational Wear Prediction of UHMWPE in Knee Replacements

---

**ABSTRACT:** A multibody dynamic contact model predicted the damage sustained by two tibial inserts tested under different conditions on an AMTI knee simulator machine. The model required a wear factor of  $7.7 \times 10^{-7}$  mm<sup>3</sup>/Nm to match the wear volume measured from the first insert after 0.86 million cycles of simulated gait. The model matched the medial and lateral damage depths measured from the second insert to within 0.3 mm after 5 million cycles of simulated gait and stair (10:1 ratio). Computational models may be valuable for screening new knee implant designs rapidly and performing sensitivity studies of component positioning issues.

**KEYWORDS:** computational wear prediction, dynamic contact simulation, knee simulator, total knee replacement

### Introduction

Wear of ultrahigh molecular weight polyethylene remains a primary limitation in extending the longevity of total knee replacements (TKRs) [1]. Consequently, knee simulator machines are commonly used to evaluate wear performance of new knee implant designs and materials [2]. These machines typically have multiple stations, each providing multiaxial motion and load control of the TKR components in a physiological environment. Wear testing on a simulator machine is time consuming and expensive due to the large number of low-frequency cycles that must be run [3]. Moreover, different stations on the same test machine sometimes produce different wear results.

In contrast, computer simulation can be a fast and reproducible method for predicting TKR performance [4]. For example, computer simulations have been used to predict tibial insert damage under *in vivo* conditions [5]. These simulations required between 10 and 20 min of CPU time on a typical PC workstation to predict tibial insert wear, creep, and damage (=wear+creep) for a specified number of loading cycles of gait and stair activities. While fluoroscopic measurements can provide accurate *in vivo* motion inputs to such simulations [6,7], accurate *in vivo* load inputs are difficult to obtain and an estimated number of motion cycles must be used for each simulated activity. Simulation of a simulator machine overcomes these limitations since the motion and load inputs as well as number of loading cycles are known accurately for each simulated activity, as is the sequence of simulated activities. Thus, simulator machines provide a well-controlled test bed for evaluating computational approaches to TKR damage prediction.

This study evaluates the ability of a multibody dynamic contact model of an AMTI knee simulator machine to predict tibial insert damage in two knee implants of the same design. Wear volume was measured gravimetrically for one insert after 0.86 million cycles of simulated gait while damage depths were estimated via laser scanning for another insert after 5 million cycles of simulated gait and stair. Computer simulations were used to predict wear volume for the first insert and damage depths for the second. Sensitivity studies were also performed for the second insert to evaluate the extent to which predicted damage depths varied with changes in femoral component position and orientation in the AMTI machine.

---

Manuscript received October 18, 2005; accepted for publication April 10, 2006; published online May 2006. Presented at ASTM Symposium on Wear of Articulating Surfaces on 8 November 2005 in Dallas, TX; S. A. Brown, L. N. Gilbertson, and V. D. Good, Guest Editors.

<sup>1</sup> Department of Mechanical & Aerospace Engineering, University of Florida, 231 MAE-A Building, P.O. Box 116250, Gainesville, FL 32611-6250, e-mail: fregly@ufl.edu

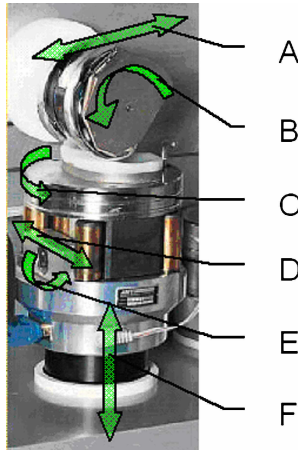


FIG. 1—Degrees of freedom for one station of the AMTI knee simulator machine. A=anterior/posterior translation, B=flexion/extension, C=internal/external rotation, D=medial/lateral translation, E=varus/valgus rotation, and F=vertical translation.

**Multibody Dynamic Contact Model**

The AMTI simulator studied in this paper has six stations. On each station, the implant components are mounted and immersed in a sealed, temperature controlled, fluid bath. Loads and motions are programmed through the control system in order to simulate walking, stair climbing, or other physiologic motions. The machine has displacement control for anterior/posterior translation, flexion extension, and internal/external rotation and force control for superior/inferior translation (Fig. 1).

A multibody dynamic contact model of one station of an AMTI knee simulator machine was constructed to predict TKR damage in a single cruciate-retaining knee implant design (Genesis II, Smith & Nephew, Inc., Memphis, TN). The multibody model was implemented within the Pro/MECHANICA MOTION simulation environment (PTC, Waltham, MA) (Fig. 2). The femoral component was connected to the ground via a planar joint, the tibial tray to the machine base via another planar joint, and the

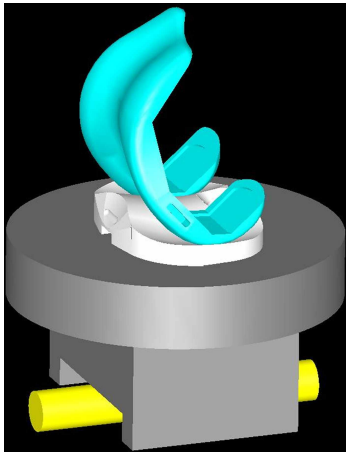


FIG. 2—Multibody dynamic contact model of the AMTI knee simulator developed within the Pro/MECHANICA MOTION simulation environment.

machine base to the ground via a 6 degree-of-freedom (DOF) joint. The joint between the femur and insert possessed 6 DOFs and was utilized to measure relative (i.e., joint) kinematics for contact calculations. Each DOF in the model was either motion or load controlled to mimic the function of each DOF in the AMTI machine. Femoral component and tibial insert contact surfaces were extracted from the Genesis II CAD models and refitted with single-surface representations using commercial software (Geomagic Studio, Research Triangle Park, NC) to improve computational efficiency.

A deformable contact model based on elastic foundation theory was incorporated into the multibody dynamic model to predict contact forces and pressures between the implant surfaces. The contact model utilizes springs distributed over the articulating surfaces of the tibial insert to prevent excessive interpenetration. The contact pressure  $p$  for any spring was calculated from

$$p = \frac{(1 - \nu)E(p)}{(1 + \nu)(1 - 2\nu)} \frac{d}{h} \quad (1)$$

where  $E(p)$  is Young's modulus of the elastic layer, which was either constant or a nonlinear function of  $p$ ,  $\nu$  is Poisson's ratio of the elastic layer,  $h$  is the layer thickness at the spring location, and  $d$  is the spring deflection, defined as the interpenetration of the undeformed surfaces in the direction of the local surface normal (see [8] for further details). The distance  $d$  was computed each time instant given the current position and orientation of the tibial insert and femoral component obtained from the 6 DOF joint in the multibody dynamic model.

### Computational Wear and Creep Model

The time history of contact pressures and slip velocities experienced by each element were input into a computational wear model to develop element-by-element damage predictions. The total damage depth for each element was the combination of the material lost due to mild wear and the surface deformation due to compressive creep.

$$\delta_{Damage} = N\delta_{Wear} + \delta_{Creep}(N) \quad (2)$$

where  $\delta_{Damage}$  is the total damage depth,  $N$  is the total number of cycles,  $\delta_{Wear}$  is the wear depth per cycle, and  $\delta_{Creep}(N)$  is the creep depth for  $N$  cycles.

The depth of material removed from an element over one cycle due to mild wear was predicted using Archard's classic law for mild wear [9]. The model predicts the wear depth of an element on the contact surface based on the wear rate, contact pressure and sliding distance.

$$\delta_{Wear} = k \sum_{i=1}^n p_i d_i = k \sum_{i=1}^n p_i |v_i| \Delta t_i \quad (3)$$

where  $k$  is the wear rate,  $p_i$  is the contact pressure and the sliding distance is calculated as the product of the slip velocity magnitude  $|v_i|$  multiplied by the time increment  $\Delta t_i$ .

UHMWPE creep is the time dependent deformation of a loaded viscoelastic material. UHMWPE that experiences creep deformation will have some elastic recovery when the load is removed. Based on the research of Lee and Pienkowski [10], creep of each element in a UHMWPE can be estimated as a function of contact pressure and compression time.

$$\delta_{Creep} = \left[ C1 + C2 \left( \text{Log} \left( N \sum_{i=1}^n \Delta t_{ci} \right) - 4 \right) \right] \frac{\sum_{i=1}^n p_i \Delta t_{ci}}{\sum_{i=1}^n \Delta t_{ci}} h \quad (4)$$

where  $R$  is the relaxation rate,  $C1 = 3.491 \times 10^{-3}$  and  $C2 = 7.966 \times 10^{-4}$  are constants,  $N$  is the total number of cycles,  $\Delta t_{ci}$  is the time increment when the contact pressure  $p_i$  is nonzero, and  $h$  is the initial thickness. The unit for pressure is MPa, the unit for time minutes, and the unit for thickness mm.

### Comparison with Worn Inserts

Two sets of simulations were performed with the model to emulate the conditions experienced by the two Genesis II implants tested on the AMTI machine. The first set was configured to mimic component

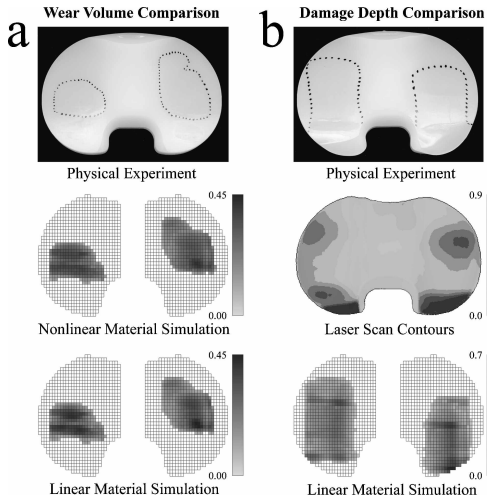


FIG. 3—Visualization of experimental and simulated damage of a commercial knee implant tested on an AMTI simulator machine under two test configurations. (a) First test where experimental wear volume was measured gravimetrically after 0.86 million cycles of simulated gait. (b) Second test where experimental damage depths were measured via laser scanning after 5 million cycles of simulated gait and stair.

positioning and loading during 0.86 million cycles of simulated gait. Linear ( $E=463$  MPa) and nonlinear ( $\epsilon_0=0.0257$ ,  $\sigma_0=15.9$ ,  $n=3$ ) material models ( $\nu=0.46$  for both models) were used in the elastic foundation contact model to investigate the influence of material properties on wear area and volume predictions. The predicted wear volume for a range of wear factors was compared to the actual wear volume measured gravimetrically. The second set of simulations was configured to mimic different component positioning and loading during 5 million cycles of simulated gait and stair (10:1 ratio). Only the linear material model was used and the wear factor was set to  $1 \times 10^{-7}$  mm<sup>3</sup>/Nm based on measurements of the average femoral component surface roughness (not available for the first implant) and data reported in [11]. The predicted damage depths for this one wear factor were compared to actual damage depths estimated by laser scanning the worn and a matched unworn insert and measuring the deviation between the two sets of contact surfaces with commercial software (Geomagic Studio, Research Triangle Park, NC). Changes in wear, creep, and damage depths for variations in femoral component position and orientation in the AMTI machine ( $\pm 3$  mm or  $\pm 3^\circ$  in each direction) were also predicted. All simulations used a contact element grid of  $40 \times 30$  in both compartments and required less than 20 min of CPU time on 2.0 GHz Xeon work station.

**Results and Discussion**

For the first insert, a wear factor of  $7.7 \times 10^{-7}$  mm<sup>3</sup>/Nm was needed in the wear model to match the gravimetrically measured wear volume of 21.7 mm<sup>3</sup> (Fig. 3(a)). This value corresponds to an average femoral component surface roughness of approximately 0.1 μm which is likely higher than that of the component used in the test. Wear areas and volumes predicted using the two material models (linear and nonlinear) were nearly identical, indicating that choice of material model had little influence on these quantities. Damage regions predicted by the simulations were in excellent agreement with those observed on the central portion of each insert contact surface. However, small posterior damage regions observed experimentally were not reproduced by the simulation, possibly because the feedback control system of the simulator machine did not follow the commanded load waveform closely during portions of the cycle. Posterior damage would have increased the predicted wear volume and caused a corresponding decrease in the wear factor necessary to match the experimentally measured wear volume.

For the second insert, the predicted damage depths of 0.6 and 0.8 mm on the medial and lateral sides,

TABLE 1—Sensitivity of predicted wear, creep, and damage (=creep +wear) depths to, variations in femoral component position ( $\pm 3$  mm or  $\pm 3^\circ$  in each direction).

	Wear Depth (mm)		Creep Depth (mm)		Damage Depth (mm)	
	medial	Lateral	Medial	Lateral	Medial	Lateral
Nominal	0.11	0.17	0.45	0.59	0.56	0.76
+Xtrans	0.10	0.36	0.54	0.89	0.64	1.14
-Xtrans	0.12	0.15	0.46	0.51	0.54	0.66
+Ytrans	0.12	0.18	0.48	0.59	0.60	0.76
-Ytrans	0.09	0.16	0.49	0.56	0.58	0.69
+Ztrans	0.11	0.17	0.47	0.57	0.58	0.70
-Ztrans	0.11	0.18	0.47	0.58	0.57	0.75
+Xrot	0.10	0.19	0.47	0.59	0.52	0.76
-Xrot	0.12	0.16	0.57	0.55	0.69	0.68
+Yrot	0.09	0.16	0.52	0.53	0.54	0.66
-Yrot	0.15	0.17	0.51	0.58	0.66	0.75
+Zrot	0.12	0.19	0.47	0.61	0.58	0.74
-Zrot	0.11	0.16	0.45	0.51	0.56	0.64
Experiment	...	...	...	...	0.92	0.92

respectively, were within 0.3 mm of the measured depths of 0.9 and 0.9 mm (Fig 3(b)). Increasing the wear factor to  $2 \times 10^{-7}$  mm<sup>3</sup>/Nm, consistent with the roughest regions on the femoral component, increased the predicted damage depths to 0.7 and 0.9 mm. The predicted damage regions were in good agreement with the actual damage regions, though the predicted locations of maximum damage did not correspond well with reality. Modifying the femoral component position by  $\pm 3$  mm or orientation by  $\pm 3^\circ$  created a standard deviation of at most  $\pm 0.06$  mm in predicted wear depth,  $\pm 0.10$  mm in predicted creep depth, and  $\pm 0.13$  mm in predicted damage depth on either side, indicating that predicted damage depth was not highly sensitive to femoral component malalignment in the simulator machine (Table 1). The most likely explanation for poor prediction of maximum damage locations was observed changes over time of the motion and load outputs produced by the simulator machine.

These results suggest that a multibody dynamic model can produce reasonable predictions of TKR damage generated in a knee simulator machine. Such models may prove valuable in the future for screening new knee implant designs rapidly or performing sensitivity studies that would be too time consuming to complete with physical simulator machines.

### Acknowledgments

This study was supported by an NSF CAREER award to B.J. Fregly and by Smith & Nephew Orthopaedics.

### References

- [1] Sharkey, P. F., Hozack, W. J., Rothman, R. H., Shastri, S., and Jacoby, S. M., "Why are Knee Replacements Failing Today?" *Proceedings of the Knee Society*, Dallas, TX, February 2002.
- [2] Walker, P. S., Blunn, G. W., Broome, D. R., Perry, J., Watkins, A., Sathasivam, S., Dewar, M. E., and Paul, J. P., "Knee Simulating Machine for Performance Evaluation of Total Knee Replacements," *J. Biomech.*, Vol. 30, 1997, pp. 83–89.
- [3] Muratoglu, O. K., Perinchieff, R. S., Bragdon, C. R., O'Connor, D. O., Konrad, R., and Harris, W. H., "Metrology to Quantify Wear and Creep of Polyethylene Tibial Knee Inserts," *Clin. Orthop. Relat. Res.*, Vol. 410, 2003, pp. 155–164.
- [4] Godest, A. C., Beaugonin, M., Haug, E., Taylor, M., and Gregson, P. J., "Simulation of a Knee Joint Replacement During a Gait Cycle Using Explicit Finite Element Analysis," *J. Biomech.* Vol. 35, 2002, pp. 267–276.
- [5] Fregly, B. J., Sawyer, W. G., Harman, M. K., and Banks, S. A., "Computational Wear Prediction of a Total Knee Replacement from in vivo Kinematics," *J. Biomech.*, Vol. 38, 2005, pp. 305–314.
- [6] Banks, S. A. and Hodge, W. A., "Accurate Measurement of Three-dimensional Knee Replacement

- Kinematics Using Single-Plane Fluoroscopy," *IEEE Trans. Biomed. Eng.*, Vol. 43, 1996, pp. 638–649.
- [7] Ranawat, C. S., Komistek, R. D., Rodriguez, J. A., Dennis, D. A., and Anderle, M., "Three-Dimensional Determination of Femoral-Tibial Contact Positions Under in vivo Conditions Using Fluoroscopy," *Clin. Biomech. (Bristol, Avon)*, Vol. 13, 2004, pp. 455–472.
- [8] Fregly, B. J., Bei, Y., and Sylvester, M. E., "Experimental Evaluation of an Elastic Foundation Model to Predict Contact Pressures in Knee Replacements," *J. Biomech.*, Vol. 36, 2003, pp. 1659–1668.
- [9] Archard, J. F. and Hirst, W., "The Wear of Metals Under Unlubricated Conditions," *Proceedings of the Royal Society*, Vol. A236, 1956, pp. 397–410.
- [10] Lee, K. Y. and Pienkowski, D., "Compressive Creep Characteristics of Extruded Ultrahigh Molecular-Weight Polyethylene," *J. Biomed. Mater. Res.*, Vol. 39, 1998, pp. 261–265.
- [11] Fisher, J., Dowson, D., Hamdzah, H., and Lee, H. L., "The Effect of Sliding Velocity on the Friction and Wear of UHMWPE for use in total artificial joints," *Wear*, Vol. 175, 1994, pp. 219–225.

## **SECTION II: VERTEBRAL DISC**

Steven Kurtz,<sup>1</sup> Ryan Siskey,<sup>2</sup> Lauren Ciccarelli,<sup>2</sup> André van Ooij,<sup>3</sup> John Pelozo,<sup>4</sup> and Marta Villarraga<sup>5</sup>

## Retrieval Analysis of Total Disc Replacements: Implications for Standardized Wear Testing

---

**ABSTRACT:** The purpose of this study was to evaluate the wear and surface damage mechanisms of polyethylene in retrieved CHARITÉ total disc replacements. The retrieved implants showed evidence of adhesive/abrasive wear mechanisms in the central domed region of the implants. In addition, there was also evidence of macroscopic rim damage, including radial cracking, plastic deformation, and third body damage. The retrieved total disc replacements (TDRs) displayed surface damage observed previously in both hip and knee replacements. The information from this study will be useful for engineers seeking to adequately replicate long-term, clinically relevant damage modes of TDRs using *in vitro* testing methods.

**KEYWORDS:** total disc arthroplasty, wear, surface damage, fatigue, fracture, retrieval analysis, polyethylene

### Introduction

The goal of total disc arthroplasty is to replace a degenerated and painful intervertebral disc, thereby restoring the motion and load-carrying capacity of a functional spinal unit [1]. The production of wear debris from artificial discs, as well as other spine implants, is a clinical concern. Wear-debris induced osteolysis has been implicated as a potential mechanism for late onset spine pain following the failure of stainless steel and titanium instrumented fusions [2]. Osteolysis has also been observed around certain total disc replacement designs, such as the Acroflex artificial disc [3], and case studies of osteolysis around CHARITÉ disc replacements have also been reported [4,5]. Although the reported occurrence of osteolysis with metal-on-polyethylene total disc replacements has thus far been relatively rare, the long-term wear behavior of artificial discs remains of clinical importance.

The international spine community is still in the early stages of developing standards for wear testing of total disc replacements (TDRs). Multiple test protocols have been proposed under the auspices of ASTM International and ISO. The specifics of the draft protocols have evolved slowly over time, but the continuing debate centers on the extent of cross-shear to be produced in the testing, and as to whether the wear mechanism is more “hip-like,” involving substantial cross-shear motion, or more “knee-like,” involving reduced cross-shear. ASTM Standard F 2423-05, Guide for the Functional, Kinematic, and Wear Assessment of Total disc Prostheses, has been recently approved, giving a user the option of choosing one of three approaches to evaluate lumbar TDR prostheses: (1) sequential single motion parameters (flexion/extension, lateral bending, and axial rotation); (2) one single motion followed by the other two motions coupled; or (3) all motions coupled in one test. In the absence of data from retrieval studies, the debate on the proper kinematics of spine simulators has been solely theoretical and remains thus far unresolved.

We have previously developed white light interferometry techniques to quantify the wear and surface

---

Manuscript received January 13, 2006; accepted for publication March 24, 2006; published online May 2006. Presented at ASTM Symposium on Wear of Articulating Surfaces on 8 November 2005 in Dallas, TX; S. A. Brown, L. N. Gilbertson, and V. D. Good, Guest Editors.

<sup>1</sup> Principal Engineer, Exponent, Inc., and Research Professor, Drexel University, 3401 Market St., Suite 300, Philadelphia, PA 19104.

<sup>2</sup> Associate Engineer, Exponent, Inc., 3401 Market St., Suite 300, Philadelphia, PA 19104.

<sup>3</sup> Orthopedic Surgeon, University of Maastricht, Maastricht, Netherlands.

<sup>4</sup> Orthopedic Surgeon, Center for Spine Care, Dallas, TX.

<sup>5</sup> Principal Engineer, Exponent, Inc., and Research Associate Professor, Drexel University, 3401 Market St., Suite 300, Philadelphia, PA 19104.

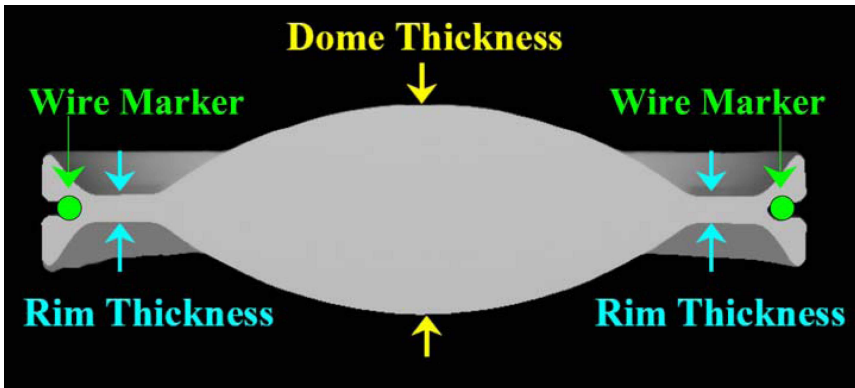


FIG. 1—Cross section view of locations where dimensional analysis was performed.

damage mechanisms of retrieved metallic and polymeric total hip replacement components [6]. In the present study, we applied our surface analysis technique in a retrieval study to evaluate the wear mechanisms of a well-established lumbar total disc replacement, the CHARITÉ Artificial Disc (DePuy Spine, Raynham, MA), formerly known as the SB CHARITÉ III. Assessment of wear and damage modes, in combination with direct measurement of surface roughness and waviness of retrieved TDRs, will provide the ultimate data for the validation of current spine simulators. Based on the data from a series of long-term implanted total disc replacements, we provide the technical foundation upon which to base recommendations for enhanced wear and mechanical testing of lumbar disc designs.

### Materials and Methods

Sixteen implants were analyzed from 14 patients undergoing TDR revision surgery. The components were implanted between 2.9–16.0y. The implantation dates ranged between 1989 and 2002; 8/16 components (50 %) were implanted prior to 1997, corresponding to the year that the manufacturer began gamma sterilization in nitrogen [7]. Therefore, the components that were implanted prior to 1997 were unambiguously gamma sterilized in air.

Revisions were performed between 2003 and 2005 due to intractable pain and facet degeneration (in all cases). The following complications were noted: subsidence ( $n=6$ ), anterior migration ( $n=3$ ), lateral subluxation ( $n=1$ ), wear with wire marker fracture ( $n=1$ ), endplate loosening ( $n=2$ ), and osteolysis ( $n=1$ ).

The retrieved implant components were cleaned using institutional procedures and examined at magnifications of up to  $40\times$  using optical microscopy. Because machining marks in polyethylene are on the order of  $3\text{--}5\ \mu\text{m}$  in height, their presence was used to identify relatively unworn regions on the implant. We studied the central domed portion of the cores for the presence of machining marks.

The origin and trajectory of transverse and radial cracks were examined in detail using both optical microscopy and microCT-based methods [8]. The components were scanned at  $18\ \mu\text{m}$  voxel resolution using a commercial microCT scanner ( $\mu\text{CT}80$ , Scanco, Switzerland). The three-dimensional reconstructions of the component and the two-dimensional sections taken through the components were evaluated for the presence of surface, through-thickness, and internal cracks.

### Dimensional Analysis

The dimensions of the UHMWPE components were measured using a calibrated micrometer and calipers with a precision of 0.001 mm. Measurements were performed in the central domed region of the core (Fig. 1), which is intended to serve as the primary load bearing region of the disc replacement. The original central thickness of the core was known from sizing information available from the manufacturer in all cases. The clinical penetration rate was calculated by dividing the change in central thickness by the total

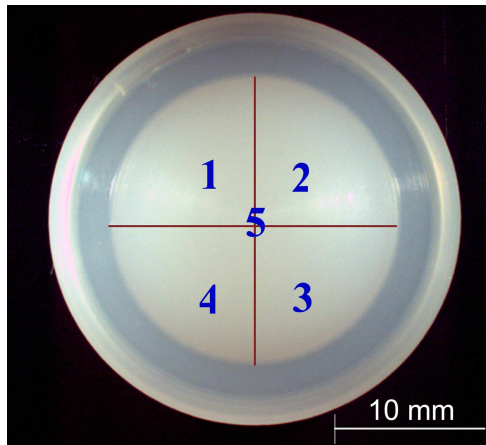


FIG. 2—Regions of interest for interferometer measurements on a new CHARITÉ polyethylene core.

implantation time. We also measured the thickness of the rim (Fig. 1), both in regions of impingement and wear, as well as in unworn regions, which were easily identified by the presence of machining marks.

#### *White Light Interferometry of Polyethylene Cores*

For the present study, the surface topology of both sides of 16 retrieved CHARITÉ polyethylene components and one new (never implanted) CHARITÉ was analyzed by white light interferometry using a NewView 5000 Model 5032 equipped with advanced texture analysis software (Zygo, Middlefield, CT). The interferometer had an out-of-plane resolution of 0.1 nm in a field of view of 0.3 by 0.4 mm. Using a 10× objective lens, the field of view was sampled in a 640 by 480 array of data points. The instrument was calibrated using a step-height reference standard traceable back to the National Institute of Standards and Technology (Gaithersburg, MD).

Five regions of interest were analyzed for each side of all of but one of the components (Fig. 2). The fatigue damage was too severe to permit measurement of surface roughness in one of the regions of interest of one retrieved component. Specifically, one scan was taken from each of the four quadrants of each component. The fifth region was sampled at the pole. The measured surface morphology for every sampled region was then classified into one of the following three general categories, as done previously for acetabular liners [6]:

- *Machining Marks*—All fields of view that contained evidence of machining marks were placed into this general category. Rather than developing further categories for partially worn machining marks, we assumed that the magnitude of the average surface waviness would more appropriately quantify changes in the morphology of surface regions in this category.
- *Adhesive/Abrasive Wear*—Surface regions with no evidence of machining marks in the waviness profile were considered worn if they appeared burnished. Typical surface features for these regions included multidirectional scratches associated with the adhesive/abrasive wear mechanism for UHMWPE [9–12]. These worn regions were relatively smooth as compared with the other two surface categories.
- *Plastic Deformation*—Surface regions with no evidence of machining marks in the waviness profile were considered plastically deformed if they appeared irregular and were not burnished. It was not possible to analyze further the mechanism producing this irregular morphology based on white light interferometry alone. Thus, these locations were labeled as having “irregular morphology.”

A baseline (least-squares) spherical surface was first mathematically subtracted from each field of view collected by the interferometer. The surface data were then Fourier transformed to deconvolve the low-frequency features (i.e., the waviness), which were intended to encompass the machining marks, from the high-frequency features (i.e., the roughness). Distinguishing between waviness and roughness is useful in

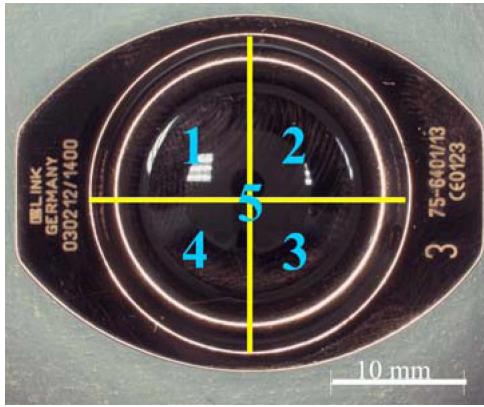


FIG. 3—Regions of interest for interferometer measurements on a new CHARITÉ endplate.

terms of quantifying wear-related changes to surface topography with respect to specific length scales. For example, a cut-off of 0.08 1/μm, which was associated with a spatial wavelength of 12.5 μm, was used in the current study to discriminate between the waviness and roughness of the articulating surface, as described previously [13]. In particular, adhesive/abrasive wear in hip replacements has been associated with reductions in waviness, as the machining marks are progressively worn away [13]. Highly burnished regions of adhesive/abrasive wear on polyethylene may also be associated with lower roughness (i.e., high frequency features) as compared with an as-machined surface [13]. Although the frequency cutoff in the current study was previously identified based on the analysis of machining marks in acetabular components, it was used in this study to provide a direct comparison with previous research [13].

For each field of view, standard surface roughness and waviness metrics were computed. Specifically, we examined the arithmetic mean roughness ( $R_a$ ) and arithmetic mean waviness ( $W_a$ ). The arithmetic mean roughness is calculated using the following equation [14,15],

$$R_a = \frac{1}{l_x l_y} \int_0^{l_x} \int_0^{l_y} |n(x,y)| dx dy \tag{1}$$

where  $n(x,y)$  is the surface roughness profile as a function of  $x$  and  $y$  location, and  $l_x$  and  $l_y$  are the length parameters of the field of view in the  $x,y$  scalar coordinate system.  $W_a$  is also calculated using Eq 1, with the exception that the waviness profile is substituted for the surface roughness profile,  $n(x,y)$ .

Unlike new components, in which the surface features are normally distributed [13], the surface features of retrieved components generally do not conform to a normal or Gaussian distribution [14]. Hence, nonparametric statistical methods (e.g., Kruskal-Wallis and Mann-Whitney tests) are generally preferred for the analysis of such data. Statistical analyses were performed using JMP Discovery Software (Version 5.0, SAS Institute, Cary, NC), and  $p$ -values of less than 0.05 were interpreted as statistically significant.

*White Light Interferometry of the CoCr Endplates*

In addition to the polyethylene cores, the surface topology of 29 cobalt-chrome endplates consisting of pairs from 14 CHARITÉ retrievals and a single endplate from the new CHARITÉ was characterized using the NewView 5000 Interferometer. Each endplate was measured in five regions of interest, four quadrants and the pole (Fig. 3). Unlike the polyethylene components, where different types of surface morphology were regularly encountered, the surfaces of the endplates displayed a more uniform surface pattern, consistent with abrasive wear. Consequently, for each field of view of the endplates, standard surface roughness and waviness metrics were computed. Specifically, we examined the arithmetic mean roughness ( $R_a$ ) and arithmetic mean waviness ( $W_a$ ) of each surface.

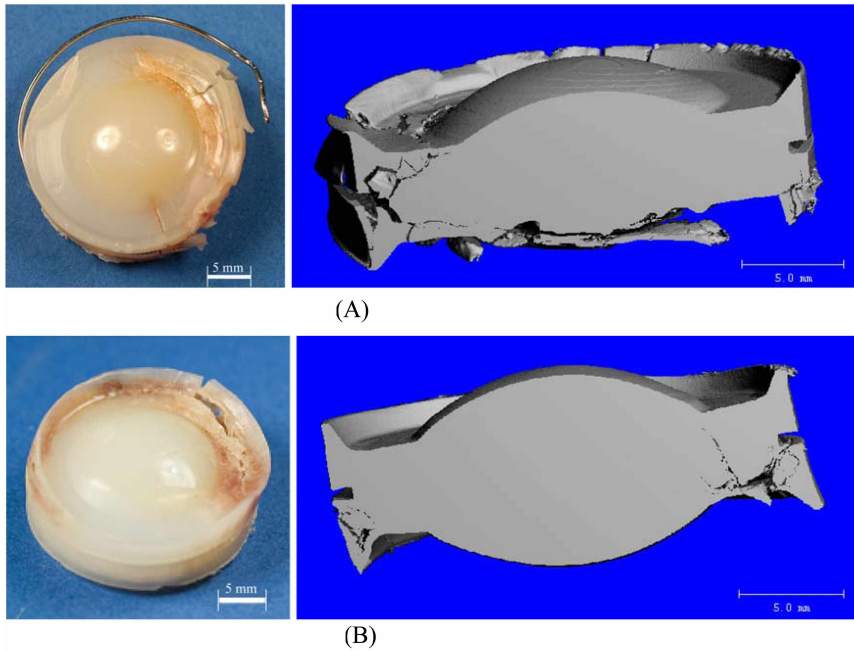


FIG. 4—Long-term CHARITÉ retrievals Maa014 (a) and Maa015 (b) showing transverse cracks using optical microscopy (left) and MicroCT (right). Maa014 and Maa015 were implanted at L4/L5 for 13.5 years and 16.0 years, respectively.

## Results

Microscopic, multidirectional scratching was observed on the central bearing surfaces of the polyethylene cores, consistent with an adhesive/abrasive wear mechanism. There was also evidence of macroscopic rim damage, including radial cracking, transverse cracking, plastic deformation, and third body damage. A broad spectrum of fatigue and fracture modes were manifested in the rims of the retrieved polyethylene implants. Cracks were oriented transversely in 10/16 cases (63%), and radially around the rim in 10/16 cases (63%). Among the eight implants that were implanted prior to 1997, transverse cracks and radial cracks were observed in six and seven cases, respectively. Among the eight implants that were implanted after 1997, transverse cracks and radial cracks were observed in four and three cases, respectively.

We confirmed the presence of transverse cracks using a combination of transmission optical microscopy and MicroCT analysis. Transverse cracks included internal cracks, along with cracks observed on the surfaces of the retrieved components. Internal cracks were confirmed by viewing a cut plane through a three-dimensional reconstructed MicroCT image. Examples of cracks observed with both optical microscopy and MicroCT are illustrated in Fig. 4.

### Dimensional Analysis

The central height of the retrieved polyethylene cores ranged between 7.3 and 11.4 mm. The corresponding endplate penetration (a combination of dome wear and creep) ranged from 0.1 to 0.9 mm (average: 0.3 mm, median: 0.3 mm). Both the average and the median penetration rate measured in the center of the dome was 0.04 mm/y (range: 0.02 to 0.14 mm/y).

Three retrievals were excluded from the rim wear analysis due to excessive rim damage. The thickness of the polyethylene core at the rim ranged between 0.9 and 5.0 mm. The endplate penetration measured at the rims of the remaining 13 implants ranged from 0.02 to 0.8 mm (average: 0.3 mm).

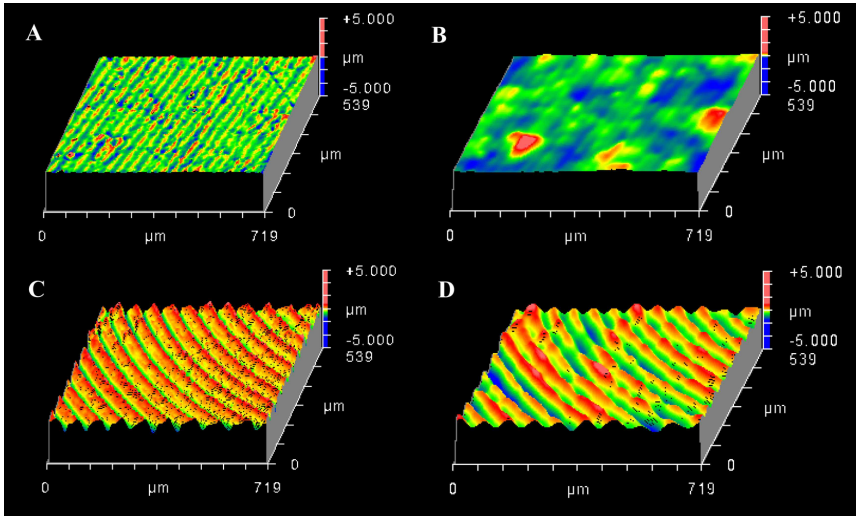


FIG. 5—Surface roughness and waviness oblique plots for regions classified as machining marks in retrieved CHARITÉ (a, b) and a never implanted CHARITÉ (c, d). (a) Retrieval  $R_a=0.04 \mu\text{m}$ ; (b) Retrieval  $W_a=0.09 \mu\text{m}$ ; (c) New  $R_a=0.36 \mu\text{m}$ ; (d) New  $W_a=0.35 \mu\text{m}$ . The retrieval was implanted for 3.1 years at L5/S1.

*White Light Interferometry of Polyethylene Cores*

Machining marks, adhesive/abrasive wear, and irregular morphology locations were identified as three different surface morphologies in the surface regions of the retrieved components (Figs. 5–8, Tables 1–3). However, it was rare to observe all three categories of surface morphologies in an individual component. Specifically, 37 of the 159 (23.3 %) surface regions sampled from the retrievals had evidence of machining marks. Of the 159 surface regions sampled, 110 (69.2 %) had evidence of adhesive/abrasive wear, and 12 of the 159 (7.6 %) surface regions sampled had evidence of irregular morphology.

There was no significant difference between the average surface roughness ( $R_a$ ) of the three classifications of surface morphology for the retrieved CHARITÉ discs ( $p>0.05$ , Kruskal-Wallis). However, differences in average surface waviness ( $W_a$ ) between the three types of morphology of the retrieved CHARITÉ were significant ( $p<0.05$ , Kruskal-Wallis).

Regions on the retrieved CHARITÉ implants identified with machining marks, adhesive/abrasive wear, and irregular morphology exhibited significantly lower surface roughness ( $R_a$ ) than similarly clas-

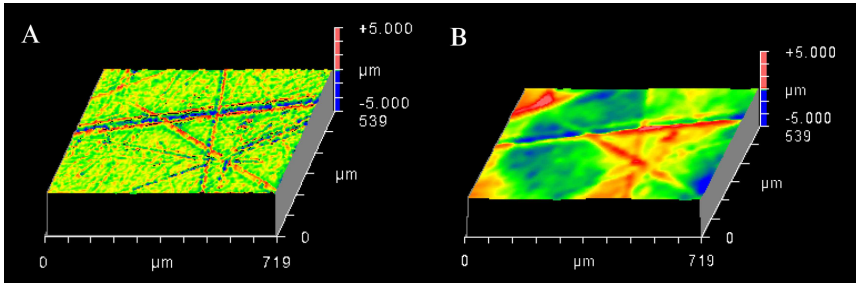


FIG. 6—Surface roughness and waviness oblique plots for regions classified as adhesive/abrasive wear in a retrieved CHARITÉ. In these surface regions, no evidence of machining marks was observed. (a) Retrieval  $R_a=0.06 \mu\text{m}$ ; (b) Retrieval  $W_a=0.14 \mu\text{m}$ . The retrieval was implanted for 12.7 years at L4/L5.

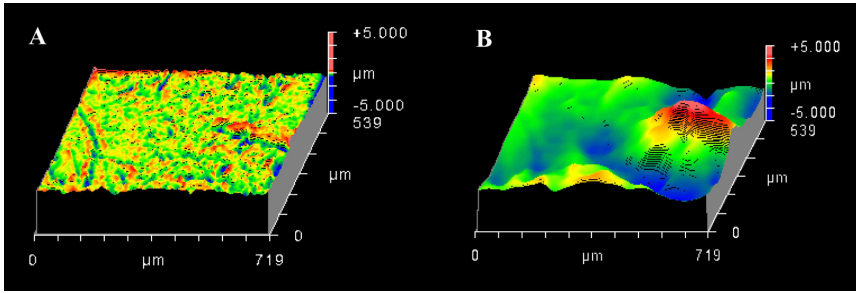


FIG. 7—Surface roughness and waviness oblique plots for regions classified as irregular morphology in retrieved CHARITÉ (a, b). In these surface regions, no evidence of machining marks was observed, and the surface morphology was highly irregular. (a) Retrieval  $R_a=0.13 \mu\text{m}$ ; (b) Retrieval  $W_a=0.94 \mu\text{m}$ . The retrieval was implanted for 6.5 years at L5/S1.

sified surface regions in short-term implanted conventional gamma inert-sterilized acetabular liners ( $p < 0.05$ , Mann-Whitney tests). However, there was no significant difference in the average surface waviness ( $W_a$ ) between CHARITÉ implants and acetabular implants when comparing the average surface waviness in regions classified as adhesive/abrasive wear, machining marks, or irregular morphology ( $p > 0.05$ , Mann-Whitney tests).

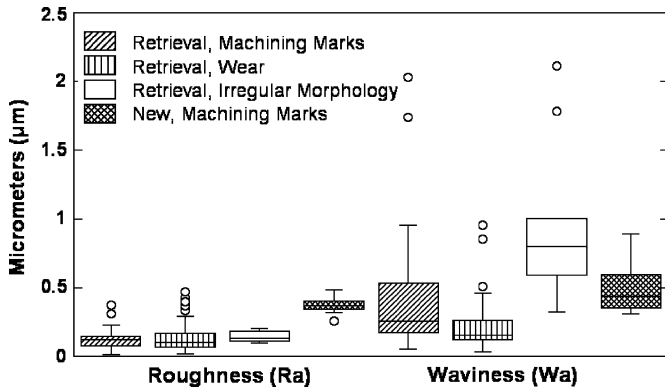


FIG. 8—Box plot comparison of average surface roughness and waviness for  $n=169$  observations from 16 retrieved CHARITÉ polyethylene cores and one never implanted core.

TABLE 1—Summary of average surface roughness ( $R_a$ ) and waviness ( $W_a$ ) for surface regions classified with machining marks from the retrieved CHARITÉ polyethylene cores, compared with previous values reported for conventional, gamma sterilized acetabular liners for total hip replacements (THA) [6].

	No. Observations	Median ( $\mu\text{m}$ )	IQR <sup>a</sup> ( $\mu\text{m}$ )
Roughness ( $R_a$ )			
Retrieved CHARITÉ	37	0.122	0.073
New CHARITÉ	10	0.366	0.056
Retrieved THA	28	0.171 <sup>b</sup>	0.048
Waviness ( $W_a$ )			
Retrieved CHARITÉ	37	0.255	0.371
New CHARITÉ	10	0.437	0.243
Retrieved THA	28	0.221	0.067

<sup>a</sup>IQR=Interquartile Range.

<sup>b</sup>Significantly higher than the Retrieved CHARITÉ ( $p < 0.05$ ).

TABLE 2—Summary of average surface roughness ( $R_a$ ) and waviness ( $W_a$ ) for surface regions classified with adhesive/abrasive wear from the retrieved CHARITÉ polyethylene cores, compared with previous values reported for conventional, gamma sterilized acetabular liners for total hip replacements (THA) [6].

Roughness ( $R_a$ )	No. Observations	Median ( $\mu\text{m}$ )	IQR <sup>a</sup> ( $\mu\text{m}$ )
Retrieved CHARITÉ	110	0.101	0.104
Retrieved THA	70	0.193 <sup>b</sup>	0.053
Waviness ( $W_a$ )			
Retrieved CHARITÉ	110	0.158	0.143
Retrieved THA	70	0.168	0.196

<sup>a</sup>IQR=Interquartile Range.

<sup>b</sup>Significantly higher than the Retrieved CHARITÉ ( $p < 0.05$ ).

*White Light Interferometry of Endplates*

Irregular morphology locations were identified in the surface regions of the retrieved endplates (Figs. 9 and 10, Table 4).

TABLE 3—Summary of average surface roughness ( $R_a$ ) and waviness ( $W_a$ ) for surface regions classified with irregular morphology from the retrieved CHARITÉ polyethylene cores, compared with previous values reported for conventional, gamma sterilized acetabular liners for total hip replacements (THA) [6].

Roughness ( $R_a$ )	No. Observations	Median ( $\mu\text{m}$ )	IQR <sup>a</sup> ( $\mu\text{m}$ )
Retrieved CHARITÉ	12	0.131	0.064
Retrieved THA	22	0.207 <sup>b</sup>	0.046
Waviness ( $W_a$ )			
Retrieved CHARITÉ	12	0.797	0.349
Retrieved THA	22	0.712	0.274

<sup>a</sup>IQR=Interquartile Range.

<sup>b</sup>Significantly higher than the Retrieved CHARITÉ ( $p < 0.05$ ).

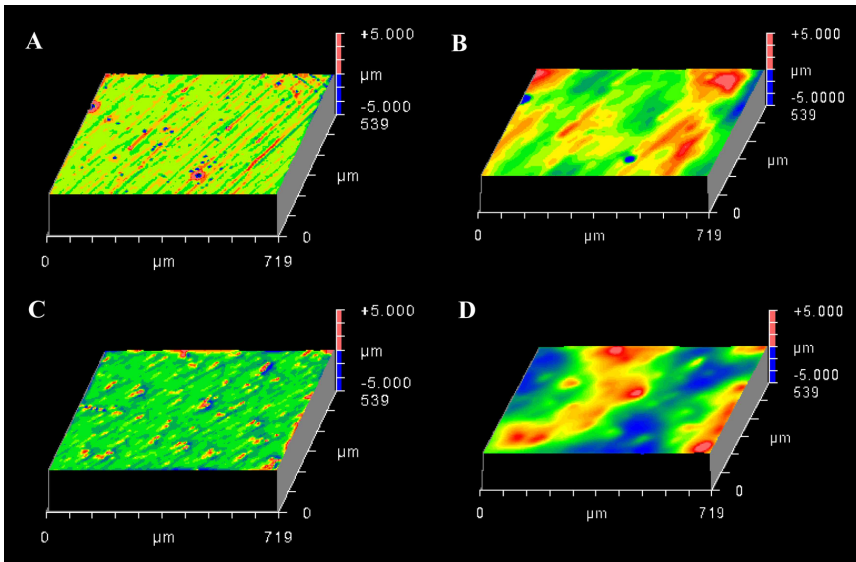


FIG. 9—Surface roughness and waviness oblique plots for endplate regions in a retrieved CHARITÉ (a, b) and a never implanted CHARITÉ (c, d). (a) Retrieval  $R_a=0.01 \mu\text{m}$ ; (b) Retrieval  $W_a=0.01 \mu\text{m}$ ; (c) New  $R_a=0.01 \mu\text{m}$ ; (d) New  $W_a=0.03 \mu\text{m}$ . The retrieval was implanted for 16 years at L4/L5.

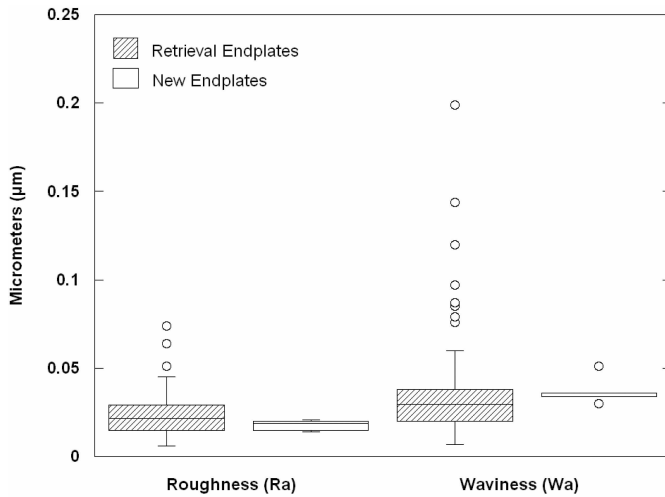


FIG. 10—Box plot comparison of average surface roughness and waviness for  $n=145$  observations from 28 retrieved CHARITÉ endplates and one never implanted endplate.

## Discussion

Based on long-term retrievals, the TDR exhibited wear and surface damage mechanisms previously observed in both hip and knee replacements. Interestingly, the domes of the implants were typically associated with adhesive/abrasive wear mechanisms previously observed in total hip replacements. According to our white light interferometry analysis, 69 % of sampled regions had evidence of adhesive/abrasive wear. On the rims of the polyethylene components, evidence of plastic deformation, radial fractures, and transverse fractures were common; these damage modes have historically been most frequently associated with total knee replacements as opposed to total hip replacements [16].

Optical microscopy and white light interferometry detected multidirectional scratches and burnishing on at least one of the poles of all retrievals. Furthermore, based on a quantitative assessment of the surface morphology, we are unable to distinguish between the waviness values in the worn regions of the domes for the polyethylene cores and regions of conventional total hip replacements that exhibit adhesive/abrasive wear, machining marks, and irregular morphologies (Tables 1–3). The sampled regions of the retrieved total disc replacements had significantly lower roughness than acetabular liners, regardless of the characterization of the surface morphology (Tables 1–3). Although statistically significant, the clinical ramifications of this observation remain unclear, beyond providing additional support that the surfaces of retrieved disc replacements may become burnished, as in hip replacements.

Based on our observations, we recommend that wear simulators of the lumbar spine be tuned to produce multidirectional motions, similar to the types of motion used to simulate wear for hip replace-

TABLE 4—Summary of average surface roughness ( $R_a$ ) and waviness ( $W_a$ ) for surface regions classified with irregular morphology from the retrieved CHARITÉ CoCr endplates, compared to a new, never implanted CHARITÉ CoCr endplate and previous values reported for the retrieved CoCr femoral heads from total hip replacements (THA) [14].

	No. Observations	Median ( $\mu\text{m}$ )	IQR <sup>a</sup> ( $\mu\text{m}$ )
<b>Roughness (<math>R_a</math>)</b>			
Retrieved CHARITÉ Endplates	140	0.021	0.014
Retrieved Femoral Heads (THA)—Worn		0.010	0.009
New CHARITÉ Endplate	5	0.019	0.006
Retrieved Femoral Heads (THA)—Unworn		0.003	0.002
<b>Waviness (<math>W_a</math>)</b>			
Retrieved CHARITÉ Endplates	140	0.034	0.007
New CHARITÉ Endplate	5	0.029	0.018

<sup>a</sup>IQR=Interquartile Range.

ments. Accordingly, the first option currently offered in the recently approved ASTM Standard for wear testing of TDRs using unidirectional motion is likely not an appropriate option. In addition, besides differentiating between linear and multidirectional wear mechanisms, we are unable to make a more specific recommendation about the extent of cross-shear based solely on the dispositions of the wear surfaces. It is clear, however, that simulators that only produce unidirectional wear tracks are unsuitable for producing the wear mechanisms generated in the lumbar spine; it remains to be seen, however, whether articulating discs from the cervical spine show a preponderance of unidirectional and multidirectional wear tracks.

Our study also provides information on the *in vivo* penetration rates of the CHARITÉ and can be helpful to tune the magnitude of wear produced by spine simulators, provided of course that the fundamental wear mechanism produced by the simulator is clinically relevant (i.e., valid). In total hip and knee simulators, one million cycles corresponds roughly to one year of *in vivo* use for a typical patient, but in clinical practice the range of wear rates varies considerably [17]. Similar to hip and knee replacements, a broad range of clinical penetration rates was observed with the total disc replacements in our study. If the philosophy of the wear simulator is to produce “typical” penetration rates, then a reasonable target, based on our retrieval data, may be 0.04 mm/year, corresponding to the median penetration rate from our study. This target may be useful to provide a bridge between the wear rate in the spine simulator and the clinical situation.

The retrievals analyzed in this study were obtained following revision surgery, and thus may not necessarily represent the “typical” TDR patient with a well-functioning implant. Nevertheless, the retrievals were collected in a consecutive series of revisions by two surgeons, and therefore represent a random sample of implants from failed TDR surgery. Analysis of TDR components collected at autopsy would be useful to evaluate the mechanism of well-functioning implants. However, the intended patient population for TDRs is relatively young, presenting a considerable challenge in conducting such an autopsy retrieval study. Although the results of our research should be interpreted with some caution when extrapolating back to the clinical situation, analysis of implants from revision surgery has proven to be indispensable in the validation of joint simulators [10,11]. Similarly, the analysis of retrieved disc replacements is expected to provide a crucial, previously unavailable, benchmark for spine implant simulators.

The surface morphology in the domed regions of the CoCr endplates showed minimal evidence of roughening or chronic damage from third-body debris. Although we observed one case of third-body damage to the rim of one polyethylene core, this damage was not found to adversely impact the surface roughness in the dome of the endplate. Therefore, the retrievals collected thus far do not support a strong need to conduct abrasive wear testing of lumbar total disc replacements, at least not for uncemented designs similar to the CHARITÉ. On the other hand, abrasive wear testing conditions are clinically relevant for hip and knee replacements. Additional retrievals will be useful to further establish the prevalence of third-body wear in disc replacements.

An important finding of this study is the prevalence of impingement-related damage and fractures at the rim of the polyethylene cores. Radial and transverse cracks were frequently observed in components that were implanted before and after 1997, which was the year during which the manufacturer changed from gamma irradiation in air to gamma irradiation in nitrogen [7]. Extensive rim fracture was observed in a highly oxidized, retrieved implant analyzed by David and colleagues [7]. Although oxidation—whether on the shelf or *in vivo*—will clearly lower the resistance of the core to rim damage, the precise levels of oxidation associated with radial and transverse rim cracks remain unclear, and will be explored in future research.

Because of the prevalence of impingement seen in these retrievals, the authors recommend that impingement fatigue tests be developed to evaluate the performance of total disc replacements. For the design evaluated in this study, impingement can occur during regular flexion or extension activities and has been shown with *in vitro* cadaveric tests [18]. Impingement can also occur due to subsidence, subluxation, or migration of the endplates. Because resistance to chronic impingement damage is desirable, fatigue test methods should be developed to reproduce the rim fracture modes observed in the retrievals presented in this study. Once validated, the protocol could be used to screen implant materials for fatigue resistance under a clinically relevant loading conditions. It is likely, based on consideration for the potential for oxidation, that test specimen preconditioning using accelerated aging, will need to be conducted prior to rim fatigue tests.

The recommendations for standardized wear testing in this study are based on long-term wear findings of retrieved components of a single lumbar total disc design. It remains to be seen how generalized these findings are to other total disc replacement designs in the lumbar spine, particularly those with other material couples, as well as to cervical spine designs. We have had the opportunity to study two short-term implanted metal-on-metal lumbar disc replacements [19]. In both cases, we observed wear patterns and biofilm deposits that were consistent with metal-on-metal hip joints. Although preliminary, the limited information from metal-on-metal designs supports our conclusion, that the domed articulating surfaces of lumbar disc replacements have wear mechanisms closely approximating those of total hip replacements.

#### Acknowledgments

This research was supported by a grant from Medtronic Sofamor Danek. The authors thank Stan Bialecki from Zygo Corporation for his assistance and many helpful discussions.

#### References

- [1] Buttner-Janzen, K., Hochschuler, S. H., and McAfee, P. C., *The Artificial Disc*, Springer, Berlin, 2003.
- [2] Hallab, N. J., Cunningham, B. W., and Jacobs, J. J., "Spinal Implant Debris-induced Osteolysis," *Spine*, Vol. 28, No. 20, 2003, pp. S125–S138.
- [3] Fraser, R. D. et al., "AcroFlex Design and Results," *Spine*, Vol. 4, (6 Suppl), 2004, pp. 245S–251S.
- [4] Thorpe, P. L. P. J. and Licina, P. "Osteolysis and Complications Associated with Artificial Disc Replacement," Annual Meeting of the Spine Society of Australia, 2004, p. Poster 21.
- [5] van Ooij, A. and van Rhijn, L., "Complications of the Charité Disc Prosthesis in 55 Patients and Retrieval in 6 Patients," in *Back into Motion: NASS Spring Break*, Bal Harbour, Florida, April 6–9, 2005.
- [6] Kurtz, S. M. et al., "Assessment of Surface Roughness and Waviness Using White Light Interferometry for Short-term Implanted, Highly Crosslinked Acetabular Components," *Highly Crosslinked and Thermally Treated Ultra-High Molecular Weight Polyethylene for Joint Replacements*, ASTM STP 1445, S. M. Kurtz, R. Gsell, and J. Martell, Eds., ASTM International, West Conshohocken, PA, 2004.
- [7] David, T., "Revision of a Charite Artificial Disc 9.5 years in vivo to a New Charite Artificial Disc: Case Report and Explant Analysis," *Eur. Spine J.*, Vol. 14, No. 5, 2005, pp. 507–511.
- [8] Kurtz, S. M. et al., "Analysis of a Retrieved Polyethylene Total Disc Replacement Component," *Spine*, Vol. 5, No. 3, 2005, pp. 344–350.
- [9] Wang, A., Stark, C., and Dumbleton, J. H., "Mechanistic and Morphological Origins of Ultra-high Molecular Weight Polyethylene Wear Debris in Total Joint Prostheses," *Proceedings*, Institution of Mechanical Engineers, Vol. 210, 1996, pp. 141–155.
- [10] Wang, A. et al., "Lubrication and Wear of Ultra-high Molecular Weight Polyethylene in Total Joint Replacements," *Tribol. Int.*, Vol. 31, No. 1–3, 1998, pp. 17–33.
- [11] McKellop, H. A. et al., "The Origin of Submicron Polyethylene Wear Debris in Total Hip Arthroplasty," *Clin. Orthop. Relat. Res.*, Vol. 311, 1995, pp. 3–20.
- [12] Jasty, M. et al., "Wear of Polyethylene Acetabular Components in Total Hip Arthroplasty. An Analysis of One Hundred and Twenty-eight Components Retrieved at Autopsy or Revision Operations," *J. Bone Jt. Surg., Am. Vol.*, Vol. 79, No. 3, 1997, pp. 349–358.
- [13] Kurtz, S. M. et al., "Deconvolution of Surface Topology for Quantification of Initial Wear in Highly Cross-linked Acetabular Components for THA," *J. Biomed. Mater. Res.*, Vol. 63, No. 5, 2002, pp. 492–500.
- [14] Elfick, A. P. D. et al., "The Influence of Femoral Head Surface Roughness on the Wear of Ultrahigh Molecular Weight Polyethylene Sockets in Cementless Total Hip Replacement," *J. Biomed. Mater. Res.*, Vol. 48, No. 5, 1999, pp. 712–718.
- [15] Bhushan, B., "Solid State Surface Characterization," *Principles and Applications of Tribology*, John Wiley & Sons, Inc., New York, 1999, pp. 99–197.
- [16] Kurtz, S. M., *The UHMWPE Handbook: Ultra-High Molecular Weight Polyethylene in Total Joint Replacement*, Academic Press, New York, 2004.

- [17] Sauer, W. L., and Anthony, M. E., "Predicting the Clinical Wear Performance of Orthopaedic Bearing Surfaces," *Alternative Bearing Surfaces in Total Joint Replacement*, J. J. Jacobs and T. L. Craig, Eds., ASTM International, West Conshohocken, PA, pp. 1–29.
- [18] O'Leary, P. et al., "Response of Charite Total Disc Replacement Under Physiologic Loads: Prosthesis Component Motion Patterns," *Spine*, Vol. 5, No. 6, 2005, pp. 590–599.
- [19] Kurtz, S. M. et al., "In Vivo Wear Mechanisms of a Retrieved Metal-on-metal Total Disc Replacement," *12th International Meeting on Advanced Spine Techniques (IMAST)*, Banff, Alberta, Canada, July 7–9, 2005.

Philippe E. Pare,<sup>1</sup> Frank W Chan, Patrick Buchholz, Steven Kurtz, and Peter McCombe

## Surface Texture Analysis of Artificial Disks Wear-Tested Under Different Conditions and Comparison to a Retrieved Implant

---

**ABSTRACT:** Total disk arthroplasty is growing in popularity and becoming an alternative to fusion for the treatment of some degenerative disk diseases. To date, there is little consensus regarding the appropriate *in vitro* techniques with which to evaluate the biotribological properties of these devices. The current study evaluated the surface texture and topography of lumbar metal-on-metal artificial disks tested in a spine wear simulator compared to an explanted device after twelve months *in situ*. Six implants were tested under a constant load and unidirectional flexion-extension motion as defined by the ASTM standard guide. One implant was tested under a variable load using a combination of flexion-extension, lateral bending, and axial rotation as specified by the ISO standard. While the retrieved disk retained its initial mirror-like surface finish, implants tested under unidirectional motion were severely damaged by abrasive wear resulting in a significant increase in roughness. The implant tested under combined motions exhibited a multi-directional wear scar with limited surface damage. Although only a single retrieved implant was characterized, the current study suggests that wear testing under unidirectional motion may not produce clinically-relevant surface morphology of metal-on-metal artificial disks.

**KEYWORDS:** wear, spine, artificial disk, tribology, surface characterization, roughness, retrieved implant

### Introduction

The current standard of care for degenerative disk disease is fusion of the vertebrae of the diseased segments. However, degeneration of adjacent levels is a potential complication associated with fusion [1,2]. In recent years, interest has grown within the orthopaedic community toward the preservation of motion in the spine with the use of disk arthroplasty devices. These intervertebral disk prostheses would preserve mobility, restore disk height, alleviate pain, and possibly mitigate the occurrence of adjacent level degeneration.

Currently, there are nine artificial disks in clinical trials in the United States with several poised to gain approval in the marketplace within the next two years. It is predicted that over 400 000 total disk arthroplasty procedures will be performed annually by 2009 in the United States alone [3]. It is, therefore, interesting to note that in comparison to the state-of-the-art in large joint arthroplasty, the development of artificial disks is in its infancy. Furthermore, there is little consensus within the community regarding the appropriate techniques to characterize the biomechanical and biotribological properties of these devices. As a result, myriad testing parameters have been proposed, making comparisons of different artificial disk designs next to impossible.

In 2005, ASTM International published a standard guide [4] on wear testing of total disk prostheses. Since limited information is currently available on clinically-realistic activities of daily living, the standard guide proposes rather severe testing conditions. A constant load with three main options for the combination of load and motions are proposed: (1) sequential application of single motions, (2) sequential application of single and coupled motions, and (3) combined concurrent motions. For the first and second cases, the same device is tested for 10 million cycles under flexion-extension (FE) followed by 10 million cycles of lateral bending (LB) followed or coupled with 10 million cycles of axial rotation (AR). In the case of combined motions, all three degrees of freedom for motion are applied simultaneously with a constant

---

Manuscript received September 30, 2005; accepted for publication February 24, 2006. Presented at ASTM Symposium on Wear of Articulating Surfaces on 8–10 November 2005 in Dallas, TX; S. Brown, L. Gilbertson, and V. Good, Guest Editors.

<sup>1</sup> Research Engineer, Medtronic Sofamor Danek, Memphis, TN 38132.

axial load. Whenever concurrent motions are employed, the user can elect whether or not to phase the motion profiles.

The International Organization for Standardization (ISO) is also developing a standard [5] to characterize the wear of spinal disk prostheses. To accomplish this objective, a single profile is proposed for loads and motions. The four degrees of freedom (FE, LB, AR, and axial load) are applied simultaneously with defined amplitudes, frequency, and phasing for 10 million cycles.

As physiologic loads and motions representing activities of daily living become better characterized, more clinically-realistic testing parameters can be implemented. For the time being, artificial disk prostheses will be tested according to the available standards and any comparisons between implants will continue to be challenging because of the numerous testing conditions allowed for within and between the ASTM and ISO standards. In addition to different load and motion profiles, both standards propose different testing frequencies, types of serum, and protein concentrations.

To date, no published study has compared the effect on wear of the different testing conditions allowed for in both the ASTM and ISO wear testing standards. The purpose of the current study was to characterize and compare the surface topography between metal-on-metal artificial disks wear-tested under different conditions and a retrieved metal-on-metal implant.

**Materials and Methods**

Metal-on-metal lumbar artificial disks were manufactured from high carbon content cobalt chromium molybdenum (CoCrMo) alloy which conformed to the ASTM standard F 1537-00, frequently used for metal-on-metal hip implants and for knee femoral components. Numerous studies have demonstrated the superior wear resistance of this alloy [6,7] and noted a self-polishing action observed when two CoCrMo surfaces articulate against each other [8-10].

This study involved the Maverick™ lumbar artificial disk (Medtronic, Memphis, TN) and a similar device (identified as device “A”) with different size and additional feature. Six Maverick™ implants were tested for 1.0 million cycles at 2 Hz under a constant load and with unidirectional FE motion per the conditions defined by the ASTM standard guide (Table 1; Group 1 and 2). One device “A” specimen was tested under combined motion per the conditions recommended by the ISO standard at 1 Hz and for 1.75 million cycles (Table 1; Group 3) (Fig. 1). The same implant was then tested for an additional 1.5 million cycles of combined motion (Table 1; Group 4) at a frequency of 2 Hz to explore the influence of frequency on wear. The explanted device was a Maverick™ retrieved from a 43-year-old female after twelve months in situ due to nerve root impingement. The patient activity was classified as medium to low.

Unidirectional wear testing was conducted using a multi-station, custom-manufactured spine wear simulator (Fig. 2) and the combined motion testing, using a single-station, custom test system adapted to an MTS 858 Mini Bionix® test system (MTS® Corp., Eden Prairie, MN) (Fig. 3). The implants were

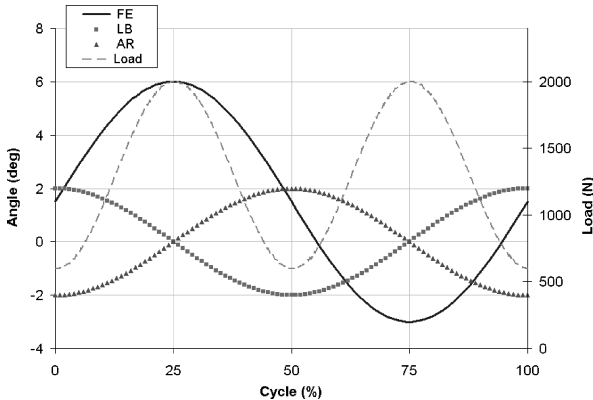


FIG. 1—Load and motion used for the combined wear test.



FIG. 2—Multi-station spine wear simulator.



FIG. 3—Single-station spine wear simulator.

mounted on fixtures designed to align both the simulator and artificial disk centers of rotation. During testing, the specimens were submerged in a solution of Alpha Calf™ Fraction (HyClone, Logan, UT) diluted by volume to 25 % with deionized water leading to a protein concentration of 11.5 g/L. Penicillin-streptomycin antibiotic and Fungizone® antimycotic (Life Technologies LTD, Paisley, Scotland) were added to the serum solution, with a concentration of 0.15 and 0.25 % per volume, respectively, to prevent bacteria and fungus growth. The solution was maintained at 37°C during testing. The serum solution was changed and specimens cleaned thoroughly at least every 0.5 million cycles.

Topography and surface texture of the articular surfaces were measured using white light interferometry (NewView 5000™, Zygo, Middlefield, CT) and quantified with MetroPro® ver. 8.1.3 software (Zygo). The average surface roughness was calculated from measurements taken at five locations on each articular surface. Since the Maverick™ implants were not available for surface analysis prior to testing or implan-

TABLE 1—Summary of the testing conditions.

Group	Standard	Load (N)	Specimen	FE	LB	AR	Freq (Hz)
1	ASTM F 2423-05	Constant 1200	Maverick™ (n=6)	±10°	...	...	2
2	ASTM F 2423-05	Constant 1200	Device "A" (n=6)	±10°	...	...	2
3	ISO 18192-1	Cyclic 600 to 2000	Device "A" (n=1)	-3° / +6°	±2°	±2°	1
4	ISO <sup>a</sup> 18192-1	Cyclic 600 to 2000	Device "A" (n=1)	-3° / +6°	±2°	±2°	2

<sup>a</sup>Frequency of testing higher than the 1 Hz specified in standard [5].

TABLE 2—Surface texture of artificial disks tested under unidirectional motion (ASTM).

Group	Device	Initial Ra (nm)	Cycles (million)	Final Ra (nm)
1	Maverick™ (n=6)	9±2	1.0	322±87
2	Device "A" (n=6)	10±4	1.0	69±84

tation, the surface roughness presented was calculated from ten new implants. Qualitative observations as well as photographs were taken using a stereo microscope (Nikon, SMZ-2T, Japan) equipped with a digital camera (PAXcam ARC™, MIS, Franklin Park, IL).

**Results**

The surface texture of new Maverick™ implants and device "A" test specimens was measured prior to testing. The articular surfaces for both disks exhibited very low roughness values (Table 2) with an homogeneous distribution of peaks and valleys (Figs. 4 and 5). After completion of 1 million cycles under constant load and unidirectional motion (FE), the surfaces of both devices were characterized by severe abrasive wear aligned with the sliding direction (Figs. 6 and 7) along the sagittal plane. The average surface roughness increased by 3600 and 700 % for groups 1 and 2, respectively (Table 2).

Surface analysis of group 3 was performed after completion of 0.25 and 1.75 million cycles. The surface roughness increased by 340 % during the first segment and decreased by 50 % from 0.25 to 1.75 million cycles (Table 3). At both time intervals, the surface was characterized by ellipsoidal (longer axis in the anterior-posterior direction) wear tracks with evidence of crossing-path motion (Fig. 8). Device "A" was then tested under the same load and motion profiles but with a higher frequency (2 Hz). After an additional 1.5 million cycles, the surface roughness doubled to reach 35 nm with the wear pattern exhibiting the same multidirectional wear scars observed with the lower frequency test.

The retrieved device was characterized after one year in vivo (Table 4). The metallic implant conserved its initial mirror-like finish. Some micro-scratches were visible under magnification. The latter were multidirectional but with a preferential orientation along the anterior-posterior direction (Fig. 9).

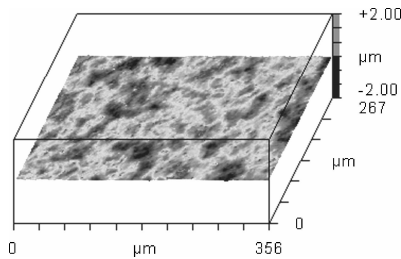


FIG. 4—Surface topography of a specimen from group 1 before testing (Ra=13 nm).

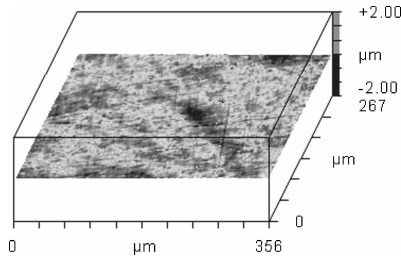


FIG. 5—Surface topography of a specimen from group 2 before testing (Ra=9 nm).

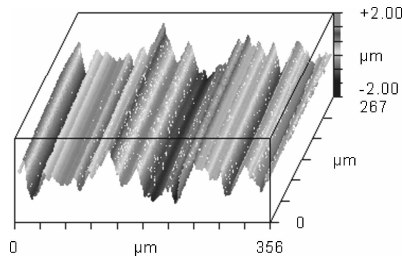


FIG. 6—Surface topography of a specimen from group 1 after testing ( $Ra=430$  nm).

**Discussion**

This is the first work to study the influence of different wear testing parameters on the surface texture of artificial disks. Two metal-on-metal artificial disks were investigated: (1) the Maverick™, and (2) a similar design identified as device “A”. Both disks had a mirror-like surface finish prior to testing with an average surface roughness of approximately 10 nm. After 1 million wear testing cycles under constant load and unidirectional motion (FE), the surfaces of both groups of devices exhibited severe abrasive wear aligned with the sliding direction. In general, the surface roughness increased after testing by approximately one order of magnitude. The load and motion conditions used to evaluate these devices were taken from the ASTM standard guide. Although this test standard does allow for combined, concurrent motions, artificial disks have more commonly been tested under unidirectional motion in FE followed by unidirectional

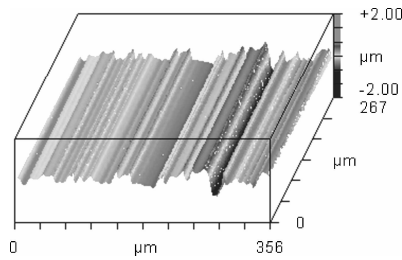


FIG. 7—Surface topography of a specimen from group 2 after testing ( $Ra=260$  nm).

TABLE 3—Surface texture of artificial disk tested under combined motions (ISO).

Group	Device	Initial Ra (nm)	Cycles (million)	Final Ra (nm)
3	Device “A” (n=1)	10±3	0.25	34±7
			1.75	17±10
4	Device “A” (n=1)	17±10	1.5	35±22

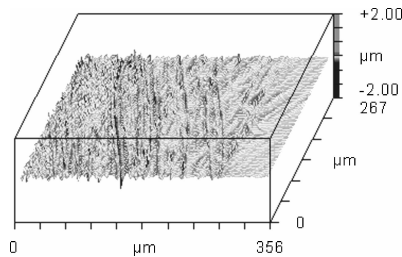


FIG. 8—Surface topography of a specimen from group 3 after 0.25 million cycles ( $Ra=58$  nm).

TABLE 4—Surface texture of a retrieved metal-on-metal implant (one year in vivo).

Group	Device	Initial Ra (nm)	Time (year)	Final Ra (nm)
Retrieval	Maverick™ (n=1)	9±2	1 year in vivo	21±11

motion in LB sometimes coupled with AR. Since the surface is severely damaged under unidirectional FE, subsequent testing in a new direction relative to the original anterior-posterior wear scar will further exacerbate surface damage.

Alternatively, the device subjected to combined motion and variable loading proposed by the ISO test standard exhibited multidirectional scratching with evidence of crossing-path motion. An ellipsoidal wear pattern was observed with the main axis aligned in the anterior-posterior direction. Although the surface roughness increased by a factor of three after testing, further testing at the higher frequency did not alter the characteristics of the wear pattern. It is noteworthy that a multidirectional wear scar was also evident in the single explanted device although the surface morphology of the tested device still exhibited greater damage than that of the explant. In spite of this, the implant evaluated under the combined motion conditions was markedly closer in morphological appearance to the explant than the devices evaluated under the more simplistic, unidirectional, and constant load conditions. As the explant was from a medium to low activity patient (patient ambulated with crutches), it is reasonable that the explant was not representative of a typical patient with a well-functioning disk arthroplasty. Therefore, we recognize the limitation in our comparison of in vitro-tested implants to a single explant. This underlies the great importance of analyzing every available explanted total disk device so that in vitro wear performance evaluation techniques can be adequately calibrated and validated.

It is well known that the effect of kinematics on wear can be different for different materials. For CoCrMo self-articulating bearings, crossing-path motion produced from combined motion kinematics may reduce wear through a self-polishing action [6–8]. In comparison, polymeric materials such as ultra-high-molecular-weight-polyethylene (UHMWPE) have exhibited markedly lower wear under unidirectional motion than under multidirection, crossing-path motion due to the propensity of polymer chains to preferentially orient under unidirectional motion [11]. Furthermore, other test conditions such as the type of loading, test frequency, protein concentration of the lubricant, and lubricant temperature can also affect the wear performance of artificial disks. For example, a constant load applied throughout a test cycle may prevent the occurrence of a squeeze film that may otherwise have provided a lubricant layer separating and thereby protecting the articulating surfaces from wear. Also, the frequency of testing can influence wear since fluid film protection (and thus lower wear) is more likely to occur for some design under higher entrainment velocities. Elevated frequencies can also affect wear since serum proteins can denaturalize at higher temperature and change the extent of surface protection through boundary lubrication. Another factor influencing surface protection is the ability of the serum to provide boundary lubrication. While wear testing standards recommend using a minimum protein concentration of 17 g/L to represent synovial fluid in hip and knee joints [12,13], the appropriate concentration for use with artificial disks remains unknown. The ASTM and ISO standard for wear testing of artificial disks propose a protein concentration of 20 and 30 g/L, respectively. In the present study, a lower concentration (11.5 g/L) was used in view of the fact that the intervertebral disk complex is not a synovial joint.

It should be noted that there is currently no generally accepted correlation between number of cycles

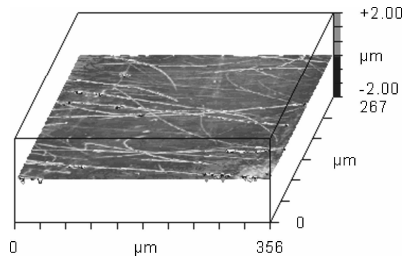


FIG. 9—Surface topography of a retrieved Maverick™ after one year in vivo (Ra=5 nm).

and time in vivo. Two recent publications reflect differences in interpretation of number of cycles experienced in one year in situ. Mathews et al. [14] used 317 460 cycles per year as a conversion while Dooris et al. [15] considered 125 000 cycles of activity per year. Interestingly, both were based on the same study [16] which proposed only as an example that there are 125 000 significant bends experienced by the lumbar spine yearly. As long as the characterization and number of duty cycles per year remained uncertain, comparison with simulator-tested devices will be difficult. Further work is needed to characterize the load and motion profiles for activity of daily living as well as the number of cycles per annum of in situ service.

The current study does not report on wear rates or wear particle morphology of artificial disks. It is important to note that the validation of testing conditions must compare these metrics between in vitro-tested implants and retrieved components in addition to surface morphology. Despite the single retrieved component used as comparison in this analysis, the current study is the first documented comparison between simulator-tested and retrieved artificial disks and does suggest that unidirectional motion under a constant load may not produce clinically-relevant surface morphology of metal-on-metal total disks. The applicability of a more sophisticated set of testing conditions (i.e., combined motions, variable loading, phasing, etc.) for the evaluation of artificial disks is the subject of further scientific evaluation.

## References

- [1] Errico, T. J., "Lumbar Disk Arthroplasty," *Clin. Orthop. Relat. Res.*, No. 435, 2005, pp. 106–117.
- [2] Ghiselli, G., Wang, J. C., Bathia, N. N., Hsu, W. K., and Dawson, E. G., "Adjacent Segment Degeneration in the Lumbar Spine," *J. Bone Jt. Surg., Am. Vol.*, Vol. 86, 2004, pp. 1497–1503.
- [3] Viscogliosi, A. G., Viscogliosi, J. J., and Viscogliosi, M. R., "Beyond Total Disk—The Future of Spine Surgery," *Spine Industry Analysis Series*, Viscogliosi Bros., LLC, May 2004.
- [4] ASTM Subcommittee F04.25, "Standard Guide for Functional, Kinematic, and Wear Assessment of Total Disk Prostheses," F 2423-05, 2005.
- [5] ISO Technical Committee TC 150/SC 5, "Implants for Surgery—Wear of Total Intervertebral Spinal Disk Prostheses—Part 1: Loading and Displacement Parameters for Wear Testing and Corresponding Environmental Conditions for Test," ISO/DIS18192-1, 2005.
- [6] John, K. R., Zardiackas, L. D., and Poggie, R. A., "Wear Evaluation of Cobalt-Chromium Alloy for Use in a Metal-on-Metal Hip Prosthesis," *J. Biomed. Mater. Res., Part B: Appl. Biomater.*, Part B: Applied Biomaterial, No. 68B, 2004, pp. 1–14.
- [7] Dowson, D., Hardaker, C., Flett, M., and Isaac, G. H., "A Hip Joint Simulator Study of the Performance of Metal-on-Metal Joints," *J. Arthroplasty*, Vol. 19, No. 8, 2004, pp. 118–123.
- [8] Pare, P. E., Medley, J. B., Chan, F. W., and Young, S. K., "Role of Lambda in Simulator Wear of Metal-on-Metal Hip Implants Under Conditions of Mixed Film Lubrication," *Tribology Series 41*, Elsevier, UK, 2003, pp. 281–329.
- [9] Schey, J. A., "Systems View of Optimizing Metal-on-Metal Bearings," *Clin. Orthop. Relat. Res.*, Vol. Aug., No. 329 Supplement, 1996, pp. 115–127.
- [10] Chan, F. W., Boby, J. D., Medley, J. B., Krygier, J. J., Yue, S., and Tanzer, M., "Engineering Issues and Wear Performance of Metal-on-Metal Hip Implants," *Clin. Orthop. Relat. Res.*, Vol. Dec., No. 333, 1996, pp. 96–107.
- [11] Bragdon, C. R., O'Connor, D. O., Lowenstein, J. D., Jasty, M., Syniuta, W. D., "The Importance of Multidirectional Motion on the Wear of Polyethylene," *Proceedings of the Institution of Mechanical Engineers*, Vol. 210, No. 3, 1996, pp. 157–165.
- [12] ISO Technical Committee TC 150/SC 4, "Implants for Surgery—Wear of Total Hip-Joint Prostheses—Part 1: Loading and Displacement Parameters for Wear-Testing Machines and Corresponding Environmental Conditions for Test," ISO14242-1, 2002.
- [13] ISO Technical Committee TC 150/SC 4, "Implants for Surgery—Wear of Total Knee-Joint Prostheses—Part 1: Loading and Displacement Parameters for Wear-Testing Machines and Corresponding Environmental Conditions for Test," ISO14243-1, 2002.
- [14] Mathews, H. H., LeHuec, J. C., Friesem, T., Zdeblick, T., and Eisermann, L., "Design Rationale and Biomechanics of Maverick Total Disk Arthroplasty with Early Clinical Results," *Eur. Spine J.*, Vol. 4, 2004, pp. 268–275.

- [15] Dooris, A. P., Ares, P. J., Gabriel, S. M., and Serhan, H. A., "Wear Characterization of an Artificial Disk Using ASTM Guidelines," *Trans. Annu. Meet. - Orthop. Res. Soc.*, 2005, Poster No. 1335.
- [16] Hedman, T. P., Kostuik, J. P., Fernie, G. R., and Hellier, W. G., "Design of an Intervertebral Disk Prosthesis," *Spine*, Vol. 16, No. Suppl. 6, 1991, pp. 256–260.

## **SECTION III: LUBRICANTS AND GENERAL**

Joanne L. Tipper,<sup>1</sup> Alison L. Galvin,<sup>2</sup> Eileen Ingham,<sup>1</sup> and John Fisher<sup>2</sup>

## Estimation of the Osteolytic Potential of Noncrosslinked and Crosslinked Polyethylenes and Ceramic-on-Ceramic Total Hip Prostheses

**ABSTRACT:** There is currently considerable interest in the wear debris and osteolytic potential of different types of bearings used in total joint replacements. The aim of this study was first to characterize the wear and wear particles generated from two different grades of UHMWPE acetabular cups with different levels of crosslinking in a hip joint simulator. Secondly, the results for the polyethylenes were compared to an alumina ceramic-on-ceramic hip prosthesis. The wear rates of the two noncrosslinked material types were very similar at  $49 \pm 8 \text{ mm}^3$  per million cycles for the GUR 1020 and  $45.6 \pm 1.4 \text{ mm}^3$  per million cycles for the GUR 1050. Moderate crosslinking (4 MRad) significantly ( $P < 0.05$ ) reduced the wear rate of the GUR 1020 material by 30 % to  $35 \pm 9 \text{ mm}^3$  per million cycles. High levels of crosslinking of GUR 1050 (10 MRad) produced a highly significant ( $P < 0.01$ ) 80 % reduction in wear volume. Although reduced wear volumes were observed with moderate levels of crosslinking for the 4 MRad GUR 1020 material, little benefit was conveyed by crosslinking, in terms of predicted overall biocompatibility and estimated osteolytic potential. Introducing high levels of crosslinking (10 MRad) into the GUR 1050 material reduced wear and osteolytic potential by up to five-fold compared to the other GUR 1050 materials. However, compared to the non-crosslinked and moderately crosslinked GUR 1020 materials, the highly crosslinked GUR 1050 UHMWPE had only a two-fold lower osteolytic potential. The alumina ceramic-on-ceramic hip prostheses produced extremely low wear rates under both standard and microseparation simulation conditions, and consequently the osteolytic potential of the alumina bearings was estimated to be  $>20$ -fold lower than the highly crosslinked polyethylene.

**KEYWORDS:** wear, UHMWPE, alumina ceramic, crosslinking, wear debris, hip prostheses, osteolytic potential, microseparation

### Introduction

Ultrahigh molecular weight polyethylene (UHMWPE) is used extensively as a bearing surface in artificial hip and knee joints. It is the material of choice for acetabular cups in hip prostheses and tibial inserts in knee prostheses. In the hip it is combined with either a metallic or alumina ceramic femoral component. Although, in the short to medium-term, replacement joint prostheses generally provide excellent clinical performance; in the longer term, aseptic loosening is a major cause of failure of both hip and knee prostheses. As the replacement joint articulates, UHMWPE wear particles are released from the articulating surfaces and are phagocytosed by macrophages in the periprosthetic tissues. Micrometre and submicrometre-sized polyethylene wear particles have been shown to activate macrophages, which release pro-inflammatory cytokines leading eventually to osteolysis [1]. In the past five years considerable improvements have been made to polyethylene in an attempt to reduce wear. Sterilization with gamma irradiation in the presence of oxygen was shown to increase oxidation and wear of UHMWPE and is no longer used [2]. As a result, alternative sterilization methods and oxidation-resistant or stabilized materials have been introduced. These include nonirradiation sterilization methods such as ethylene oxide or gas plasma sterilization [3], or irradiation in an inert atmosphere [4]. The latter approach introduces crosslinks into the material, which used alone or in conjunction with post-irradiation heat treatments to combine residual free radicals, can produce intentionally crosslinked materials. There is currently some discussion

Manuscript received September 27, 2005; accepted for publication March 28, 2006. Presented at ASTM Symposium on Wear of Articulating Surfaces on 8 November 2005 in Dallas, TX; S. A. Brown, L. N. Gilbertson, and V. D. Good, Guest Editors.

<sup>1</sup> EPSRC Advanced Research Fellow and Professor of Clinical Immunology, respectively, Institute of Medical & Biological Engineering, Faculty of Biological Sciences, University of Leeds, Leeds, LS2 9JT, UK.

<sup>2</sup> Research Fellow and Professor of Mechanical Engineering, respectively, Institute of Medical & Biological Engineering, School of Mechanical Engineering, University of Leeds, Leeds, LS2 9JT, UK.

Copyright © 2006 by ASTM International, 100 Barr Harbor Drive, PO Box C700, West Conshohocken, PA 19428-2959.

over whether oxidative degradation or crosslinking, or both, continues within the UHMWPE acetabular components after manufacture, and whether current remelting or annealing procedures do enough to prevent these events from taking place. Wannomae et al. [5] found that post-irradiation annealing at a temperature below the melting point of the UHMWPE did not eliminate oxidation, whereas UHMWPE that had been irradiated and remelted had no detectable residual free radicals and no oxidation present. The implication being that irradiated and annealed UHMWPE may have a lower oxidative stability in the long term, and hence a lower wear resistance.

Typically two different levels of crosslinking have been introduced, moderately crosslinked UHMWPE using 4–5 MRad of irradiation, and highly crosslinked UHMWPE using 7.5–10 MRad of irradiation. As it became apparent that the introduction of crosslinks into the polyethylene component caused a decrease in the wear rate, the irradiation dose was increased with the aim of increasing the concentration of crosslinks in the UHMWPE material. There are now a number of highly crosslinked UHMWPE clinical products, which are irradiated with between 7.5 and 10 MRads of irradiation. Crosslinking of UHMWPE has been shown to produce substantial reductions in the wear rate of UHMWPE acetabular cups when articulated against smooth femoral counterfaces in wear simulators [6–9]. Several studies have demonstrated that crosslinking with 5 MRad of irradiation reduced UHMWPE wear by approximately 80 % in the hip simulator compared to noncrosslinked materials [6,7]. Muratoglu et al. [8] also demonstrated an 85 % reduction in wear with 10 MRad crosslinked material. However, Endo et al. [10] demonstrated smaller reductions in wear with crosslinked materials, in the order of 30 %. The former studies used 90–100 % (v/v) bovine serum as a lubricant, whereas the latter study used the more physiological concentration of 25 % (v/v) bovine serum, as recommended in the current international standard. Other studies have shown a reduction in wear rate of conventional 2.5 MRad polyethylene tested in serum with high concentrations of protein [11]. It is thought that the serum proteins may provide a lubricating protein boundary layer, which causes a reduction in polyethylene wear. This may be enhanced when serum protein concentrations are high.

Early clinical radiographic studies of both moderately and highly crosslinked polyethylene have recently been reported. Moderately crosslinked UHMWPE cups showed a 50 % reduction in volume change compared to conventional polyethylene at two to three years [12]. For highly crosslinked UHMWPE cups a 42 to 50 % reduction in volume change compared to conventional polyethylene at two years has been reported [13]. In addition, Digas et al. reported a 50 % reduction in femoral head penetration with highly crosslinked UHMWPE cups compared to the control [14]. These early clinical studies all show a more modest reduction in wear compared to those predicted by the *in vitro* simulator studies. However, deformation and creep may be masking very low wear rates during the first two years *in vivo*. More recent clinical studies with slightly longer-term follow-up times of up to four years, have reported greater percentage reductions in wear with crosslinked UHMWPE cups [15–17]. Heisel et al. [15] reported an 81 % reduction in the wear of 5 MRad crosslinked acetabular cups compared to gamma in air sterilized UHMWPE cups. Röhrli et al. [16] reported an 85 % reduction in head penetration with 10 MRad gamma irradiated highly crosslinked UHMWPE acetabular cups and Manning et al. [17] reported a 96 % reduction in wear of highly crosslinked UHMWPE acetabular cups compared to traditional polyethylene cups at a four year follow-up. These studies indicate that highly crosslinked UHMWPE may deliver the reductions in wear that have been predicted from hip simulator wear testing.

Other measures introduced to reduce UHMWPE wear include the increased use of damage resistant alumina ceramic femoral heads, which have been shown to reduce the wear of UHMWPE by up to 50 % compared to metallic femoral heads [18]. Interest in alternative bearing materials such as the low wearing alumina ceramic-on-ceramic hip prostheses has increased as a result of the well documented problems associated with UHMWPE particles. Ceramic-on-ceramic hip prostheses have been used for over 30 years. The first generation alumina ceramics were prone to head fracture; however, the more modern hot isostatically pressed alumina ceramics introduced in the 1990s have increased fracture toughness, due to a refined grain size. The hot isostatically pressed alumina has reduced porosity, smaller grain size, and improved strength. The *in vivo* wear rates of retrieved ceramic-on-ceramic prostheses have generally been much lower than the alternatives, and are typically in the order of 1–5 mm<sup>3</sup> per year [19]. Under ideal conditions in the laboratory extremely low wear rates of 0.01–0.1 mm<sup>3</sup> per million cycles have been reported [20], which are much lower than those reported clinically. Retrieved clinical specimens also exhibited a stripe of wear on the head and the rim of the cup, which was not replicated in the early

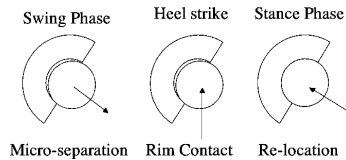


FIG. 1—Schematic illustration of microseparation motion.

simulator studies. Fluoroscopy studies have shown that separation of the ball and socket occurs during the swing phase load of walking [21], and that this may be involved in the initiation of stripe wear observed on the retrieved specimens. The introduction of microseparation of the alumina ceramic components into the *in vitro* wear simulation reproduced clinically relevant wear rates, wear patterns, and mechanisms [20]. The microseparation motion is shown schematically in Fig. 1. In addition, the wear particles released from ceramic-ceramic couples are generally in the nanometer size range, with a small number of wear particles in the micrometre size range [22]. Consequently, the biological activity of alumina ceramic wear particles is low, as only small volumes of debris in the most biologically active size ranges are released [22]. Hence, alumina ceramics make an attractive choice as a bearing material for hip arthroplasty.

At present two grades of UHMWPE are commonly used in the manufacture of hip replacement components, GUR 1020 and GUR 1050. These materials differ in both their molecular weight and processing method. GUR 1020 is compression molded and has a molecular weight of  $4.4 \times 10^6$  g mol<sup>-1</sup>, whereas GUR 1050 has a higher molecular weight ( $7.3 \times 10^6$  g mol<sup>-1</sup>) and is ram extruded [23]. The lower molecular weight GUR 1020 UHMWPE has been used since 1960, whereas the higher molecular weight GUR 1050 material was introduced into clinical practice more recently. Studies on the tribological properties of these two materials have demonstrated differences in their wear resistance and particle distributions [24,25]. The clinical performance of joint prostheses cannot be predicted by volumetric wear alone, the size, morphology, and biological activity of the wear particles released are equally important [26]. Further consideration is now being given to the recent findings that both higher molecular weight polyethylenes [25,27] and crosslinked polyethylenes [10,27] produce smaller and more biologically active wear particles, which may negate some of the benefits of a lower wear volume.

The aim of this study was two-fold, first to investigate the wear and to characterize the wear particles generated in an anatomical physiological hip joint simulator, in terms of their size, morphology, and volumetric concentrations as a function of size for two grades of UHMWPE, GUR 1020 and GUR 1050, at different levels of crosslinking. Specifically these were noncrosslinked GUR 1020 and GUR 1050, conventional 2.5 MRad GUR 1050, moderately crosslinked (4 MRad GUR 1020), and highly crosslinked GUR 1050 (10 MRad). Secondly, to compare the results for the different polyethylenes to an alumina ceramic-on-ceramic total hip prosthesis tested under standard and microseparation conditions in a hip joint simulator. This detailed wear particle analysis will allow prediction of the osteolytic potential of the different materials.

## Materials

GUR 1020 was sterilized either with ethylene oxide gas and was not crosslinked, or was irradiated with 4 MRad of irradiation in a vacuum and then foil packed (GVF), and hence was moderately crosslinked. GUR 1050 was either noncrosslinked (0 MRad), gamma irradiated in air with 2.5 MRad of irradiation, or highly crosslinked with 10 MRad of irradiation, followed by remelting above 155°C for 24 h to eliminate residual free radicals. The GUR 1020 4Mrad GVF UHMWPE acetabular cups were off the shelf clinical products supplied by DePuy International, a Johnson & Johnson Company. All the other UHMWPE acetabular cups were manufactured specifically for this study. The details of all the UHMWPE acetabular cups tested in this study are summarized in Table 1. All UHMWPE components were tested within three months of manufacture and irradiation. This was to minimize the effects of oxidative degradation and continuing crosslinking on the wear of the components. Twenty-eight millimetre femoral heads were manufactured from medical grade cobalt chromium alloy and were highly polished with  $R_a$  values of  $<0.02$   $\mu\text{m}$ . Ceramic-on-ceramic components were manufactured from medical grade hot isostatically pressed (HIPed) BIOLOX Forte alumina ceramic (CeramTec AG; ISO 6474).

TABLE 1—Details of the polyethylenes tested in the hip joint simulator.

Material	Molecular Weight (g·mol <sup>-1</sup> )	Processing Method	Radiation Dose (MRad)	Atmosphere for Irradiation	Post-irradiation Treatment
0 MRad GUR 1020	4.4 × 10 <sup>6</sup>	Compression Molded	0	...	...
4 MRad GUR 1020	4.4 × 10 <sup>6</sup>	Compression Molded	4	Vacuum	None
0 MRad GUR 1050	7.3 × 10 <sup>6</sup>	Ram Extruded	0	...	...
2.5 MRad GUR 1050	7.3 × 10 <sup>6</sup>	Ram Extruded	2.5	Air	None
10 MRad GUR 1050	7.3 × 10 <sup>6</sup>	Ram Extruded	10	Nitrogen	Remelting at 155°C for 24 h

## Methods

### Hip Joint Simulators

**UHMWPE Components**—A minimum of three 28 mm prosthesis pairs of each UHMWPE material were studied under standard simulation conditions in a ten-station Leeds ProSim hip joint simulator for five million cycles [28]. The cups were positioned superiorly and inclined at 35 deg to the horizontal plane in an anatomical configuration. The simulator applied two independently controlled motions. The head underwent flexion/extension (+30° and -15°) and the acetabular insert ±10° rotation. These two motions have been previously compared to a three-axis motion simulation [28] and have been found to produce similar wear rates for polyethylene acetabular cups. A twin peak time dependent loading curve was applied with a peak load of 3 kN at heel strike and toe off, and a swing phase load of 50N.

Tests were carried out in 25 % (v/v) newborn calf serum (Harlan Seralabs, UK) with 0.1 % (w/v) sodium azide to retard bacterial growth. The lubricant was changed every 330 000 cycles when the components and articulating cell were cleaned *in situ*. Serum lubricants were stored frozen at -20°C until required for wear debris analysis. Wear was determined volumetrically every million cycles. The three-dimensional geometry of the cups was determined before the test and every million cycles using a coordinate measuring machine (Kemco 400 3D, Keeley Measurement Co., UK). The volume change corresponded to wear plus creep. Previous studies have shown that creep predominately occurs in the first million cycles and after that period volume loss and penetration are predominantly due to wear [28]. The surface topography of the CoCr alloy femoral heads was measured prior to testing and at the end of the tests using a contacting profilometer (Form Talysurf, Taylor Hobson Ltd., Leicester, UK).

**Alumina Ceramic Components**—Three 28 mm diameter “BIOLOX forte” HIPed alumina ceramic-on-ceramic prostheses were tested in a six-station physiological hip joint simulator under the standard conditions described above. Wear volumes were determined gravimetrically every million cycles to five million cycles. Prior to weighing, the femoral heads and acetabular cups were cleaned by ultrasonication in isopropanol, to allow accurate measurement of wear and surface topography. The first million cycles represented “bedding in” wear, which has been described previously for hard-on-hard bearings [29]. The surface roughness of the femoral heads was measured before and after testing using a contacting Form Talysurf (Taylor Hobson Ltd., Leicester, UK) with a cut off length of 0.8 mm. The initial surface roughness ( $R_a$ ) was 0.005–0.008 µm for all femoral heads. The diametral clearances of the ceramic components were 60–80 µm.

Two 28 mm “BIOLOX forte” HIPed alumina ceramic-on-ceramic prosthesis were tested under simulation conditions that incorporated microseparation. To allow comparison to the standard simulator tests, the alumina ceramic components were tested in the same six-station physiological hip joint simulator, which had one vertical load and two degrees of motion (flexion/extension and internal/external rotation). To achieve the microseparation motion the vertical load was reduced to 1.7 kN and a force of 400N was applied in the medio-lateral direction using a spring. This force combined with a low swing-phase load of <200N allowed the joint to separate. On heel strike the displaced head contacted the rim of the cup before relocating during the stance phase. The initial displacement was 800 µm, which decreased to approxi-

mately 200  $\mu\text{m}$  after 100 000 cycles. The microseparation simulations were run in 25 % (v/v) bovine serum supplemented with sodium azide for 800 000 cycles. Serum lubricants from all simulator tests were collected and stored at  $-20^\circ\text{C}$  until required for wear debris characterization.

#### *Isolation and Characterization of Wear Debris*

*Characterization of UHMWPE Particles by SEM*—For the GUR 1050 acetabular cups, the wear debris was isolated for each material from serum lubricants collected between 1 and 2 million cycles from three articulating stations of the hip simulator. For the GUR 1020 acetabular cups wear debris was collected between 1 and 2 million cycles from two articulating stations of the simulator. Approximately 80 mL of serum was digested according to the method of Tipper et al. [30]. Briefly, the lubricating serum was digested with 5M potassium hydroxide at  $60^\circ\text{C}$  for 48 h. Contaminating proteins and lipids were removed by extraction with chloroform:methanol followed by centrifugation at 500 g for 10 min. The extraction was repeated three times and the lipid-free supernatants were subjected to precipitation with ice-cold ethanol (99.7 % v/v) for 24 h followed by high-speed centrifugation (15 000 g) for 30 min. The resulting supernatants were diluted with pyrogen-free water and sequentially filtered through 1.0  $\mu\text{m}$  and 0.1  $\mu\text{m}$  Cyclopore<sup>®</sup> polycarbonate filter membranes (Whatman International Ltd.). The filters were dried under infrared lamps and then observed using either standard SEM or field emission gun scanning electron microscopy (Leo 1530 FEG SEM). A small section of each filter was mounted onto an aluminum stub and coated with a thin (10 nm) layer of chromium before loading into the microscope chamber. The samples were observed under low voltage conditions (1–3 kV) at high resolution. Digital images were obtained and the wear particles were characterized by image analysis using Image Pro Plus (Media Cybernetics, USA). Maximum diameter and area measurements were taken for a minimum of 150 particles per sample to generate size and area distributions for the particles from the different materials. The area distributions were converted to percentage volume distributions as a function of size, assuming a constant thickness, and the volumetric concentration,  $C(r)$ , was plotted as a function of particle size. Previous studies have shown that the constant thickness assumption was a reasonable approximation when two-dimensional image data were compared with three-dimensional volumes determined by weight [31]. Percentage data were arcsine transformed and the means  $\pm 95$  % confidence limits calculated (where  $n=3$ ). Where  $n=2$  for the GUR 1020 UHMWPE materials no statistical analyses were performed. The transformed data were analyzed by two-way ANOVA and minimum significant differences between materials were calculated using the T-method [32]. Data were back transformed to percentages for illustrative purposes.

*Characterization of Alumina Ceramic Wear Particles by TEM*—Serum was collected after 1 million and 400 000 cycles from standard and microseparation simulations, respectively, and the wear debris was characterized from the serum by TEM [33]. Approximately 100 mL of serum was centrifuged at 12 000 g for 10 min to pellet the wear particles and the supernatant was discarded. The pellet was fixed in 2.5 % (v/v) glutaraldehyde in phosphate buffered saline (PBS) at pH 7.4 for 2 h at  $4^\circ\text{C}$ . The samples were then washed three times in PBS for 2 h at  $4^\circ\text{C}$ , and fixed in 1 % (w/v) osmium tetroxide for 1–2 h at  $4^\circ\text{C}$ . The samples were washed in PBS for 15 min and dehydrated through graded ethanols (70, 90, and 100 % (v/v)) at room temperature for 10–20 min. The samples were polymerized in araldite resin for 24 h at  $70^\circ\text{C}$  and then 100 nm sections were cut using an LKB ultramicrotome fitted with a diamond knife. The sections were transferred to copper grids for staining with lead nitrate and sodium citrate for 1–2 min. The samples were double stained with 15 % (v/v) uranyl acetate. The sections were observed using a Jeol 1200 EX transmission electron microscope and representative photographs of the wear debris were taken at magnifications of  $\times 25$ –75 K. Particles were identified by energy dispersive X-ray (EDX) analysis (Link Isis, Oxford Instruments).

All wear debris was characterized using digital image analysis (Image Pro Plus, Media Cybernetics, USA) using mean maximum diameter measurements (length). A minimum of 100 particles per sample was measured by image analysis. Statistical analysis of the data was carried out using single classification analysis of variance (ANOVA), followed by determination of the minimum significant difference using the T-method [32].

*Prediction of Osteolytic Potential of Wear Particles*—The osteolytic potential of the wear particles generated in the hip simulators was predicted using the method of Fisher et al. [26] to predict functional

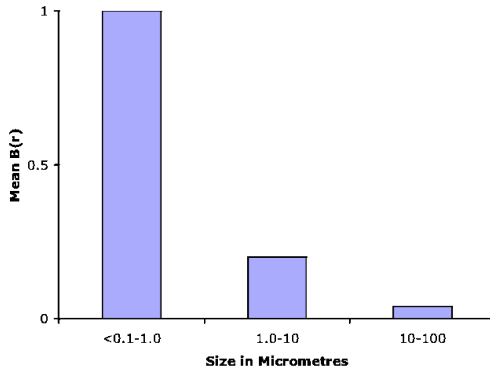


FIG. 2—Biological activity  $B(r)$  as a function of particle size derived from *in vitro* cell culture studies.

biological activity (FBA). This approach integrated the volumetric concentration of wear particles in three different size ranges (<0.1–1.0, 1.0–10, and >10  $\mu\text{m}$ ) with the biological activity index for wear particles in each of the three size ranges (determined in previous studies [34,35]). The percentage volumetric concentration of wear as a function of particle size,  $C(r)$ , was determined by isolating the particles from the bovine serum lubricant from laboratory wear simulations as described above. Using the particle area distributions, and assuming a constant particle thickness, a volume distribution was determined, giving the volumetric concentration of wear particles in each of the three size ranges, <0.1–1, 1–10, and 10–100  $\mu\text{m}$ , for all materials.

The biological activity function  $B(r)$  for polyethylene wear debris was determined as a function of particle size,  $r$ , at fixed volumetric concentrations. The wear particles were used to stimulate primary human macrophages obtained from six human donors in triplicate [34].  $\text{TNF}\alpha$  was used as a marker of biological activity as it has previously been shown to correlate with bone resorption [36]. The biological activity,  $B(r)$ , was normalized with respect to the lowest size range, which was assigned a value of unity (see Fig. 2). Normalization was carried out on each donor with the mean from at least three replicates, in order to eliminate donor-to-donor variability. The index of specific biological activity (SBA) of polyethylene wear debris is defined as the relative biological activity per unit volume. It is calculated by integrating the biological activity function,  $B(r)$ , and the volumetric concentration function,  $C(r)$ , over the size range of the wear particles:

$$\text{SBA} = \int_{0.1}^{100} C(r)B(r)dr$$

In this case the total size range studied was <0.1–100  $\mu\text{m}$ .

Determining the volumetric concentration of wear particles in each size range for each material and then integrating these values with the biological activity function for either polyethylene or alumina ceramic allowed the SBA for each material tested to be determined. The SBA was then integrated with the volumetric wear rate in  $\text{mm}^3/\text{million cycles}$  to give a measure of functional biological activity (FBA).

$$\text{FBA} = V \times \text{SBA}$$

where  $V$  has units of  $\text{mm}^3/10^6$  cycles or  $\text{mm}^3/\text{year}$ . The values of SBA and FBA were compared for the wear particles from all materials.

**Results**

*Volumetric Wear Rates*

The wear rates and wear particles have been reported previously for both the GUR 1020 UHMWPE cups [9] and the alumina ceramic-on-ceramic hip prostheses [36]. The volumetric wear rates for the two grades

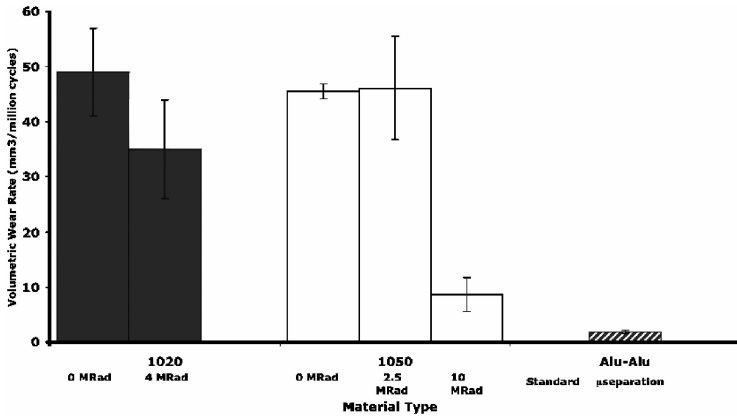


FIG. 3—Mean volumetric wear rates (mean  $\pm$  95 % confidence limits) for noncrosslinked and crosslinked GUR 1020 and GUR 1050 UHMWPE and alumina ceramic-on-ceramic hip prostheses under standard and microseparation simulation conditions.

of UHMWPE are shown in Fig. 3. The wear rate for the noncrosslinked GUR 1020 material ( $49 \pm 8$  mm<sup>3</sup>/million cycles) was significantly higher than the wear rate for the moderately crosslinked GUR 1020 material ( $35 \pm 9$  mm<sup>3</sup>/million cycles). The crosslinking induced by 4 MRad of gamma irradiation reduced the wear rate of the GUR 1020 material by approximately 30 %. The wear rate of the GUR 1050 irradiated with 2.5 MRad of irradiation was not significantly different than the noncrosslinked material, indicating that low levels of crosslinking did not produce a reduction in wear volume, as observed with the GUR 1020 material. However, high levels of crosslinking (10 MRad of irradiation) produced an 80 % reduction in wear volume for the GUR 1050 material. The wear rate of the 10 MRad crosslinked material was  $8.7 \pm 3.1$  mm<sup>3</sup>/million cycles, and was statistically significantly lower than all the other UHMWPE materials ( $p < 0.05$ ; ANOVA).

The wear of the alumina ceramic-on-ceramic hip prostheses under both simulation conditions was extremely low compared to the polyethylene materials (Fig. 3). Under standard simulation conditions the wear rate was  $0.08 \pm 0.03$  mm<sup>3</sup>/million cycles, and under microseparation simulation conditions the wear rate increased to  $1.8 \pm 0.3$  mm<sup>3</sup>/million cycles. However, this was still 4.5-fold lower than the wear rate for the highly crosslinked GUR 1050 UHMWPE. The wear stripe often seen clinically on the femoral head was reproduced under microseparation simulation conditions. The wear stripes were approximately 4-mm wide, and there was a small amount of wear on the rim of the acetabular cups. SEM analysis of the wear stripes revealed intergranular fracture of the alumina.

### Surface Roughness

There was no change in surface roughness detected for the cobalt chromium alloy femoral heads tested against the different UHMWPE materials, with all heads remaining smooth and scratch free. There was also no change in surface roughness detected for the alumina ceramic heads tested under standard simulation conditions. However, for the alumina ceramic heads subjected to microseparation simulation conditions there was an increase of surface roughness from  $R_a$  0.007  $\mu$ m to  $R_a$  0.03  $\mu$ m, as the surface was damaged along the wear stripe.

### Wear Particles

The majority of the UHMWPE particles observed by SEM were small submicron-sized granule type particles as shown in Fig. 4(a). This was the case for all the UHMWPE materials tested. A very small number of larger flakes were also observed (Fig. 4(b)). Molecular weight and the processing method did not greatly affect particle morphology or particle size distributions (Fig. 5). The GUR 1020 materials produced slightly lower numbers of particles in the submicron size range compared to the GUR 1050

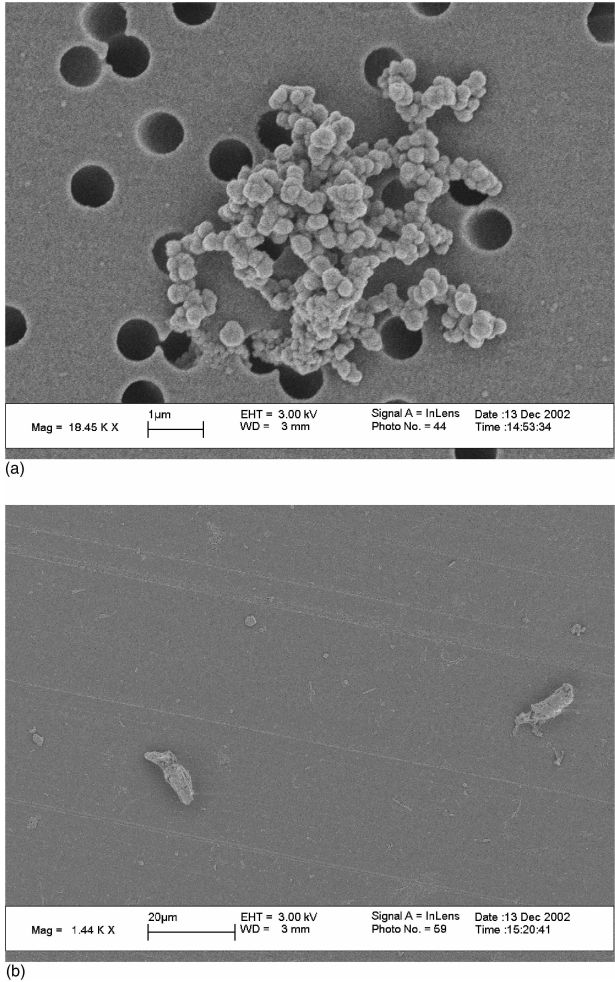


FIG. 4—Scanning electron micrographs of (a) submicrometre-sized wear particles (magnification  $\times 18\,450$ , size bar  $1\ \mu\text{m}$ ) and (b) larger wear particles (magnification  $\times 1\,440$ , size bar  $20\ \mu\text{m}$ ) from moderately crosslinked GUR 1020 UHMWPE tested in the ProSim hip simulator.

materials, although this difference was not statistically significant. In addition, the GUR 1020 materials produced slightly higher numbers of particles in the  $1\text{--}10\ \mu\text{m}$  size range compared to the GUR 1050 materials. The crosslinked GUR 1020 material produced slightly higher numbers of particles in the submicron size range compared to the noncrosslinked GUR 1020, although this difference was not significant. Crosslinking the GUR 1050 material had little effect on particle size distribution.

Analysis of the volumetric concentrations of the particles as a function of size revealed some differences between the particles produced by the different polyethylenes. For the noncrosslinked GUR 1020 material the mode of the distribution for the volumetric concentrations of particles as a function of size was in the  $1\text{--}10\ \mu\text{m}$  size range (Fig. 6). However, for the crosslinked GUR 1020 material the mode was in the submicron size range, with  $>40\%$  of the wear volume made up of submicron particles (Fig. 6). For all the GUR 1050 materials, there were significantly higher ( $p < 0.05$ ) volumetric concentrations of particles in the submicron size range compared to the other size ranges. For all GUR 1050 materials,  $>80\%$  of the wear volume was comprised of submicron particles (Fig. 6).

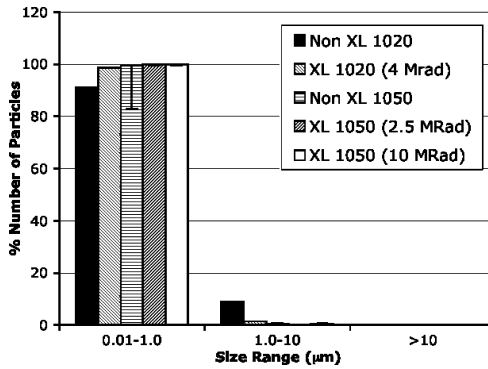


FIG. 5—Frequency distributions as a function of particle size (mean  $\pm 95$  % confidence limits) for noncrosslinked and crosslinked GUR 1020 and GUR 1050 UHMWPEs.

The alumina ceramic-on-ceramic hip prostheses generated only small particles under standard simulator testing conditions (2–30 nm). Two size ranges of particles: small (4–100 nm) and large (0.1–1  $\mu\text{m}$ ) were generated under microseparation testing. Under standard simulator testing, the mean size of the particles was  $9.2 \pm 0.5$  nm, and under microseparation simulator testing, the mean sizes were  $5.1 \pm 0.3$  nm for the small particles and  $140 \pm 50$  nm for the large particles. The majority of the alumina ceramic wear particles characterized by TEM from the serum lubricant from standard testing and microseparation testing were oval to round in shape and appeared as electron dense aggregates of wear particles [Fig. 7(a) and 7(b)]. Shards were also observed. The larger wear particles (0.1–1  $\mu\text{m}$ ) generated under microseparation testing were also oval to round, but with some polygonal particles observed (Fig. 8). Particles from both simulation conditions were identified as alumina by EDX analysis.

#### Osteolytic Potential of Wear Particles

The specific biological activity (SBA) and functional biological activity (FBA) indices for the UHMWPE materials and the alumina ceramic materials tested under different conditions are shown in Table 2. The noncrosslinked GUR 1020 material had the lowest SBA of all the different types of UHMWPE, due to it having the lowest volumetric concentration of wear particles in the submicron size range (Table 2). When moderate levels of crosslinking were introduced this material produced a two-fold increase in the volume of particles in the submicron size range and a 1.5-fold increase in SBA. The GUR 1050 materials had substantially higher volumetric concentrations of particles in the submicron size range, and therefore had

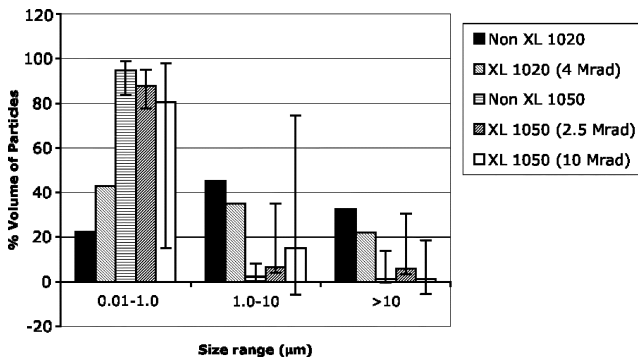
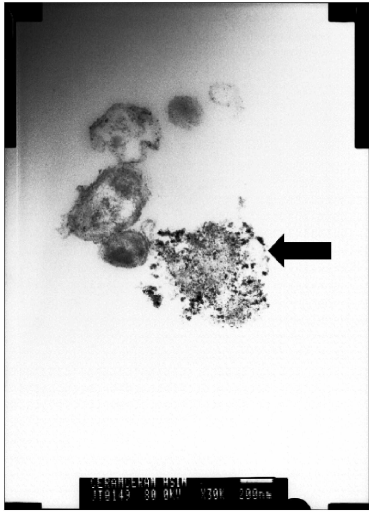
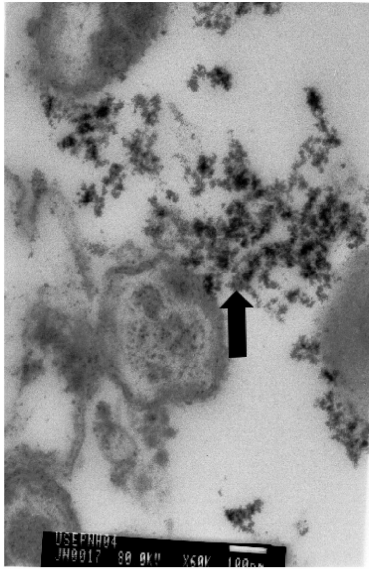


FIG. 6—Volumetric concentration distributions as a function of particle size (mean  $\pm 95$  % confidence limits) for noncrosslinked and crosslinked GUR 1020 and GUR 1050 UHMWPEs.



(a)



(b)

FIG. 7—Transmission electron micrographs of nanometre-sized alumina ceramic wear debris (arrows) isolated from *in vitro* wear simulations under (a) standard testing conditions ( $\times 30\,000$ , bar 200 nm); (b) microseparation testing conditions ( $\times 60\,000$ , bar 100 nm).

1.5 to three-fold higher SBA indices compared to the GUR 1020 materials. For the GUR 1020 material, the introduction of moderate levels of crosslinking caused a significant reduction in wear rate of 30 %; however, an increased volume of more biologically active submicron particles were generated. Therefore, there was little difference in the overall osteolytic potential (FBA) of the crosslinked GUR 1020 material compared to the noncrosslinked material (Table 2). For the GUR 1050 materials, the introduction of low levels of crosslinking had little effect on wear rate, but did cause a slight reduction in the volumetric

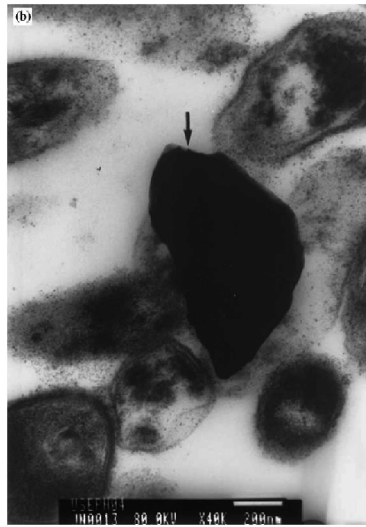


FIG. 8—Transmission electron micrographs of micrometre-sized alumina ceramic wear debris (arrow) isolated from *in vitro* wear simulations under microseparation motion ( $\times 60\,000$ , bar 200 nm).

concentration of wear particles in the submicron size range. Hence, there was a slight nonsignificant decrease in FBA for the 2.5 MRad GUR 1050 material compared to the noncrosslinked GUR 1050 material (Table 2). However, for the highly crosslinked GUR 1050 material, although the volumetric concentration of wear particles in the submicron size range was  $>80\%$ , the reduction in wear volume was enough to cause a dramatic statistically significant ( $p < 0.05$ ) six-fold decrease in FBA compared to the noncrosslinked GUR 1050 material, and a significant ( $p < 0.05$ ) 5.8-fold decrease compared to the 2.5 MRad GUR 1050 material (Table 2). However, the highly crosslinked GUR 1050 material had only a two-fold lower osteolytic potential than the noncrosslinked and moderately crosslinked GUR 1020 materials. The alumina ceramic hip prostheses produced very low SBA values, and these coupled with the very

TABLE 2—Results for crosslinked and noncrosslinked UHMWPEs and alumina ceramic-on-ceramic bearings under different simulation conditions.

Material	Volumetric Wear Rate ( $\text{mm}^3/10^6$ cycles) $\pm 95\%$ Confidence Limits	% No. of Particles < $1\ \mu\text{m}$ ( $\pm 95\%$ Confidence Limits)	% Volume of Particles < $1\ \mu\text{m}$ ( $\pm 95\%$ Confidence Limits)	SBA <sup>a</sup> ( $\pm 95\%$ Confidence Limits)	FBA <sup>b</sup> ( $\pm 95\%$ Confidence Limits)
0 MRad 1020	49 $\pm$ 8	91	22.3	0.32	16
4 MRad 1020	35 $\pm$ 9	99	43	0.5	18
0 MRad 1050	45.6 $\pm$ 1.3	99.8 $\pm$ 0.1 -16.6	95.2 $\pm$ 4.4 -11.0	0.96 $\pm$ 0.07	43 $\pm$ 3
2.5 MRad 1050	46.1 $\pm$ 9.4	99.9 $\pm$ 0.1 -0.5	87.6 $\pm$ 7.4 -9.9	0.89 $\pm$ 0.06	41 $\pm$ 2.6
10 MRad 1050	8.7 $\pm$ 3.1	99.9 $\pm$ 0.1 -0.3	79.3 $\pm$ 17.2 -64.5	0.83 $\pm$ 0.4	7 $\pm$ 3.5
Alumina-Alumina (Standard)	0.08 $\pm$ 0.03	100	100	...	...
Alumina-Alumina (Microseparation)	1.8 $\pm$ 0.3	100	100	0.19	0.35

<sup>a</sup>Specific biological activity.

<sup>b</sup>Functional biological activity.

low wear rates gave rise to extremely low FBA indices (Table 2). The osteolytic potential for the wear particles produced by the alumina ceramic-on-ceramic tested under microseparation simulation conditions was >20-fold lower than the lowest wearing 10 MRad UHMWPE.

## Discussion

The 80 % reduction in volume change of highly crosslinked polyethylene compared to conventional polyethylene was not as great as the reduction in wear reported for comparative simulator studies [6–9]. This study also showed a higher finite wear rate for the highly crosslinked material than has previously been reported, with a total volume change rate of 8.7 mm<sup>3</sup>/million cycles after 5 million cycles. In addition, we found no reduction in wear with the 2.5 MRad GUR 1050 UHMWPE compared to the noncrosslinked material, which was in contrast to previous studies [6,8]. The simulator studies reported here used a lower concentration of serum proteins and different simulator kinematics in line with the ISO standard recommendations. In these tests, a lower serum protein concentration was used, 25 % compared to 90 % in other studies. Wang et al. [7] reported that higher serum protein concentrations reduced wear rates. Additionally, a peak load of 3 KN as per the ISO standard was applied in this study, as opposed to 2.5 KN in other studies. Different simulator kinematics were also applied in this study in comparison with the previous simulator studies on crosslinked polyethylene [6,9]. Our previous studies on the effects of different kinematics within our own laboratory simulators [28] have shown that when provided cross shear was introduced into the kinematics, similar wear rates were achieved.

Wear particle morphologies were comparable to UHMWPE wear particles isolated from periprosthetic tissues from explanted failed hip prostheses [30,37]. Molecular weight and the introduction of crosslinking did not affect particle morphology, but did affect the volumetric concentration distributions as a function of particle size. The wear rates for the two noncrosslinked UHMWPE materials were similar; however, the wear particles produced had some differences in their size distributions that affected the osteolytic potential of the two materials. The noncrosslinked GUR 1020 material produced larger volumes of larger wear particles compared to the noncrosslinked GUR 1050 material. Previous research has shown that UHMWPE wear particles in the 0.1–1.0 μm size range are the most biologically active, in terms of production of osteolytic cytokines and bone resorption [34,36,38]. This was reflected in the osteolytic potential or functional biological activity (FBA) predictions for the different materials. The noncrosslinked GUR 1050 material had greater predicted osteolytic potential than the noncrosslinked GUR 1020 material. These results are supported by previous studies by Ingram et al. [25,27], which compared the biological activity of the two different grades of UHMWPE. These authors found that when using simple configuration wear tests the GUR 1050 material produced a higher volumetric concentration of particles in the submicron size range, and that as a result the GUR 1050 material had a 10 to 100-fold increase in biological activity compared to the GUR 1020 material when tested *in vitro*.

The introduction of moderate levels of crosslinking (4 MRad) into the GUR 1020 material produced a significant reduction in the volumetric wear rate, but also caused an increase in the volumetric concentration of wear particles in the more biologically active submicron size range. Hence the SBA was increased, and the net result was that there was little difference in FBA or osteolytic potential. With the GUR 1050 materials, there was little benefit afforded by introducing low levels of crosslinking (2.5 MRad), in that there was no significant reduction in wear rate, SBA or FBA. Previous studies have shown a reduction in wear rate for conventionally sterilized UHMWPE compared to noncrosslinked UHMWPE *in vitro*. Therefore, *in vivo* it is possible that the conventionally sterilized material may exhibit lower wear and hence, lower osteolytic potential. This is supported by Hopper et al. [12] who reported a 50 % reduction in wear of conventionally sterilized UHMWPE acetabular cups *in vivo* compared to ethylene oxide sterilized acetabular cups. However, these authors reported little difference in the wear rate of the conventionally sterilized acetabular cups and moderately crosslinked acetabular cups (5 MRad Marathon) [12].

When high levels of crosslinking (10 MRad) were introduced, the volumetric wear rate was significantly reduced. Consequently, the FBA or osteolytic potential was significantly lower compared to the noncrosslinked and the 2.5 MRad irradiated materials. The highly crosslinked GUR 1050 material produced a relatively modest two-fold lower FBA index compared to the noncrosslinked and moderately crosslinked GUR 1020 materials. This was due to the very high volumetric concentrations of wear par-

ticles in the submicrometre size range. It was the large reduction in wear volume, afforded by the high levels of crosslinking in the GUR 1050 material, which caused the reduction in the predicted osteolytic potential. However, as already discussed the wear rates reported for the highly crosslinked polyethylene in this study are higher than some previous studies, and consequently, it is possible that the osteolytic potential of this material could be lower than predicted here. The highly crosslinked GUR 1050 UHMWPE gave the lowest predicted FBA of all the UHMWPE materials tested.

The alumina ceramic-on-ceramic prostheses produced very low wear rates and hence, small volumes of wear particles. The majority of the wear particles produced were in the nanometre size range regardless of simulation method. However, some larger micrometre-sized alumina particles were generated when microseparation of the prosthesis components was introduced into the simulation. Hatton et al. [35] demonstrated that alumina ceramic wear particles generated under microseparation conditions were less biologically reactive compared to UHMWPE particles in the same size range. In addition, these authors concluded that as the wear rates of alumina ceramic-on-ceramic prostheses *in vivo* were very low, and the volumetric concentration of wear particles required to elicit an osteolytic response was very high, it was unlikely that an osteolytic response would be generated *in vivo*. This is supported by the predictive methodology for the determination of osteolytic potential, which revealed that the alumina ceramic-on-ceramic prostheses generated very low specific biological activity and functional biological activity indices, even under the most severe microseparation wear simulation conditions. These results indicate that alumina ceramic-on-ceramic hip joint prostheses have the potential to deliver over 20 years osteolysis-free *in vivo* lifetimes.

Three independent samples of wear simulator lubricant were analyzed in the characterization of the GUR 1050 UHMWPE wear particles for each material. However, there was considerable variation between the three samples, which led to large error bars on the volumetric concentration graph. For future studies it is recommended that a minimum number of five samples per material are analyzed. At present there is no clinical validation for the methodology used in this study to estimate osteolytic potential of a material. The results reported here differ from previous simulator studies [6,8] and from some *in vivo* results [12]. However, as highly crosslinked UHMWPE acetabular components have been in clinical use for a relatively short period of time, in the order of six years, and the maximum clinical follow-up times reported so far are in the order of three to four years, longer-term results are not known. These early clinical data indicate that highly crosslinked acetabular cups are performing well compared to non-crosslinked and conventionally sterilized cups and wear rates are predicted to remain low over the longer term. Our predictive model shows good agreement with this, calculating that the highly crosslinked UHMWPE will have an 80 % reduction in osteolytic potential compared to the noncrosslinked material. However, to date there is little or no data on the wear particles produced from highly crosslinked UHMWPE acetabular cups *in vivo*.

This study shows that the use of predictive methodology to rank the osteolytic potential of different materials is advantageous and demonstrates that wear rate alone is not always an adequate indicator of clinical performance.

## Conclusion

Although the introduction of moderate levels of crosslinking (4 MRad) into GUR 1020 UHMWPE acetabular cups produced a 30 % reduction in wear volume, when the biological activity of the wear particles was examined, higher volumes of more biologically active particles were produced compared to the noncrosslinked GUR 1020 material. The net result was little change in the predicted osteolytic potential for the moderately crosslinked GUR 1020 UHMWPE. However, the introduction of high levels of crosslinking (10 MRad) into GUR 1050 UHMWPE produced a statistically significant 80 % reduction in the wear rate and predicted osteolytic potential compared to noncrosslinked and conventionally sterilized GUR 1050 polyethylene. The alumina ceramic-on-ceramic hip prostheses produced extremely low wear rates, and in addition, the osteolytic potential was estimated to be 20-fold lower than the highly crosslinked UHMWPE. These estimates indicate that alumina ceramic-on-ceramic bearings could deliver *in vivo* osteolysis-free lifetimes in excess of 20 years.

*Acknowledgments*

The work reported in this paper was performed in independent studies supported by the EPSRC, the ARC, DePuy International, a Johnson & Johnson Company, and Stryker International Research and Development. JLT is supported by an EPSRC Advanced Fellowship.

**References**

- [1] Schmalzried, T. P., Jasty, M., and Harris, W. H., "Periprosthetic Bone Loss in Total Hip Arthroplasty. Polyethylene Wear Debris and the Concept of the Effective Joint Space," *J. Bone Jt. Surg., Am. Vol.*, Vol. 74-A, 1992, pp. 849–863.
- [2] Fisher, J., Chan, K. L., Hailey, J. L., Shaw, D., and Stone, M. H., "Preliminary Study of the Effect of Aging Following Irradiation on the Wear of Ultra High Molecular Weight Polyethylene," *J. Arthroplasty*, Vol. 10, 1995, pp. 689–692.
- [3] Reeves, E. A., Barton, D. C., Fitzpatrick, D., and Fisher, J., "Comparison of Gas Plasma and Gamma Irradiation in Air Sterilization on the Delamination Wear of the Ultra-High Molecular Weight Polyethylene used in Knee Replacements," *Proceedings of the Institution of Mechanical Engineers*, Vol. 214, Part H, 2000, pp. 249–255.
- [4] Wang, A., Stark, C., and Dumbleton, J. H., "Mechanistic and Morphological Origins of Ultra High Molecular Weight Polyethylene Wear Debris in Total Joint Replacement Prostheses," *Proceedings of the Institution of Mechanical Engineers*, Vol. 210H, 1996, pp. 141–152.
- [5] Wannomae, K. K., Christensen, S. D., Freiberg, A. A., Bhattacharyya, S., Harris, W. H., and Muratoglu, O. K., "The Effect of Real-time Aging on the Oxidation and Wear of Highly Crosslinked UHMWPE Acetabular Liners," *Biomaterials*, Vol. 27, 2006, pp. 1980–1987.
- [6] McKellop, H., Shen, F., Lu, B., Campbell, P., and Salovey, R., "Development of an Extremely Wear-Resistant Ultra High Molecular Weight Polyethylene for Total Hip Replacements," *J. Orthop. Res.*, Vol. 17, 1999, pp. 157–167.
- [7] Wang, A., Essner, A., Polineni, V. K., Stark, C., and Dumbleton, J. H., "Lubrication and Wear of Ultra High Molecular Weight Polyethylene in Total Joint Replacements," *Tribol. Int.*, Vol. 31, 1998, pp. 17–33.
- [8] Muratoglu, O. K., Bragdon, C. R., O'Connor, D. O., Jasty, M., Harris, W. H., Gul, R., and McGarry, F., "Unified Wear Model for Highly Crosslinked UHMWPE," *Biomaterials*, Vol. 20, 1999, pp. 1463–1470.
- [9] Muratoglu, O. K., Bragdon, C. R., O'Connor, D., Perinchieff, R. S., Estok, D. M., Jasty, M., and Harris, W. H., "Larger Diameter Femoral Heads Used in Conjunction with a Highly Crosslinked Ultra High Molecular Weight Polyethylene," *J. Arthroplasty*, Vol. 16, Suppl. 1, 2001, pp. 24–30.
- [10] Endo, M., Tipper, J. L., Barton, D. C., Stone, M. H., Ingham, E., and Fisher, J., "Comparison of Wear, Wear Debris and Functional Biological Activity of Moderately Crosslinked and Non-crosslinked Polyethylenes in Hip Prostheses," *Proceedings of the Institution of Mechanical Engineers*, Vol. 216, Part H, 2002, pp. 111–122.
- [11] Wang, A., Essner, A., and Schmidig, G., "The Effects of Lubricant Composition on *in vitro* Wear Testing of Polymeric Acetabular Components," *J. Biomed. Mater. Res.*, Vol. 68B, 2004, pp. 45–52.
- [12] Hopper, R. H., Young, A. M., Orishimo, K. F., and McAuley, J. P., "Correlation Between Early and Late Wear Rates in Total Hip Arthroplasty With Application to the Performance of Marathon Crosslinked Polyethylene Liners," *J. Arthroplasty*, Vol. 18, 2003, pp. 60–67.
- [13] Martell, J. M., Verner, J. J., and Incavo, S. J., "Clinical Performance of a Highly Crosslinked Polyethylene at Two Years in Total Hip Arthroplasty: A Randomized Prospective Trial," *J. Arthroplasty*, Vol. 18, 2003, pp. 55–60.
- [14] Digas, G., Kärrholm, J., Thanner, J., Malchau, H., and Herberts, P., "Highly Crosslinked Polyethylene in Cemented THA," *Clin. Orthop. Relat. Res.*, Vol. 417, 2003, pp. 126–138.
- [15] Heisel, C., Silva, M., Dela Rosa, M. A., and Schmalzried, T. P., "Short-term *in vivo* Wear of Crosslinked Polyethylene," *J. Bone Jt. Surg., Am. Vol.*, Vol. 86A, 2004, pp. 748–751.
- [16] Röhrli, S., Nivbrant, B., Mingguo, L., and Hewitt, B., "In vivo Wear and Migration of Highly Crosslinked Polyethylene Cups," *J. Arthroplasty* Vol. 20, 2005, pp. 409–413.

- [17] Manning, D. W., Chiang, P. P., Martell, J. M., Galante, J. O., and Harris, W. H., "In vivo Comparative Wear Study of Traditional and Highly Crosslinked Polyethylene in Total Hip Arthroplasty," Vol. 20, 2005, pp. 880–886.
- [18] Minakawa, H., Stone, M. H., Wroblewski, B. M., Lancaster, J. G., Ingham, E., and Fisher, J., "Quantification of Third-body Damage and its Effect on UHMWPE Wear with Different Types of Femoral Head," *J. Bone Jt. Surg., Br. Vol.*, Vol. 80-B, 1998, pp. 894–899.
- [19] Nevelos, J. E., Ingham, E., Doyle, C., Fisher, J., and Nevelos, A. B., "Analysis of Retrieved Alumina Ceramic-ceramic Components from Mittelmeier Total Hip Prostheses," *Biomaterials*, Vol. 20, 1999, pp. 1833–1840.
- [20] Nevelos, J. E., Ingham, E., Doyle, C., Streicher, R., Nevelos, A. B., Walter, W., and Fisher, J., "Microseparation of the Centers of Alumina-alumina Artificial Hip Joints During Simulator Testing Produces Clinically Relevant Wear Rates and Patterns," *J. Arthroplasty*, Vol. 15, 2000, pp. 793–795.
- [21] Mallory, T. H., Dennis, D. A., Komistek, R. D., Northcut, E. J., Lombardi, A. V., and Herrington, S. M., "Do Total Hip Arthroplasties Piston During Leg Length Maneuvers and Gait? An *in vivo* Determination of Total Hip Arthroplasty Separation During Abduction/Adduction Leg Lift and Gait," *J. Am. Acad. Orthop. Surg.*, 1999, Scientific Exhibit 66.
- [22] Hatton, A., Nevelos, J. E., Nevelos, A. B., Banks, R. E., Fisher, J., and Ingham, E., "Alumina-alumina Artificial Hip Joints. Part I: A Histological Analysis and Characterization of Wear Debris by Laser Capture Microdissection of Tissues Retrieved at Revision," *Biomaterials*, Vol. 23, 2002, pp. 3429–3440.
- [23] Kurtz, S. M., Muratoglu, O. K., Evans, M., and Edidin, A. A., "Advances in the Processing Sterilization and Crosslinking of Ultra High Molecular Weight Polyethylene for Total Joint Arthroplasty," *Biomaterials*, Vol. 20, 1999, pp. 1659–1688.
- [24] Endo, M. M., Barbour, P. S. M., Barton, D. C., Wroblewski, B. M., Fisher, J., Tipper, J. L., Ingham, E., and Stone, M. H., "A Comparison of the Wear and Debris Generation of GUR 1020 (Compression Molded) and GUR 4150HP (Ram Extruded) Ultra High Molecular Weight Polyethylene," *Biomed. Mater. Eng.*, Vol. 9, 1999, pp. 113–124.
- [25] Ingram, J. H., Matthews, J. B., Tipper, J. L., Stone, M. H., Fisher, J., and Ingham, E., "Comparison of the Biological Activity of Grade GUR 1120 and GUR 415HP UHMWPE Wear Debris," *Biomed. Mater. Eng.*, Vol. 12, 2002, pp. 177–188.
- [26] Fisher, J., Bell, J., Barbour, P. S. M., Tipper, J. L., Matthews, J. B., Besong, A. A., Stone, M. H., and Ingham, E., "A Novel Method for the Prediction of Functional Biological Activity of Polyethylene Wear Debris," *Proceedings of the Institution of Mechanical Engineers*, Vol. 215, Part H, 2001, pp. 127–132.
- [27] Ingram, J. H., Stone, M. H., Fisher, J., and Ingham, E., "The Influence of Molecular Weight, Crosslinking and Counterface Roughness on TNF-alpha Production by Macrophages in Response to Ultra High Molecular Weight Polyethylene Particles," *Biomaterials*, Vol. 17, 2004, pp. 3511–3522.
- [28] Barbour, P. S. M., Stone, M. H., and Fisher, J., "A Hip Joint Simulator Study Using Simplified Loading and Motion Cycles Generating Physiological Wear Paths and Rates," *Proceedings of the Institution of Mechanical Engineers*, Vol. 214, Part H, 1999, pp. 455–467.
- [29] Medley, J. B., Chan, F. W., Krygier, J. J., and Bobyn, J. D., "Comparison of Alloys and Designs in a Hip Simulator Study of Metal on Metal Implants," *Clin. Orthop. Relat. Res.*, Vol. 329S, 1996, pp. 148–159.
- [30] Tipper, J. L., Ingham, E., Hailey, J. L., Besong, A. A., Fisher, J., Wroblewski, B. M., and Stone, M. H., "Quantitative Analysis of Polyethylene Wear Debris, Wear Rate and Head Damage in Retrieved Charnley Hip Prostheses," *J. Mater. Sci.: Mater. Med.*, Vol. 11, 2000, pp. 117–124.
- [31] Besong, A. A., Tipper, J. L., Ingham, E., Stone, M. H., Wroblewski, B. M., and Fisher, J., "Quantitative Comparison of Wear Debris from UHMWPE that Has and Has Not Been Sterilised by Gamma Irradiation," *J. Bone Jt. Surg., Br. Vol.*, Vol. 80-B, 1998, pp. 340–344.
- [32] Sokhal, R. R., and Rohlf, F. J., "*Biometry*", 2nd ed., W.H. Freeman & Company, New York, 1981.
- [33] Tipper, J.L., Hatton, A., Nevelos, J. E., Ingham, E., Doyle, C., Streicher, R., Nevelos, A. B., and Fisher, J., "Alumina-alumina Artificial Hip Joints. Part II: Characterization of the Wear Debris from *in vitro* Hip Joint Simulations," *Biomaterials*, Vol. 23, 2002, pp. 3441–3448.
- [34] Matthews, J. B., Besong, A. A., Green, T. R., Stone, M. H., Wroblewski, B. M., Fisher, J., and

- Ingham, E., "Evaluation of the Response of Primary Human Peripheral Blood Mononuclear Phagocytes to Challenge with *in vitro* Generated Clinically Relevant UHMWPE Particles of Known Size and Dose," *J. Biomed. Mater. Res.*, Vol. 52, 2000, pp. 296–307.
- [35] Hatton, A., Nevelos, J. E., Matthews, J. B., Fisher, J., and Ingham, E., "Effects of Clinically Relevant Alumina Ceramic Wear Particles on TNF- $\alpha$  Production by Human Peripheral Blood Mononuclear Phagocytes," *Biomaterials*, Vol. 24, 2003, pp. 1193–1204.
- [36] Green, T. R., Fisher, J., Matthews, J. B., Stone, M. H., and Ingham, E., "Effect of Size and Dose on Bone Resorption Activity of Macrophages by *in vitro* Clinically Relevant Ultra High Molecular Weight Polyethylene Particles," *J. Biomed. Mater. Res.*, Vol. 53, 2000, pp. 490–497.
- [37] Howling, G. I., Barnett, P. I., Tipper, J. L., Stone, M. H., Fisher, J., and Ingham, E., "Quantitative Characterisation of Polyethylene Debris Isolated from Periprosthetic Tissue in Early Failure Knee Implants and Early and Late Failure Charnley Hip Implants," *J. Biomed. Mater. Res., Part B: Appl. Biomater.*, Vol. 58, 2001, pp. 415–420.
- [38] Green, T. R., Fisher, J., Stone, M. H., Wroblewski, B. M., and Ingham, E., "Polyethylene Particles of a 'Critical Size' are Necessary for Induction of Cytokines by Macrophages *in vitro*," *Biomaterials*, Vol. 19, 1998, pp. 2297–2302.

Yen-Shuo Liao<sup>1</sup> and Mark Hanes<sup>2</sup>

## The Effects of Implant Temperature on Lubricant Protein Precipitation and Polyethylene Wear in Joint Simulation Studies

---

**ABSTRACT:** Implant temperature increases as soon as a wear test starts. Frictional heating is the main reason for the temperature increase. Factors that affect the magnitude of the increase include the thermal conductivity of the implant materials, testing speed, and serum volume of the test chamber. High implant temperature can cause precipitation of soluble proteins in the serum lubricant. The protein precipitates can form a film at the wear interface and may affect laboratory wear evaluation of polyethylene liners. The effects of the implant temperature (of cobalt-chromium and zirconia femoral components) and the amount of protein precipitation from serum lubricant on the wear of UHMWPE liners has been demonstrated in a previous study using an external temperature control device. Furthermore, the nonlinear relationship of the implant temperature and the polyethylene wear has been discussed in another study, using moderately crosslinked UHMWPE liners tested against cobalt-chromium, zirconia, and alumina/zirconia composite femoral components at various temperatures. The results from both studies demonstrated that the temperature around the hip joint implants during a simulation can affect the wear rate of polyethylene. One guideline for minimizing the thermal effects on *in vitro* testing include circulation of coolant at an appropriate temperature to avoid overheating (due to nonstop running of the simulator) thus preventing excessive protein precipitation. This recommendation should help producing wear surfaces and wear debris that are more comparable to *in vivo* outcomes.

**KEYWORDS:** wear simulation, UHMWPE, cobalt-chromium alloy, zirconia, wear debris, lubrication, frictional heating, temperature, protein precipitation

### Introduction

The objective of wear simulation is to evaluate implant performance and predict how the implant will behave under *in vivo* conditions. The ultimate goal in the design of a hip joint simulator and the associated test protocol is to produce the type of wear and the amount of wear that occur clinically. Various hip simulation studies have been conducted using different simulators in different labs to evaluate implant wear performance [1–11], in which various loads, motions, and lubricants [3,12–16] were used. Due to the similar composition of bovine serum and joint fluid, and due to the similar wear morphologies between tested (using serum lubricant) and retrieved implants, investigators have almost universally adopted bovine serum as a lubricant for use in joint simulators. This is also specified as a test condition in the ISO test standard [17].

The loading and kinematic inputs used to simulate human gait are applied during each testing cycle in a hip simulation. However, the continuous testing protocol results in simulations that do not reproduce the intermittent motion that occurs with *in vivo* use. Excessive accumulation of frictional heating at the articulating surface may occur during a nonstop continuous testing protocol. This was reported in a previous study in which polyethylene bearings (GUR 415 UHMWPE) were articulated against balls of alumina, cobalt-chromium, or zirconia [18]. An array of thermocouples were embedded in various locations of the ball-cup assembly to record the temperatures generated during a wear simulation. The prostheses were tested at one cycle per second under a Paul-type, physiological load profile with 2030 N maximum force, with the load cycle synchronized to the motion cycle. The steady state temperatures of the

---

Manuscript received September 15, 2005; accepted for publication March 7, 2006; published online March 2006. Presented at ASTM Symposium on Wear of Articulating Surfaces on November 8, 2005 in Dallas, TX; S. A. Brown, L. N. Gilberston, and V. D. Good, Guest Editors.

<sup>1</sup> Principal Scientist, DePuy Orthopedics, Inc., a Johnson & Johnson Company.

<sup>2</sup> Director of Materials Research, DePuy Orthopaedics, Inc., a Johnson & Johnson Company.

Copyright © 2006 by ASTM International, 100 Barr Harbor Drive, PO Box C700, West Conshohocken, PA 19428-2959.

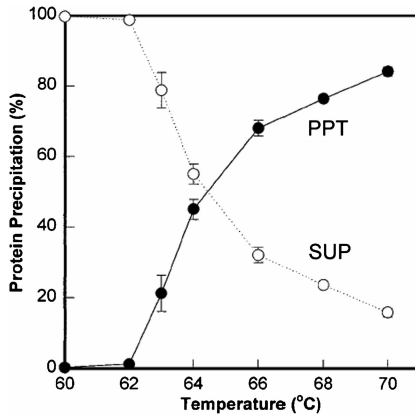


FIG. 1—Serum protein precipitation as a function of temperature [19]. Serum was heated at the indicated temperatures for 4 h and protein precipitates were collected by centrifugation. The protein content of washed precipitates is presented as mg protein per mL of starting serum. The protein content of the supernatant (SUP) and the precipitate (PPT) were added to obtain the total protein of the sample.

bulk lubricant were 33, 36, and 38 °C for the alumina, cobalt-chromium, and zirconia heads, respectively. However, the corresponding surface temperature of the polyethylene, calculated with a finite element model, were 45, 60, and 99 °C for the alumina, cobalt-chromium, and zirconia heads, respectively [18]. The range of surface temperatures resulted in varying amounts of soluble proteins precipitating from the serum lubricant, which affected the wear results [10]. The protein precipitates appeared to be fluffy, yellow clumps adhered to the inside of the acrylic wall of the testing chamber when testing at room temperature.

This review paper summarizes the interaction of temperature on the protein precipitation and wear performance including bearing surface morphology and debris distribution.

### Temperature and Protein Precipitation

A series of experiments were conducted [10] to quantify protein precipitation as a function of temperature and time. Bovine serum was diluted to 90 % by adding sodium azide and EDTA to duplicate the lubricant used in the wear test. Samples of serum were heated in a water bath to 60, 62, 63, 64, 66, 68, or 70 °C for 4 h. The protein content of the precipitates and the remaining proteins in the supernatants were analyzed [10]. A key observation of the heating experiments was that little or no protein precipitation occurred at temperatures below 60 °C. The proteins started to precipitate at temperature above 60 °C (Fig. 1). The amount of precipitation increased markedly with increasing temperature between 62 and 66 °C. At temperatures of 66 and 70 °C, about 60 and 80 % of available proteins were precipitated, respectively (Fig. 1).

To determine how quickly the proteins precipitated when the temperature was high enough to initiate the process, serum samples at concentrations of 20, 40, and 90 % were incubated at 70 °C, and the amount of protein precipitate was measured after 5, 10, 20, 40, 60, and 120 min [10]. The results showed the time-dependent sensitivity of serum proteins to thermal precipitation (Fig. 2). For comparison, the rate of protein precipitation was monitored during a wear test of UHMWPE cups bearing against balls of alumina, cobalt-chromium, and zirconia [10]. Serum samples were analyzed at various test cycles for protein content in the precipitates. Serum proteins precipitated as a function of wear cycles (Fig. 3) and the bulk lubricant temperatures were higher than room temperature for all three materials (i.e., 29, 31, and 35 °C for the cobalt-chromium, alumina, and zirconia, respectively). These results suggested that serum protein precipitation was due to the accumulation of frictional heat at the bearing surfaces in a hip simulator. In addition, the rate of precipitation would depend on the length of time that a particular portion of the lubricant was in close proximity to the high-temperature bearing surfaces.

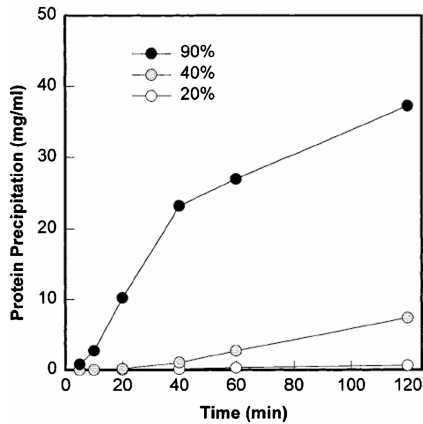


FIG. 2—Serum protein precipitation as a function of incubation time [19]. Three different concentrations of serum (20, 40, and 90 %) were heated at 70°C for various times prior to protein analysis of washed precipitates.

### Protein Precipitation and Wear

To reduce the overheating at bearing surfaces during testing (especially a polyethylene cup bearing against a zirconia ball), one approach was to reduce the cycling speed (e.g., 0.5 Hz). This resulted in a lower serum lubricant temperature but higher polyethylene wear than cycling at 1 Hz, suggesting the protein precipitates might partially shield the bearing surface and reduce polyethylene wear at high cycling speed.

A direct approach without sacrificing testing speed was to control the temperature around the bearings. In a previous study that evaluated wear performance of polyethylene cups (GUR 1050 UHMWPE) against balls of cobalt-chromium and zirconia [19], an external cooling device was used and the stems for the femoral components were modified to allow coolant circulation through the center of the balls at 4°C. Thermocouples were embedded at various locations to measure the temperatures during the test. The amount of protein precipitation and the corresponding wear rates, including the morphology of wear debris were reported (Table 1).

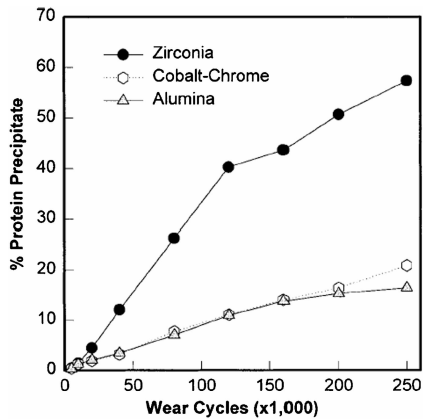


FIG. 3—Lubricant protein precipitation as a function of wear cycles [19]. The standard wear protocol was used with three different femoral component materials bearing against UHMWPE cups. Samples (1 mL) of lubricant were removed and replaced with fresh lubricant at each analysis point. The protein content of washed precipitates is presented as mg protein per mL of starting serum lubricant.

TABLE 1—Summary of results [19].

	Without Cooling		With Cooling (4°C)	
	CoCr/PE	Zirconia/PE	CoCr/PE	Zirconia/PE
Temperature close to the ball surface (°C)	41±5	55±14	8±2	18±3
Temperature of the bulk serum lubricant (°C)	32±3	34±5	9±1	14±2
Reduction in protein concentration due to precipitation	33 %	50 %	15 %	15 %
Average frictional torque (Nm)	2.5	2.5	1.8	2.1
Wear rate (mg/million cycles)	36.9±2.3	19.1±0.5	24.5±3.3	32.9±9.5
Surface morphology of the UHMWPE cup	Polished	Polished	Textured	Textured
Composition of wear debris (granules vs. fibrils)	Granule (80 %)	Granule (70 %)	Fibrils (60 %)	Fibrils (80 %)

Without cooling, the wear of polyethylene against zirconia was about 48 % lower than with cobalt-chromium alloy, but the steady state temperature of the zirconia ball was higher (55°C versus 41°C, measured at 0.5 mm to the apex of the ball), and there was more protein precipitation from the serum, which sometimes formed an adherent layer on the surface of the zirconia. With cooling at 4°C, wear of the polyethylene against cobalt-chromium was about 26 % lower than against zirconia, but the macroscopic and microscopic appearance of the worn polyethylene surfaces were unlike that typically generated *in vivo*. The morphology of the polyethylene debris was similar to that generated *in vivo* with or without cooling. However, the ratio of fibrillar to granular debris was reversed at the two cooling conditions (Table 1).

**Temperature and Wear**

In another study [20], the effect of the temperature on polyethylene wear was reported. The wear of moderately crosslinked polyethylene cups (GUR 1020 UHMWPE subjected to gamma irradiation at 40 kGy in a vacuum foil bag) against balls of cobalt-chromium, zirconia, and alumina/zirconia composite was evaluated. A temperature control unit was utilized to allow direct cooling/heating the center of the balls at 4, 20, 37, and 45°C in addition to the conventional no temperature control method. Results showed that the polyethylene wear was affected nonlinearly by the coolant temperature (Fig. 4). The wear generated by articulation against a cobalt-chromium alloy was similar to that generated by an alumina/zirconia composite without temperature control. However, the cobalt-chromium alloy generated 50 % more wear than the alumina/zirconia composite did when the coolant temperature was above 20°C. The results

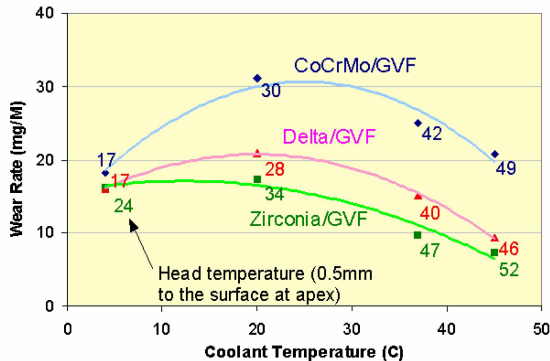


FIG. 4—Wear rates of polyethylene cups as a function of coolant temperature [20]. This study evaluated the wear performance of cobalt-chromium, zirconia, and alumina/zirconia composite (Delta) heads against moderately crosslinked ultra-high-molecular-weight polyethylene liners (GVF) under different temperature conditions. A temperature control unit was utilized to allow direct cooling/heating the center of the ball components at 4, 20, 37, and 45°C in addition to the conventional no temperature control method. Results showed that the polyethylene wear was affected by the coolant temperature. The temperatures of the femoral balls (0.5 mm to the apex) were showed as footnotes with each data point.

suggested that the composite material would have better *in vivo* wear performance than the cobalt-chromium alloy because the human body is maintained at a constant temperature (37°C). The zirconia ball generated the lowest wear rate of the three groups in all temperature conditions (Fig. 4).

The fact that the head temperature was higher than the coolant temperature suggested that frictional heating occurred at the wear surface (Fig. 4). The circulated coolant actively dissipated some of the frictional heat from the center of the balls. A low thermal conductivity, i.e., less ability to conduct heat, caused the zirconia ball to have the highest head temperature in the three groups of testing materials. Similar to the previous study [19], the elevated temperature at the interface would cause certain proteins to precipitate from the serum lubricant. Consequently, the precipitated proteins acted as an enhanced lubrication that protected the polyethylene cups and resulted in low wear with the zirconia balls. Similarly, wear reduction occurred in all three groups when circulating serum at high temperature (45°C) due to the extra heat-induced protein precipitation (Fig. 4).

It was unanticipated that all three groups would have a similar lower wear when the coolant temperature was very low (4°C). The results suggest that low wear implants might be achieved if a low interface temperature could be maintained [20].

When the coolant was controlled at 4°C, the bearing surface temperatures were cooled to 24°C for the zirconia balls, and 17°C for both cobalt-chrome alloy and alumina/zirconia composite (Fig. 4). The amount of protein precipitation was reduced but still exists at such low temperature. The fact that protein precipitation still occurred may be due to the flash temperatures at the contacting asperities might be high enough (higher than 60°C) to initiate protein precipitation in the nearby lubricant, but too short in duration to be detected by the thermocouple embedded 0.5 mm below the surface [18]. Alternatively, factors other than heat may have contributed to protein precipitation; these may include high pressure or shear force, or both between the ball and cup [19].

Although the coolant temperatures of 4 and 45°C are nonphysiological, it provided two extreme conditions to assess the effect of the temperature on the wear performance of the joint implants. The studies [19,20] suggested that lubricant be held at a temperature that might cause the interface temperature to approximate physiologic temperature. Further study is required for maintaining the interface temperature in a reasonable range by adjusting coolant temperature.

## Conclusion

Unlike the continuous cycling of a hip simulation, neither normal persons nor patients with prosthetic joints typically walk continuously without stopping, sometimes resting for several hours, during which the temperatures of the bearings and joint fluid return to the ambient 37°C. Thus, it is likely that the maximum temperatures of the bearing surfaces and adjacent lubricant are much lower *in vivo*, with the possible exception of extended activities, such as marathon running. Therefore, the effects of thermally induced protein precipitation observed in a joint simulator should be considered a potential artifact.

Factors for overheating at bearing surfaces include testing speed, bearing material properties (e.g., friction coefficient, thermal conductivity, etc.), chamber size (serum volume), and ambient temperature.

Controlling the bearing temperature within a desired range is recommended for hip simulations involving materials that tend to accumulate frictional heat. Forced cooling is one of the approaches to compensate for this overheating at the bearing surfaces.

## References

- [1] Simon, S. R., and Radin, E. L., "Lubrication and Wear of the Charnley, Charnley-Muller, and McKee-Farrar Prostheses with Special Regard to their Clinical Behavior," *Proceedings of the First Open Scientific Meeting of the Hip Society: The Hip*, St. Louis, 1973.
- [2] Dowson, D., and Harding, R. T., "The Wear Characteristics of Ultrahigh Molecular Weight Polyethylene Against a High Density Alumina Ceramic Under Wet (Distilled Water) and Dry Conditions," *Wear*, Vol. 75, 1982, pp. 313-331.
- [3] Kumar, P. et al., "Low Wear Rate of UHMWPE Against Zirconia Ceramic (Y-PSZ) in comparison to Alumina Ceramic and SUS 316L Alloy," *J. Biomed. Mater. Res.*, 25, 1991, pp. 813-828.
- [4] Mejia, L. C., and Brierley, T. J., "A Hip Wear Simulator for the Evaluation of Biomaterials in Hip

- Arthroplasty Components," *Biomed. Mater. Eng.*, Vol. 4, No. 4, 1994, pp. 259–271.
- [5] McKellop, H. A. et al., "The Origin of Submicron Polyethylene Wear Debris in Total Hip Arthroplasty," *Clin. Orthop.*, Vol. 311, 1995, pp. 3–20.
- [6] Bragdon, C. R., O'Connor, D. O., Lowenstein, J. D., Jasty, M., and Syniuta, W. D., "The Importance of Multidirectional Motion on the Wear of Polyethylene," *Proceedings, Institution of Mechanical Engineers*, Vol. 210, No. 3, 1996, pp. 157–165.
- [7] Saikko, V. O., "A Three-Axis Hip Joint Simulator for Wear and Friction Studies on Total Hip Prostheses," *Proceedings, Institution of Mechanical Engineers*, Vol. 210, No. 3, 1996, pp. 175–185.
- [8] Bigsby, R. J. A., Hardaker, C. S., and Fisher, J., "Wear of Ultra-High Molecular Weight Polyethylene Acetabular Cups in a Physiological Hip Joint Simulator in the Anatomical Position Using Bovine Serum as a Lubricant," *Proceedings, Institution of Mechanical Engineers*, Vol. 211, 1997, pp. 265–269.
- [9] Wang, A., Polineni, V. K., Essner, A., Stark, C., and Dumbleton, J. H., "Effect of Head/Cup Clearance on the Wear of UHMWPE in Total Hip Replacement," *24th Annual Meeting on the Society for Biomaterials*, San Diego, CA, April 22–26, (1998).
- [10] Liao, Y.-S., Benya, P., and McKellop, H., "Effect of Protein Lubrication on the Wear Properties of Materials for Prosthetic Joints," *J. Biomed. Mater. Res.*, Vol. 48, No. 4, 1999, pp. 465–473.
- [11] Barbour, P. S. M., Stone, M. H., and Fisher, J., "A Hip Joint Simulator Study Using New and Physiologically Scratched Femoral Heads with Ultra-high Molecular Weight Polyethylene Acetabular Cups," *Proceedings of the Institution of Mechanical Engineers, Part H: Journal of Engineering in Medicine*, Vol. 214, No. 6, 2000, pp. 569–576.
- [12] McKellop, H., Clarke, I. C., Markolf, K., and Amstutz, H., "Wear Characteristics of UHMW Polyethylene: A Method for Accurately Measuring Extremely Low Wear Rates," *J. Biomed. Mater. Res.*, Vol. 12, 1978, pp. 895–927.
- [13] Roberts, B. J., Unsworth, A., and Mian, N., "Modes of Lubrication in Human Hip Joints," *Ann. Rheum. Dis.*, Vol. 41, 1982, pp. 217–224.
- [14] Good, V. D., Clarke, I. C., and Anissian, L., "Water and Bovine-Serum Lubrication Compared in Simulator PTFE/CoCr Wear Model," *J. Biomed. Mater. Res.* Vol. 33, 1996, pp. 275–283.
- [15] Saikko, V., and Ahlroos, T., "Phospholipids as Boundary Lubricants in Wear Tests of Prosthetic Joint Materials," *The 7th Nodic Symposium on Tribology* [Preprints from the 7th Nordic Symposium on Tribology, NORTRIB' 96], Bergen, Norway, June 16th–19th, 1996.
- [16] Wang, A., Polineni, V. K., Essner, A., Stark, C., and Dumbleton, J. H., "Role of Proteins and Hyaluronic Acid in the Lubrication and Wear of UHMWPE Aetabular Cups," *24th Annual Meeting of the Society for Biomaterials*, San Diego, April 22–26, 1998.
- [17] *ISO: 14242-1: Implants for Surgery—Wear of Total Hip Joint Prostheses—Part 1: Loading and Displacement Parameters for Wear-Testing Machines and Corresponding Environmental Conditions for Test*, 2002.
- [18] Lu, Z., and McKellop, H., "Frictional Heating of Bearing Materials Tested in a Hip Joint Wear Simulator," *Proceedings, Institution of Mechanical Engineers*, Vol. 211, 1997, pp. 101–108.
- [19] Liao, Y.-S., McKellop, H., Lu, Z., Campbell, P., and Benya, P., "The Effect of Frictional Heating and Forced Cooling on the Serum Lubricant and Wear of UHMW Polyethylene Cups Against Cobalt-Chromium," Vol. 24, No. 18, 2003, pp. 3047–3059.
- [20] Liao, Y.-S., Hanes, M., Fryman, J. C., and DiSilvestro, M., "Phase Stability of Zirconia and Alumina/Zirconia Composite Heads Against UHMWPE Liners in a Temperature-Controlled Hip Simulation Study," *Bioceramics*, New Orleans, LA, December 8–11, 2004.

Thorsten Schwenke,<sup>1</sup> Erich Schneider,<sup>2</sup> and Markus A. Wimmer<sup>1</sup>

## Load Profile and Fluid Composition Influence the Soak Behavior of UHMWPE Implants

**ABSTRACT:** Wear of total joint replacements is determined gravimetrically in simulator studies. A mix of bovine serum, distilled water, and additives is intended to replicate the lubrication conditions in vivo. Load soak stations are used to correct for weight gain due to fluid absorption. Although the implementation of a soak station is considered only as an option for wear testing, this study indicated that fluid absorption depends on the lubricant composition as well as on the applied load profile. Two different fluid recipes were tested with three load scenarios each. Standard ultra-high molecular weight polyethylene (UHMWPE) pins acted against commercially available ceramic hip balls. Dynamic (0 to 1000 N), static (1000 N), and no load were applied for 23.1 days (or  $2 \cdot 10^6$  cycles). Both lubricant recipes based on the same mix of deionized water and newborn calf serum (final protein content: 30 g/L), and differed in the chemicals admixed to the fluid to minimize bacterial growths and to prevent protein precipitation. After test completion, the group of samples tested in fluid B gained 2.4-, 3.6-, and 4.2-fold the weight of samples submersed in fluid A for the dynamically, statically, and unloaded samples, respectively. The specimens showed a significantly higher weight gain under dynamic load than subjected to static or no load for both fluids. The results of this study suggest the implementation of a load-soak control station for every wear test when UHMWPE materials are examined.

**KEYWORDS:** test lubricant, fluid absorption, joint simulator, soak control, wear

### Introduction

Wear testing of medical implants, such as artificial knee, hip, and spinal disc replacements, is an integral part of development and certification procedures, as well as of later performance evaluations. Such testing is typically performed on multistation, multidegrees-of-freedom simulator devices which mimic the joint specific load and motion. One of the great challenges with these wear tests is the simulation of the biological environment, since the testing environment has to closely replicate in vivo conditions in order to generate clinically relevant results. The practical inability to harvest synovial fluid in sufficient amounts calls for the use of an alternative testing fluid.

Distilled water alone does not suffice to recreate in vivo conditions in artificial bearings [1–5]. Simulator wear rates differed significantly compared to what has been reported in vivo. The wear pattern and particle morphology deviated, a clear indication for an altered wear mechanism between the bodies in contact [6–8]. Bovine serum was introduced due to its similarities to human synovial fluid with regard to proteins and other organic as well as anorganic constituents, and is still the basis for most lubricants today [9]. However, varying protein levels and composition ratios (albumin versus globulin) have been suggested by different laboratories and impact the wear rates of polyethylene [1,10–15]. In addition, different additives have been used to stabilize the lubricant and minimize protein degeneration [10,16]. Buffer chemicals like Tris (tris-hydroxymethyl-aminomethan) have been added to keep the pH value of the serum constant and to minimize precipitation of phosphates [17]. Others used Ethylenediaminetetraacetic Acid (EDTA) to bind calcium and magnesium preventing potentially detrimental third body effects from metal ion sulfates [18]. Antimicrobials, antibiotics, as well as sodium azide have been admixed to keep bacterial contamination minimal [10,16], since a typical test period lasts 0.5 million cycles, i.e., nearly full six days (at a 1 Hz frequency) in a nonsterile environment. Alternatively, chemicals like phenoxetol (1-phenol-2-

Manuscript received January 13, 2006; accepted for publication April 19, 2006; published online June 2006. Presented at ASTM Symposium on Wear of Articulating Surfaces in Dallas, TX on 8 November 2005; S. A. Brown, L. N. Gilbertson, and V. D. Good, Guest Editors.

<sup>1</sup> Tribology, Department of Orthopedic Surgery, Rush University Medical Center, Chicago, IL, USA.

<sup>2</sup> AO Research Institute, Davos, Switzerland.

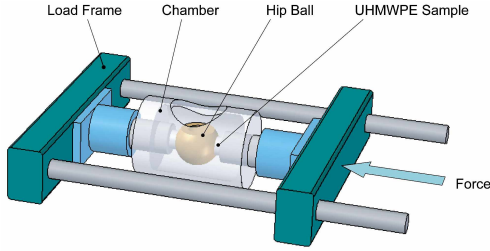


FIG. 1—Pin-on-Ball simulator concept: The two pins are pressed against the hip ball with identical loads. Polyethylene samples, ball, and fixtures are submersed in testing fluid and heated with external warming foils to body temperature.

propanol) have been used by research groups to retard bacterial growth and to avoid handling of hazardous chemicals like sodium azide [16]. The effects of the various additives on fluid soak on wear outcome are unknown. However, it has become apparent that changes in the additive composition of the lubricant impact the test results of standard tests conform to ISO and ASTM standards [19].

Wear of artificial implants is typically assessed using gravimetric techniques where the weight loss of implant components after thorough cleaning and drying is equated with the material loss due to wear. Plastic implant materials such as ultra-high molecular weight polyethylene (UHMWPE) and its recently established highly cross-linked version, however, have been found to absorb fluid while being exposed to a fluidal environment during testing. Thus, implant components, especially those with comparatively low wear rates might even gain weight during testing. To correct for the fluid soak effect, control stations with compressive loads only are run in parallel and their weight gain is subtracted from the weight of the wear implants at each measurement interval. While the use of a load-soak control station is highly recommended, not every simulator setup is equipped with such a station. At the same time, thorough soaking of implants prior to testing to assume full saturation is not sufficient. Previous studies indicated that the change in loading scenario between presoaking and testing influences the weight gain due to fluid absorption of UHMWPE samples [19].

The present study investigates confounding factors during fluid soak; in particular whether lubricant additives and loading protocol affect the soak behavior of polyethylene. It is hypothesized that the fluid soak behavior of UHMWPE samples is dependent on the lubricant composition as well as the loading scenario.

**Materials and Methods**

Cylindrical pins with a 12 mm radius and 12 mm length have been used for this study. The pins were flat on one and concave on the other end. They were turned from commercially available GUR 1050. The concave end was machined to fit with a ceramic hip ball (diameter: 28 mm) on a pin-on-ball wear testing device [20]. The test apparatus consists of six stations; each station comprises a test frame with pneumatic cylinder for load application and a temperature controlled chamber (Fig. 1). By having two pins symmetrically loaded against the ceramic ball, both pins experience the same force. A computer controlled pneumatic valve applies different loading patterns to the stations. No motions were applied in this study.

Two testing fluids were examined. Their detailed compositions can be found in Table 1. Each fluid was conforming to the applicable testing standards for artificial joint testing [21,22]. They were based on a mix of deionized water and new-born calf serum (Hyclone, Inc., Logan, UT) with a factory protein content of

TABLE 1—Compositions of the two testing fluids. The hydrochloric acid in fluid B was used to set the pH value to 7.4. The pH value of fluid A was not controlled.

	Base	Serum	Additives
Fluid A	Deionized		EDTA (200 mg/L)
Fluid B	Water	Bovine Calf	NaCl (9 g/L), Phenoxetol (15 ml/L), Tris (27 g/L), HCl (~55 ml)

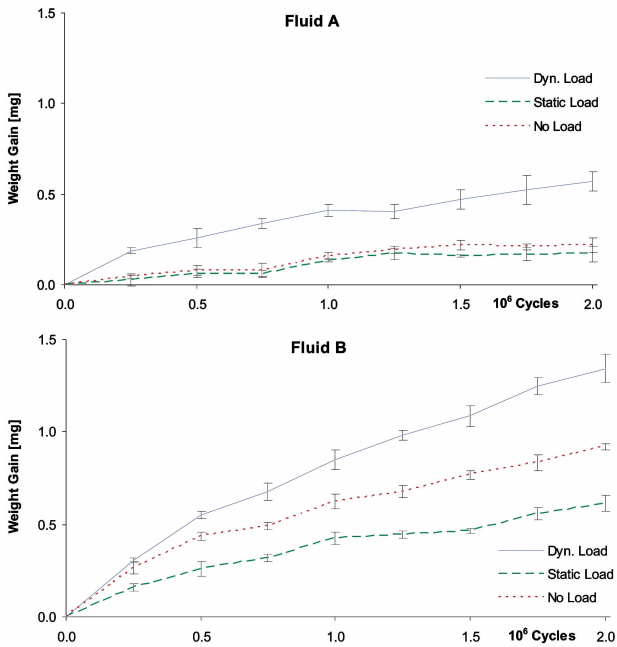


FIG. 2—Average weight gain and standard deviation for the six sample groups.

58 g/L. The fluids were set to a final protein content of 30 g/L. Different additives were admixed to each fluid that have been used for a variety of research studies previously [23]. Each chamber contained 80 ml of testing fluid.

Three loading scenarios were applied to a sample group of four pins each. Every pin was mounted in a sample holder and submersed in fluid at  $37^{\circ}\text{C} \pm 1^{\circ}\text{C}$ . The first group of specimens was not subjected to any load and only manually brought into contact with the balls. A constant load of 1000 N was applied to the specimens of group two. Specimens of group three were subjected to a saw tooth shaped loading profile alternating from 0 to 1000 N at 1 Hz cycle frequency. Each test lasted for  $2 \cdot 10^6$  cycles (or the equivalent of 23.1 days). The experiments were stopped to clean, weigh, and dry each specimen according to ASTM Standard F 732 every 250 k cycles or 2.9 days. Specimens were weighed, remounted onto the test apparatus, and the chambers were filled with fresh lubricant. Specimens were microscopically inspected (5x, Nikon, Inc., Melville, NY) to look for morphological changes of the surfaces, adhering particles, and discoloration. Independent-samples T tests were performed to test for significant differences between weight measurements at two million cycles. The significance level was chosen to  $p=0.05$ .

## Results

Significant differences in fluid uptake between lubricants were observed. Samples submersed in fluid A experienced a lower weight gain than those tested in fluid B, comparing samples tested under the same loading scenario (Fig. 2;  $p < 0.01$ ).

Comparing loading scenarios within the same fluid, again differences were observed in the fluid absorption of the pins. Specimens that were dynamically loaded experienced a 3.4- and 2.2-fold higher weight gain for fluids A and B, respectively, than the samples that were exposed to a constant load ( $p < 0.01$ ). No statistically significant difference was found between nonloaded and statically loaded samples for fluid A ( $p=0.15$ ). Surprisingly, in fluid B, the nonloaded specimens experienced a 1.5-fold higher weight increase compared to the statically loaded samples, once again statistically significant ( $p < 0.01$ ).

The microscopic analysis of the pins revealed no change in surface structure or adhering particles that might have lead to weight changes.

### Discussion

The fluid uptake of standard UHMWPE samples was dependent on the admixed additives as well as the applied load regimen. Dynamic loading significantly increases fluid uptake. The differences in weight gain are of concern because they introduce a systematic error into the measurement of wear. It is extremely difficult, if not impossible, to replicate the loading conditions of a moving joint in a “resting” control station. A considerable portion of the contact force arises due to friction while moving. Further, the compressive force vector does not stand still in a moving joint but describes a trajectory of variable size during each loading cycle. Although unknown, it is conceivable that the addition of shear, as well as the changing contact location will further increase the weight gain of the UHMWPE. This additional weight gain can easily mask the material loss due to wear as seen in the previous studies using cross-linked polyethylene [24].

Surprisingly, “no load” resulted in a higher weight gain than “static load.” While this phenomenon was only statistically significant for fluid B, it may be best explained with the available surface area for fluid uptake. Under static compressive loads the fluid transport to the contacting pin surfaces was reduced. Hence, the available area for fluid absorption was also decreased.

Although it was expected to see variations in fluid uptake dependent on loading protocol, the huge differences dependent on fluid recipe were not anticipated. Here, fluid B differs from fluid A most likely due to the addition of phenoxetol. It is used as an antimicrobial agent in skin care products. In the respective safety sheets it is classified as harmful (but not toxic). Historically, it was therefore chosen as a replacement for sodium azide which is not only extremely toxic but also explosively reactive and very dangerous to handle inside a laboratory. As a long chain glycoether, also used as a degreasing agent, it is believed to interact with UHMWPE’s ability to bin fluid. More detailed studies are necessary to proof this mechanism.

### Conclusion

In summary, the results of the study indicate a complex interplay of fluid additives on the soak behavior of UHMWPE. The loading scenario plays an important role as well. The implementation of a load-soak control stations for wear testing of UHMWPE materials is therefore suggested.

### Acknowledgment

The authors would like to thank Dr. Rieker of Zimmer Switzerland GmbH for his support in this study.

### References

- [1] Yao, J. Q., Laurent, M. P., Johnson, T. S., Blanchard, C. R., and Crowninshield, R. D., “The Influences of Lubricant and Material on Polymer/CoCr Sliding Friction,” in *Trans Wear of Materials*, 2003, Washington, DC.
- [2] Good, V. D., Clarke, I. C., and Anissian, L., “Water and Bovine Serum Lubrication Compared in Simulator PTFE/CoCr Wear Model,” *J. Biomed. Mater. Res.*, Vol. 33, No. 4, 1996, pp. 275–283.
- [3] McKellop, H., Clarke, I. C., Markolf, K. L., and Amstutz, H. C., “Wear Characteristics of UHMW Polyethylene: A Method for Accurately Measuring Extremely Low Wear Rates,” *J. Biomed. Mater. Res.*, Vol. 12, No. 6, 1978, pp. 895–927.
- [4] Clarke, I. C., Starkebaum, W., Hosseinian, A., McGuire, P., Okuda, R., Salovey, R., and Young, R., “Fluid-Sorption Phenomena in Sterilized Polyethylene Acetabular Prostheses,” *Biomaterials*, Vol. 6, No. 3, 1985, pp. 184–188.
- [5] Good, V. D., Clarke, I. C., Gustafson, G. A., Downs, B., Anissian, L., and Sorensen, K., “Wear of Ultra-High Molecular Weight Polyethylene and Polytetrafluoroethylene in a Hip Simulator: A Dose-response Study of Protein Concentration,” *Acta Orthop. Scand.*, Vol. 71, No. 4, 2000, pp. 365–369.
- [6] Bell, J., Besong, A. A., Tipper, J. L., Ingham, E., Wroblewski, B. M., Stone, M. H., and Fisher, J.,

- "Influence of Gelatin and Bovine Serum Lubricants on Ultra-High Molecular Weight Polyethylene Wear Debris Generated in In Vitro Simulations," *Proc. Inst. Mech. Eng., Part H: J. Eng. Med.* Vol. 214, No. 5, 2000 pp. 513–518.
- [7] Besong, A. A., Tipper, J. L., Mathews, B. J., Ingham, E., Stone, M. H., and Fisher, J., "The Influence of Lubricant on the Morphology of Ultra-High Molecular Weight Polyethylene Wear Debris Generated in Laboratory Tests," *Proc. Inst. Mech. Eng., Part H: J. Eng. Med.* Vol. 213, No. 2, 1999, pp. 155–158.
- [8] Liao, Y-S, McNulty, D., and Hanes, M., "Wear Rate and Surface Morphology of UHMWPE Cups are Affected by the Serum Lubricant Concentration in a Hip Simulator Test," *Trans Wear of Materials*, 2003, Washington, DC.
- [9] Scales, J. T., and Winter, G. D., "Clinical Consideration in the Choice of Materials for Orthopedic Internal Prostheses," *J. Biomed. Mater. Res.*, Vol. 9, No. 4, 1975, pp. 167–176.
- [10] Clarke, I. C., Chan, F. W., Eisner, A., Good, V., Kaddick, C., Lappalainen, R., Laurent, M., McKellop, H., McGarry, W., and Schroeder, D., "Multi-Laboratory Simulator Studies on Effects of Serum Proteins on PTFE Cup Wear," *Wear*, Vol. 250, No. 1–12, 2001, pp. 188–198.
- [11] Tanner, S., DesJardins, J., Pace, T. B., Winbrenner, D., LaBerge, M., "Development of a Clinically Relevant TKR Simulation Test Lubricant," *Trans Soc. Biomat., 29th Annual Meeting*, 2003. Reno, NV.
- [12] Wang, A., Polineni, V. K., Essner, A., Stark, C., and Dumbleton, J. H., "Role of Proteins and Hyaluronic Acid in the Lubrication and Wear of UHMWPE Acetabular Cups," *Trans Soc. Biomat., 24th Annual Meeting*, 1998, San Diego, CA.
- [13] Wang, A., Schmidig, G., Essner, A., and Serekian, P., "Effect of Lubricant Protein Composition On The Outcome Of Hip Joint Simulator Testing," *Trans Orthopaedic Research Society, 46th Annual Meeting*, 2000, Orlando, FL.
- [14] Yao, J. Q., Laurent, M. P., Gilbertson, L. N., Blanchard, C. R., Crowninshield, R. D., and Jacobs, J. J., "A Comparison of Biological Lubricants to Bovine Calf Serum for Total Joint Wear Testing," *Trans Orthopaedic Research Society, 48th Annual Meeting*, 2002, Dallas, TX.
- [15] Noordin, S., Schmalzried, T. P., Campbell, P., and Amstutz, H. C., "Synovial Fluid From Patients With Prosthetic Joint Arthroplasty: Protein Concentration and In Vivo Wear of Polyethylene," *Trans Orthopaedic Research Society, 43rd Annual Meeting*, 1997, San Francisco, CA.
- [16] Shen, M., Norris, J., and Rieker, J., "Serum Effect on Wear of UHMWPE Tibial Insert in Knee Simulator Testing," *Trans Society for Biomaterials, 29th Annual Meeting*, 2003, Reno, NV.
- [17] Streicher, R. M., Semlitsch, M., Schon, R., Weber, H., and Rieker, C., "Metal-On-Metal Articulation for Artificial Hip Joints: Laboratory Study and Clinical Results," *Proc. Inst. Mech. Eng., Part H: J. Eng. Med.*, Vol. 210, No. 3, 1996, pp. 223–232.
- [18] McKellop, H., Lu, B., and Benya, P., "Friction, Lubrication and Wear of Cobalt-Chromium, Alumina and Zirconia Hip Prostheses on a Joint Simulator," *Trans World Biomaterials Congress*, 1992, Berlin, Germany.
- [19] Schwenke, T., Kaddick, C., Schneider, E., and Wimmer, M. A., "Fluid Composition Impacts Standardized Testing Protocols in Ultra-High Molecular Weight Polyethylene Knee Wear Testing," *Proc. Inst. Mech. Eng., Part H: J. Eng. Med.*, Vol. 219, 2005, pp. 457–464.
- [20] Nassutt, R., Wimmer, M. A., Schneider, E., and Morlock, M. M., "The Influence of Resting Periods on Friction in the Artificial Hip," *Clin. Orthop.*, Vol. 407, 2003, pp. 127–138.
- [21] ISO 14242, "Implants for Surgery—Wear of Total Hip-Joint Prostheses," International Standard, 2001, Geneva, Switzerland.
- [22] ISO 14243, "Implants for Surgery—Wear of Total Knee-Joint Prostheses," International Standard, 2004, Geneva, Switzerland.
- [23] Rieker, C. B., Schoen, R., Liebentritt, G., Gnepf, P., Desjardins, J., and LaBerge, M., "The Influence of Mobile Bearing Knee Prostheses Kinematics on Their Wear Behavior," *Trans World Biomaterials Congress*, 2004, Vol. 1129, Sydney, Australia.
- [24] Muratoglu, O. K., Bragdon, C. R., O'Connor, D. O., Jasty, M., and Harris, W. H., "A Novel Method of Cross-Linking Ultra-High-Molecular-Weight Polyethylene to Improve Wear, Reduce Oxidation, and Retain Mechanical Properties. Recipient of the 1999 HAP Paul Award," *J. Arthroplasty*, Vol. 16, No. 2, 2001, pp. 149–160.

Yen-Shuo Liao<sup>1</sup> and Mark Hanes<sup>1</sup>

## The Effects of Load Soak Control on the Wear of UHMWPE at Various Hydration Levels in a Joint Simulation Study

**ABSTRACT:** The study was to investigate the effects of various hydration levels on the wear of ultra-high molecular weight polyethylene (UHMWPE) in a hip simulation testing, and to assess the effect of load soak control on the implant wear rates. Three types of polyethylene liners (28 mm ID) made from GUR 1050 UHMWPE bars were evaluated: noncrosslinked (XL0), gamma irradiated (thermally-treated) at nominal doses of 5 and 10 Mrads (XL5 and XL10, respectively). Three hydration processes were applied: (1) presoaked in water for four weeks, i.e., standard protocol; (2) exposed in air for four weeks; and (3) presoaked in water at 900 psi (approximately 60 atm) in a pressurized chamber for three weeks. Six groups of interest were selected and tested on a hip simulator with load soak control stations. The group that was subjected to 900 psi pressure gained  $11.9 \pm 0.4$  mg of water after three weeks, which was about eight times the groups that presoaked in water. After the wear simulation started, the highly hydrated group lost almost 10 mg during the first 0.5-million cycle interval, which was due to the pumping motion of the load soak stations. All soak control liners achieved similar hydration levels after one million cycles of testing. The overall wear rating was inversely related to the amount of crosslinking. Without load soak correction, the initial wear rate of XL5 with pressurized soaking was twice the corrected wear; however, the wear rate remained similar after one million cycles with or without corrections.

**KEYWORDS:** wear simulation, UHMWPE, load soak control, hydration levels

### Introduction

Components made from low-wear polymers such as highly crosslinked, ultra-high molecular weight polyethylene (UHMWPE) without presoaking may show a net increase in weight during the initial wear intervals due to fluid sorption [1]. Presoaking the polyethylene components before a wear test may reduce fluid sorption of the components during a wear simulation [2]. However, a surgeon does not presoak liners prior to operation. The polyethylene liners are directly implanted into a patient right after the packages are opened. The difference in presoaking and nonsoaking protocol raises concerns on whether the hydration level will affect in vitro polyethylene wear and the degree of resemblance in the wear surfaces between laboratory hip simulation and clinically retrieved components. Additionally, the hydration level that results from an in vivo exposure that may exceed 20 years is unknown. If this results in an elevated hydration level, the effect on the wear behavior is unknown.

Another issue in wear testing is whether it is necessary to use a load soak control to correct fluid sorption of the implants during testing. Compared to conventional soak controls, where test components are simply immersed in the test lubricant without loading, the load soak control components are subjected to the same loading conditions as experienced by the components on the wear test stations but without motion (therefore, no wear will occur). The wear of the tested components were determined by the weight loss of each component at the time of weighing, corrected by the average weight gain of the control components due to the fluid absorption. This is critical in the weight loss calculation, as the repeated loading may affect the fluid sorption of both of the test and control components.

Previous studies showed conflicting results on how hydration affected the wear of polyethylene. One study showed that longer periods of presoaking reduced polyethylene wear [3]. However, this study did not report the weight gain after various hydration periods and did not utilize load soak controls. Another

---

Manuscript received September 15, 2005; accepted for publication June 28, 2006; published online August 2006. Presented at ASTM Symposium on Wear of Articulating Surfaces on 8 November 2005 in Dallas, TX; S. A. Brown, L. N. Gilbertson, and V. D. Good, Guest Editors.

<sup>1</sup> Principal Scientist and Director of Materials Research, respectively, DePuy Orthopedics, Inc., a Johnson & Johnson Company.

TABLE 1—Material and summary of test groups.

Gamma-Irradiated and Thermally-Treated	Sterilization Method	Material ID	Pre-Soak Conditions	Group ID
0 Mrad (non-crosslinked)	Gas plasma	XL0	Water (4 weeks)	A
			No water (4 weeks)	B
5 Mrad	Gas plasma	XL5	Water (4 weeks)	C
			No water (4 weeks)	D
10 Mrad	Gas plasma	XL10	Pressurized (900 psi for 3 weeks)	E
			No water (4 weeks)	F

study demonstrated increased polyethylene wear with higher hydration [4]. However, in this test a constant load was applied and the test was performed on pin-on-disk equipment, in which the geometry and kinematics were different than those of the ball-socket configuration in a hip simulator.

The purpose of this study was to investigate the effects of various hydration levels on the wear of UHMWPE components in a hip simulation test. The effect of load soak control on the final implant wear rates was also analyzed.

### Materials and Methods

Three polyethylene materials were produced by the following methods. Extruded bars of GUR 1050 UHMW polyethylene (Poly Hi, Ft. Wayne, IN) were vacuum packaged in foil bags and subjected to gamma irradiation (Steris Isomedix, Whippany, NJ) at nominal doses of 5 and 10 Mrads (labeled as XL5 and XL10, respectively). After irradiation, all bars were remelted to extinguish free radicals. The bars were then cooled to room temperature and machined into acetabular liners (28 mm ID). Noncrosslinked polyethylene liners (XL0) were machined directly from GUR 1050 bars. Final sterilization was by gas plasma.

Three hydration processes were applied: (1) presoaking in water for four weeks (standard test protocol), which was widely accepted in most labs; (2) exposure to air for four weeks (control group), which was to simulate the surgeon protocol; and (3) presoak in water at 900 psi (approximately 60 atm) in a pressurized chamber for three weeks. The high pressure was to induce the maximum fluid absorption of the polyethylene components to simulate the long-term soaking effect, and this value was the capacity of the pressure chamber in our lab. All were performed at room temperature. The weight of each liner was measured before and after each hydration process to determine the amount of hydration.

The wear test matrix is shown in Table 1 ( $N=2$  for each group). Due to the limited number of test stations ( $N=12$ ), only the groups of interest were tested in this study.

The liners were placed in metal shells and run against 28 mm CoCr heads (DePuy, Warsaw, IN) at 1 Hz on a 12-station OBM type simulator (Shore Western, Monrovia, CA) synchronized with a Paul-type hip load curve with a peak force of 2000 Newtons. The components were lubricated with 90 % bovine serum (HyClone, UT) resulting in a protein concentration of 63 mg/mL with 0.2 %  $\text{NaN}_3$  and 20 mM EDTA added. The serum volume was 160 mL and was changed every 250 K cycles.

To determine wear, the liners were removed from the simulator every half-million cycles, cleaned ultrasonically, vacuum dried, and weighed on a high precision analytical balance (Mettler, Toledo, OH). The absorption of fluid by a worn liner was corrected for by increasing its measured weight loss by the mean weight gain of two cyclically loaded but nonoscillated soak-controlled liners of the same material. The wear rate (mg/million cycles) was calculated by the slope of the linear regression line through the measured weight loss data. The test was performed for three million cycles.

### Results

The group that was subjected to 900 psi pressure (E) gained  $11.9 \pm 0.4$  mg of water after three weeks, which was about eight times the groups that were presoaked in water (A and C) for four weeks (Fig. 1), where Group A gained  $1.5 \pm 0.1$  and Group C gained  $1.3 \pm 0.1$  mg, respectively. The groups that were exposed to air (B, D, and F) gained no more than 0.5 mg (Fig. 1), which may be due to the influence of moisture in the air.

After the wear simulation started, the highly hydrated group (E) lost almost 10 mg during the first 0.5-million cycle interval, which was due to the repeated loading that expelled the absorbed water (Fig. 2).

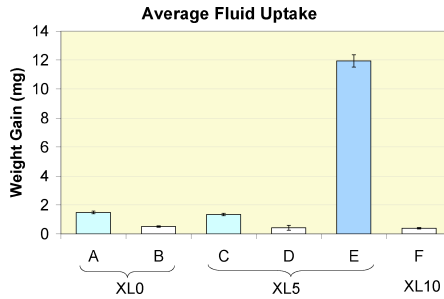


FIG. 1—The averaged weight change for each group after various hydration processes. The three material groups were: noncrosslinked polyethylene (XL0), gamma-irradiated (at 5 Mrad) thermally-treated polyethylene (XL5), and gamma-irradiated (at 10 Mrad) thermally-treated polyethylene (XL10).

The trend continued and stabilized after one million cycles. In contrast, the groups that were exposed to air (B, D, and F) gained weight and stabilized at similar hydration levels after one million cycles of the wear test (Fig. 2).

The overall wear rating was inversely related to the amount of crosslinking. The corrected wear rates for every material group were calculated and are presented in Fig. 3. For noncrosslinked polyethylene with presoaking (A), there was no significant difference in wear rate compared to nonpresoaking (B). For moderately crosslinked thermally-treated polyethylene (C, D, and E), the wear rates were identical and were independent of different initial hydration levels (Fig. 3). For the highly crosslinked thermally-treated polyethylene (F), the wear rate was similar to a previous study with standard presoaking protocol [5].

If the load soak correction is not applied (only the weight loss of each liner is reported without compensating the fluid absorption), the wear rate of the polyethylene is affected for the first million cycles, especially for Group E (Fig. 4). However, the stabilized wear rates for each group were not affected (Table 2).

**Discussion**

This study showed that pressurized soaking could effectively enhance the hydration of polyethylene (thermally-treated, crosslinked at 5 Mrad gamma irradiation) up to eight times that produced from a standard soaking protocol. However, the hydration levels had no significant effect on polyethylene wear performance. The repeated loading in the hip simulator results in the water absorbed in the test compo-

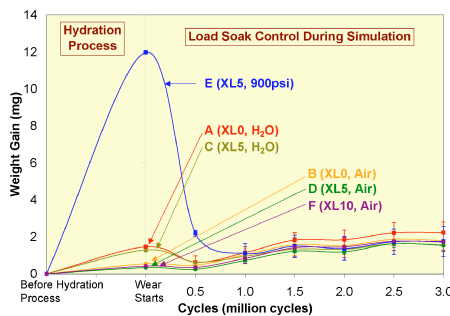


FIG. 2—The weights of load soak control components during hydration period and wear testing. As soon as the wear test started, the highly hydrated group (E) lost weight during the first 0.5-million cycle interval, which was due to the repeated loading that expelled the absorbed water. All components achieved similar hydration levels after one million wear cycles.

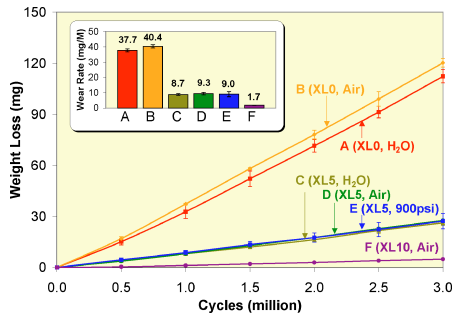


FIG. 3—Wear rates with load soak control correction. The greater wear was inversely related to irradiation dose. With load soak control correction, the wear rates appeared to be linear throughout the wear test.

nents quickly being expelled once the wear test began. The results suggested that the different hydration levels between current laboratory test protocols and a surgeon's clinical procedures had a minimal effect on polyethylene wear.

With load soak control correction, the wear rates appeared to be linear throughout the wear test (Fig. 3). Without load soak control correction, the wear rates were affected by the changing of hydration levels in the first 0.5 million cycles (Fig. 2). This phenomenon was most prominent for Group E, where the wear rate was  $19.6 \pm 1.3$  mg in the first million cycles (Fig. 4), which was more than double that with load soak control correction. In addition, the impact of this correction will be higher on the low wear components (Table 2), as the percentage change is based on the small denominator. Although the wear rates appeared similar with or without correction after one million cycles, the load soak control method is recommended in the test protocol in order to obtain a better estimation of component wear.

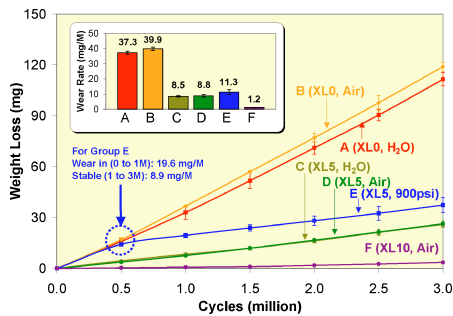


FIG. 4—Wear rates without applying load soak control. The initial wear of Group E doubled. The overall wear rate ranking for the three polyethylene materials remained the same.

TABLE 2—Effect of Load Soak Correction on PE Wear Rate.

		Wear Rate (mg/million cycles)					
		XL0		XL5		XL10	
		A	B	C	D	E	F
Test Cycles	Load Soak Correction	H <sub>2</sub> O	Air	H <sub>2</sub> O	Air	900psi	Air
0–1M (wear-in)	yes	32.7±4.0	37.3±0.5	8.0±0.9	8.1±0.5	8.7±1.3	1.2±0.2
	No	33.0±4.0	36.8±0.5	8.4±0.9	7.7±0.5	19.6±1.3	0.8±0.2
1–3M (stable)	Yes	39.7±0.3	41.4±1.6	9.2±0.4	9.8±1.0	9.2±1.8	1.9±0.0
	No	39.2±0.3	41.0±1.6	8.9±0.4	8.4±1.0	8.9±1.8	1.4±0.0

This study demonstrated the effect of hydration levels on the wear of UHMWPE with or without load soak correction. The limitation was a small sample number for each group ( $N=2$ ). However, it revealed important factors in wear evaluation.

### References

- [1] McKellop, H., Clarke, I. C., et al., "Wear Characteristics of UHMW Polyethylene: A Method for Accurately Measuring Extremely Low Wear Rates," *J. Biomed. Mater. Res.*, Vol. 12, 1978, pp. 895–927.
- [2] ASTM Standard F 1714-96, "Standard Guide for Gravimetric Wear Assessment of Prosthetic Hip Designs in Simulator Devices," ASTM International, West Conshohocken, PA, 2002, pp. 1098–1104.
- [3] Taylor, S. K., Serekian, P., et al., "The Effect of Serum Pre-soak Duration on UHMWPE Acetabular Insert Wear Under Hip Joint Simulation—An Apparent Artifact," 44th Annual Meeting, Orthopaedic Research Society, New Orleans, LA, 1998.
- [4] Yao, J. Q., Blanchet, T. A., et al., "Effect of Fluid Absorption on the Wear Resistance of UHMWPE Orthopedic Bearing Surfaces," *Wear*, Vol. 255, Nos. 7–12, 2003, pp. 1113–1120.
- [5] Liao, Y.-S., Greer, K., et al., "Effects of Resin and Dose on Wear and Mechanical Properties of Crosslinked Thermally Stabilized UHMWPE," Society for Biomaterials, the 7th World Biomaterials Congress, Sydney, Australia, 2004.

Joachim Kunze, Dipl.Ing.<sup>1,2</sup> and Markus A. Wimmer, Ph.D.<sup>2</sup>

## A Tracer Method to Determine Extremely Low Wear Rates of Ultrahigh Molecular Weight Polyethylene

**ABSTRACT:** Wear testing protocols of ultrahigh molecular weight polyethylene (UHMWPE), which rely on gravimetric or topographic measurements, or both, for wear determination, are usually complicated due to fluid absorption or creep, or both, of the polyethylene samples. In this study we report the feasibility of using a tracer material to quantify wear of polyethylene. Europium (Eu), a rare earth element, has been identified as a suitable tracer material. Eu can be quantified with ICP-MS. Nascent UHMWPE powder has been mixed with a solution of Eu-acetate. Different mixing techniques were tried to homogenize the tracer distribution before consolidation. After molding, the 10-mm diameter pins were worn on a pin-on-disk testing apparatus. In addition, lubricant samples were taken at regular time intervals. The Eu content was analyzed and the derived polyethylene wear rate was compared with the weight loss of the pins.

**KEYWORDS:** polyethylene, wear, wear measurement, tracer material, marker

### Introduction

Recent developments of cross-linked ultrahigh molecular weight polyethylene (UHMWPE) push the limits of applicable wear testing standards for total joint replacement. The respective testing protocols rely on gravimetric or topographic measurements, or both, for accurate wear determination. These testing protocols are being complicated due to fluid absorption or creep, or both, of the polyethylene samples which can be in the same order of magnitude as the wear itself [1–7]. In this study we report the feasibility of using a tracer material to quantify wear of polyethylene. Europium (Eu), a rare earth material, has been identified as the tracer material of choice. Eu can still be detected at a concentration of as low as  $10^{-13}$  g/g in aqueous solutions using inductively coupled plasma mass spectrometry (ICP-MS). Its occurrence is limited to two stable isotopes, which greatly simplifies mass spectrometry. In addition, previous studies have shown good biocompatibility where Eu has been used in cell and animal studies as fluorescent marker [8–11]. Nascent UHMWPE powder has been mixed with concentrated Eu-acetate solution and lyophilized. Liquid nitrogen milling was tried to further homogenize the tracer distribution before consolidation. Tracer homogeneity was then assayed by scanning electron microscopy, as well as by backward concentration measurements.

### Materials and Methods

#### Tracer Preparation

A solution of 1.0824 g Europium acetate,  $\text{Eu}(\text{OOCCH}_3)_3$ , (Alfa Aesar<sup>®</sup>)<sup>1</sup> in 50 mL of deionized water  $>15 \text{ M}\Omega$  (Milli-Q<sup>TM</sup>)<sup>2</sup> has been prepared. This solution contains 10 mg/mL Europium. Stoichiometric data: Europium acetate,  $\text{Eu}(\text{OOCCH}_3)_3$ : 328.96 g/mol, Eu: 151.96 g/mol.

Manuscript received November 28, 2005; accepted for publication June 12, 2006; published online August 2006. Presented at ASTM Symposium on Wear of Articulating Surfaces on 8 November 2005 in Dallas, TX; S. A. Brown, L. N. Gilbertson, and V. D. Good, Guest Editors.

<sup>1</sup> Director, Hamburg University of Technology, Laboratory for Analytical Chemistry, Eißendorfer Str. 38, D-21073 Hamburg, Germany and Faculty of Rush University Medical Center, Chicago, Illinois Visiting Instructor in the Department of Orthopedic Surgery, Rush University, 1653 W. Congress Parkway, Chicago, Illinois 60612–3864.

<sup>2</sup> Ass. Professor & Director, Section of Tribology, Department of Orthopedics, Rush University Medical Center, Amour Academic Facilities, Suite 761, 1653 W. Congress Parkway, Chicago, IL 60612.

<sup>1</sup>Alfa Aesar Johnson Mathey GmbH, Karlsruhe, Germany.

<sup>2</sup>Millipore, Bedford, MA, USA.

TABLE 1—Microwave sample preparation system, Perkin-Elmer® multiwave.

Phase	Power (W)	Time (mm:ss)	Power(W)	Fan
1	100	5:00	500	1
2	500	15:00	800	1
3	0	15:00	0	3

Note: Parameter for quartz glass vessels, 50 mL, operating pressure up to 74 bar (7400 kPa), solution reaches a temperature of 190°C during digestion process.

### Mixing Process

Ten grams of nascent GUR 412 UHMWPE powder were weighed in a 50 mL round flask, and seven crystal balls of 8-mm diameter were added. The powder was mixed with 20 mL of Eu-acetate solution and homogenized by use of an ultrasonic bath for 5 min. The powder was dried on a rotary evaporator for 20 min. The remaining water was then removed by drying over phosphorus oxide ( $P_2O_5$ ) in a desiccator. Dried powder was put aside and labeled as material “#3.” To further homogenize the sample, the remaining portion of the powder was transferred into an agate ball mill of 80-mm diameter with three agate balls of 25-mm diameter each. After the addition of liquid nitrogen the powder was milled for 3 min. This material was then labeled “#5.” The intended concentration of the tracer (Eu) was 20 per mill in both cases. Tracer homogeneity was then assayed by scanning electron microscopy as well as by backward concentration measurements. Different masses of Tracer-UHMWPE-powder (T-powder) have been used to study the homogeneity of the tracer. A Perkin-Elmer<sup>3</sup> microwave digestion system (Multiwave) with a six-position rotor with 50-mL quartz glass vessels was used prior analysis. Five-milligram samples of T-powder #5 were weighed into the microwave quartz containers and nitric acid was added. One millilitre of deionized water ( $>15 M\Omega$ ) and 2 mL of  $HNO_3$  (sub-boiling distilled, suprapure grade) were added. The digestion was carried out as described below (see Table 1). Six replicates for each mass of T-powder have been analyzed.

### Manufacturing of Pins for Wear Testing

A 2-mm layer of the T-powder (either #3 or #5) was placed in the bottom of a 3-in. (76.2-mm) diameter puck mold and covered with enough virgin GUR 1050 UHMWPE to mold a 1 in. (25.4-mm) thick puck. The molding pressure and temperature protocol was similar to those typically applied for GUR 1050. Wear pins, 0.375 in. (9.53 mm) by 0.750 in. (19.1 mm) in length, were machined from the molded puck by Zimmer, Inc. The as-molded condition of the bottom (Eu-containing side) of the puck was maintained. In addition, pins without tracer were manufactured. All wear pins were then packaged in a nitrogen environment in foil pouches and gamma sterilized at 26–35 kGy.

### Wear Test

An OrthoPOD<sup>TM</sup> (Advanced Mechanical Technology, Inc.) multidirectional pin-on-disk wear tester was used. A 5-mm by 5-mm square motion pattern was applied to generate crossing motion trajectories. Testing was conducted at a 1 Hz cycle frequency and with a constant applied load to generate a nominal contact pressure of 3 MPa. These exact same conditions have been used previously by others [12]. Each pin articulated against a polished cobalt-chromium disk ( $Ra=0.020 \mu m$ ). In a pilot test three samples (materials #3, #5, and control) were evaluated. Each articulation was submersed in 15 mL of new born calf serum diluted to a protein content of 30 g/L. Additives were added to the fluid to stabilize the pH value at 7.6 throughout each testing interval of 250 k cycles, avoid calcium precipitation, and retard bacterial growth. The temperature of the lubricant was maintained at 37°C. The complete test lasted for 2 million cycles. Serum samples were taken at nine defined intervals (0, 250 k, 500 k, ..., 2,000 k cycles). These samples were tested for the presence of the rare earth tracer via ICP-MS and a *chemical* wear rate was determined. Additionally, changes in mass were determined every 250 k cycles and corrected using a soak control. Those *gravimetric* wear rates were compared with chemically determined wear. Cleaning and weighing procedures followed the respective ASTM standards and recommendations.

<sup>3</sup>Perkin-Elmer Live and Analytical Sciences, Inc., Boston, MA, USA.

TABLE 2—ICP-MS conditions for the measurement of Eu.

Isotopes, Eu	151, 153 m/z
Internal Standard, Rh	103 m/z
Elemental standard stock solutions	Eu, Rh: 1000 mg/L
	B. Kraft <sup>6</sup>
H <sub>2</sub> O Millipore	Milli-Q <sup>TM</sup>
HNO <sub>3</sub> (65 %)	Sub-boiling distillation grade, lab made
Calibration	0 / 0.1 / 0.5 / 1 / 2 / 5 / 10 µg/L Eu
Linearity of the curve Eu 153 m/z	0.999973
ICP RF power	1100 W
Argon gas flow	15 L/min

<sup>6</sup>B. Kraft, Duisburg, Germany.

### Analysis of Tracer Content

At each specific time interval, 2 mL of serum were pipetted into a single polypropylene (PP) sample tube with the help of a 1 mL syringe. The samples were transported to the Laboratory of Analytical Chemistry and thoroughly mixed by ultrasound prior to digestion. A 1 mL sub-sample of serum was then pipetted into a microwave container. The pipettes used were Eppendorf<sup>TM</sup> 4. Two millilitres of HNO<sub>3</sub> were added to the serum. The containers were shut and embedded into the microwave six-vessel rotor with a six-vessel capacity. Then the rotor is placed into the microwave oven for driving the temperature/time program as listed below (Table 1).

After cooling to room temperature the containers were opened under a Heraeus<sup>TM</sup> 5 clean bench with filter, capable of providing class 10 clean air to protect the operator from possible NO<sub>x</sub> generation and to protect the samples from contamination. The clear solution was transferred into a 20 mL glass flask and adjusted with deionized water. Prior to measurement the samples have to be diluted with H<sub>2</sub>O Millipore and adjusted to contain 2 µg/L of Rh as an internal standard. A simultaneous measurement of Europium isotopes 151 (isotopic abundance: 47.8%) and 153 (isotopic abundance: 52.2%) was made using a quadrupole inductively coupled plasma mass spectrometer (ICP-MS). As both isotopes give nearly the same readings, Eu 153 was used for calculation. A Perkin-Elmer SCIEX ELAN<sup>®</sup> 6000 quadrupole ICP-MS was used, equipped with an AS-91 auto sampler. For the conditions to determine Europium, see Table 2.

### Results

GUR 412 powder has a characteristic microstructure. The cauliflower-like particles, which have a size of 50 to 150 µm depict a substructure of 1 to 2 µm spheres that are connected by thin fibers (Fig. 1).

Some of the connecting polyethylene fibers break during this process facilitating the homogeneous distribution of the Eu-tracer (Fig. 2).

While the mixing procedure turned out satisfactorily in terms of achieved homogeneity—the coefficient of variation turned out to be less than 2.5% for the milled powder #5 (Table 3), from a quantitative aspect the results were less agreeable. Approximately one-third of the tracer was lost during the preparation and milling process (i.e., 13.6 instead of 20 per mill; Table 3). The hygroscopic Eu-acetate most likely attached to the walls of glass vessels and/or marble walls, or both, of the milling chamber. Further tracer material was possibly lost during molding of the pins.

Apart from those quantitative inconsistencies, the determined gravimetric and chemical wear rates were very similar as depicted in Fig. 3. The Eu concentration followed qualitatively and quantitatively the weight loss of the pin. Hence, gravimetric and chemical wear rates were highly correlated (adj.  $r^2 = 0.88$ ;  $p < 0.05$ ). Despite this satisfactory correlation, the slope was different from one when UHMWPE weight loss was calculated based on a 20 per mill Eu concentration. This was consistent with the mixing inconsistencies summarized in Table 3. Figure 4 compares the overall wear of the three different materials. Due to the pilot character of the study, conclusions with regard to tracer effect on UHMWPE wear performance cannot be made.

<sup>4</sup>Eppendorf AG, Germany.

<sup>5</sup>Heraeus Holding GmbH, Hanau, Germany.

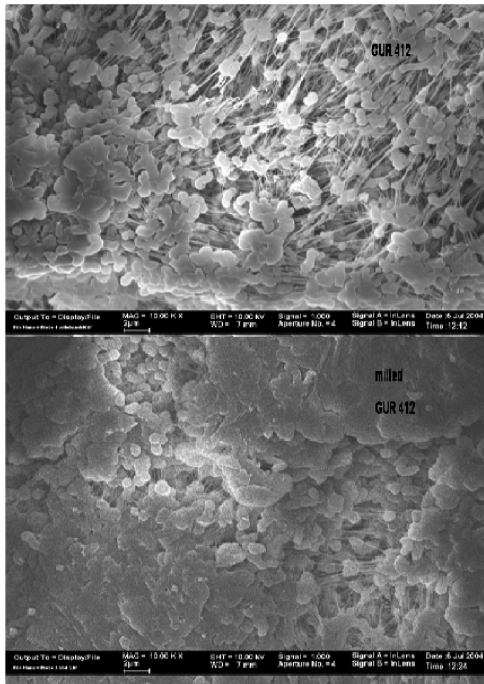


FIG. 1—Comparison of GUR 412 before (above) and after (below) liquid nitrogen milling.

**Discussion**

The presented technique is capable in quantifying wear of polyethylene (UHMWPE) in extremely low masses of wear debris. As a first approach Eu-acetate has been applied as a tracer substance. Homogeneity of the water-soluble tracer and its ability to be mixed with UHMWPE powder are considered satisfactory. The influence of the mixing technique is demonstrated and showed absorbents effects of the tracer with the glassware used for the process of staining. Nevertheless, scanning electron microscopy observation and

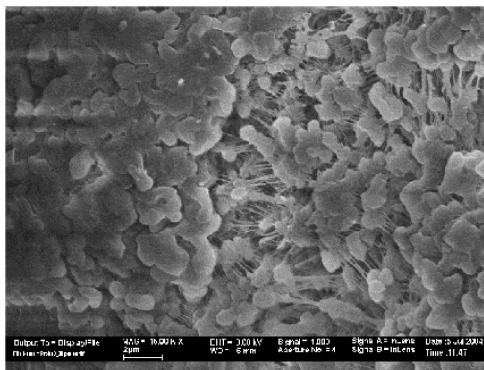


FIG. 2—T-powder. White spots represent Europium-acetate particulates that appear bright due to their high density using backcentered imaging. The existence of Eu was confirmed with energy dispersive X-ray analysis (data not shown).

TABLE 3—Concentration measurements for homogeneity studies (material #5). Distribution of the Eu-acetate within six 5 mg samples of the GUR412 powder.

T-Powder Samples	Eu [per mill]
S1 (4.9 mg)	14.2
S2 (4.8 mg)	13.5
S3 (4.8 mg)	13.5
S4 (4.9 mg)	13.6
S5 (4.6 mg)	13.6
S6 (4.7 mg)	13.3
Mean	13.6
Standard deviation	0.306

ICP-MS measurements demonstrated the availability of a homogeneously distributed tracer, with a relatively small coefficient of variation of better than 2.5%. The concentration of Europium of 13.6 per mill after milling was further reduced due to the applied molding process as suggested by the mismatch of weight loss and chemical data. The exact remaining Eu content within the pin is therefore currently investigated.

The question whether the addition of a tracer affects the wear behavior of polyethylene could not be answered due to the pilot character of this study. The wear rates of the pins with tracer fluctuated around

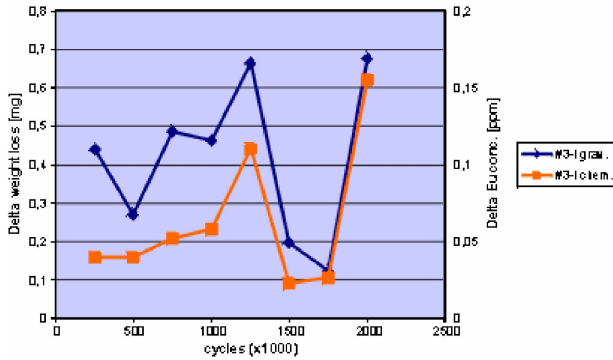


FIG. 3—Comparison of gravimetric and chemical wear measurement techniques. The graph displays the weight loss determined for each wear interval (left vertical axis) versus the europium concentration measurement of the same testing interval (right vertical axis). Note that both measurements carry similar information.

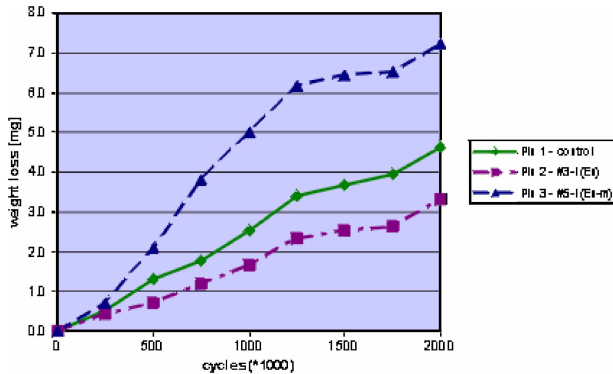


FIG. 4—Gravimetric wear. Comparison of T-powder #3 and #5 against control.

the wear rate of the control pin. However, all wear rates of this study were smaller than those presented by Turell et al. [12] who used identical load and motion characteristics with their Orthopod investigating the same material combination.

Future studies will focus on the synthesis of nonwater-soluble Eu compounds to achieve superior homogeneity and reduced concentration levels of the tracer within the powder. Whereas this study demonstrated the general feasibility of adding a rare earth tracer to polyethylene, future studies are necessary to quantify the influence of the tracer on the wear properties of UHMWPE itself. Further, the effects of a water-soluble substance on the long-term mechanical properties as well as fatigue performance have to be determined.

#### Acknowledgments

The support of Zimmer Inc. in molding the testing samples is acknowledged.

#### References

- [1] Kurtz, S. M., *The UHMWPE Handbook*, Elsevier Academic Press, San Diego, CA, 2004.
- [2] Kaddick, C. and Wimmer, M. A., "Hip Simulator Wear Testing According to Newly Introduced Standard 14242," *Proc. Inst. Mech. Eng., Part H: J. Eng. Med.*, Vol. 215, No. H5, 2001, pp. 429–442.
- [3] Endo, M., Tipper, J. L., Barton, D. C. et al., "Comparison of Wear, Wear Debris and Functional Biological Activity of Moderately Crosslinked and Non-crosslinked Polyethylenes in Hip Prostheses," *Proc. Inst. Mech. Eng., Part H: J. Eng. Med.*, Vol. 216, No. H2, 2002, pp. 111–122.
- [4] Besong, A. A., Tipper, J. L., Mathews, B. J. et al., "The Influence of Lubricant on the Morphology of Ultra-high Molecular Weight Polyethylene Wear Debris Generated in Laboratory Tests," *Proc. Inst. Mech. Eng., Part H: J. Eng. Med.*, Vol. 213, No. H2, 1999, pp. 155–158.
- [5] Fisher, J., Bell, J., Barbour, P. S. et al., "A Novel Method for the Prediction of Functional Biological Activity of Polyethylene Wear Debris," *Proc. Inst. Mech. Eng., Part H: J. Eng. Med.*, Vol. 215, No. H2, 2001, pp. 127–132.
- [6] Mc Kellop, H. A., Shen, F. W., Campbell, P. et al., "Effect of Molecular Weight, Calcium Stearate, and Sterilization Methods on the Wear of Ultra High Molecular Weight Polyethylene Acetabular Cups in a Hip Joint Simulator," *J. Orthop. Res.*, Vol. 17, No. 3, 1999, pp. 329–339.
- [7] Oparaugo, P. C., Clarke, I. C., Malchau, H. et al., "Correlation of Wear Debris-induced Osteolysis and Revision with Volumetric Wear-Rates of Polyethylene: A Survey of 8 Reports in Literature," *Acta Orthop. Scand.*, Vol. 72, No. 1, 2001, pp. 22–28.
- [8] Ogawa, Y., Suzuki, S. et al., *Toxicity Study of Europium Chloride in Rats*, 1995.
- [9] Nakamura, Y., Tsumara, Y., Tonogai, Y. et al., "Differences in Behavior Among the Chlorides of Seven Rare Earth Elements Administered Intravenously to Rats," *Fundam. Appl. Toxicol.*, Vol. 37, No. 2, 1997, pp. 106–116.
- [10] Das, T., Sharma, A., and Talukder, G., "Effects of Lanthanum in Cellular Systems. A review," *Biol. Trace Elem. Res.*, Vol. 18, 1988, pp. 201–228.
- [11] Bingham, D., and Dobrota, M., "Binding of Lanthanides to Cell Membranes in the Presence of Ligands," *J. Inorg. Biochem.*, Vol. 59, No. 1, 1995, pp. 39–52.
- [12] Turell, M., Wang, A., and Bellare, A., "Quantification of the Effect of Cross-path Motion on the Wear Rate of Ultra-high Molecular Weight Polyethylene," *Wear*, Vol. 255, No. 7, 2003, pp. 1034–1039.

## **SECTION IV: TOTAL HIP**

Georg Reinisch,<sup>1</sup> Joachim Schoerg,<sup>2</sup> Eva Leder,<sup>3</sup> Kurt P Judmann,<sup>4</sup> Wolfgang Plitz,<sup>5</sup> and Friedrich Franek<sup>6</sup>

## Differences of the Mechanical Setup of Hip Simulators and Their Consequences on the Outcome of Hip Wear Testing

**ABSTRACT:** The search for improved wear resistant materials for hip endoprotheses has lead to an international standard for wear testing of total hip joint prosthesis (ISO 14242). The displacement and load curves in this standard are derived from clinical gait analysis. However the standard leaves the interpretation of its displacement curves open since no coordinate system is defined in the document. By reviewing the development of the standard, the apparent coordinate system is identified and its application from both, an anatomical point of view and a technical perspective for designing hip simulators is explained. The study examines the coordinate transformations necessary for using common gait analysis data with the standard. On the basis of these transformations, the relative movements of the articulating surfaces are compared with existing hip simulators, the situation in vivo and the guidelines of the ISO standard. Thus possible consequences on the outcome of hip wear testing are discussed.

**KEYWORDS:** hip simulator, wear, tribology, artificial hip joint

### Nomenclature

$k$  = wear factor ( $10^{-6}$  mm<sup>3</sup>/Nm)  
 $L$  = Load (N)  
 $N$  = number of load cycles ( $\cdot 10^6$ )  
 $s$  = length of relative movement (mm)  
 $V$  = volume of material removed (mm<sup>3</sup>)

### Introduction

Since its introduction by Charnley [1], the development of new, highly wear resistant materials for the articulating surfaces of total hip endoprotheses has led to an increasing demand for testing and durability studies of these products. Such testing and research include not only testing for bio-compatibility and static load carrying capacity, but also tribological investigations.

---

Manuscript received September 27, 2005; accepted for publication May 2, 2006; published online June 2006. Presented at ASTM Symposium on Wear of Articulating Surfaces on 8 November 2005 in Dallas, TX; S. A. Brown, L. N. Gilbertson, and V. D. Good, Guest Editors.

<sup>1</sup> Ph.D., Institute of Sensor and Actuator Systems, Microsystems Technology, Vienna University of Technology, Floragasse 7, A 1040 Vienna, Austria. Corresponding address: Biomechanische Forschungs-Gesellschaft m.b.H., Rechte Wienzeile 5/2, A 1040 Vienna, Austria. Electronic address: reinisch.bmf@jic.at

<sup>2</sup> M.Sc., Otto Bock, Healthcare Products GmbH, Kaiserstraße 39, A 1070 Vienna, Austria.

<sup>3</sup> M.D., Biomechanische Forschungs-Gesellschaft m.b.H., Rechte Wienzeile 5/2, A 1040 Vienna, Austria.

<sup>4</sup> Professor, Ph.D., Institute for Computer Technology, Vienna University of Technology, Gußhausstraße 27-29, A 1040 Vienna, Austria.

<sup>5</sup> Professor, Ph.D., M.D., Labor für Biomechanik und Experimentelle Orthopaedie, Marchioninistraße 23, D 81377 Munich, Germany.

<sup>6</sup> Professor, Ph.D., Institute of Sensor and Actuator Systems, Microsystems Technology, Vienna University of Technology, Floragasse 7, A 1040 Vienna, Austria.



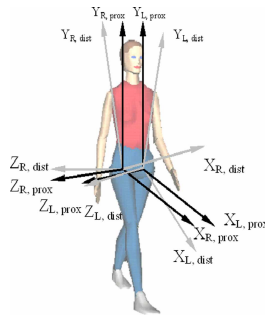


FIG. 2—Coordinate systems at walking according to the definition of the ISB [12] with their origins in the joint center.

ity. For example, a positive rotation of the femur about the horizontal axis in the frontal plane in a left-handed coordinate system on the left body side and in a right-handed coordinate system on the right body side both result in a flexion of the leg (see Fig. 1). The international standard for testing leg prostheses ISO Standard 10328 [11] adopts this convention using the cases f (forward), o (outward), and u (upward). As these definitions show, it is necessary to clearly define the direction of rotation, especially for its anatomical denotation.

In clinical assessment it is generally acknowledged to use right-handed coordinate systems for the right body side and left-handed coordinate systems for the left body side. The notation of the axes with  $x$ ,  $y$ , and  $z$  is arbitrary, but it seems practical to locate the  $x$  and  $y$  axes into the sagittal plane of the object according to two-dimensional models.

To describe the spatial rotation of a specific extremity relative to another part in an orthogonal coordinate system it is necessary to specify not only the single displacements, but also the sequence of rotation. In other words: If the spatial rotation of a hip joint is described by three rotations in a coordinate system, the amount of every single rotation is dependent on the sequence of the rotation. Thus not only angles, but also the sequence has to be defined in order to uniquely describe a spatial rotation movement.

The International Society of Biomechanics (ISB) [12] recommends an unequivocal description of kinematic data. The ISB recommendation defines a reference coordinate system which is placed independent of the side of the body into the mass center of the extremities with the  $y$  axis directed superior, the  $x$  axis in the direction of motion—as for normal walking—and the  $z$  axis orthogonal in the sense of a right-handed coordinate system; i.e., on the right body side (index  $R$ ) in lateral and on the left side (index  $L$ ) in medial direction.

For the application with hip joint movements a modification of this coordinate system seems practical to reduce the complexity of the mathematical description [13]. The origin of this modified coordinate system is defined to be in the center of the joint to describe the displacement of the femur (distal joint member, index *dist*) relative to the pelvis (proximal joint member, index *prox*) only by rotations (without translations; see Fig. 2). It is also assumed that the joint is perfectly spherical. By moving the origins of the coordinate system into the hip joint on each side as described, the  $4 \times 4$  matrices of the ISB recommendation are reduced to merely rotational  $3 \times 3$  matrices for the application in the hip joint.

Rotations are commonly described by matrices.

$$R_i(\varphi) = \begin{bmatrix} C_{11} & C_{12} & C_{13} \\ C_{21} & C_{22} & C_{23} \\ C_{31} & C_{32} & C_{33} \end{bmatrix} \quad (1)$$

The single rotations about individual axes as defined above read:

Rotation about the  $z$  axis [flexion/extension (FE)]

$$R_z(\alpha) = \begin{bmatrix} \cos \alpha & -\sin \alpha & 0 \\ \sin \alpha & \cos \alpha & 0 \\ 0 & 0 & 1 \end{bmatrix} \quad (2)$$

Rotation about the  $y$  axis [inward/outward rotation (IOR)]

$$R_y(\beta) = \begin{bmatrix} \cos \beta & 0 & \sin \beta \\ 0 & 1 & 0 \\ -\sin \beta & 0 & \cos \beta \end{bmatrix} \quad (3)$$

Rotation about the  $x$  axis [adduction/abduction (AA)]

$$R_x(\gamma) = \begin{bmatrix} 1 & 0 & 0 \\ 0 & \cos \gamma & -\sin \gamma \\ 0 & \sin \gamma & \cos \gamma \end{bmatrix} \quad (4)$$

The ISB defines in its recommendation [13] the sequence of the displacements from the normal position using the angles  $\alpha$ ,  $\beta$ ,  $\gamma$  with

First	$\alpha$ ... rotation about the $z$ axis (FE)
Second	$\beta$ ... rotation about the $y$ axis (IOR)
Third	$\gamma$ ... rotation about the $x$ axis (AA)

The rotation matrix follows the matrix product of Eqs 2–4 in the sequence AA before IOR before FE (AA  $\rightarrow$  IOR  $\rightarrow$  FE).

$$R_z(\alpha)R_y(\beta)R_x(\gamma) = \begin{bmatrix} \cos \alpha \cos \beta & \cos \alpha \sin \beta \sin \gamma - \sin \alpha \cos \gamma & \cos \alpha \sin \beta \cos \gamma + \sin \alpha \sin \gamma \\ \sin \alpha \cos \beta & \sin \alpha \sin \beta \sin \gamma + \cos \alpha \sin \gamma & \sin \alpha \sin \beta \cos \gamma - \cos \alpha \sin \gamma \\ -\sin \beta & \cos \beta \sin \gamma & \cos \beta \cos \gamma \end{bmatrix} \quad (5)$$

The individual rotation angles can be found as follows:

$$\alpha = \arcsin(C_{21}/\cos \beta) \quad (6a)$$

$$\beta = -\arcsin(C_{31}) \quad (6b)$$

$$\gamma = \arcsin(C_{32}/\cos \beta) \quad (6c)$$

The rotation order about single axes in a Cartesian coordinate system (Euler's rotation angles), can be regarded as the "definition" of another, nonorthogonal, coordinate system [13]. In such a system the axes are defined as follows: The first axis of rotation in the Cartesian system is a proximal body-fixed axis of the joint. The third axis of the rotation sequence is the distal body-fixed rotation axis and the remaining axis becomes the floating axis, which is always perpendicular to the two other axes. This new coordinate system is generated by the determination of the rotation sequence, however, within this new system the sequence of rotation is arbitrary [13].

Such a coordinate system is defined by the sequence of rotations as flexion/extension (FE) before adduction/abduction (AA) before inward/outward rotation (IOR). The inward/outward rotation axis is fixed to the femur, the flexion/extension axis is fixed to the pelvis, and the floating adduction/abduction axis stands always perpendicular to the plane originated by the FE and IOR axes. Thus flexion/extension is always accomplished about an axis that is permanently fixed relative to the pelvis, regardless of the two other displacements. The IOR axis coincides to the longitudinal axis of the femur in any leg position (see Fig. 3) [14].

As an example, another way of describing the same body-related system according to more mechanical than anatomical terms is shown: Considering the proximal part (pelvis) of the joint as the reference system, the flexion/extension axis never changes its position. The adduction/abduction axis is displaced

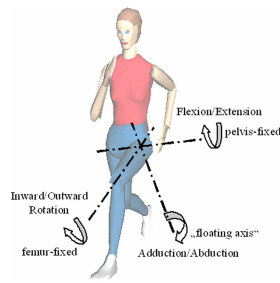


FIG. 3—Coordinate system according to Grood and Suntay [14].

because of the flexion or extension of the femur (not because of the inward/outward rotation); the inward/outward rotation axis follows both rotations, namely, about the flexion/extension axis and about the adduction/abduction axis.

A mechanical simulation of the system described would be realized by a ring that is borne on a horizontal axis (FE axis) with a swing hanging perpendicular from the ring allowing the swing a rotational movement (AA). The swing holds a cradle with a rotational axis (IOR) again orthogonal to the swing (see Fig. 4).

Conversely to the derivation of a mechanical simulation from an abstract anatomical coordinate system, any existing hip simulator determines a coordinate system according to Grood and Suntay [14] by its own mechanics. However, this system requires a specific rotation sequence in a distal Cartesian coordinate system. Defining the proximal component of the joint as an inertial system and thus regarding the inverse movement of this component as the generic motion of the distal part, a rotation sequence is necessary for the distal coordinate system, where the initial (generic) movement has to be applied first in the rotation sequence (see below: *ISO Specification and Hip Simulators*).

#### Displacement Values and Load Curves

Diverging underlying coordinate systems for displacement and load curves are found in gait analysis systems, scientific publications on hip biomechanics, descriptions of hip simulators and related equipment, as well as in the ISO Standard 14242-1. While most sources are oriented on specific applications, and therefore are generically different, the ISO standard is intended to be the source for common and comparable applications of hip wear testing.

#### Gait Analysis

Relative angles and thus displacement curves of the hip joint are collected since the 1960s through optometric human gait analysis [6,15]. Depending on the definition of the coordinate system of the gait analysis setup, a transformation of coordinates will be necessary to apply the collected values to hip simulator testing. For example, a common gait analysis system (Vicon Motion Capture™)<sup>7</sup> uses the ISB recommendation on coordinate systems and the transformation necessary will be explained in detail by an

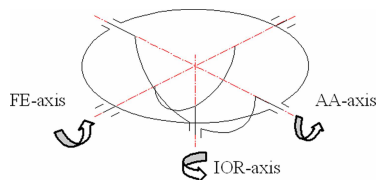


FIG. 4—Mechanical setup of an anatomical coordinate system.

<sup>7</sup>Vicon Peak, 9 Spectrum Pointe Drive, Lake Forest, CA 92630.

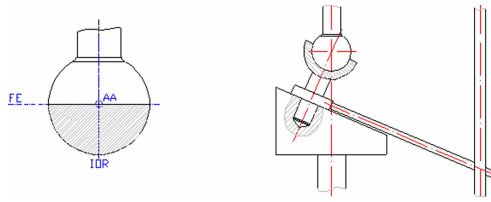


FIG. 5—Illustration of the principle of the OBM (orbital bearing machine); FE flexion/extension, AA adduction/abduction, IOR inward/outward rotation.

example. Another gait analysis system by Motion Analysis (OrthoTrak™)<sup>8</sup> uses a right-handed coordinate system for flexion/extension (FE) about the laterally oriented  $z$  axis on the right body side and a left-handed coordinate system on the left body side. The adduction/abduction (AA) is accomplished about the ventrally orientated  $y$  axis and the inward/outward rotation (IOR) about the inferior directed  $x$  axis. To reach the origin from any displacement position the rotation order FE before AA before IOR is used. Conversely a displacement is committed in the reciprocal sequence (IOR  $\rightarrow$  AA  $\rightarrow$  FE).

#### Definitions Used With Wear Test Equipment

The following examples will show that in many cases the mechanical setup of a hip simulator belongs to one specific movement applied to an articulating bearing. In the popular orbital bearing machines (OBM—hip wear machines) [16] one bearing partner of the hip joint (in most cases the femoral ball head) is fixed and the other component is mounted eccentrically on an inclined, rotating block. In addition an antirotation pin provides for an oscillating rotation about the part's own axis (see Fig. 5).

In a no longer used three-axial hip simulator (HUT-3) by Saikko [17] the acetabular cup performs the IOR and the ball head located above completes the AA and the FE. The mechanical setup of this simulator can be interpreted as an implementation of a coordinate system according to Grood and Suntay [14]. Thus, the rotation sequence in that system according to the ISB recommendation is defined as IOR  $\rightarrow$  AA  $\rightarrow$  FE.

The motion of this hip simulator is quite comparable to that found in gait analysis, however it has no degree of freedom in its mechanical setup to approximate the nonsinusoidal motion of the gait analysis data.

To simulate the kinematics of human gait as closely as possible a hip simulator has to provide three independent rotation actuators (three degrees of freedom) to produce a spatial relative motion with a load regime ideally moving in an oval pathway also relative to the acetabular component [18,19].

#### The ISO 14242-1 Displacement and Load Curves and Wear Measurement

The displacement curves of ISO Standard 14242-1 are based upon the recommendation of the ISB using an orthogonal coordinate system with a rotation order  $z, y, x$ , i.e., with application to the human hip FE  $\rightarrow$  IOR  $\rightarrow$  AA. The motion describes the movement of the femoral part of a total hip joint relative to the acetabular component. For the interpretation of the ISO curves the definitions according to the ISB recommendations apply. The values for the angular movement and the variation of force are described in diagrams with tolerances of  $3^\circ$  and  $\pm 90$  N, respectively [5].

ISO Standard 14242-1 determines the direction of the load into an axis  $30^\circ$  inclined (depending on the design and recommendations of the suppliers) to the vertical axis of the acetabular component (and fixes it there). The temporal amount of the load follows a double peak curve [7].

According to the second part of this standard the volumetric wear is to be measured at 500,000 cycles and then every  $1 \cdot 10^6$  cycles thereafter by gravimetric means or by a three-dimensional measurement method [20].

<sup>8</sup>Motion Analysis Corporation, 3617 Westwind Blvd., Santa Rosa, CA 95403.

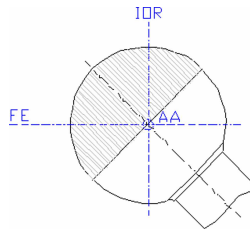


FIG. 6—Projected area of the femoral ball head (hatched hemisphere) used in Figs. 7–10 by an equivalent azimuthal projection looking from above the IOR axis); FE flexion/extension, AA adduction/abduction, IOR inward/outward rotation.

## Tribological Factors in Hip Simulator Testing

### *Relative Motion in the Articulating Zone*

Among others one criteria for the assessment of wear simulation is the characteristics of wear tracks of specific points on the surface of the femoral ball head or acetabular cup within the articulating zone. Especially for polyethylene used as articulating liners a multidirectional trajectory seems to be of essential importance [21,22]. While the track of an arbitrary single point on the surface of, e.g., the acetabular cup can be generated by rotations about only two axes (biaxial movement), only a three axial motion determines the common properties of the trajectories of all points on the surface. Thus, a two-axial system can position the force vector in any specific position on either surface, but it cannot produce the rotation about the load vector axis which is encountered in vivo.

Figure 6 describes the projected area of the femoral ball head (hatched hemisphere) used in the Figs. 7–10 by an equivalent azimuthal projection looking from the direction of the IOR axis. Tracks of randomly chosen points of the acetabular cup are presented in Figs. 7–10 on the surface of the femoral ball head in the sagittal and frontal plane, computed from (a) the ISO standard, (b) a cohort of 60 patients, (c) a patient with an artificial hip joint, and (d) the OBM hip wear machine. The projected area of the femoral ball head viewed from above the IOR axis is displayed. Each closed loop represents the relative movement of one single point on the surface of the object.

Figure 7 shows the wear tracks on the femoral ball head for the ISO 14242 motion as projected to the plane, whereas Fig. 8 illustrates an average gait cycle derived from 60 healthy patients in gait laboratory investigation. The gait data used represent the most common displacement angles and are used as reference data of the gait laboratory. Figure 9 depicts the computed wear tracks derived from gait analysis data of one single patient wearing an artificial hip joint at normal level walking. The wear tracks generated by the OBM simulator are calculated and shown in Fig. 10. As in the original setup of OBM simulators [16] the test specimen are inserted inverted with the femoral component fixed relative to the load. In order to make the diagram of the OBM wear tracks comparable as for the change of load introduction (the load vector is fixed to the femoral component at OBM simulators) the wear tracks on the surface of the acetabular cup (instead of the femoral ball head) have been used for visualization in Fig. 10. The circular wear track around the origin in this figure shows the trajectory of the load vector in the acetabular cup.

The shape of two specific motion tracks are compared in the following: These tracks are generated by the movement of the virtual intersection point of the load vector on the femoral head ball surface. The wear track of the load vector following the ISO standard is displayed on the right-hand side of Fig. 11 and compared to the wear tracks of the resulting load vector with a  $12^\circ$  medial inclination [19] computed from gait analysis of a patient with total hip replacement (THR). Qualitatively the two tracks differ, however an inclination of the load vector seems negligible resulting only in a displacement of the worn area on the femoral ball head, but without any alteration of the wear characteristics such as type of wear and spatial circumference. The shape of the wear tracks are dominated by the flexion/extension displacement, resulting an oval outline. The quantitative analysis of these track lengths is given in Table 1.

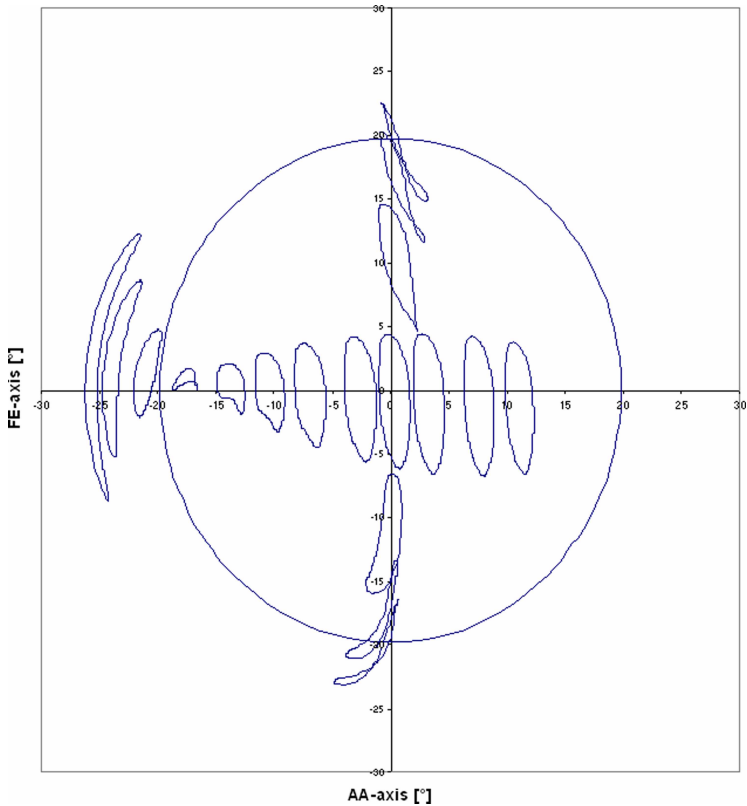


FIG. 7—Wear tracks of the motion derived from the ISO 14242-1. Standard on the surface of the femoral ball head. Flexion/extension (FE) and adduction/abduction (AA) in spatial angles.

#### The Wear Factor

Another important characteristic in wear testing is the wear factor  $k$  described in ISO/TR Standard 9326 [23]. It is defined as *the volume of material removed proportionally to the area under the curve obtained by plotting the values of force  $L$ , in newtons, to a base of corresponding relative movements  $x$ , in metres, in the dynamic load cycle, in newton metres* [23] as expressed in Eq 7.

$$k = \frac{V}{N \int Lds} \quad (7)$$

The value of  $\int ds$  (mm) reflects the length of the motion track and the value of the integral  $\int Lds$  (Nm) presents the work applied by the force along this track for a specific simulation. Numeric values of these integrals are given for the displacement and load curves of the ISO Standard 14242, the OBM wear machine with a double peak load curve of max. 3 kN, a cohort of 60 healthy subjects and one patient with total hip replacement (Table 1). The values derived from gait analysis of patients are based on an inclination of the load vector  $12^\circ$  medially as described by Bergmann et al. [19] to match the wear tracks of the load input of the ISO Standard and the OBM hip simulator at  $0^\circ$  inclination. The values of the ISO standard are computed from the displacement and load curves as they are printed in the standard. A tolerance of  $\pm 3^\circ$  displacement and  $\pm 90$  N load is presented for these data, resulting in a range of 18.61 mm to 26.50 mm for the length of the wear track and 23.28 Nm to 37.71 Nm for the integral  $\int Lds$ . The length of the wear tracks differ slightly between the measurement of the gait analysis and the one specified by the

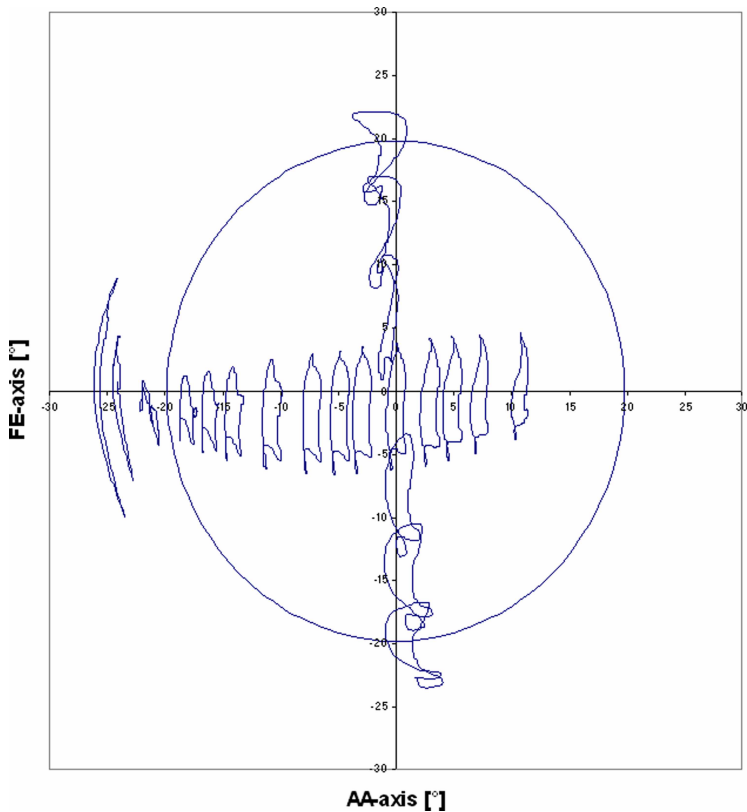


FIG. 8—Wear tracks on the surface of the femoral ball heads of 60 test subjects. Flexion/extension (FE) and adduction/abduction (AA) in spatial angles.

ISO standard. The differences in the work integrals are caused by the high load input (3 kN) from the standard as compared to the measurement of gait analysis at normal level walking [19]. The track length for the OBM machine exceeds the clinical reference values by 53 %, which is in accordance to the findings of Saikko and Calonius [24], whereas the work integral is exceeded by 34 % due to less load input of OBM machines [25,26].

#### *ISO Specification and Hip Simulators*

As shown above the mechanical setup of a simulator determines an appropriate coordinate system to describe displacements generated by its mechanics. For a hip simulator that meets the ISO Standard 14242-1 the transformation needed to use the ISO displacement values as input are shown in this section. According to the ISB recommendation on the displacement of the distal (femoral) components only, the mechanical setup would require that all displacements are applied to the femoral part. The load is introduced and fixed to the acetabular cup in the vertical  $y$  axis of the proximal coordinate system.

Since the rotation axis is identical to the action line of the load it does not make any difference for the inward/outward rotation whether the acetabular cup or the femoral ball head is rotated. A transformation of the inward/outward rotation from the distal (femoral) component to the proximal (acetabular) component is possible. However, it is important to change the sequence of rotation. In the following example (Fig. 12) this is achieved by a ring (1) that is borne on a horizontal axis (FE axis) with a swing (2) hanging from the

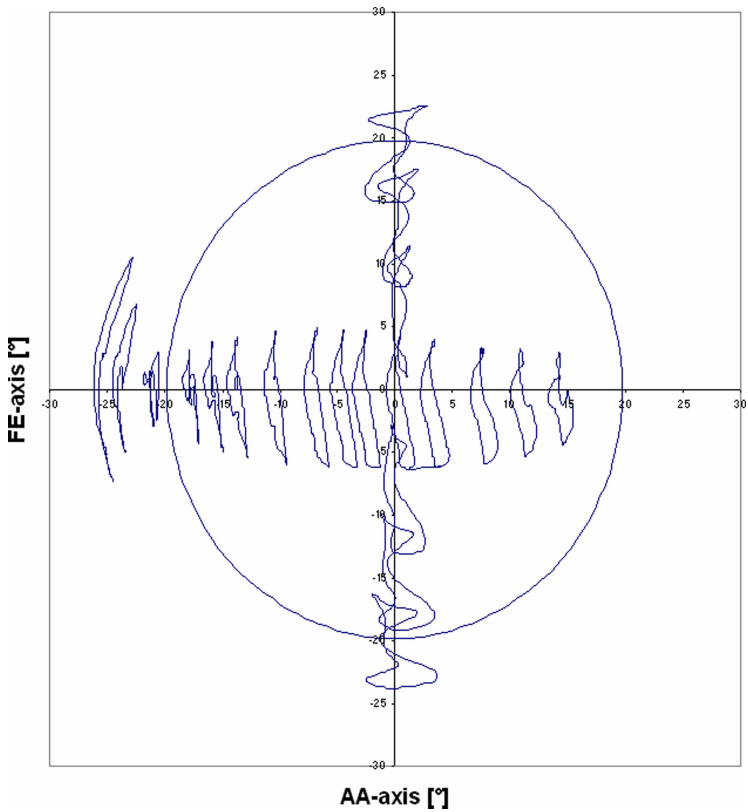


FIG. 9—Wear tracks on the surface of the femoral ball head of a patient wearing a total hip endoprostheses. Flexion/extension (FE) and adduction/abduction (AA) in spatial angles.

ring allowing the swing a rotational movement (AA) perpendicular to the displacement of the ring. The IOR is now accomplished by the acetabular component (3) (compare with Fig. 4).

Again, looking at the proximal (acetabular) component as an inertial system, the distal (femoral) component follows now the rotation sequence IOR → FE → AA, as the inward/outward rotation has been transferred to the proximal component. Holding the simulator ostensive by its IOR axis, the whole simulator would twist about the acetabular cup, while in the simulator the ring would do the flexion/extension movement and in the ring the swing would abduct/adduct. Denoted in a co-ordinate system according to Grood and Suntay [14] the IOR axis becomes proximally fixed, the AA axis is distally fixed, and the FE axis represents the floating axis. By transforming the inward/outward rotation from the distal component to the proximal component, a system is created in which the mechanical displacements of the simulator can be more easily conducted and studied from the mechanical point of view, even if a transformation of the

TABLE 1—Characteristic values of the wear track length and the work integral of the ISO Standard 14242, a cohort of 60 healthy subjects, one patient with total hip replacement and the OBM wear simulator.

	ISO 14242	60 Healthy subjects	Patient with THR	OBM simulator
Inclination of resulting force vector	0°	12°	12°	0°
Wear track length $\int ds$ (mm)	22.46	22.5	23.3	34.3
Integral $\int Lds$ (Nm)	29.99	25.5	30.6	40.1

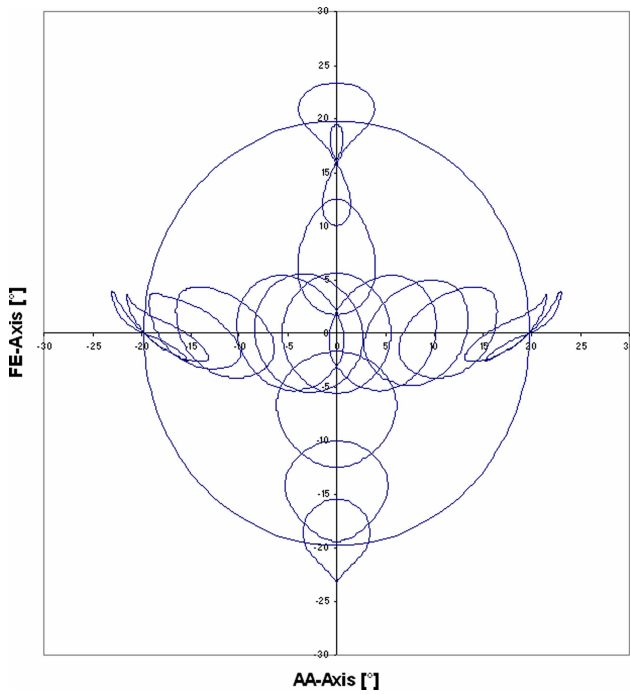


FIG. 10—Wear tracks on the surface of the acetabular cup in an OBM-wear test machine (Fig. 5). Flexion/extension (FE) and adduction/abduction (AA) in spatial angles.

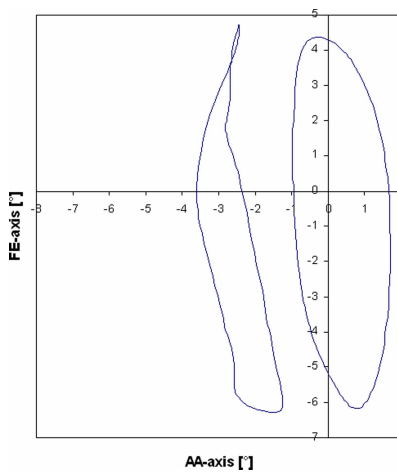


FIG. 11—Comparison of the wear tracks on the surface of the femoral ball head of the ISO Standard 14242 and a patient wearing a total hip replacement (THR) recorded in gait analysis. Flexion/extension (FE) and adduction/abduction (AA) in spatial angles.

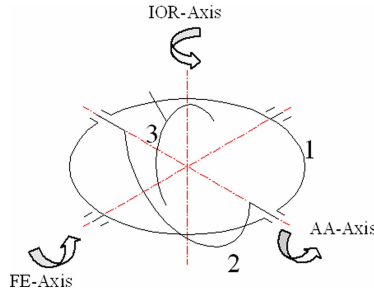


FIG. 12—Principle of an ISO hip simulator; with inward/outward rotation accomplished by the proximal (acetabular) component. FE flexion/extension, AA adduction/abduction, IOR inward/outward rotation.

anatomical situation is necessary to use gait laboratory data as input values for hip simulators. The rotation matrix of the three axial movement results from the multiplication of Eqs 2–4 in the sequence below:

$$R_y(\beta)R_z(\alpha)R_x(\gamma) = \begin{bmatrix} \cos \alpha \cos \beta & -\sin \alpha \cos \beta \sin \gamma + \sin \beta \sin \gamma & \sin \alpha \cos \beta \sin \gamma + \sin \beta \cos \gamma \\ \sin \alpha & \cos \alpha \cos \gamma & -\cos \alpha \sin \gamma \\ -\sin \beta \cos \alpha & \sin \alpha \sin \beta \cos \gamma + \cos \beta \sin \gamma & -\sin \alpha \sin \beta \sin \gamma + \cos \beta \cos \gamma \end{bmatrix} \quad (8)$$

The individual rotation angles can be found as follows:

$$\alpha = \arcsin(C_{21}) \quad (9a)$$

$$\beta = -\arcsin(C_{31}/\cos \alpha) \quad (9b)$$

$$\gamma = -\arcsin(C_{23}/\cos \alpha) \quad (9c)$$

By the transformation of the displacement angles 10 all points of the acetabular cup surface follow the correct trajectories—now independent of the coordinate system applied. The equation of the transformation 10 results from the input of the rotation matrix 5 and 9.

$$\alpha_{SIM} = \arcsin(\sin \alpha_{ISO} \cos \beta_{ISO}) \quad (10a)$$

$$\beta_{SIM} = -\arcsin\left(\frac{-\sin \beta_{ISO}}{\cos \alpha_{SIM}}\right) \quad (10b)$$

$$\gamma_{SIM} = -\arcsin\left(\frac{\sin \alpha_{ISO} \sin \beta_{ISO} \cos \gamma_{ISO} - \cos \alpha_{ISO} \sin \gamma_{ISO}}{\cos \alpha_{SIM}}\right) \quad (10c)$$

### Gait Analysis Data and Hip Simulator

As many gait-analysis laboratories use the ISB recommendation for their coordinate systems the displacements collected by such systems can be used directly as input values of the hip simulator described above, provided the transformation 9 is performed as the inward/outward rotation has been shifted from the distal to the proximal component of the joint (Fig. 13).

Analog to the transformation above the relationship between the displacement angles of another frequently used gait analysis system OrthoTrak™ (index OT) and the simulator defined above follows: The definition of the axes *x*, *y*, and *z* in Eqs 11 and 12 refer to the ISB recommendation [12].

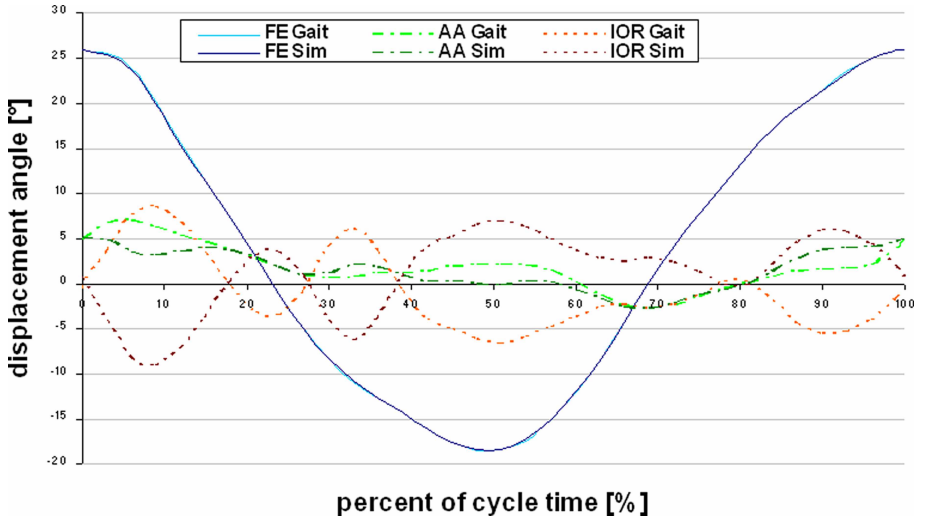


FIG. 13—Transformation of gait analysis data from Vicon Motion Capture™ for implementation in a hip simulator as developed in “ISO specification and hip simulators.”

$$R_y(\beta)R_x(\gamma)R_z(\alpha) = \begin{bmatrix} \sin \alpha \sin \beta \sin \gamma + \cos \alpha \cos \beta & \cos \alpha \sin \beta \sin \gamma - \sin \alpha \cos \beta & \sin \beta \cos \gamma \\ \sin \alpha \sin \gamma & \cos \alpha \sin \gamma & -\sin \gamma \\ \sin \alpha \cos \beta \sin \gamma - \cos \alpha \sin \beta & \cos \alpha \cos \beta \sin \gamma + \sin \alpha \sin \beta & \cos \beta \cos \gamma \end{bmatrix} \quad (11)$$

The input angles of the hip simulator are presented in Eqs 9a–9c; using now transformation 11 of the gait analysis system OrthoTrak™ as input leads to the results in Eq 12.

$$\alpha_{\text{SIM}} = \arcsin(\sin \alpha_{\text{OT}} \sin \gamma_{\text{OT}}) \quad (12a)$$

$$\beta_{\text{SIM}} = -\arcsin\left(\frac{-\sin \alpha_{\text{OT}} \cos \beta_{\text{OT}} \sin \gamma_{\text{OT}} - \cos \alpha_{\text{OT}} \sin \beta_{\text{OT}}}{\cos \alpha_{\text{SIM}}}\right) \quad (12b)$$

$$\gamma_{\text{SIM}} = -\arcsin\left(\frac{-\sin \gamma_{\text{OT}}}{\cos \alpha_{\text{SIM}}}\right) \quad (12c)$$

Using these transformations 12a–12c displacement values from the gait analysis software OrthoTrak™ can also be used for the three axial hip simulator defined above.

## Conclusion

Due to the different coordinate systems and sequence of rotation between the ISO standard, based on the ISB recommendation and many hip simulators currently in use a transformation of the rotational displacement angles (depending on the mechanics of the simulator) as shown exemplary above is needed to execute the movements as defined by the standard.

The ISO patterns of movement of the articulating surfaces correspond closely to the data from healthy patients and a subject wearing a hip joint replacement.

Existing biaxial hip simulators are capable to produce ISO compatible movements of a single point (e.g., the fictional intersection of the load vector). However, the tribologic active zone is spread on an area of the surface of both, the femoral ball head and the acetabular cup [27,28]. Thus, a variety of model points

(asperity tips [28]) are involved in the tribologic action for which only a three-axial simulator concept can provide wear tracks according to the situation in-vivo.

As for the OBM simulator, displacements are given which differ remarkably from those obtained from gait analysis measurements and the ISO standard. Moreover the kinematics of this simulator type produces a 53 % longer track length and a work integral exceeding 34 % gait analysis and the ISO standard [24,25]. This results in an excessive energy consumption leading to unphysiological high frictional heating between bearing partners [29,30]. However, physiological wear results have been produced by these simulators for a metal-on-polyethylene material combination, but their capability is to be monitored for the new challenging material combinations such as metal-on-metal, ceramic-on-ceramic, cross-linked polyethylene, and newly developed material combinations.

### Acknowledgments

The authors would like to thank Ing. Mag. A. Kranzl, Orthopaedisches Spital Speising, Vienna, Austria for providing gait analysis data and Dipl.-Ind. Roland Mueksch, Ph.D., Oxford Orthopaedic Engineering Centre, Oxford, United Kingdom, for providing gait analysis data of a patient wearing a total hip replacement.

### References

- [1] Charnley, J., *Low Friction Arthroplasty of the Hip – Theory and Practice*, Springer-Verlag, Berlin, 1979.
- [2] Schmalzried, T. P., Jasty, M., and Harris, W. H., “Periprosthetic Bone Loss in Total Hip Arthroplasty: The Role of Polyethylene and the Concept of the Effective Joint Space,” *J. Bone Jt. Surg., Am. Vol.* Vol. 74A, 1992, pp. 849–856.
- [3] Harris, W. H., “The Problem Is Osteolysis,” *Clin. Orthop. Relat. Res.* Vol. 311, 1995, pp. 46–53.
- [4] ASTM Standard F 1714, “Standard Guide for Gravimetric Wear Assessment of Prosthetic Hip-Designs in Simulator Devices,” Annual Books of ASTM Standards, Section 13, Vol. 13.01, West Conshohocken, PA, 1996 (reapproved 2002).
- [5] ISO Standard 14242, “Implants for Surgery-Wear of Total Hip Joint Prosthesis-Part 1: Loading and Displacement Parameters for Wear Testing Machines and Corresponding Environmental Conditions for Test,” ISO, CH 1211, Geneva 20, 2000.
- [6] Johnston, R. C., and Smidt, G. L., “Measurement of Hip-Joint Motion During Walking. Evaluation of an Electrogeniometric Method,” *J. Bone Jt. Surg., Am. Vol.* Vol. 51A, No. (6), 1969, pp. 1082–1094.
- [7] Paul, J. P., “Forces Transmitted by Joints in the Human Body,” *Proc. Inst. Mech. Eng.* Vol. 181, 1966/67, pp. 8–15.
- [8] Woltring, H. J., “3-D Attitude Representation of Human Joints: A Standardization Proposal,” *J. Biomech.* Vol. 27, No. (12), 1994, pp. 1399–1414.
- [9] BIOMCH-L. Various discussions in the archives (February, March 1990, January-May 1992) retrievable by sending commands of the form SEND BIOMECH-LOGgyymm in the main body of an e-mail note to [LISTSERV@HEARN.BITNET](mailto:LISTSERV@HEARN.BITNET) or [LISTSERV@NIC.SURFNET.NL](mailto:LISTSERV@NIC.SURFNET.NL), 1990, 1992.
- [10] Wittenburg, J., *Dynamics of Systems of Rigid Bodies*, Stuttgart: B. G. Teubner, 1977.
- [11] ISO Standard 10328, “Prosthetics – Structural Testing of Lower-Limb Prostheses,” ISO, CH 1211, Geneva 20, 1996.
- [12] Wu, G., and Cavanagh, P. R., “ISB Recommendations for a Standardization in the Reporting of Kinematic Data,” *J. Biomech.*, Vol. 28, No. (10), 1995, pp. 1257–1261.
- [13] Wu, G., Siegler, S., Allard, P., Kirtley, C., Leardini, A., Rosenbaum, D., Whittle, M., D’Lima, D. D., Cristofolini, L., Witte, H., Schmid, O., and Stokes, I., “ISB Recommendation on Definitions of Joint Coordinate System of Various Joints for the Reporting of Human Joint Motion – Part 1: Ankle, Hip, and Spine,” *J. Biomech.*, Vol. 35, No. (4), 2002, pp. 543–548.
- [14] Grood, E. S., and Suntay, W. J., “A Joint Coordinate System for the Clinical Description of Three-Dimensional Motions: Application to the Knee,” *J. Biomech. Eng.*, Vol. 105, 1983, pp. 136–144.
- [15] Andriacchi, T. P., and Hurwitz, D. E., “Gait Biomechanics and the Evolution of Total Joint Replacement,” *Gait and Posture*, Vol. 5, 1997, pp. 256–264.

- [16] Medley, J. B., Krygier, J. J., Bobyn, J. D., Chan, F. W., Lippincott, A., and Tanzer, M., "Kinematics of the MATCO™ Hip Simulator and Issues Related to Wear Testing of Metal-Metal Implants," *Proc. Inst. Mech. Eng., Part H: J. Eng. Med.*, Vol. 211, 1997, pp. 89–99.
- [17] Saikko, V., "A Three Axis Hip Joint Simulator for Wear and Friction Studies on Total Hip Prostheses," *Proc. Inst. Mech. Eng., Part H: J. Eng. Med.*, Vol. 210, 1996, pp. 175–185.
- [18] Viceconti, M., Cavallotti, G., Andrisano, A. O., and Toni, A., "Discussion on the Design of a Hip Joint Simulator," *Med. Eng. Phys.*, Vol. 18, No. (3), 1996, pp. 234–240.
- [19] Bergmann, G., Deuretzbacher, G., Heller, M., Graichen, F., Rohlmann, A., Strauss, J., and Duda, G. N., "Hip Contact Forces and Gait Patterns From Routine Activities," *J. Biomech.*, Vol. 34, No. (7), 2001, pp. 859–871.
- [20] ISO Standard 14242, "Implants for Surgery—Wear of Total Hip Joint Prosthesis—Part 2: Methods of Measurement," ISO, CH 1211, Geneva 20, 2000.
- [21] Bragdon, C. R., O'Connor, D. O., Lowenstein, J. D., Jasty, M., and Syniuta, W. D., "The Importance of Multidirectional Motion on the Wear of Polyethylene," *Proc. Inst. Mech. Eng., Part H: J. Eng. Med.*, Vol. 210, 1996, pp. 157–165.
- [22] Wang, A., Polineni, V. K., Essner, A., Sokol, M., Sun, D. C., Stark, C., and Dumbleton, J. H., "The Significance of Nonlinear Motion in the Wear Screening of Orthopaedic Implant Materials," *J. Test. Eval.*, Vol. 25, No. (2) 1997, pp. 239–245.
- [23] ISO/TR Technical Report 9326, "Implants for Surgery—Partial and Total Hip Joint Prostheses—Guidance for Laboratory Evaluation of Change of Form of Bearing Surfaces," ISO, CH 1211, Geneva, 20, 1989.
- [24] Saikko, V., and Calonijs, O., "Slide Track Analysis of the Relative Motion Between Femoral Head and Acetabular Cup in Walking and in Hip Simulators," *J. Biomech.*, Vol. 35, No. (4), 2002, pp. 455–464.
- [25] Maxian, T. A., Brown, T. D., Pedersen, D. R., and Callaghan, J. J., "3-Dimensional Sliding/Contact Computational Simulation of Total Hip Wear," *Clin. Orthop. Relat. Res.*, Vol. 333, 1996, pp. 41–50.
- [26] Saikko, V., Calonijs, O., and Keranen, J., "Effect of Extent of Motion and Type of Load on the Wear of Polyethylene in a Biaxial Hip Simulator," , Vol. 65B, No. (1), 2003, pp. 186–192.
- [27] Chan, F. W., Bobyn, J. D., Medley, J. B., Krygier, J. J., Tanzer, M., "Wear and Lubrication of Metal-on-Metal Hip Implants," *Clin. Orthop. Relat. Res.*, Vol. 369, 1999, pp. 10–24.
- [28] Schey, J. A., "Systems View of Optimizing Metal on Metal Bearings," *Clin. Orthop. Relat. Res.*, Vol. 329S, 1996, pp. S115–S127.
- [29] Lu, B., and McKellop, H., "Frictional Heating of Bearing Materials Tested in a Hip Joint Wear Simulator," *Proc. Inst. Mech. Eng., Part H: J. Eng. Med.*, Vol. 211, 1997, pp. 101–108.
- [30] Liao, Y. S., McKellop, H., Lu, Z., Campbell, P., and Benya, P., "The Effect of Frictional Heating and Forced Cooling on the Serum Lubricant and Wear of UHMW Polyethylene Cups Against Cobalt-Chromium and Zirconia Balls," *Biomaterials*, Vol. 24, No. (18), 2003, pp. 3047–3059.



[www.astm.org](http://www.astm.org)

Stock # STP1472